INFORMATION TO USERS

This manuscript has been reproduced from the microfilm master. UMI films the text directly from the original or copy submitted. Thus, some thesis and dissertation copies are in typewriter face, while others may be from any type of computer printer.

The quality of this reproduction is dependent upon the quality of the copy submitted. Broken or indistinct print, colored or poor quality illustrations and photographs, print bleedthrough, substandard margins, and improper alignment can adversely affect reproduction.

In the unlikely event that the author did not send UMI a complete manuscript and there are missing pages, these will be noted. Also, if unauthorized copyright material had to be removed, a note will indicate the deletion.

Oversize materials (e.g., maps, drawings, charts) are reproduced by sectioning the original, beginning at the upper left-hand corner and continuing from left to right in equal sections with small overlaps. Each original is also photographed in one exposure and is included in reduced form at the back of the book.

Photographs included in the original manuscript have been reproduced xerographically in this copy. Higher quality 6" x 9" black and white photographic prints are available for any photographs or illustrations appearing in this copy for an additional charge. Contact UMI directly to order.

UMI

A Bell & Howell Information Company
300 North Zeeb Road, Ann Arbor MI 48106-1346 USA
313/761-4700 800/521-0600

MODELING OF ARCTIC STRATUS CLOUD FORMATION AND THE MAINTENANCE OF THE CLOUDY ARCTIC BOUNDARY LAYER

A

THESIS

Presented to the Faculty

of the University of Alaska Fairbanks

in Partial Fulfillment of the Requirements

for the Degree of

DOCTOR OF PHILOSOPHY

By

Qiuqing Zhang

B.S., M.S.

Fairbanks, Alaska

May 1999

MODELING OF ARCTIC STRATUS CLOUD FORMATION AND THE MAINTENANCE OF THE CLOUDY ARCTIC BOUNDARY LAYER

By

Qiuqing Zhang

RECOMMENDED:

Dr. Jerry Harrington

Dr. Davis Sentman

Dr. Brenton Watkins

Dr. Knut Stamnes (Advisory Committee Chair)

Dr. Brenton Watkins (Department Head)

APPROVED:

Dean, College of Science, Engineering and Mathematics

Dean of the Graduate School

3-19-99

Date

Abstract

The formation of Arctic stratus clouds (ASCs) and the maintenance of the cloudy Arctic boundary layer are studied with two models: a one-dimensional radiative-convective model and a three-dimensional large eddy simulation (LES) model.

The one-dimensional radiative-convective model consists of a comprehensive radiative module, a cloud parameterization with detailed microphysics and a convective adjustment scheme. The model is designed specifically for studying ASC formation. With this model, the roles of radiation and cloud microphysics in the formation of ASCs and multiple cloud layers are investigated. The simulations reproduce both single and multiple cloud layers that were observed with inversions of temperature and humidity occurring near the cloud top. The detailed cloud microstructure produced by the model also compares well with the observations.

The physics of the formation of both single and multiple cloud layers is investigated. Radiative cooling plays a key role during the initial stage of cloud formation in a atmosphere. It leads to a continual temperature decrease promoting water vapor condensation on available cloud condensation nuclei. The vertical distribution of humidity and temperature determines the radiative cooling and eventually where and when the cloud forms. The observed temperature inversion may also be explained by radiative cooling.

The three-dimensional LES model is adopted to evaluate the one-dimensional model, especially the convective adjustment scheme. The advantages and limitations of the one-dimensional model are discussed. The LES results suggest that the convective adjustment scheme is capable of capturing the main features of the vertical heat and moisture fluxes in the cloudy Arctic boundary layer.

The LES model is also used to investigate the maintenance of the cloudy Arctic boundary layer. The turbulence in the cloudy Arctic boundary layer is primarily maintained by the buoyancy effect due to the cloud top cooling. It is found that weak large scale downward motion aids in cloud development and maintenance.

Contents

List of Figures

List of Tables

Acknowledgements

First and foremost, my sincere appreciation is expressed to my advisor Dr. Knut Stamnes for his constant support, encouragement and excellent advising. Furthermore, I wish to thank Drs. Oystein Lie-Svendsen, Jerry Harrington, Peter Olsson, Brenton Watkins and Davis Sentman for their comments, stimulating discussions, suggestions and criticisms. I would also like to thank Drs. Victor Filyushkin, Chin-Hoh Moeng and Douglas Lilly for their assistance in improving my understanding of the large eddy simulation model. Thanks to Jennifer, Michael and all fellows in our group for their help and cooperation.

Finally, I would like to extend my heartfelt gratitude toward my wife, Lihong Yu, for her years of unconditional support and love. Her assistance in developing the parallel version of the large eddy simulation model was critical for this research. Without the parallel version of this model, the large eddy simulations would never have been done.

This research was supported by NSF DPP-Polar Ocean & Climate Systems Grant OPP94-15350, and by the Environmental Science Division of the U.S. Department of Energy as part of the Atmospheric Radiation Measurement Program through U.S. Department of Energy contract 091574-A-Q1 with the University of Alaska. It was also supported by the Center for Global Change and Arctic System Research under the 1996 Student Research Grant. Support was also provided by the Arctic Region Supercomputing Center by giving access to supercomputer resources.

Chapter 1

Introduction

1.1 The climatic significance of Arctic stratus clouds

The importance of the Arctic region and Arctic clouds to global climate has been highlighted by climate research in recent years. The results of climate modeling with doubled CO_2 concentrations suggest that the Arctic region is of particular importance and vulnerability to global climate change (e.g., Manabe et al., 1991). Unfortunately, high-latitude climate modeling skills lag behind those of other regions. This deficiency is at least partly due to the fact that climate models are unable to adequately represent Arctic cloud systems as well as the interactions among clouds, atmosphere, surface albedo and radiative transfer (Walsh and Crane, 1992). Studies also show that the interactions between cloud and radiation play an important role in global climate (e.g. Wetherald and Manabe, 1988; Mitchell and Ingram, 1992).

Low-level stratus clouds are a persistent, summertime feature in the Arctic region. These Arctic stratus clouds (ASCs) dominate over the Arctic Ocean during the summer months from May through September. They are one of the most significant features of the local climate. Previous studies suggested that ASCs have an important influence on global climate by affecting not only the surface radiation balance but also the vertical structure of the boundary layer (Vowinckel and Orvig, 1964, 1970; Herman, 1977, 1980).

They have an influence on the vertical transfer of heat, moisture and momentum and hence impact the melting rate of the pack ice (Curry et al., 1993). These cloud modulate the radiative energy budget at high latitudes, by reflecting solar radiation back to space as well as intercepting outgoing infrared radiation and returning a large fraction of it back to Earth by reflection, absorption and reemission. Over the annual cycle, modeling studies have shown that ASCs warm the lower atmosphere (Curry et at., 1993) and cause an earlier onset of springtime snowmelt than otherwise would occur under a clear sky (Zhang et al., 1996). ASCs may also exert an influence on the global energy budget by interacting with radiation.

Unfortunately, current climate models poorly simulate Arctic boundary-layer clouds. The physical processes giving rise to ASCs in the Arctic cloud boundary layer are poorly understood. The parameterizations for Arctic cloud processes used by many climate models are developed based on environments vastly different from the Arctic region. Because of the different thermodynamic and radiative environments existing in the Arctic, those parameterizations may be inappropriate for representing the cloud feedback processes over the Arctic Ocean (Curry et al., 1996). Studies of the formation and persistence of ASCs are therefore of importance both for understanding the local climate at high latitudes and for regulating the global climate (Stamnes et al., 1999). It is also important to study the processes occurring within the ASC boundary layer and the interaction among Arctic clouds, radiation and dynamics.

Arctic clouds present unique challenges for satellite remote sensing. The determination of polar cloud characteristics often uses current satellite observations. Significant obstacles are encountered because the Arctic clouds are predominately optically thin and low lying and the underlying snow/ice surface presents little visible, thermal, or microwave contrast between the clouds and the underlying surface. ASCs can affect satellite remote sensing of the surface. In such cases one needs to know the characteristics of the interaction as well as cloud particle properties. Therefore, further detailed study is required of the temporal and spatial motion scales as well as underlying basic

physical processes.

Some difficulties exist in studying ASCs due not only to lack of observational data but also to their unique properties, especially the frequent appearance of multiple cloud layers. Therefore, not only intensive observations but also modeling studies are required in order to enhance our understanding of the processes responsible for the formation of ASCs and the Arctic climate.

1.2 An overview of observational studies

ASCs are one of the most prevalent features over the Arctic Ocean. Monthly-averaged low cloud cover amounts are up to 70% for the summer months from May through September (Huschke, 1969; Vowinckel and Orvig, 1970) (Figure 1.1). The cloud amounts significantly decrease in winter. A steep increase occurs during April and a rapid decrease occurs in October.

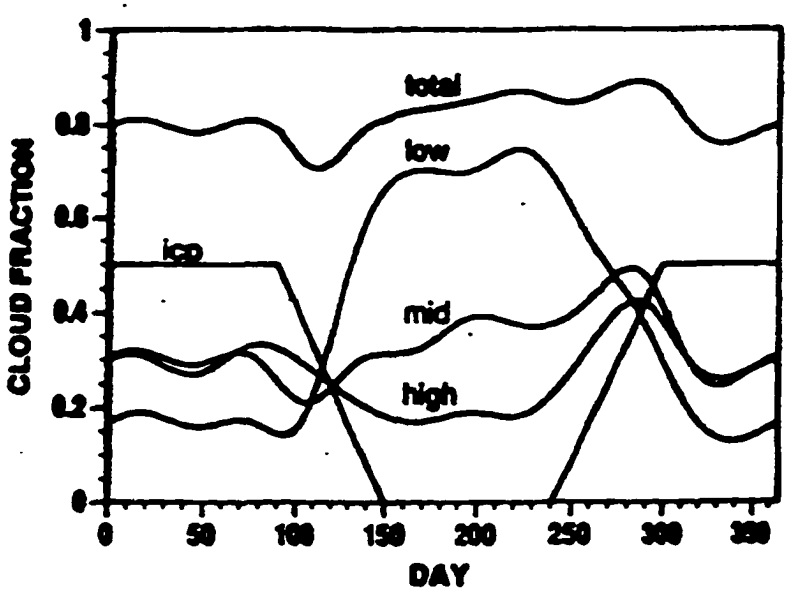

Figure 1.1. Annual cycle of cloud fraction, including lower-tropospheric ice crystal precipitation (from Huschke, 1969).

A number of major field experiments were or are being conducted over the Arctic

region in recent years. The Arctic Stratus Experiment (ASE) was conducted during June 1980 over the Beaufort Sea. A series of case studies have been presented based on the observations obtained during this experiment (e.g., Tsay and Jayaweera, 1984; Curry and Herman, 1985; Curry, 1986; Curry et al., 1988; Tsay et al., 1989). FIRE (the First ISCCP Regional Experiment) phase III was initiated in 1995. It led to an Arctic Cloud Experiment field campaign, conducted over the Beaufort Sea ice off the north coast of Alaska in the spring of 1998, aimed at assessing the role of Arctic clouds in the high latitude climate system. Collaborations between FIRE III, SHEBA (Surface Heat Budget of the Arctic Ocean) and ARM (Atmospheric Radiation Measurement) programs have led to a unique data set.

1.2.1 Structure of a cloud boundary layer

The structure of ASCs boundary layer is quite complex and variable from observation to observation. ASCs occur within the lower atmosphere below about 2000 meters. They have a thickness of a few hundred meters (usually from 150 to 500 meters) (Dergach et al., 1966). They are tenuous, and frequently observed to be laminated or comprised of two or more separate, well defined layers (Jayaweera and Ohtake, 1973; Herman, 1977). Up to five distinguishable cloud layers have been observed so far. Frequently, the lowest layer may reach the earth surface.

Curry et al. (1988) categorized ASC boundary layers into three broad groups. The first group is characterized by a stable boundary layer with thin, patchy clouds that may occur in numerous layers. The second is characterized by a stable cloudy layer occurring near the surface surmounted by a cloud-topped mixed layer. The third is characterized by a cloud-topped mixed layer that extends from the surface.

The characteristics of the ASC boundary layer essentially depend upon the airflow in which they form. It was found that ASCs form in three synoptic situations (Tsay and Jayaweera 1984).

(1) When clouds occur in cold polar air flowing over a warmer sea-ice surface, ASCs

are formed by a convective-type process and have an elevated base and a low liquid water content (LWC).

(2) When warm moist air flows over the arctic ocean, clouds form very near the sea-ice surface, and more than one cloud layer may form depending on the availability of moisture aloft.

(3) ASCs form as a result of occluded and surviving frontal systems. In this case, they have complex morphologies, and their microstructures are different from the other two situations.

The structure of the ASC boundary layer is further determined by the optical and thermal properties of liquid water drops and ice crystals (Polar Group, 1980). The presence of temperature and humidity inversions right above cloud top is a dominant feature in the cloudy Arctic boundary layer. The vertical fluxes in a upper cloud layer may decouple from the surface fluxes (Curry et al., 1988).

1.2.2 Cloud microphysical properties

Cloud microphysical properties that have significant effects on cloud radiative properties include the amount of cloud water, the density and size of the cloud particles, and the phase and shape of the particles.

Observations during the Arctic Stratus Experiment show that the microstructure of ASCs observed over the Beaufort Sea has considerable similarity with those of stratus or stratocumulus elsewhere (Tsay and Jayaweera, 1984). The summertime clouds usually had LWC less than 0.5 g/m^3. The mean LWC is characteristic of the air mass forming the clouds and it is essentially determined by the mean drop concentration. The vertical profiles of LWC show values that generally increase with height because of an increase in droplet size rather than concentration. There is a marked horizontal homogeneity (except near the cloud top) in the average values of drop diameter, concentration, and LWC. In the lower halves of the cloud layers, droplet concentrations and LWC remained constant or increased with height. Fluctuations in droplet concentrations and LWC were

observed only in the upper halves of the cloud layers. These fluctuations are wavelike with crests separated by about 1 km. The droplet concentration changes by about a factor of 2. There is no significant change in mean size. This suggests that dry air entrainment at the cloud top causes little change in the shape of the drop spectrum, but can lead to substantial fluctuations in droplet concentration.

Observations show that values of the measured liquid water paths (LWP in units of g/m^2) ranged from 11 to 117 g/m^2 (Tsay and Jayaweera, 1984). Supersaturations were usually smaller than 1%. Cloud droplet concentrations range from values as low as 50 cm^{-3} to a maximum of 500 cm^{-3}. Droplet equivalent radius (defined to be the average droplet radius weighted by the droplet cross-sectional area) ranged from 3.6 to 11.4 μm with an average value of 7.5 μm.

Tsay and Jayaweera (1984) found that for all single cloud layers and the upper cloud layers observed in Arctic Stratus Experment, the droplet distribution changed from a single mode near the cloud base to a double mode (with peaks at 6 μm and 16 μm in diameter) near the cloud top. The drop size distribution was related to the nature of the clouds. They pointed out that in the upper half of the cloud, where bimodal distributions were observed, the droplet concentration decreased vertically with height but fluctuated horizontally.

Theoretical models of mixing processes predict the evolution of a bimodal distribution in the regions where mixing takes places. The bimodal distributions occur through inhomogeneous mixing when the frequency of infiltration of the cloud by air parcels is low (Baker et al., 1980). Horizontal and vertical cloud microstructures suggest that inhomogeneous mixing of dry air occurs.

1.2.3 Radiative properties

Several studies (e.g., Herman and Curry, 1984; Curry and Herman, 1985; Tsay et al., 1989) discuss the optical properties of the summertime ASCs based on the observations during the Arctic Stratus Experiment. The single-scattering properties of the cloud drops

(e.g., volume extinction coefficient and single scattering albedo) as well as the cloud bulk radiative properties (i.e., reflectance, transmittance, absorptance and emittance) depend significantly upon the drop size distribution. According to Herman and Curry (1984), values of shortwave optical depth for the summertime ASCs range from 2 to 24. The cloud reflectances and transmittances lie in the range from 0.2 to 0.82 and from 0.8 to 0.25. respectively. The reflectance of the cloud plus surface determined by Herman (1977) ranged from 60 to 75%.

Curry and Herman (1985) determined the bulk cloud emittances and found that they ranged from 0.4 to 1.0. Cloud absorptances were more difficult to ascertain and were found to vary strongly with droplet effective radius. Peak shortwave cloud radiative warming rates were determined to lie between 0.4 and 1.6 K/hour (Curry, 1986; Tsay et al., 1989), with the peak warming rates occurring just below cloud top. Peak cloud-top longwave cooling rates were determined to be in a range between -2 and -7 K/hour. Net in-cloud warming rates were generally negative although there may be net heating in the lower portion of the cloud where shortwave heating dominates. The cloud longwave radiative extinction depths, which describes the distance below cloud top over which the net longwave flux is reduced by e^{-1}, were determined to vary from 32 to 120 m.

1.2.4 Formation, persistence and dissipation processes

ASCs may form under a broad range of meteorological conditions which influence their overall thermodynamic and microphysical structure. The characteristics of ASCs essentially depend upon the air flow in which they form. ASCs might form under three types of meteorological conditions (Tsay and Jayaweera, 1984):

- The first is in cold polar air flowing over a warmer sea-ice surface. In this case, ASCs form by convective-type processes, and the cloud has an elevated base and a low LWC.

- The second is in warm moist air flows over the Arctic Ocean. Clouds form very

near the sea-ice surface, and more than one cloud layer may form depending on the availability of moisture aloft.

- The third is a result of occluded and surviving frontal systems. In this case. cloud microstructures are different from the other two situations. and cloud morphologies are complex.

Herman and Goody (1976) suggested that ASCs might form when the atmosphere is either in a convective or nonconvective state. When clouds form in a convective state. the air mass is initially colder than the sea-ice surface. The top of the cloud undergoes continuous lifting. These clouds have a high base and near-saturated adiabatic conditions exist below. When clouds form in a nonconvective state the air mass is initially warmer than the sea-ice surface. These clouds form by diffusive cooling of the air mass in contact with the sea ice. They are relatively thin and have very low bases that often reach the ice surface. Once the clouds are formed, radiative effects will influence their growth. Formation of any higher cloud layers is determined by the advection of moist air that undergoes ascending motion.

Multiple layering is frequently observed to occur in the Arctic summertime boundary layer (Jayaweera and Ohtake, 1973; Tsay and Jayaweera, 1984; Curry et al., 1988). This multiple layering makes ASCs different from subtropical stratocumulus, and it is still not well understood. Three hypotheses were proposed to explain this phenomenon. Tsay and Jayaweera (1984) proposed that the upper cloud layer is formed by very weak ascent/entrainment, while the low-level cloud is an advective cloud. Herman and Goody (1976) employed a one-dimensional turbulence closure-radiative transfer model and proposed a "greenhouse" mechanism that caused condensation of an initially unsaturated air mass due to longwave emission to space and radiative and diffusive cooling to the colder surface. Cloud absorption of solar radiation in the intermediate levels of the cloud caused local evaporation and the formation of two separate cloud lyers. McInnes and Curry (1995b) suggested a third mechanism: radiative cooling leads initially to the formation of a cloud layer near the peak of the preexisting temperature and humidity

inversion where radiative cooling is the strongest. The air above the surface, which is warmer than the surface and the upper-level cloud base, cools and condenses, forming the second layer.

Persistence is a significant feature of ASCs. The cloud layer may last for days. Herman (1975) suggested that the persistence of ASCs is due to the absence of cloud dissipation mechanism (e.g., precipitation, radiative heating, convective heating of the boundary layer, and large-scale synoptic activity). Entrainment into the cloud layer seems to be of little importance in ASCs dissipation (Curry, 1986).

1.2.5 An Arctic stratus case observed on June 28, 1980

Most of the soundings used for the studies in this thesis are from data taken on June 28, 1980 during the Arctic Stratus Experiment over the Beaufort sea. Detailed descriptions of the experiment and analyses of the physical properties of the boundary layer were given by Tsay and Jayaweera (1984). Two nearly parallel layers of stratus clouds were observed (Figure 1.2). The upper layer of clouds, with its top at near 1.2 km and base at 0.8 km, has an average thickness of about 376 m. It was capped with a strong temperature inversion and a significant moisture decrease. The temperature lapse rate ($T_c = 5.7°C/km$) inside the cloud was very close to the saturated adiabatic lapse rate ($T_s = 6.0°C/km$). The maximum LWC of about 0.5 g/m^3 appears near the cloud top and decreases downward with height with a rate close to the adiabatic value. The lower cloud layer, with its top at 110 m, has a thickness of 80 m, and is located within a very stable layer near the surface. It has a maximum LWC of about 0.1 g/m^3. A weak stably-stratified layer existed between the two cloud layers.

Several studies have been conducted to investigate the formation of these two cloud layers. Three hypotheses were proposed as mentioned in the previous section.

Curry et al. (1988) showed that wind shear was weak throughout the region of the upper cloud layer and that buoyancy production dominates the turbulent kinetic energy. Wind shear was strong only near the gound.

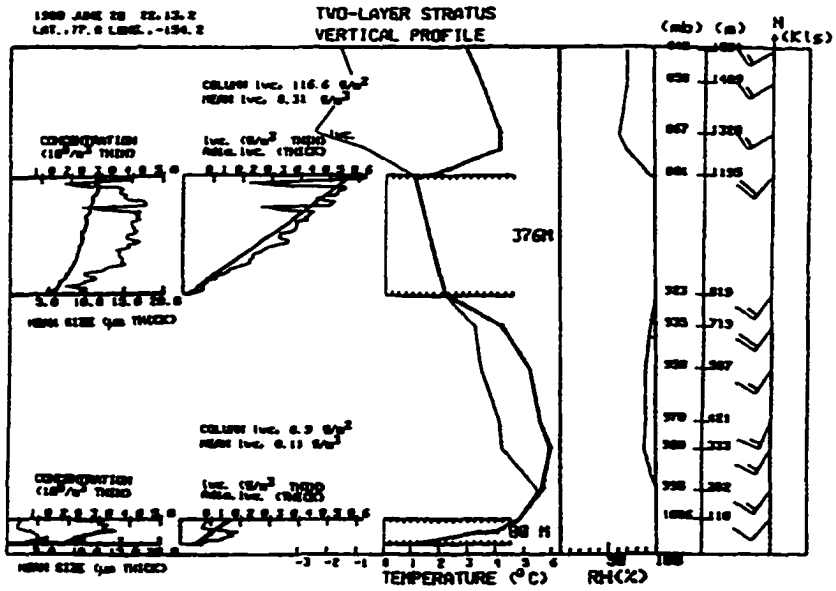

Figure 1.2. Observation on June 28, 1984 during Arctic Stratus Experiment (from Tsay and Jayaweera, 1984).

Droplet concentrations in the upper cloud layer was as large as 450 cm^{-3} (Tsay and Jayaweera, 1984). A bi-modal distribution was observed near the cloud top (peaks at 6 and 16 μm diameter) and a mono-modal distribution appeared near the cloud base (peak at 6 μm) (Figure 1.3). Such distributions can be explained in terms of cloud top entrainment, vertical mixing and, recently, radiative impacts on the growth of drops (Harrington et al., 1998) has also been put forth as a possible mechanism.

The solar radiative heating rates, as computed by Curry (1986), have a maximum of about 1.5 K/hour (about 35 K/day) while the infrared cooling rates had a maximum of -7.1 K/hour (about -170 K/day).

1.3 An overview of modeling studies

ASC processes are poorly understood due to the lack of observational data. The interpretation of ASC observational studies is rather difficult since most of the observed cases have a complicated structure such as detached cloud-subcloud layers or multiple-layer

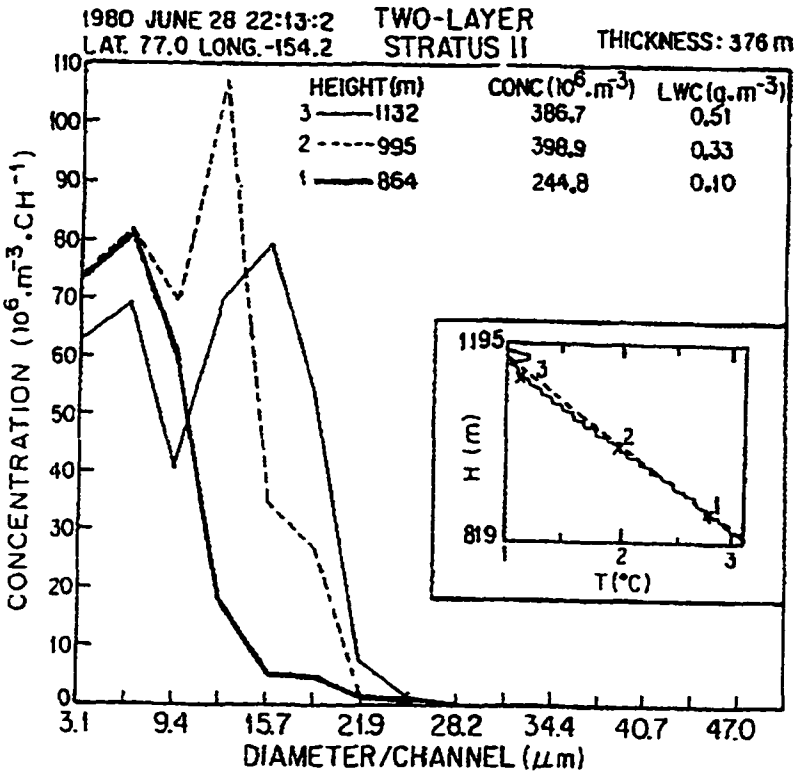

Figure 1.3. Drop-size distribution measured at three different heights for the upper-layer cloud on 28 June, 1980 (from Tsay and Jayaweera, 1984).

clouds. Also, most of the persistent stratus cloud regimes exist over the Arctic Ocean where it is difficult to conduct observational studies. Modeling studies may be used to help explain existing data, and to compensate for the lack of observational data.

The complicated structures of multiple cloud layers and the inversions of temperature as well as humidity make model simulations a challenging problem. During the past years, modeling of ASCs was developed essentially in two main directions. The first makes use of integrating mixed-layer models (eg. Busch et al., 1982). This kind of model is computationally affordable. The second makes use of one-dimensional (1-D) ensemble-averaged models. The results of Herman and Goody (1976) suggested that the occurrence of two-layered ASCs were related to the absorption of solar radiation within the cloud layer. Nevertheless, the complicated features of the boundary layer, in which

ASCs form. such as inversions of temperature as well as humidity and the existence of multiple cloud layers make it difficult to develop models based on the simplifying assumption of a well-mixed boundary layer. Based on this, Filyushkin and Lilly (1993) proposed to use a 3-dimensional (3-D) large eddy simulation (LES) approach to study the ASC-capped planetary boundary layer (PBL). The concept of the LES is to explicitly simulate the large eddies, which contain most of the energy and dominate turbulent fluxes within the PBL, and to parameterize the subgrid-scale motions, which contain less energy and are less important to our studies. With a LES model, Zhang and Filyushkin (1995) successfully simulated two ASCs cases. Also, the persistence and evolution of cloudy boundary layers has been analyzed (Zhang, et al., 1997, 1998a; Olsson et al., 1998).

Model simulation of the formation and persistence of ASCs has now attracted more and more interest. Several groups have attempted to model the formation and evolution of ASCs in recent years using a hierarcy of models. The results of Herman and Goody (1976) suggested that condensation of an initially unsaturated air mass is due to longwave emission to space and radiative and diffusive cooling to the colder surface. McInnes and Curry (1995b) suggested that radiative cooling leads initially to the formation of a cloud layer near the peak of the preexisting temperature and humidity inversion, where radiative cooling is the strongest. Zhang et al. (1998a) and Lie-Svendsen et al. (1998) investigated the cloud formation with a convective-adjustment model which includes detailed cloud microphysics.

ASCs are strongly driven by cloud-top radiative cooling (Finger and Wendling, 1990; McInnes and Curry, 1995a; Smith and Kao, 1996). Using a LES model Zhang et al. (1997, 1998a) simulated a ASC case observed on June 28, 1980 in Arctic Stratus Experiment and the results suggested that after the initial formation of ASCs their development is mainly controlled by longwave radiative cooling and vertical heat fluxes have the effect of decreasing the longwave cooling and hence slow down the cloud development. Vertical mixing provides a moisture source for the clouds. They investigated the effect of large scale vertical motion on the maintenance of cloud layers and found that weak large scale

downward motion is the most favorable situation to maintain the cloud layers. Their results differ from the 1-D simulation made by McInnes and Curry (1995a) and may suggest a limitation of a 1-D model since a 1-D model is unable to include 3-D turbulence. Olsson et al. (1998) discussed the influence of cloud microphysics on the boundary layer structure using a two-dimensional model and found that both simulations that did and did not include the effects of drizzle showed that the higher CCN concentrations produced a cloud with larger reflectivity and absorptivity, but also produced eddies that were weaker than with lower CCN concentrations.

1.4 Objectives and outline of thesis

The above sections outline the state of knowledge in terms of observations and modeling of summertime ASCs and their formation. Previous observational and modeling studies have not provided a complete understanding of the physics of ASC formation. ASCs form as a result of the interactions among dynamics, radiation and cloud microphysics. Therefore, in order to understand the physics of ASC formation, we need to understand the role of dynamics, radiation, cloud microphysics, and we need to understand the interaction among these physical processes.

Several different models have been used in modeling the formation of ASCs. These models include dynamics, radiative effects and different cloud parameterization schemes. In general, these models siumlate clouds that form in the right place. But none of them provide detailed analyses of how cloud forms and what is the most important condition leading to cloud formation. Previous model simulations did not answer the question: when and where is it most probable that clouds will form? Also those simulations did not give us a clear idea of how the cloud would evolve after its initial formation. They have not provided a clear picture of the role of radiative effects in cloud formation because those models are very complex and thus unsuitable to address such specific questions.

Solar radiation is relatively weak over the Arctic region even in summer due to the large solar zenith angle, but there is little change between day and night around summer

solstice. The surface temperature in summer is normally lower than the atmospheric temperature. Thus, we may expect that turbulence over the region may not be too strong. Therefore. attention will be focused on the combined effects of radiation and cloud microphysics. Thus. a one dimensional radiative-convective model with detailed radiative transfer and cloud microphysics is adopted in Chapter 2 to study the cloud formation problem. Based on the asumption that large-scale dynamical effects may be of relatively minor importance compared to radiation and cloud microphysics in calm atmophere, dynamical processes in the model is replaced with a simple convective adjustment scheme. This kind of simplification enable us to focus on the effects of radiation and cloud microphysics. It also enables us to make simulations with fine spatial (vertical) resolutions over long temporal scales.

In Chapter 3. I will investigate the physics of ASCs formation with this 1-D model. I will focus on studying the role of radiation in cloud formation, and I will try to answer the question: what kind of atmopheric situation is favorable to cloud formation? The effect of atmopheric temperature and humidity profiles on cloud formation (location and time) will be discussed. The initial cloud formation and the initial cloud evolution will also be discussed.

In Chapter 4, I will focus on study the formation of multiple cloud layers, which frequently appear in the Arctic. An Arctic stratus case observed on June 28, 1980 with two cloud layers will be discussed. The simulation results will be compared with the observation. Then, I will concentrate on studying the role of humidity and temperature profiles in the formation of multiple cloud layers.

As mentioned above, in the 1-D model, dynamical processes are parameterized by a convective adjement scheme. This simplifies the problem and enables one to focus on radiative and cloud microphysical processes and to investigate their influence on cloud formation in considerable detail. This simplication of dynamical processes in the 1-D model is based on the observation and modeling results (eg. Zhang et al., 1997; 1998a) that, except in unstable layers, vertical motions in the Arctic atmosphere are frequently

not very strong (Curry et al., 1988). To evaluate the limitation of this simplification in the Arctic, a 3-D large eddy simulation model is adopted. The LES model includes detailed dynamics and radiation schemes. The cloud processes are simulated with a bulk parameterization scheme. The details of the 3-D LES model are described in Appendix A. In Chapter 5 the LES model is used to assess the limitation of the 1-D model. Here, the simulation results of the 1-D model are compared with those of the 3-D LES model. Emphasis is placed on discussing the vertical motion and vertical transport of heat and humidity simulated by the 1-D model and compare and contrast them with results of the 3-D LES model.

Most of simulations of ASC processes have been made with one or two dimensional models so far. These models are based on simplifications of the dynamics and on the assumption that the ASC boundary layer is horizantally homogeneous. Three dimensional eddies cannot develop in such models. To simulate three dimensional eddies, a three dimensional model is required. In Chapter 6, a three dimensional LES model is adopted to investigate the cloudy boundary layer. A 3-D LES model is a useful tool for studying boundary layer flows. With this LES model, the three-dimensional eddy structure and the maintenance of the ASC boundary layer is investigated. Also, the effect of large scale motion on the maintenance of cloud layers is discussed.

A summary of this thesis is presented in Chapter 7, and future work is discussed.

Chapter 2

A One-dimensional Radiative-Convective Model

2.1 Introduction

Model studies of ASCs have attracted increasing attention in recent years (eg. Finger and Wendling, 1990; Smith and Kao, 1996; Zhang et al., 1997; 1998). These results have underscored the importance of longwave radiative cooling in the formation and persistence of ASCs.

The radiation environment is unique in the Arctic. Solar radiation is absent in winter and relatively weak even in summer. There is little change between day and night around summer solstice. Over the Arctic Ocean the surface temperature in summer is close to 0°C (273.15 K) and normally lower than the atmospheric temperature. Thus, we may expect that turbulence over the Arctic Ocean may not be as vigorous as in the subtropical or midlatitude regions. Small scale motion is expected. Therefore, a model with fine vertical and horizontal resolution is desirable. This implies that use of 2-D as well as 3-D models, required to simulate Arctic processes adequately, place substantial demands on computational resources. Another major difference between low and high latitudes is that we expect radiative effects to play a larger role in cloud formation at high

latitudes whereas at lower latitudes it is often controlled by dynamical processes, such as turbulent convection leading to cumulus formation, or large-scale motions associated with large frontal systems. Dynamical effects certainly play a role in the Arctic as well, but the smaller input of solar radiative energy reduces the strength of dynamical processes. Hence radiative processes, in particular in the infrared part of the spectrum, are expected to play a comparatively larger role.

Previous modeling studies of ASCs have included both radiation and turbulence schemes at various levels of sophistication. To simplify the problem and isolate some of the most important physical processes, a one-dimensional radiative-convective model with detailed cloud microphysics (Lie-Svendsen et al., 1999) is adopted in this chapter to study the formation of ASCs. The purpose here is to investigate to what extent the formation and basic characteristics of ASCs can be explained in terms of radiative and microphysical processes, and their interaction, alone, without the need to know about or include dynamical processes such as lifting (or subsidence) of air masses due to synoptic motion or wind shear. In place of a turbulent mixing scheme we use a simple convective adjustment to account for convective instabilities caused by, for example, radiative cooling at the cloud top.

Radiative and microphysical processes are "local" processes which do not depend on boundary conditions at large distances from the area under study. Although we thus regard the cloud formation as a "local" process, it is not independent of the large-scale motion of pressure systems and dynamical effects. This large-scale motion is responsible for advecting moist, warm air into the Arctic Basin, and thus providing the initial conditions needed to make water vapor condense on available cloud condensation nuclei. With the expectation that radiative processes play a larger role at high latitudes than at low latitudes, the simplification obtained by excluding dynamical effects may turn out to be reasonable.

A high-resolution 1-D model is a useful way to investigate ASC formation since it is fast and can have a fine resolution. Recent comparisons of the results of one-dimensional

models with those of three-dimensional large eddy simulation models indicate that one-dimensional models can reasonably represent the main features such as cloud water content and some turbulence statistics of a well-mixed cloudy boundary layer (Bechtold et al., 1996; Moeng et al., 1996). The observed structure of the ASCs also makes them amenable to a one-dimensional modeling approach. ASCs cover large areas (Vowinckel and Orvig, 1964) within the lower 2 km of the boundary layer and exhibit a layered, horizontally-homogeneous structure (Tsay and Jayaweera, 1984). These features justify the use of plane-parallel radiative transfer theory with multiple scattering (Herman and Goody, 1976; Tsay et al., 1989).

The one-dimensional radiative-convective model described in this chapter contains detailed cloud microphysics. It is designed to focus on the initial cloud formation and its development during the first few hours after formation, and to delineate how cloud optical and microphysical features depend on initial conditions. Processes that will be important to the long-term cloud evolution, such as coalescence and settling of water drops, and production of drizzle will be ignored.

These simplifications imply that this model is not intended to be complete in the sense that it attempts to includes all processes taking place during cloud formation and development. Instead, we are isolating and focusing on the detailed interaction between radiation and cloud microphysics to improve our basic understanding of this primary interaction. The most important advantage of this simplified approach is that it enhances understanding because it will be easier to interpret the model results. Another advantage is that this approach is also computationally less demanding than a more comprehensive model. Thus, the processes we do include can be studied in greater detail than would be possible in a 2- or 3-D model.

This simple model is able to provide us with a clear picture of the interactions between radiation and cloud microphysics and thus help us understand the role of radiation and cloud microphysics in Arctic stratus cloud formation, and in the formation of multiple cloud layers.

2.2 Model Description

The physical processes included in the model are shown in Figure 2.1. The net cooling effect of solar and infrared radiation causes temperature decrease and may eventually lead to the condensation of water vapor on available cloud condensation nuclei. The initial cloud formation will have a positive feedback to the radiative transfer that leads to further decrease in temperature. Thus more cloud drops will form. Therefore, the model consists of two main components: (1) a radiative transfer code for computing the warming/cooling rates due to solar and infrared radiation, (2) a cloud parameterization scheme with detailed microphysics simulating cloud formation and initial evolution. A convective adjustment scheme is included for the parameterization of vertical transport of heat and moisture, as well as for vertical mixing of droplet spectra.

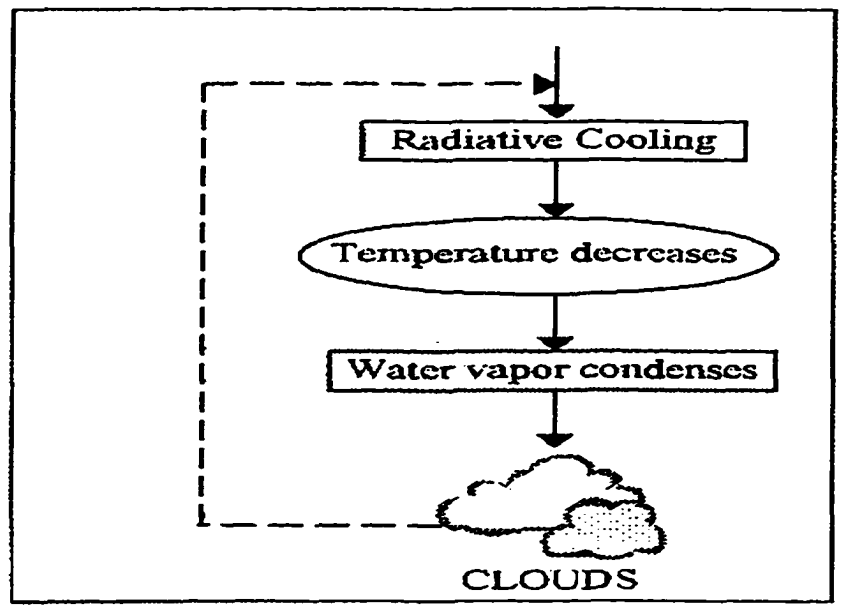

Figure 2.1. Physical processes included in the model.

2.2.1 Radiative Transfer

A well-tested radiative model is adopted as the radiative module for calculating both solar and infrared radiative effects (Stamnes et al., 1988; Tsay et al., 1989; Tsay et al., 1990). This model is designed to compute radiative transfer in the Arctic with a multi-stream discrete ordinate radiative transfer scheme, including Raleigh scattering as well as scattering, absorption and emission by gases (H_2O, CO_2, O_3), aerosols and cloud particles. In the following simulations, we consider 24 solar and 9 infrared bands. The effect of CO_2 and O_3 is included. We adopt a surface albedo of 0.7. The value for the surface albedo is not critical; with an albedo of 0.95 we obtained essentially identical results in the following simulations. In the radiative transfer computation we use two (discrete ordinate) streams, which yield warming/cooling rates within 10% of an accurate computation for a cloudy sky (Kylling et al., 1995). We have repeated the computations using multiple streams, with only minor changes in the end results.

The microphysical parameters needed in the radiative transfer scheme to compute the optical properties of clouds are the droplet density $N_d(z)$, the liquid water content W_l, the equivalent radius r_{eqv} (the ratio of the third and second moments of the droplet distribution). A study by Hu and Stamnes (1993) has shown that these moments of the distribution are sufficient to provide an accurate description of the radiation field and that the full droplet distribution is not needed. In the radiative transfer calculation we therefore parameterize the optical properties based on the liquid water content and the equivalent radius using the parameterization given by Hu and Stamnes (1993).

The droplet density is

$$N_d(z) = \int_0^\infty n(r,z)dr \quad = \quad \frac{T_0}{T}\frac{P_a}{P_0}\sum_{j=1}^{i_d(z)} n_j^d(z) \tag{2.1}$$

where the factor in front of the summation sign takes into account that n_j^d is defined at the reference level (P_0, T_0) while $N_d(z)$ is the actual density at $(P(z), T(z))$. The equivalent radius is defined to be the average droplet radius weighted by the droplet

cross-section area

$$r_{eqv} = \frac{\int n(r,z) r^3 dr}{\int n(r,z) r^2 dr} = \frac{\sum_{j=1}^{i_d(z)} n_j^d(z) r_j(z)^3}{\sum_{j=1}^{i_d(z)} n_j^d(z) r_j(z)^2}. \tag{2.2}$$

In our model the radiation field affects the cloud droplets only indirectly through the warming or cooling of the ambient air. With a given warming (cooling) rate, $h(t,z)$, the temperature as a function of time t is given as

$$T(t,z) = T(t_0,z) + \int_{t_0}^{t} h(t',z)\, dt' \tag{2.3}$$

where t_0 is the starting time.

2.2.2 Cloud parameterization with detailed microphysics

The cloud microphysics module includes droplet activation, growth, mixing and evaporation. The physics of the cloud formation module is further explained by Figure 2.2. Radiative effects will change the temperature, and then change the stability of the atmosphere. If the atmosphere is unstable, vertical mixing will result. The decrease in temperature will eventually cause condensation, which will modify the size and density of cloud droplets, and change the cloud optical properties. This change in the cloud optical properties will lead to further cooling and thus have a positive feedback on cloud formation.

(a) Growth rate of droplets

The growth rate of a droplet with radius r_j is given by (Pruppacher and Klett, 1987. Eqs. 13-28)

$$r_j \frac{dr_j}{dt} = A_3(t)(S(t) - 1) \equiv A_3(t)s(t) \tag{2.4}$$

where

$$A_3 = \frac{1}{\frac{L^2 \rho_l}{K R T^2} + \frac{\rho_l R T}{D P_{sat}}}. \tag{2.5}$$

Here $K(T)$ is the thermal conductivity, $D(T)$ the diffusivity and ρ_l the mass density of liquid water. S is the atmospheric saturation ratio, and s is the supersaturation.

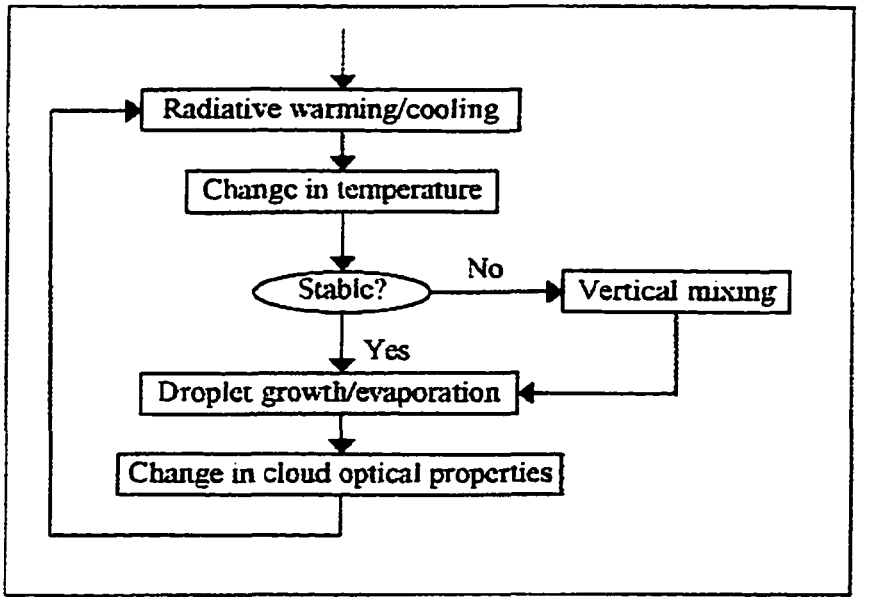

Figure 2.2. Physics of cloud formation.

The saturation vapor pressure is well approximated by the Clausius-Clapeyron equation:

$$P_{sat}(T) = P_{sat}(T_0) \exp\left[\frac{L}{R}\frac{(T - T_0)}{TT_0}\right] \tag{2.6}$$

where $R = 8.314$ J K^{-1} mol^{-1} (the ideal gas constant) and L the latent heat of evaporation of water (in J mol^{-1}).

(b) Droplet bins

The evolution of both the aerosol and cloud droplet spectra is kept track of in the model and particles are moved between the aerosol and droplet distributions as droplets form and evaporate. To simplify the bookkeeping involved, these distributions are defined at a prescribed reference temperature T_0 and ambient air pressure P_0. This has the advantage that the distributions do not have to be updated whenever the ambient air density changes. The distributions need to be updated only when new cloud condensation nuclei activate, droplets evaporate completely, or when layers mix. The actual densities

at a given altitude are then found by multiplying these distributions with a simple scale factor. The reference level (P_0, T_0) may be chosen arbitrarily (we chose the surface pressure and temperature). The atmospheric pressure at each level is a constant during the simulation.

The CCN spectrum $N_{CCN}(s)$ is defined as the number (density) of CCN particles that have activated at supersaturation s, again measured at the reference level (P_0, T_0). At the start of the calculation N_{CCN} is assumed to be prescribed and independent of altitude, corresponding to well-mixed air. As time evolves and particles activate and deactivate and layers mix, N_{CCN} will become altitude dependent.

The CCN distribution is divided into discrete bins so that n_i^a is the number of CCN particles that activate between supersaturations s_{i-1} and s_i:

$$n_i^a(z) \equiv N_{CCN}(s_i) - N_{CCN}(s_{i-1}). \tag{2.7}$$

We choose the s_i's at 100 equidistant grid points between $s = 0$ and $s = s_{max}$, where $s = s_{max}$ is chosen to cover the supersaturations anticipated in the model run. Once an altitude level becomes supersaturated the CCN particles n^a convert into cloud droplet particles n^d, the number of particles activated is determined by the supersaturation. The droplet bins $n_j^d(z)$ are not created in advance. Thus, instead of being bins of fixed radii $r_j(z)$, the droplet bins are created or removed dynamically as needed during a model run when CCN particles activate (or droplets evaporate completely). The radii $r_j(z,t)$ will therefore change with time as the droplets grow or evaporate, while $n_j^d(z)$ remains constant in the absence of mixing or complete evaporation. This means that the index j therefore does not refer to a bin of droplets of fixed size but instead indicates when the droplets of this bin were activated. We will also assume that all CCN particles that activated at the same time will grow to cloud droplets of the same size. In other words, once the CCN particles have activated they grow rapidly, and the amount of soluble or insoluble material has little impact on the growth rate.

There are two advantages to this binning scheme, as compared to the more conventional approach of using bins of fixed radii: it simplifies the bookkeeping and it is more

accurate. Bins of fixed radii require droplets to be moved between bins as they grow and evaporate. This increases the complexity of the scheme. In our approach only the radius of each bin needs to be updated as the droplet size changes. The radii are computed accurately from the growth equation and no adjustment is necessary. Hence we expect the liquid water content to be better conserved in this approach. When two cloud layers mix, however, we rebin the two mixing droplet distributions to keep the total number of bins at a reasonable value.

With the droplet distribution given, the liquid water content W_l is,

$$W_l(t) = \frac{4}{3}\pi\rho_l \frac{kT}{M_a P_a} \int r^3 n(r) dr = \frac{4}{3}\pi\rho_l \frac{kT}{M_a P_a} \sum_{j=1}^{i_d} n_j^d r_j^3 \tag{2.8}$$

where i_d is the number of droplet bins. In the most general case n_j, r_j and i_d will be time dependent, and contribute to the time dependence of S in (2.4).

(c) Latent heat release

The latent heat released or absorbed during the droplet integration is used, along with the divergence of the radiation field, to update the temperature. Let $W_l(z, t')$ be the "old" liquid water contents at time t', before the droplet integration. The latent heat released/absorbed is then the difference between the new and old W_l multiplied by the latent heat release per unit mass

$$\Delta q(z,t) = L_e^0 \rho_a(z)[W_l(z,t) - W_l(z,t_0)] \tag{2.9}$$

where

$$L_e^0 \equiv \frac{L}{M_w} \tag{2.10}$$

is the latent heat release per unit mass and ρ_a the mass density of air.

2.2.3 Convective adjustment scheme

Layers may become convectively unstable as they heat or cool at different rates. In particular, the strong infrared cooling at the cloud top leads to vigorous convection through the whole cloud layer. This turbulent mixing is a fully three-dimensional problem (not

even 2-D will suffice), and is thus outside the scope of our 1-D model. Moreover, there is no general agreement on what approximate description of turbulent mixing should be used. In this study we are not primarily interested in the dynamics of the mixing process itself. However, we need to include mixing because it has a large impact on both the evolution of the droplet spectrum and on the radiation field. In particular, the mixing process effectively transports heat (and moisture) upwards from lower levels, to partly compensate for the energy lost through radiative cooling at the cloud top. Therefore, instead of trying to model the dynamics of the mixing process (which cannot be done in 1-D) we shall use a rather simple, convective adjustment scheme, similar to the schemes used in 1-D radiative-convective climate models.

To determine if two layers are unstable we compare the lapse rate $dT/d\ln P$ between the two layers with the lapse rate Λ for adiabatically rising air. If both layers are inactive (no clouds) we set Λ to the adiabatic lapse rate for dry air

$$\Lambda = \Lambda_{dry} = \beta T \tag{2.11}$$

where

$$\beta \equiv \frac{R_a}{C_{p,a}}. \tag{2.12}$$

$R_a = 287$ J K^{-1} kg^{-1} is the ideal gas constant (per unit mass) of air and $C_{p,a}$ the constant pressure heat capacity of air. If one or both layers are active we compare with the lapse rate for saturated air (Pruppacher and Klett, 1997):

$$\Lambda = \Lambda_{sat} = \frac{R_a + \frac{1}{M_a}\frac{P_{sat}}{P}\frac{L}{T}}{\frac{C_{p,a}}{T} + \frac{1}{M_a}\frac{P_{sat}}{P}\frac{L^2}{RT^3}}. \tag{2.13}$$

The convective adjustment of two adjacent layers 'A' and 'B' is done whenever the lapse rate between 'A' and 'B' exceeds the average adiabatic lapse rate of the two layers:

$$\frac{dT}{d\ln P} > \Lambda_{ave} = \frac{1}{2}(\Lambda_A + \Lambda_B). \tag{2.14}$$

The mixing is always carried out between two adjacent layers. In a full 3-D model, cold plumes of air may move through several layers of warmer air before they finally mix, but this is beyond the scope of a 1-D model.

From Eq. (2.14) two layers will mix even when they are barely unstable. To prevent the mixing from taking place too often, which would be physically unrealistic, we specify a minimum time that must elapse between the convective adjustments. Typically, we choose 5 s as the minimum time for simulations with vertical resolution of 10 m and 2 s for simulations with vertical resolution of 5 m.

The model includes mixing of droplet spectra (when both layers have cloud droplets) as well as entrainment of clear air and new CCN particles (when at least one of the layers has clear air). When two layers mix, both the CCN and droplet spectra are mixed, the droplet spectrum is rebinned if necessary, and the temperature of the mixed air is computed.

The two layers are mixed "instantly". Thus the mixing process is assumed to be sufficiently fast so that the droplets do not have time to grow or evaporate, and new CCN particles to activate, during the mixing process. This assumption simplifies the bookkeeping of the mixing process, since the distributions are effectively fixed during the mixing. As long as the distance between the two cloud layers is small, this assumption should not lead to large errors since the air parcels do not have to travel large distances during mixing. On the other hand, if the distance between the two layers is large, instant mixing may lead to spuriously high supersaturations. Newly entrained CCN particles may then, for instance, suddenly activate after mixing with cooler and more humid air. The high supersaturations will then cause too many CCN particles to activate. To avoid (or at least alleviate) this problem we use fine layering in the regions where clouds are expected to form. This fine layering does not slow down the simulation since it is also needed to do the radiative transfer computation accurately.

The instant mixing assumption implies that the two layers mix completely and instantly. We therefore make no attempts to follow the detailed evolution of the mixing process itself. Since the scope of the model is to study the interaction between cloud microphysics and radiation on a time scale much longer than the time scale for mixing of two layers, it is the end result of the mixing that is important, not the details of the

mixing process. As mentioned, the instant mixing may cause too many CCN particles to activate, in particular if the spacing between layers is large. The sudden activation of many particles may also lead to droplet distributions that are too narrow (because droplets that activated at the same time will have the same size). But, this is prevented by using a fine altitude grid in the cloudy regions.

To do the mixing, parcels of air from the two layers are brought adiabatically along the dry adiabatc (since we do not allow for droplet growth during the mixing) to the same pressure level, where they mix, and the mixed air is then brought back to the two pressure levels of the mixing layers. For instant mixing the temperature of the mixed air is independent of the pressure level chosen for the mixing. Since the droplets are fixed in size during mixing, the resulting mixed droplet spectrum is also independent of the pressure level. Consequently, any pressure level may be chosen for the mixing. To simplify the procedure we choose to bring the parcel from level B to level A, with the pressure P_A at A as the common pressure.

If both layers contain cloud droplets prior to mixing, we need to rebin the mixed droplet distribution. Otherwise, the number of bins could double in each mixing event, exhausting both computer memory and time. We identify the smallest and largest droplet radii in the mixed distribution, and divide this range into 50 equidistant bins in which the droplets of the mixed distribution are placed. This means that the size of the original particles will be slightly adjusted to fit the new bins. To compensate for this, the new radii are slightly adjusted again, so that the total volume of the particles in the new bin equals the total volume of the original particles being put into this bin. Thus, in this rebinning scheme both the droplet number concentration and the liquid water contents will be exactly conserved.

2.2.4 Model resolution and time integration

The one-dimensional treatment, assuming slab geometry, allows us to make use of existing, comprehensive and well-tested numerical codes, based on the discrete ordinate

method, for solving the radiative transfer equation in vertically stratified atmospheres. We are able to use very fine spatial resolution to resolve the radiative cooling taking place in the cloud, especially near cloud top (less than 10 m as needed). The radiative transfer calculation is time consuming, and we therefore restrict the fine layering to regions where clouds may possibly form, and use a much coarser grid (typically 100 m resolution) outside the possible cloud layers. The model is started with an assumed, initial temperature profile $T_i(z)$ and humidity profile $W_{v,i}(z)$ (z is the altitude). We consider only cases where the air is subsaturated initially so that all water is in the vapor phase.

In accordance with the one-dimensional treatment we assume no net horizontal transport of water, no vertical flux of water from the surface, and no precipitation. Hence the total water content in the air column is conserved throughout the calculation.

The microphysical calculation is also simplified by the 1-D treatment. We can study the evolution of the detailed droplet size distribution, using a large number of bins to resolve the distribution. In a full 3-D simulation such fine resolution would not be possible due to the large memory and processing requirements. Only summer time ASCs would be considered in this thesis. Therefore, only water clouds are considered. Mixed phase, or pure ice phase clouds do not generally occur at temperatures above $-15°C$. A schematic illustration of the model structure is provided in Figure 2.3.

2.3 Case studies

There are very few soundings of atmospheric structure that coincide with cloud microphysical measurements in the Arctic. Since our study is focused on the combined role of cloud microphysics and radiation in the initial formation of ASCs, we use initial temperature and humidity profiles for clear air. We have performed two case studies based on soundings from Barrow, Alaska, where such soundings are taken twice daily by the National Weather Service.

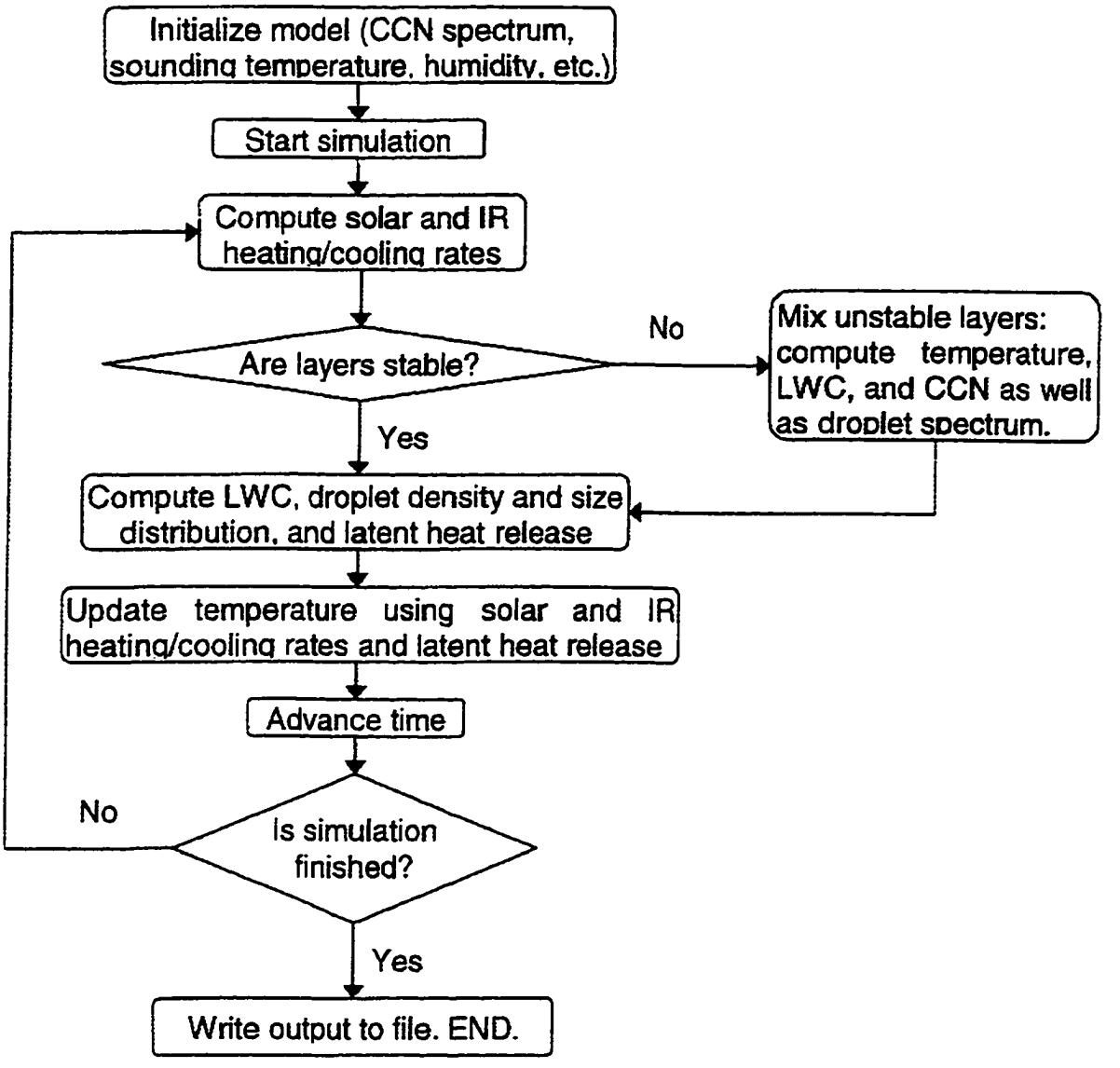

Figure 2.3. Flow chart for the model. IR stands for infrared radiation, LWC for liquid water content, and CCN for cloud condensation nuclei.

2.3.1 Case A

We chose a clear air condition deemed to be conducive to cloud formation in the 600 to 800 m altitude region, where the actual temperature is within 1 K of the dew point temperature.

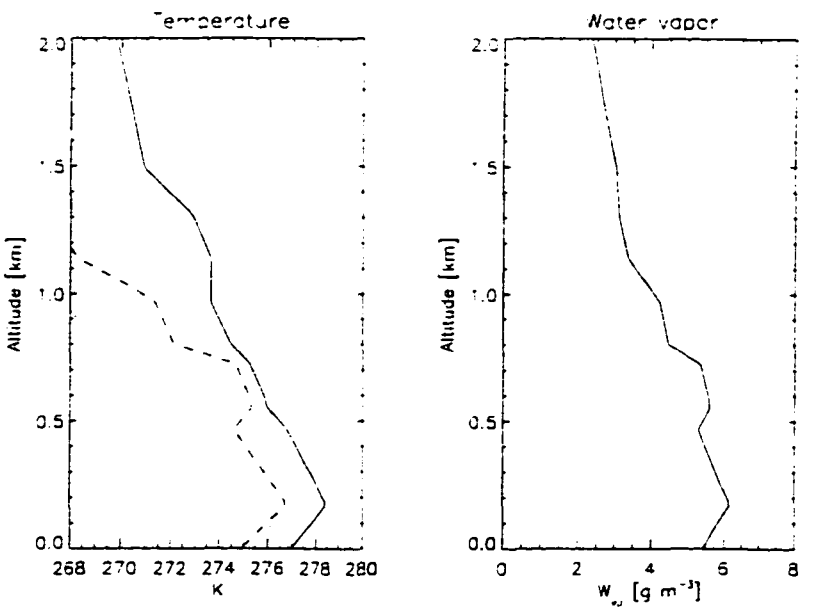

Figure 2.4. Sounding from Barrow, at 00 GMT, June 10, 1980. The solid line in the left panel is the actual temperature; the dashed line is the dew point temperature, T_c; and the dotted line is the lapse rate for dry air. The right panel shows the water vapor profile.

We adopt an initial temperature and clear-air humidity profile for Barrow, Alaska obtained at 00 GMT, June 10, 1980. The actual sounding is shown in Figure 2.4. Note that the humidity is expressed as the dew point temperature, defined by

$$T_c \equiv \frac{T_0}{1 - \frac{R}{L} T_0 \ln\left(\frac{M_a}{M_w} W_{v,i} \frac{P_a}{P_{sat}(T_0)}\right)} \tag{2.15}$$

where we have used (2.6) to express $P_{sat}(T_c)$. The dew point is below the actual temperature at all locations. However, in the 600 to 800 m altitude region, the two temperatures are within 1 K of each other. A small cooling in this region is sufficient to initiate cloud formation. The temperature gradient is initially not as steep as the dry adiabatic lapse

rate, indicating that the air is convectively stable. The surface temperature, set to the temperature in the bottom atmospheric layer as measured by the sounding, is held constant at $T_s = 277$ K but the moisture in the bottom layers is allowed to vary as layers mix. There is a small surface inversion present.

The grid spacing in the bottom 1 km. where we expect cloud formation, is set to 10 m. but a coarser grid is used up to 25 km. In total, we use 200 vertical grid points in this simulation.

Few data sets are available for Arctic CCN and they show a wide variability in number concentration. In our study we adopt an initial CCN spectrum measured in April, 1992. during the LEADEX experiment, in Deadhorse, Alaska (Hegg et al., 1995). This spectrum can be approximately represented by a power law (Twomey, 1977)

$$N_{CCN}(s) \approx c(100s)^{\kappa} \tag{2.16}$$

with $\kappa = 0.34$ and $c = 1.28 \times 10^8\ m^{-3}$, corresponding to the highest CCN concentration measured by Hegg et al. (1995).

Our simulation follows this column of air for about 16.5 hours, with cloud formation beginning at 6.5 hours at $z = 700\ m$. Figure 2.5 shows how the temperature and three moments of the droplet distribution (ratio of liquid water to water vapor, droplet density and equivalent radius) evolve with time after the cloud has formed. Initially the air cools slowly, and even 6 hours into the simulation (just prior to cloud formation) the temperature has decreased by less than 1 K. Once the cloud forms the cooling rate increases drastically in the cloud region and a temperature inversion quickly develops and deepens, due to cloud-top infrared cooling. Ten hours after cloud formation the cloud top remains at its initial 700 m location, capped by a steep inversion, but the cloud base has descended to about 250 m.

From Figure 2.4 we notice that the cloud forms in the region we expected, at the location of the smallest separation between the initial sounding temperature and the dew point temperature. The cloud top (and hence temperature inversion) stays almost at this altitude.

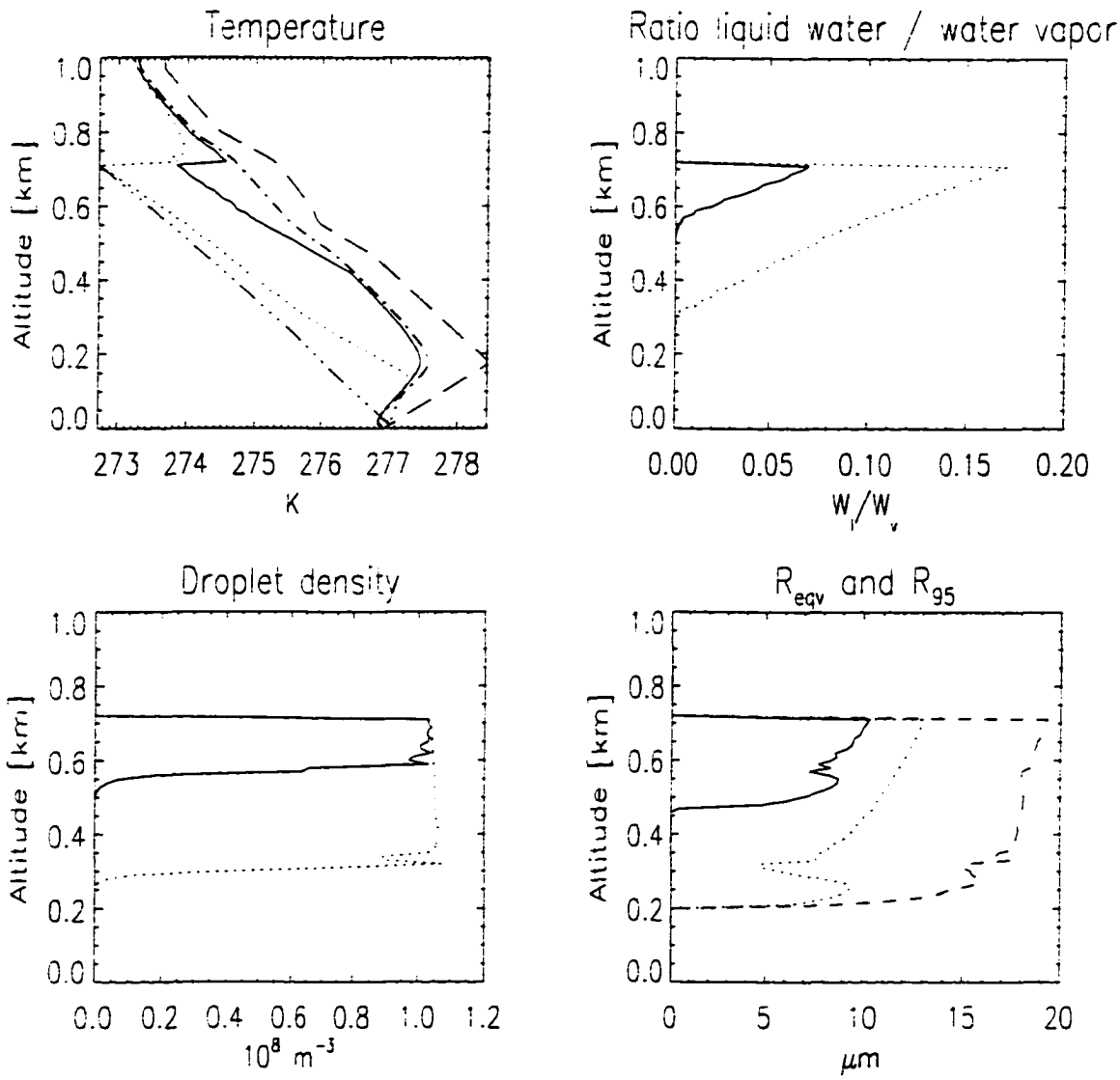

Figure 2.5. Temperature, ratio of liquid water to water vapor, droplet density and equivalent radius at 1.6 (solid line), and 10 hours (dotted line) after cloud formation. The upper left panel also shows the temperature at 28 minutes before cloud formation (dash-dot line), and the dash-dot-dot-dot line shows the corresponding saturated lapse rate temperature after 10 hours, extrapolated downwards from the actual temperature at 770 m altitude. The initial temperature from the sounding is also shown (long dashes). In the lower right panel the dashed line denotes r_{95} after 10 hours, where r_{95} is the radius below which 95% of the liquid water is contained.

The cloud top cooling will lead to cooling of the entire cloud due to the vigorous mixing, and eventually the lower parts of the cloud may become unstable relative to the cloud-free air below. The resulting mixing at cloud base will then move the cloud base downwards. In addition, with a humidity inversion, such as the one shown at approximately 500 m in Figure 2.4, this mixing will transport moisture downwards as well, which will increase the likelihood of the cloud base being lowered.

In the upper left panel of Figure 2.5 we have also plotted the temperature corresponding saturated adiabatic lapse rate temperature, using Eq. (2.13), extrapolated downwards from the cloud top. The modeled temperature profile inside the cloud is actually steeper than the saturated adiabatic value. This implies that the upward supply of heat from convective adjustment is not enough to offset the infrared cooling to space and keep the temperature at the saturated adiabatic value.

The LWC, the droplet density, and the equivalent radius in Figure 2.5 show that the cloud is initially thin, being about 150 m thick 2 hours after formation, and reaching 580 m in thickness at the end of the simulation. The maximum supersaturation, obtained during the initial cloud formation, is 0.71%. This number is rather sensitive to the altitude resolution; if we use 5 m instead of 10 m resolution in the region where the cloud forms the maximum supersaturation is lowered to about 0.5%. Since the maximum supersaturation determines how many CCN particles activate, and therefore determines the droplet density, the maximum droplet density does not significantly increase after the initial formation. The maximum droplet density found anywhere is 1.07×10^8 particles/m^3, slightly less than the (initial) concentration of CCN particles activated at 1% supersaturation of 1.28×10^8 particles/m^3. Since the droplet density does not increase significantly with time, while the LWC does, the droplets must necessarily increase in size, which is reflected in the increase in equivalent radius with time. Shortly after activation (solid line in the figure), r_{equ} has a maximum of about 10 μm while at the end of the simulation the maximum is about 13 μm.

Within the cloud the LWC generally increases with altitude, as one expects from

adiabatically rising air. The equivalent radius and r_{95}, defined as the radius below which 95% of the liquid water is contained, also show a general increase with altitude, although the trend is not as pronounced. By contrast the droplet density shows no such trend, being roughly independent of altitude. This is not unexpected. Unless the maximum supersaturation can be increased to activate new droplets, the mixing process will lead to a nearly constant droplet density with altitude. As air parcels move up or down during mixing the droplets will simply grow or evaporate to keep the air saturated, but the number does not change.

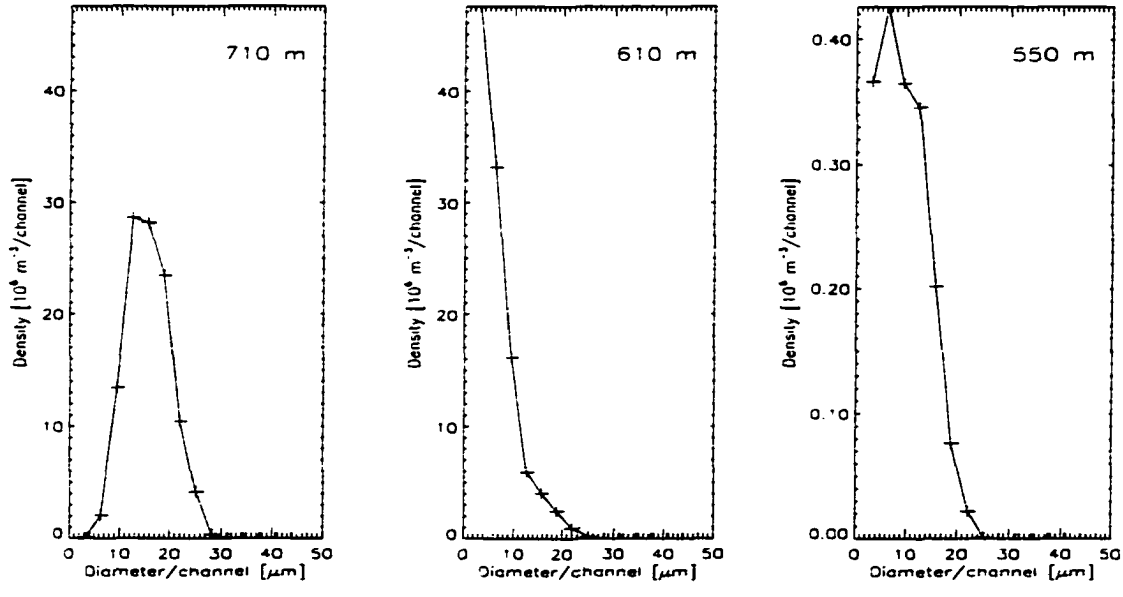

Figure 2.6. The droplet size distribution, n^d, one hour after cloud formation. The distribution has been collected in 15 equidistant bins with mean diameter 3.13 μm apart, with the pluses indicating the center of each bin. Notice the different vertical scale in the last panel.

Figure 2.6 shows the droplet size distribution near the top, middle and bottom of the cloud one hour after cloud formation. To facilitate comparison with observations (see below) we collected the distribution in 15 equidistant bins with mean diameter separated by 3.13 μm, corresponding to the resolution of the Forward Scattering Spectrometer Probe used in the Arctic Stratus Experiment conducted over the Beaufort Sea in the

summer of 1980 as reported by Tsay and Jayaweera (1984).

Figure 2.7 shows the droplet size distribution at the end of the simulation, between the cloud top at 710 m and the cloud base at 250 m. At the end of the simulation, the model has produced fairly broad size distributions in the upper parts of the cloud. The broad size distributions can be attributed to the mixing taking place throughout the cloud. Near the bottom of the cloud the distribution is generally clustered around a single peak at about 10 μm diameter or less. In the upper parts of the cloud the much broader distribution typically shows several peaks between 10 and 30 μm, and a tail extending to about 40 μm. It should be borne in mind, though, that some arbitrariness is introduced by collecting the droplet distribution in bins of fixed size, and that the location and height of individual spikes in the distribution will depend on the location of the bin boundaries. The rebinning of the droplet distribution after mixing adds to this effect, since some droplet bins may contain very few particles after mixing. In the upper parts of the cloud, we expect the number of large droplets to be overestimated since large droplets are susceptible to gravitational fallout and coalescence processes not included in our model.

Figure 2.8 shows the warming/cooling rates due to solar and infrared radiation. Note the very strong infrared cooling near cloud top, which is responsible for the deep inversion developing there. The lower panels demonstrate that even with 10 m resolution the model is not able to fully resolve the radiation field at the cloud top, yielding an almost discontinuous jump both in solar and infrared warming/cooling rates.

2.3.2 Case B

In case B we address the role of the commonly observed surface temperature and humidity inversion in the Arctic environment (Curry et al., 1996). The input sounding profile was observed at Barrow, Alaska on on June 20, 1980 with a strong near-surface inversion as shown in Figure 2.9. We choose this case to investigate the formation of a cloud layer near the surface.

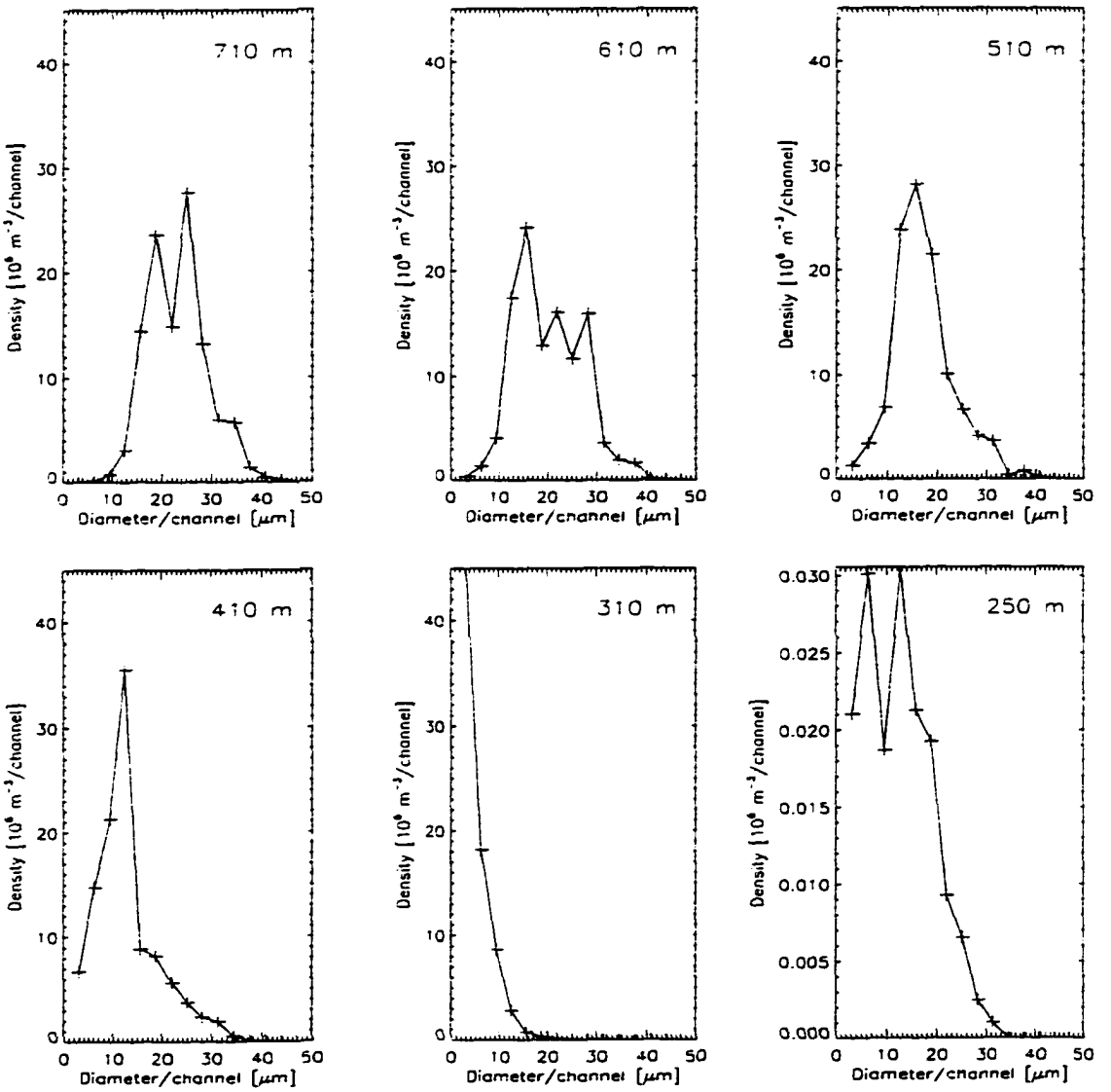

Figure 2.7. The droplet size distribution at six altitudes at the end of the run (10 hours after cloud formation). Again notice the different vertical scale in the lower right panel.

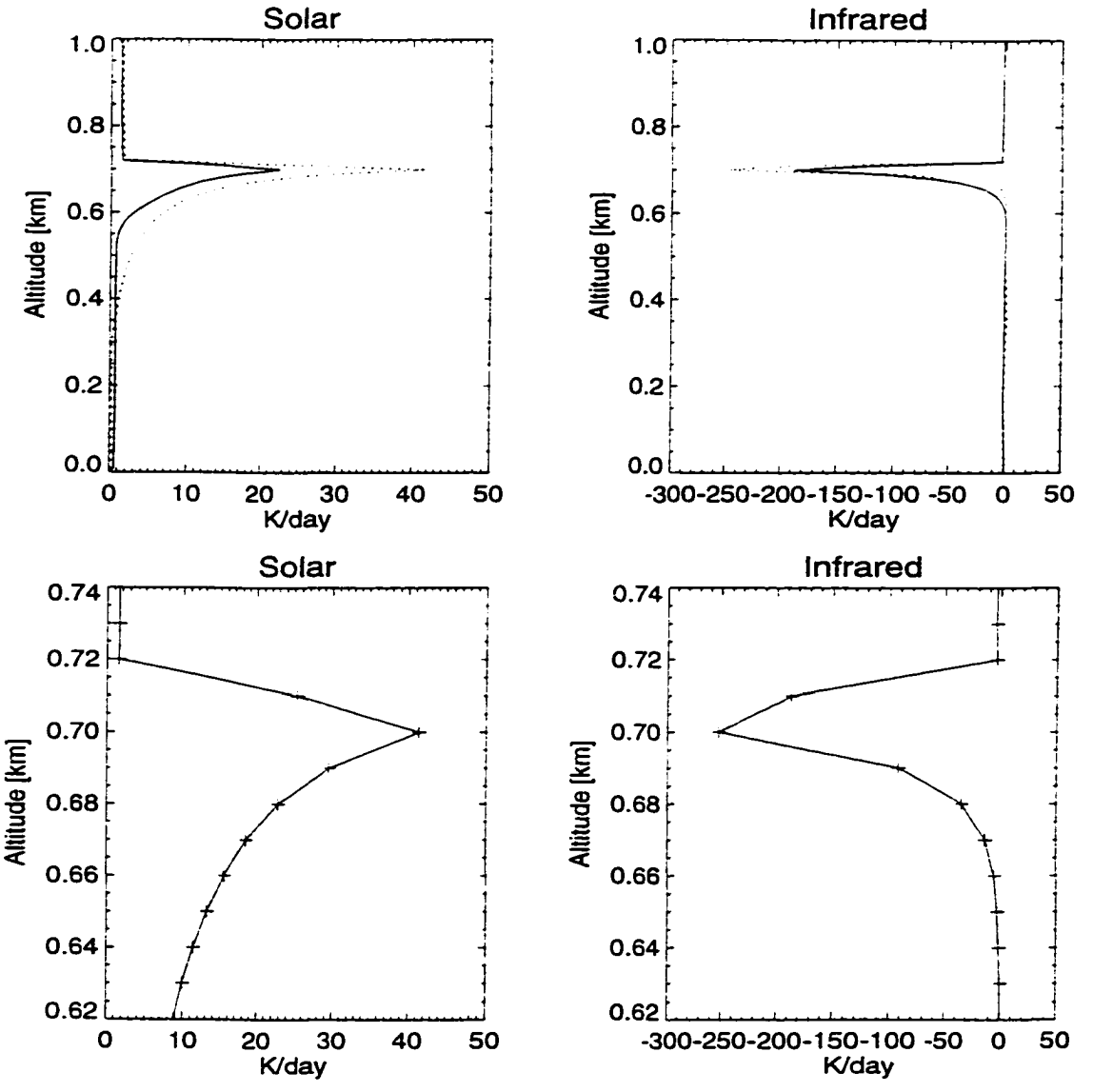

Figure 2.8. Warming/cooling rates from solar and infrared radiation. The solid lines are 1.6 hours after first cloud formation and the dotted lines at the end of the simulation. The solar zenith angle is about 60 at both times. The lower panels show the same warming/cooling rates near the cloud top at the end of the run, with the pluses indicating the actual grid points used in the computation.

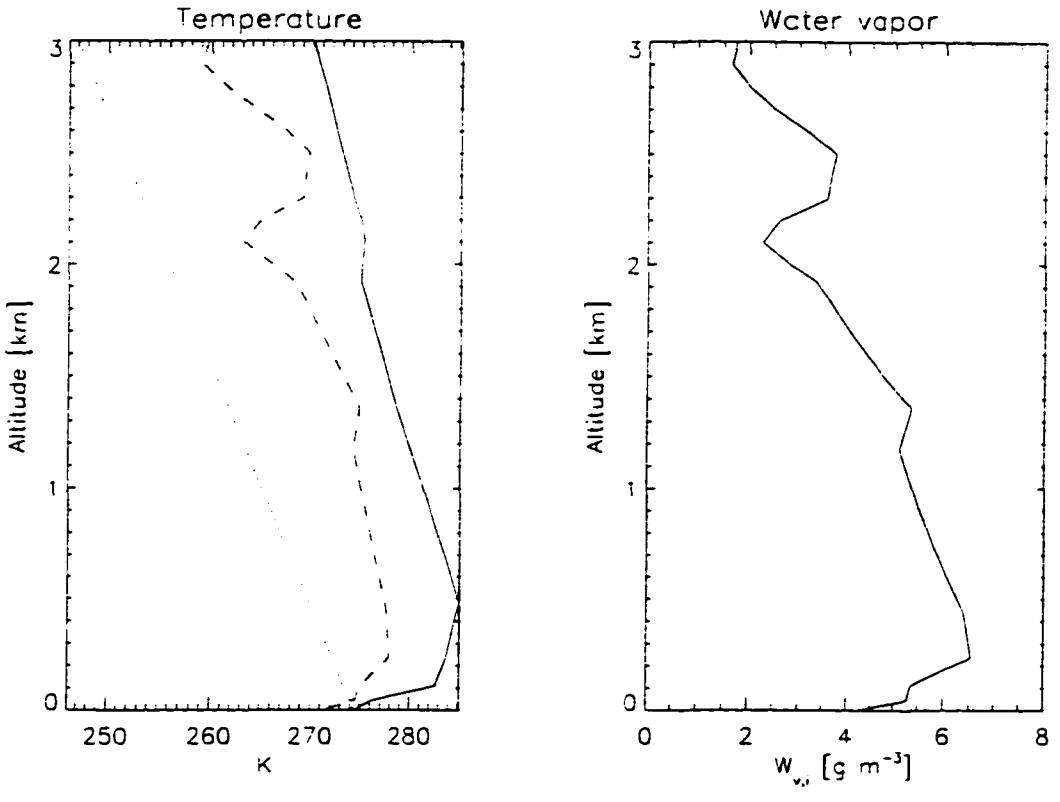

Figure 2.9. Sounding from Barrow, June 20, 1980. The solid line in the left panel is the actual temperature: the dashed line is the dew point temperature, T_c; and the dotted line is the lapse rate for dry air. The right panel shows the water vapor profile.

It takes 72 hours before a cloud layer forms initially close to the ground at the height of 250 m. Figure 2.10 shows the evolution of the temperature, liquid water, droplet density and r_{equ} and r_{95} after cloud formation. With the exception that the cloud base is now at the ground, there are many similarities to case A in Figure 2.5. In both cases the cloud-top cooling causes a strong temperature inversion to develop.

The droplet density is again almost altitude-independent while the LWC increases with altitude, showing that the increase in LWC is related to an increase in droplet size rather than density. The droplet density reaches about the same maximum value of $10^8\ m^{-3}$ as in the previous examples.

The results suggest that radiative cooling effect may cause the formation of a cloud

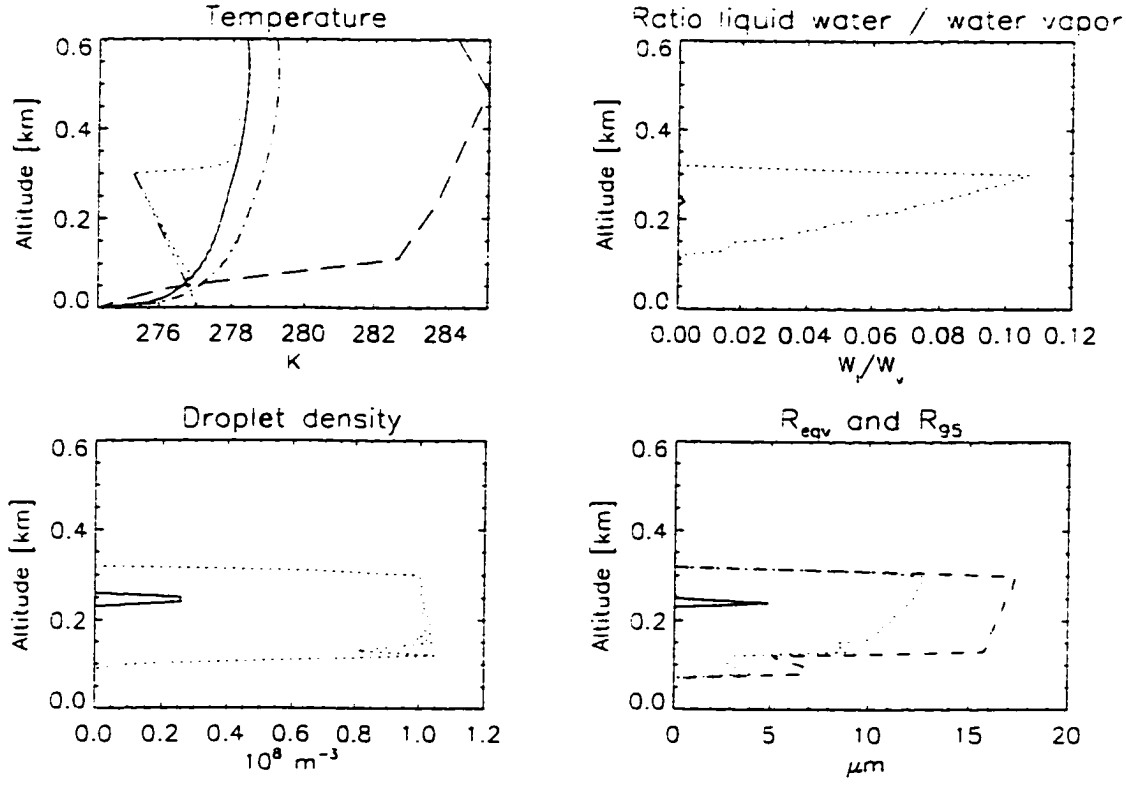

Figure 2.10. Temperature, ratio of liquid water to water vapor, droplet density and equivalent radius at the time when the cloud layer forms (solid line), and 5 hours (dotted line) after cloud formation. The upper left panel also shows the temperature at 9.5 hours before cloud formation (dash-dot line), and the dash-dot-dot-dot line shows the corresponding lapse rate temperature 5 hours after cloud formation. The initial temperature from the sounding is also shown (long dashes). In the lower right panel the dashed line denotes r_{95} after 5 hours, where r_{95} is the radius below which 95% of the liquid water is contained.

layer near the surface. However, strong wind shear may exist near the surface in naturei. The wind shear may trigger turbulence and result in cloud formation. The effect of wind shear is not included in the model.

2.3.3 Comparison with observations

During the Arctic Stratus Experiment (Tsay and Jayaweera. 1984; Curry, 1986) the microphysical properties of the ASCs were measured in situ from aircraft. Aircraft measurements cannot provide the vertical sounding profile needed for direct comparison with our model results. Our chosen initial conditions were taken from balloon sounding profiles, and therefore do not correspond to the precise conditions during the Arctic Stratus Experiment. Nevertheless, we may still compare the general properties of the modeled clouds with the aircraft observations.

Observations show that the LWC generally increases with altitude, at a rate less than or equal to the saturated adiabatic value. This increase in LWC is attributed to an increase in droplet size through condensation because the observed droplet concentration is nearly constant with altitude in a upper cloud layer (Tsay and Jayaweera, 1984). Our model yields results in agreement with these observed features. Moreover, the modeled droplet density is almost constant with altitude so that the increase in LWC is due to condensation which produces an increase in size only (as evidenced by the increase in r_{eqv} in Figure 2.5). The model also shows that the cloud is capped by a strong inversion, caused by thc cloud itself through the cloud-top infrared radiative cooling to space.

The model results qualitatively agree with these observations despite the fact that the input parameters have not been "tuned" to reproduce the observations. In both cases we computed droplet concentrations of roughly $10^8\ m^{-3}$, while the observations showed fluctuations in the range $0.5 - 4 \times 10^8\ m^{-3}$. In our model the computed droplet concentration depends on the number of CCN particles available and the maximum supersaturation. As input we used the highest CCN concentration measured by Hegg et al. (1995). However, Saxena and Rathore (1984) found CCN concentrations in late June

over the Arctic Ocean that were about 10 times higher than this. Had we used such high CCN concentrations as input, the modeled droplet density could increase by about the same amount. Clearly, more measurements are needed, of both CCN and cloud droplet concentrations, to determine whether models can reproduce observed droplet densities when CCN concentrations are known.

At the cloud top $LWC \approx 0.80\ g/m^3$ for case A and $0.60\ g/m^3$ for case B. This number is much higher than the observed values which lie in the range $0.1 - 0.5\ g/m^3$ (Tsay and Jayaweera, 1984). As seen from Figure 2.5, the LWC changes significantly with time, and even 10 hours after formation the cloud was still cooling. Moreover, the LWC depends on the initial amount of water vapor available for condensation. Since the model does not include settling of large droplets, precipitation process, and not strong enough entrainment, we in general overestimate the amount of LWC, in particular near the cloud top.

If we define the cloud top by the altitude at which LWC has its maximum value, we find for case A that the cloud top does not increase much with time while for case B the cloud top gradually lifts from 240 m to 300 m at the end of the simulation. Some of the observations during the Arctic Stratus Experiment indicate a continuous lifting of the cloud top, as does the model simulation of Herman and Goody (1976).

The droplet size distribution in the case of June 28, 1980 (Tsay and Jayaweera, 1984) showed that single-mode distributions near cloud base and double-mode distributions near cloud top. In Figure 2.7 the modeled distribution also has a single peak near cloud base but near the cloud top it is generally broader, often with two or more well-defined peaks. Qualitatively, the observed and modeled distributions are in agreement. The primary difference between the modeled distribution in Figure 2.7 and the measured distributions in the case of June 28, 1980 reported by Tsay and Jayaweera (1984) is that the modeled distribution in the upper parts of the cloud has some large droplets, with $30 - 40\ \mu$m diameter, while observations show very few particles beyond $20\ \mu m$. The modeled r_{95} radius shows a maximum value between 15 and $20\ \mu m$ while the observed

distributions have a maximum of 20 μm or less. As discussed previously, the droplet size obtained in simulation depends largely on the number of CCN. By giving small number of CCN it may produce large dorplets. The observed droplet concentrations were up to about $4 \times 10^8\ m^{-3}$ in the case of 28 June while they are only about $1 \times 10^8\ m^{-3}$ in the simulations. Tasy and Jayaweera (1984) reported that droplet spectra had 95% diameter larger than 40 μm and concentration less than $2 \times 10^8\ m^{-3}$ in some ASC cases such as observed on June 13 and June 14.

Although we obtain satisfactory agreement with most observed properties, in the cases presented here we do not obtain the multi-layered structure commonly observed. Herman and Goody (1976) attribute these layers to absorption of solar radiation within the cloud and subsequent evaporation of mid-cloud layers. From Figures 2.8 we note that the cloud-top cooling dominates the radiation budget, although some solar warming takes place inside the cloud. To determine whether the model may lead to multi-layered clouds due to radiative effects alone, it is necessary to run it for a substantially longer time (the multi-layered clouds reported by Herman and Goody (1976) typically took several days to form). An alternative explanation for the formation of multi-layered clouds would simply be that their location is determined by the initial humidity profile that largely determines where condensation starts. The sounding humidity profiles chosen as initial conditions in the two cases discussed above may not be conducive to the formation of multi-layered clouds. The formation of multiple cloud layers will be the subject of Chapter 4.

2.4 Discussion

The importance of mixing in the model underscores the need for a better understanding of this turbulent process in Arctic stratus clouds. Since the mixing is parameterized in our model, and ad hoc parameters (such as the time Δt_{mix} between mixings) were introduced to describe the mixing, this issue remains unresolved. In fact, some properties of the modeled clouds (e.g., the altitude variation of the droplet density and the maximum

supersaturation) depend quite sensitively on these parameters. A better understanding of this process will require both numerical modeling and direct measurement of the relevant quantities in ASCs. For instance, measurements of vertical wind speed and its variability will provide information about both the spatial and time scale of the mixing. Tethered, or even better, drifting balloons (in a Lagrangian sense) may be well suited for this purpose. As alluded to above, in situ measurements of both the CCN spectrum (inside and outside the cloud) and the droplet density are also valuable since they provide indirect information about the maximum supersaturation, which in turn depends sensitively on the nature of the mixing process.

Compared with observations the model creates droplets that are somewhat too large, especially near the cloud top. Also, it tends to give maximum values of the liquid water content that are somewhat larger than what is typically observed. Several factors could contribute to the overestimation of LWC by the simulation. For example, the initial CCN number adopted in the simulation may have an effect on the droplet size and thus on the droplet coalescence process. This will eventually have an influence on cloud liquid water.

In a 1-D model an air column is isolated from the environment. If an air column in the Arctic went to be isolated from the environment, its temperature would continue to decrease due to radiative cooling. Therefore, all water vapor in the air column would eventually condense. In nature, air motions occur in three dimensions. Large scale motion will bring warm air to the Arctic and bring cold air from the Arctic to lower latitudes. This process will compensate for energy loss due to radiative cooling in the Arctic.

Entrainment process may bring warm and dry air to the cloud layer. Since ASCs have large horizontal extent, horizontal entrainment may not affect the LWC inside a cloud layer significantly. However, entrainment at the cloud top may be significant, because there is usually a strong temperature inversion there. Such entrainment does bring warm air down into the cloud layer and thus compensates (somewhat) for the heat lost due to

radiative cooling. Hence, cloud-top entrainment does slow down the cooling and lead to less cloud liquid water formation. In our 1-D model, entrainment is included based on vertical mixing between two adjacent layers if one layer is unstable. However, this 1-D cloud-top entrainment process is likely to be weaker than that occuring in nature.

The lack of cloud dissipation mechanisms in the model, such as coalescence and gravitational settling may also contribute to the overestimation of LWC. The coalescence process could significantly accelerate the speed of droplet growth and lead to the creation of droplets with larger size. This will in turn increase gravitational settling that could initiate drizzle production or precipitation which will decrease cloud liquid water. Since small droplets have small collision cross sections and slow settling speeds and hence have little chance of colliding with one another, coalescence can only become significant after the droplet spectrum evolves to include a spread of sizes and fall speeds, with some droplets reaching radii of 25 to 30 μm or so (Rogers and Yau, 1988). By the time some droplets reach a radius of 30 μm in a developing cloud, coalescence is likely to be the dominant growth process. During the 10 hours after the cloud formation in our simulations, few droplets have radii larger than 20 μm. The effect of coalescence is therefore not expected to be significant in our simulations. For a droplet with a diameter of 20 μm, the terminal falling speed is about 1 cm/sec. It will take about 10 hours for it to fall down 400 meters in calm atmophere. Suppose such a droplet exists at the cloud top, then it takes about 10 hours for it fall out of the cloud layer. Therefore, the effect gravitational settling is also not expected to be significant in our simulations. To study the long-term evolution and persistence of these clouds, the effect of coalescence and gravitational settling must be included in the model.

We must note that the 1-D model may produce unrealistic supersaturation due to the simplification treatment of convective adjustment and may result in unrealistic droplet concertrations. Since the effect of three-dimensional eddy motions is unable to be included in a 1-D model, droplets may stay too long in cloud in simulations and produce more large droplets. Also, a 1-D model cannot capture the effect of stabilization below

cloud base which inhibits mixing in a "real" cloud.

The results presented here are encouraging, because they indicate that a very simple model that ignores explicit dynamics, as well as horizontal transport and inhomogeneities, and that includes only radiation, cloud microphysics, and parameterized vertical mixing, is sufficient to reproduce the general features of Arctic stratus clouds. These findings underscore the important role that radiation plays in the Arctic, and they indicate that the properties of these clouds may to a large extent be understood through the interplay between radiation and cloud microphysics. If future more comprehensive studies should confirm that Arctic stratus clouds may indeed be described in such simple terms, the treatment of these clouds in climate models may also be simplified.

2.5 Conclusions

In this chapter a one-dimensional, radiative-convective model with detailed cloud microphysics has been used to study of the formation of Arctic stratus clouds. The study is focused on the radiative and microphysical processes associated with the cloud formation. The aim is to improve our understanding of the basic interaction between radiation and cloud microphysics. In particular, I wanted to explore to what extent the properties of Arctic stratus clouds can be understood in terms of radiation and microphysics alone, in the absence of dynamical processes other than vertical mixing due to convective instability. A comprehensive radiative transfer code is used to compute solar and infrared warming/cooling rates. The radiative transfer code is coupled to a cloud microphysics module that simulates the detailed cloud droplet activation and evaporation, using the full droplet size distribution. The convective adjustment scheme allows for vertical mixing of adjacent atmospheric layers to accommodate transport of heat and moisture. It also allows droplet spectra to mix.

Use of balloon soundings from Barrow, Alaska to initialize model simulations leads to modeled cloud properties that are both qualitatively and quantitatively in good overall agreement with in situ measurements. Cloud-top infrared cooling to space leads to a

cloud-top temperature inversion in the model similar to that commonly observed. It is found that the liquid water content generally increased with altitude, while the droplet density is essentially altitude-independent. Thus, in agreement with observations, the increase in liquid water with altitude is due to an increase in droplet size, not droplet density. Finally, we obtain fairly broad droplet size distributions, with widths typically increasing with altitude and displaying more than one peak. The shape of the droplet distribution is largely dictated by the vigorous mixing, which is a consequence of the strong cloud-top cooling. The initial cloud condensation nuclei spectrum seems to be less important for the shape; it primarily determines the total number of droplets rather than the shape of the distribution.

Chapter 3

The Role of Radiative Transfer in the Formation of Arctic Stratus Clouds

In Chapter 2 a one-dimensional radiative-convective model was described which includes detailed cloud microphysical processes and a comprehensive radiative transfer scheme. It was shown that the simulated Arctic stratus cloud properties qualitatively agree with the observations. These results underscores the importance of radiative warming/cooling in the formation of ASCs. In this chapter I will use this model to study the cloud formation process. and focus on the formation of a single layer of cloud. The formation of multi-layered clouds will be discussed in the next chapter.

As mentioned in Chapter 1 three hypotheses have been proposed to explain the occurrence of multi-layered clouds. None of these three hypotheses provided a clear explanation of how a single cloud layer forms. Although the modeling results of Herman and Goody (1976) as well as McInnes and Curry (1995b) have pointed out the importance of radition in cloud formation, they did not explain in any detail how and to what extent the radiation affects the cloud formation process. They did not disscus what

determines the distribution of radiative warming/cooling rates which may be critical for cloud formation.

In this chapter I will focus on investigating the impact of radiation, especially infrared radiation, on the cloud droplet condensation and evaporation. The impact of vertical humidity and temperature gradients on radiative warming/cooling rates and in turn on cloud formation will be discussed.

3.1 Initial data and simulation design

The simulations in this study are initialized by a data set based on the observation of June 28, 1980 in the Arctic Stratus Experiment. Detailed descriptions of this case have been presented in Chapter 1 and by Tsay and Jayaweera (1984).

I will conduct a series of different simulations all starting with a clear atmosphere to investigate the cloud formation. To simplify the problem I will only focus on the formation of a single cloud layer, taken to be the upper cloud layer observed on June 28, 1980. The initial water vapor mixing ratio for the following simulation is shown in Figure 3.1 (a). To prevent a cloud layer from forming close to the surface, I reduced the water vapor amount below 0.5 km to levels significantly less than the observed ones. The water vapor mixing ratio is 5.1 g/kg between 0.5 and 1.2 km altitudes. The relative humidity is about 80%. The water vapor content decreases significantly with height between 1.2 and 1.3 km, which is in agreement with the observations. This humidity profille yields the dew point temperature profile shown by the dashed line in Figure 3.1 (b). The initial temperature decreases with height by a constant laspe rate of 1.8 K/km.

The dew point temperature is the temperature to which moist air must cool, with pressure and humidity held constant, to reach saturation with respect to water. In the data used for initialization, the difference between the initial temperature and the dew point temperature is almost constant and 2 K between 0.5 and 1.2 km. Therefore, the cooling required to form a cloud is the same at all levels between 0.5 and 1.2 km. The surface temperature is held constant at $T_s = 273.15$ K.

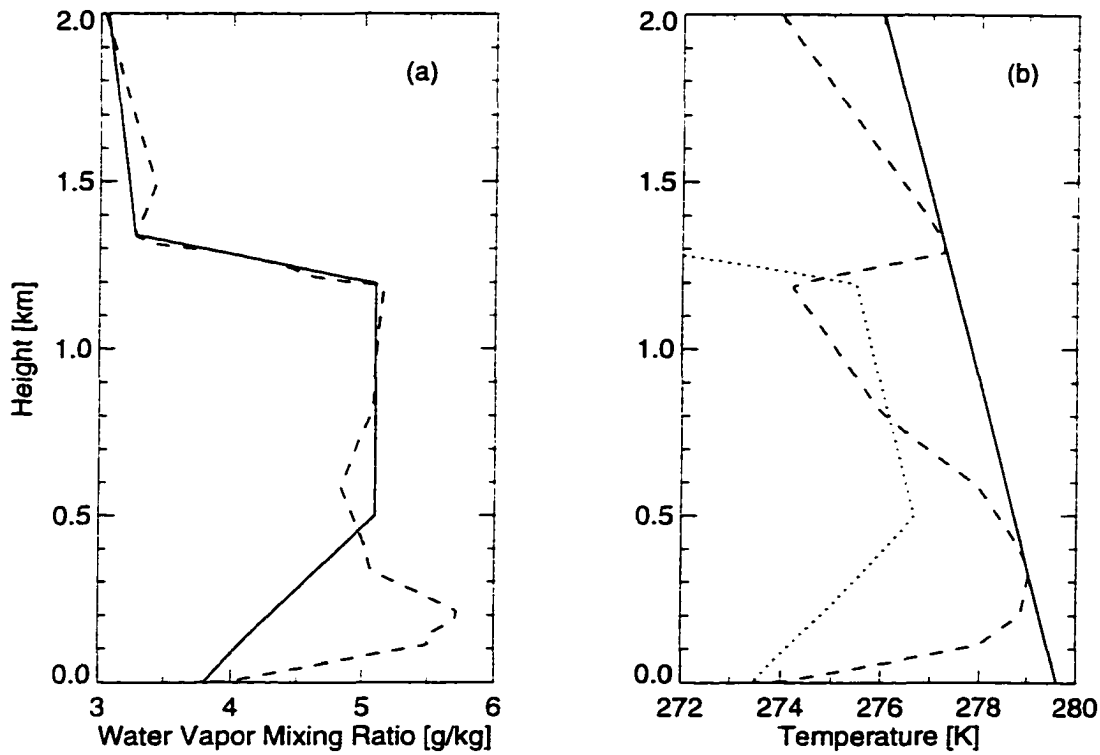

Figure 3.1. (a) Intial water vapor mixing ratio [g/kg]; (b) Initial temperature [K]. Solid lines are the initial data for simulation. Dashed lines are the observation. The dotted line in the left panel is dew point temperature.

The model vertical grid is 5 m below 2 km height, 20 m between 2 and 3 km, and it is larger than 100 m above 3 km. The top of the model for the following simulations is 35 km. The minimum time step for vertical mixing is set to 2 s.

The maximum droplet concentration observed on June 28, 1980 was about 450 cm^{-3} (Tsay and Jayaweera, 1984). The initial CCN number (N_{CCN}) for the following simulations is given by the power law (Twomey, 1977)

$$N_{CCN}(s) \approx c(100s)^{\kappa}. \tag{3.1}$$

Use of $\kappa = 0.34$ and $c = 6.4 \times 10^8\ m^{-3}$, yields N_{CCN} of about 500 cm^{-3} for a supersaturation s of 0.4%.

The diurnal cycle of solar radiation is not included in the simulations to simplify the

problem. A fixed solar zenith angle of 70° is adopted.

3.2 Simulation results

3.2.1 Formation of the cloud layer

With the initial conditions specified above, the model is integrated forward in time for 35 hours. A single cloud layer appears between 0.8 and 1.2 km (Figure 3.2 a). This cloud layer initially forms at 30.5 model hours at 1.18 km altitude, and it develops rapidly once it has formed initially. The cloud liquid water mixing ratio is about 0.78 g/kg at the end of the simulation about 4.5 hours after the cloud layer initially forms. The cloud top is lifted about 40 meters to 1.22 km and the cloud base extends downward to 0.8 km. The thickness of the cloud layer is therefore about 400 meters at the end of the simulation. The cloud liquid water content increases linearly with height at a rate close to the adiabatic value.

The vertical distribution of droplet density (Figure 3.2 b) is almost constant with height. It changes only slightly with time during the cloud evolution. The maximum droplet density found within the cloud layer is about 400 cm^{-3} consistent with the maximum supersation in the simulation which is about 0.375%. The droplet equivalent radius increases with height and the largest drops appear at the cloud top. The equivalent radius increases also with time and is about 8 μm at the end of the simulation (4.5 model hours after the initial cloud formation). These results suggest that the increase in cloud liquid water content with height and with time is related to the increase in droplet size rather than droplet density.

A detailed distribution of the droplet size produced by the model at 4.5 model hours after the initial cloud formation is shown in Figure 3.3. The droplet size distribution has been collected in 15 equidistant bins with mean diameter 3.13 μm apart, with the pluses indicating the center of each bin to enable comparison with the observations taken on June 28, 1984 (Tsay and Jayaweera, 1984). The simulation result shows that the droplet

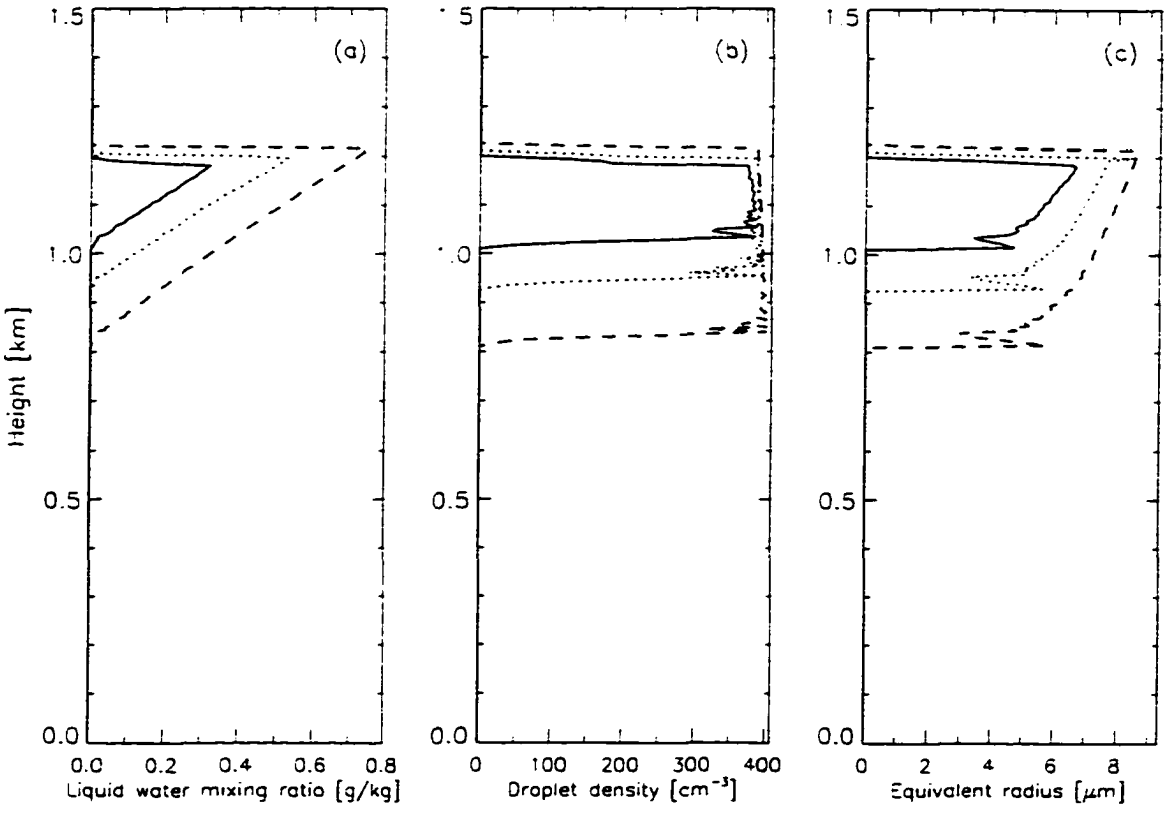

Figure 3.2. (a) Liquid water mixing ratio [g/kg]; (b) Droplet density [cm^{-3}]; (c) Equivalent radius [μm]. Solid, dotted and dashed lines correspond respectively to 1.5, 2.5 and 4.5 hours after initial cloud formation.

size increases with height. The droplet spectrum has two peaks near the cloud top with cloud drop diameters around 6 μm and 13 μm, and has a single peak at about 6 μm near the cloud base.

3.2.2 Comparison with the observations

The observations of June 28, 1984, shown in Figure 1.2, were analyzed by Tsay and Jayaweera (1984) as well as Curry (1986). The cloud layer forms in the simulation at about the same place as the observed upper cloud layer. The model simulation reflects the observed characteristics, namely that the cloud liquid water content increased linearly with height at a rate close to the adiabatic value.

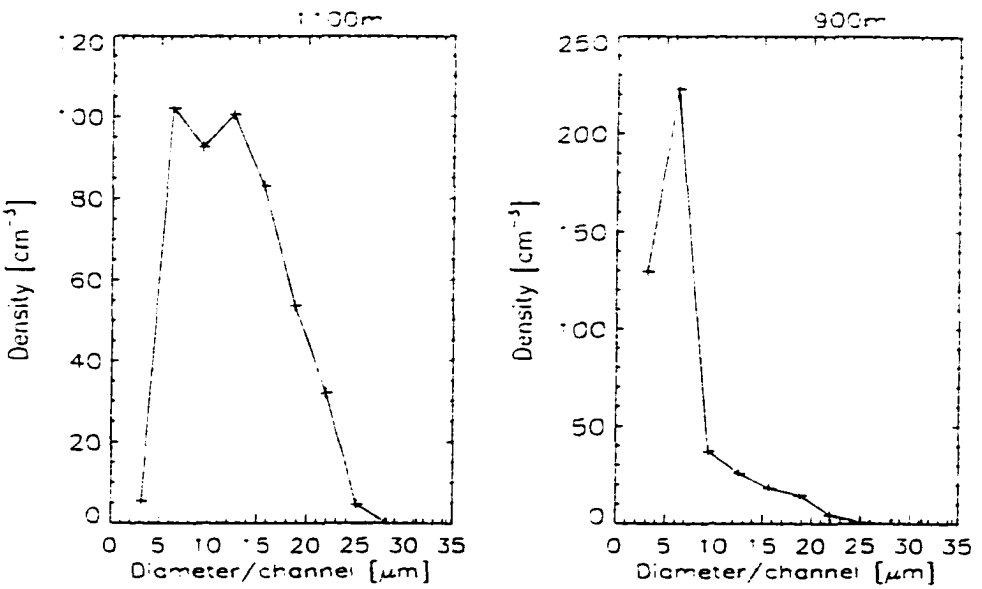

Figure 3.3. Droplet spectrum at 4.5 model hours after the initial cloud formation (35 simulation hours)

The modeled microphysical properties agree very well with the observations. The simulation shows that the vertical distribution of the droplet density is constant with height, whereas the equivalent radius increases with height, in good agreement with the observations. The observations showed that the droplet distribution (Figure 1.3) changed from a single mode (peak at 6 μm diameter) near the cloud base to a double mode (peaks at 6 and 16 μm) near the cloud top (Tsay and Jayaweera, 1984). Again, the simulated droplet spectra agree well with the observed ones.

3.3 Physics of the cloud formation and initial evolution

The above results suggest that the model well simulates the observed cloud properties. In this section I will further investigate the physics of the cloud formation and the initial cloud development, and I will focus on the role of radiative transfer, especially infrared radiation, in determining the initial cloud behavior.

First, I will discuss how the water vapor condensation occurs in the simulation. The

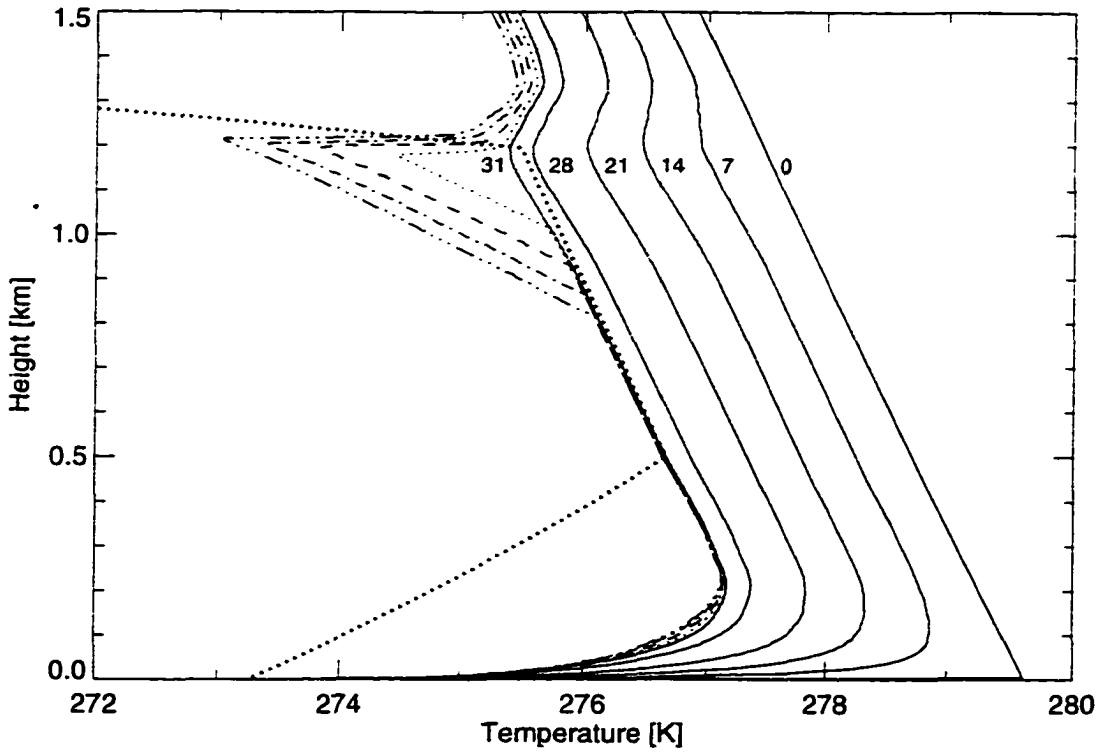

Figure 3.4. Temperature profiles. Dotted, dashed, dashed-dotted and dashed-dotted-dotted lines represent profiles at 32, 33, 34 and 35 model hours, respectively. The heavy dotted line is the dew point temperature.

dew point temperature is the atmospheric temperature at which water vapor condensation occurs. There is only a very slight change in the water vapor profile due to vertical mixing before the initial cloud formation (not shown). Therefore, the dew point temperature profile has not changed much either since the atmospheric pressure is constant during the simulation. For condensation to occur the atmospheric temperature must decrease to the dew point value. Figure 3.4 shows how the temperature evolves with time during the simulation. Before the cloud forms there is a large temperature decrease near the surface below 0.3 km because the surface temperature is much lower than the atmopheric temperature. However, between 0.3 and 1.2 km the temperature decreases slowly at a rate of only about -0.07 K/hour. At about 1.2 km, where a larger water va-

por gradient exists, the temperature decrease is somewhat larger than in adjacent layers. This gives rise to a small temperature inversion around this height after 14 model hours.

The temperature continues to decrease throughout the atmosphere during the simulation. It first reaches the dew point temperature (the heavy dotted line in Figure 3.4) at about 1.17 km at 30.5 model hours. Water vapor condensation then occurs and the cloud starts forming at this height.

After the initial cloud formation, the temperature decreases very fast in the cloud layer. Such strong temperature decrease causes considerable water vapor condensation and the cloud liquid water increases significantly with time (Figure 3.2 a).

The maximum rate of temperature change is about -1 K/hour during the first hour after initial cloud formation. It decreases to -0.3 K/hour 4.5 model hours after the cloud forms. The temperature within the cloud layer decreases about linearly with height at a rate close to the saturated adiabatic lapse rate, suggesting that strong vertical mixing takes place within the cloud layer. A strong temperature inversion appears right above the cloud top.

Figure 3.5 shows radiative warming/cooling rates before the cloud forms (at 7, 14, 21 and 28 model hours, respectively). There are three peaks in the vertical profile of the infrared cooling rate. Strong infrared radiative cooling occurs near the ground because the surface temperature is much lower than the atmospheric temperature. Two other peaks appear at about 0.5 and 1.2 km where significant water vapor gradients occur (Figure 3.1 a). The absolute magnitude of the peaks decreases with time. This may be explained by the changes in the temperature profiles as the temperature inversion develops. Also, the vertical mixing processes may cause the water vapor to become more uniformly distributed with height.

The solar warming rate does not vary with time since the solar zenith angle was fixed in this simulation. It is much smaller than the infrared cooling rate (only about 10% of the infrared cooling). There is a peak at 1.18 km in the solar warming rate. This peak coincides with the water vapor gradient.

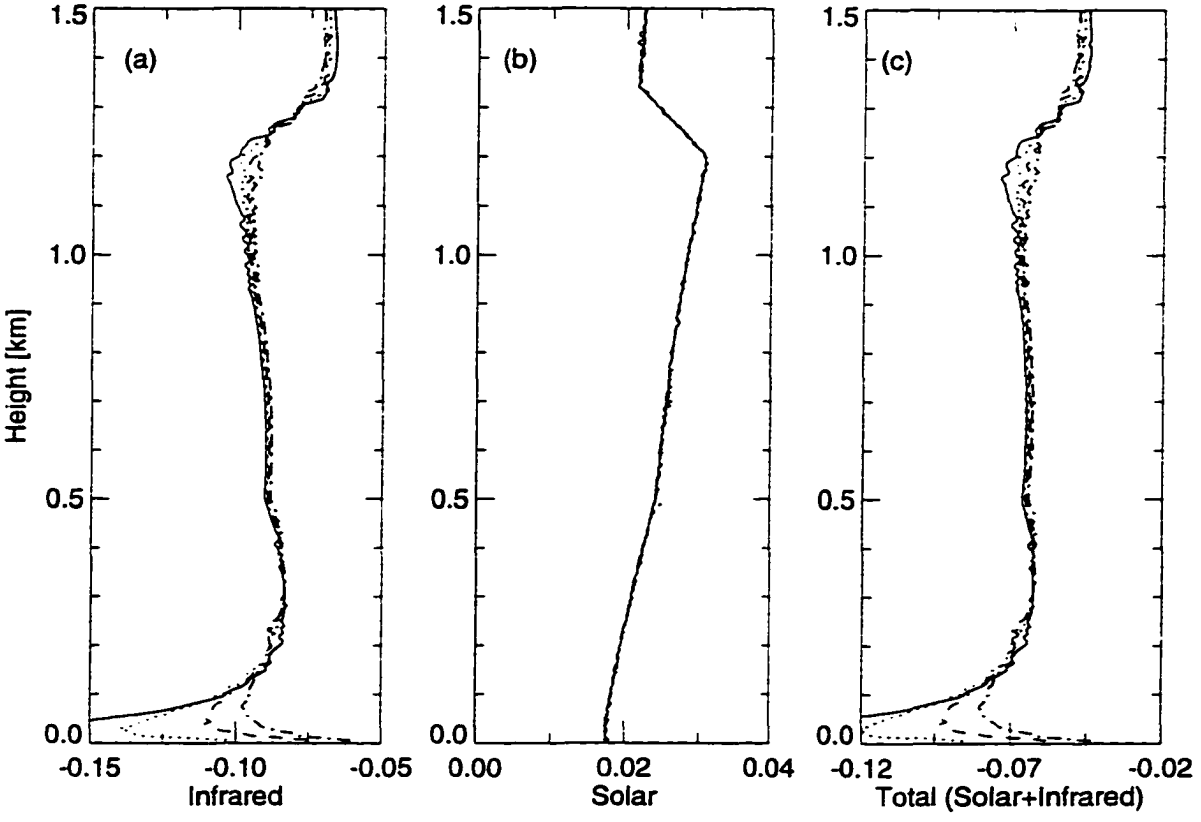

Figure 3.5. Radiative worming/cooling rates before the cloud forms. Solid, dotted, dashed and dashed-dotted lines show profiles at 7, 14, 21, and 28 model hours, respectively. Unit is K/hour. (a) Infrared; (b) solar; (c) total (infrared + solar).

The total (solar and infrared) radiative effect is negative. Thus, there is a net cooling which will cause a temperature decrease. The total radiative warming/cooling rates range from -0.025 to -0.08 K/hour between 0.3 and 1.5 km. The similar apperance of the total and infrared warming/cooling rate profiles suggest that the decrease in temperature is caused mainly by the infrared radiative cooling. Also, the changes in total radiative warming/cooling rates with time are similar to those of the infrared cooling rates. The total radiative cooling rate is close to the rate of temperature decrease, suggesting that the temperature decrease is caused primarily by the radiative cooling.

There are three peaks also in the total radiative warming/cooling rate appearing at the same heights as those in the infrared cooling rate. The peak at about 1.2 km causes

the temperature at that height to decrease more than at other heights between 0.3 and 1.5 km. This temperature decrease eventually leads to the initial cloud formation at around that height. The somewhat larger cooling rate at about 1.2 km (than at other heights between 0.3 and 1.5 km) corresponds to the large water vapor gradient there. This cooling rate leads to a small temperature inversion at this height after 14 model hours, and to the initial cloud formation at 30.5 model hours. The appearance of the temperature inversion may cause the infrared cooling rate to decrease slightly at that height which partly offsets the initial radiative cooling effect. However, the above analyses suggest that the initial condensation of water vapor at 1.2 km is due to the continual temperature decrease caused by the enhanced infrared radiative cooling associated with the significant moisture gradient at this level.

Figure 3.6 shows radiative warming/cooling rates after the cloud layer has initially formed (1.5, 2.5 and 4.5 model hours after the cloud formation). Infrared cooling rates around the cloud top (at about 1.2 km) increase significantly after the initial cloud formation. Strong infrared cooling occurs in a very thin layer near cloud top. The height of this thin layer ascends with the cloud top. The maximum infrared cooling rate increases as the cloud develops and is about 18 K/hour at 4.5 model hours after initial cloud formation. The solar warming rate is also strong only in a very thin layer near cloud top. However, it is only about 10% of the infrared cooling rate. Its maximum is about 1.7 K/hour at 4.5 model hours after intial cloud formation. The total solar and infrared warming/cooling rate yields a pronounced net cooling effect that maximizes near cloud top. This maximum net cooling rate is about 16 K/hour at 4.5 model hours after cloud formation. Strong total radiative cooling also occurs in a very thin layer near cloud top.

The rates of temperature change (Figure 3.4) are much smaller than the corresponding radiative cooling rates after the cloud forms. Nevertheless, the temperature decreases throughout the entire cloud layer which is much thicker than the layer where strong radiative cooling occurs. This suggests that the strong vertical mixing taking

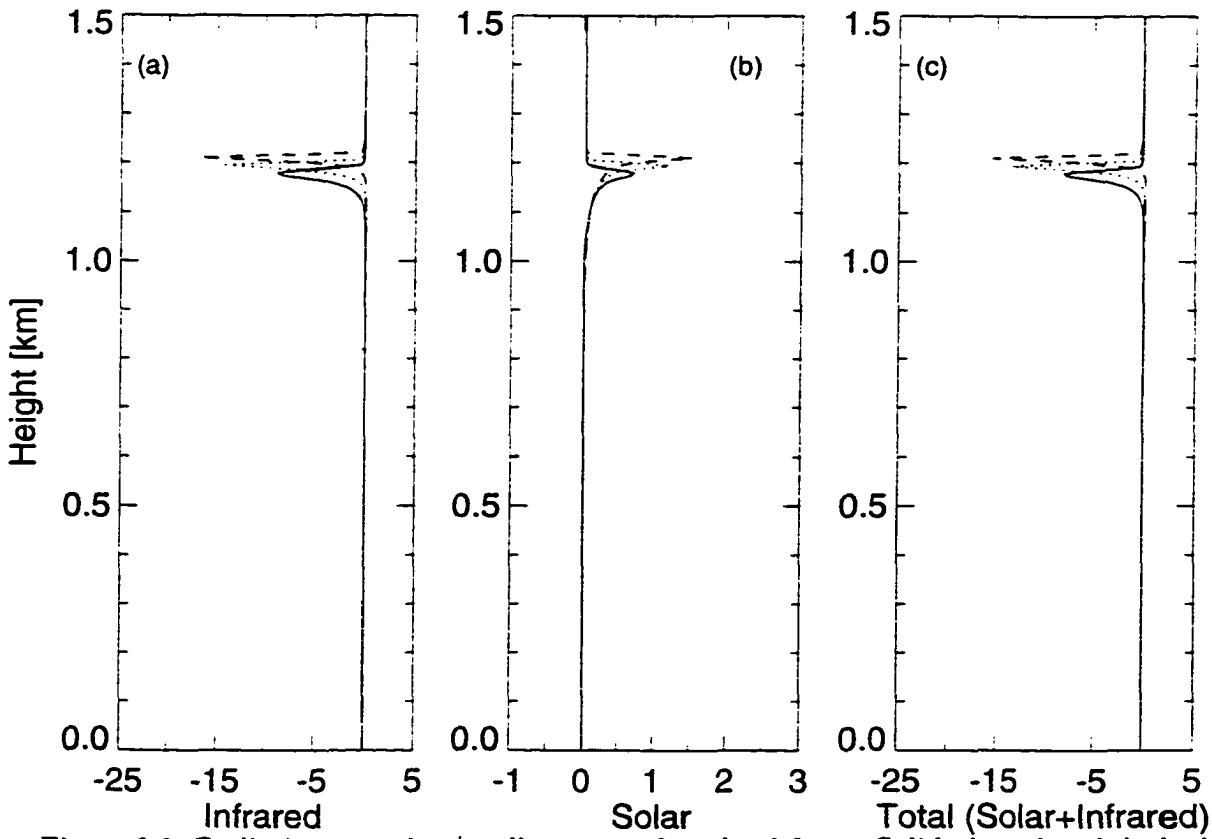

Figure 3.6. Radiative warming/cooling rates after cloud form. Solid, dotted and dashed lines are respectively 32. 33 and 35 model hours (1.5, 2.5 and 4.5 model hours after cloud form). Unit is K/hour. (a) Infared; (b) solar; (c) total (infrared + solar).

place throughout the cloud transports heat vertically upward to the cloud top. where strong radiative cooling occurs, to compensate partly for the radiative cooling. Latent heat release due to water vapor condensation may also have such a compensatory effect.

3.4 Sensitivity Studies

The above investigation shows that the cloud formation depends on the temperature decrease, which is due to radiative cooling, while the strong radiative cooling corresponds to a significant change in water vapor distribution. Several sensitivity tests will be carried out in this section to investigate how water vapor and temperature profiles affect

radiative warming/cooling. The goal is to enhance our understanding of the impact of the vertical distribution of the water vapor and temperature on radiative cooling and eventually on cloud formation. The effect of water vapor gradients, water vapor content, and temperature gradients will be discussed.

3.4.1 The effect of a water vapor gradient

It was found in the base simulation that the peaks in the solar and infrared warming/cooling appear at the height (about 1.2 km) where large vertical humidity changes occur. The peak in the total radiative cooling determines the location of initial cloud formation. The following simulations are used to investigate the relation between the water vapor gradients and radiative warming/cooling. The initial temperature profile is taken to be the same as that in the base simulation. Several kinds of idealized water vapor profiles are used to investigate their effect on radiation.

Five simulations are conducted (see Figure 3.7) to investigate the effect of humidity gradients on radiative transfer and cloud formation. The initial water vapor mixing ratios adopted for these five simulations are shown in Figure 3.7 (a). Below 1 km the initial water vapor content of the five simulations are taken to be the same; they are different only between 1 and 3 km. An abrupt change in humidity is assumed to occur at the 1 km level. The humidity gradient at the 1 km level influences the profiles of both solar and infrared warming/cooling rates, and thus the total radiative warming/cooling rates. A negative humidity gradient (humidity decreases with height at the 1 km level), yields solar warming and infrared cooling rates that are stronger below 1 km height than above, while a positive humidity gradient (humidity increases with height at 1 km level), yields solar warming and infrared cooling rates that are weaker below the 1 km level than above.

Peaks appear at 0.995 km level in the solar and infrared warming/cooling rates, and thus in the total radiative warming/cooling rates. The larger the negative humidity gradient, the larger are the peaks in radiative warming/cooling rates. This suggests that

a certain critical humidity gradient is required in order for the cloud to form.

According to observations (Tsay and Jayaweera, 1980; Curry et al., 1988) the water vapor path in the Arctic boundary layer below 2 km varies within a range from 3 g/kg to as much as 6 g/kg. The water vapor path may affect the radiative warming/cooling rate and thereby cloud formation. The simulations presented in Figure 3.8 are conducted to examine the impact of the water vapor amount on radiative warming/cooling rates and on cloud formation. As shown in Figure 3.8 (a) the water vapor gradient across the 1 km level is the same, but the water vapor path below 1 km is 3, 4, 5 and 6 g/kg, respectively, for the four cases labeled 1, 2, 3 and 4. The difference in the water vapor amount between adjacent lines is 1.0 g/kg. The amount of the water vapor influences the magnitude of both solar and infrared warming/cooling, and thus the total radiative warming/cooling. It also influences the peaks at 1 km where the constant humidity gradient is located. With increased humidity, both the solar and infrared warming/cooling rates are stronger above 1 km but they have weaker peaks just below the 1 km level. This suggests that for a fixed humidity gradient at some level, the temperature just below that level will decrease faster compared with other heights when there is less total water vapor in the atmosphere. Nevertheless, since the dew point temperature decreases with water vapor path, it may still take longer for the cloud to form when there is less water vapor. This will be further discussed later.

In order to further understand the relations among water vapor path, water vapor gradient, radiative warming/cooling and cloud formation, a series of simulations were made for a range of total humidity and a range of humidity gradients at the 1 km level. Figure 3.9 shows radiative warming/cooling rates at the height of 0.995 km. The vertical coordinate is water vapor mixing ratio below 1 km, and the horizontal coordinate is the gradient of the water vapor mixing ratio across the 1 km level. Large warming/cooling rates appear when the total humidity is small and the negative humidity gradient is large. The change in warming/cooling rates is most pronounced when the total humidity is small and the negative humidity gradient is large.

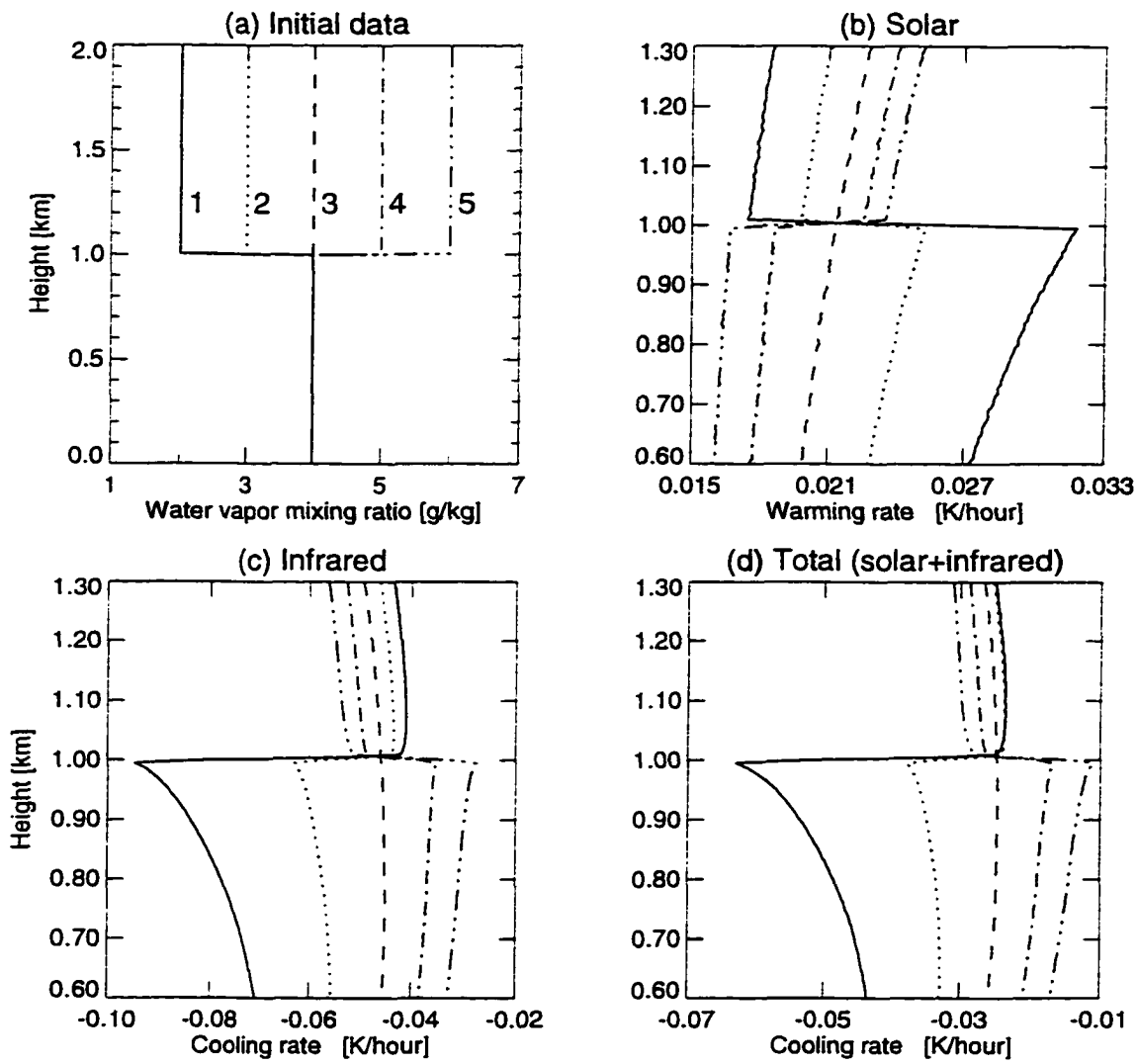

Figure 3.7. The effect of the water vapor gradient on the radiative transfer. (a) Initial water vapor mixing ratio; (b) solar only; (c) infrared only; (d) total (solar + infrared). Solid, dotted, dashed, dashed-dotted and dashed-dotted-dotted lines correspond to the different humidity profiles specified in (a), corresponding to a jump in the water vapor mixing ratio of -2, -1, 0, 1 and 2 g/kg, respectively, across the 1 km level.

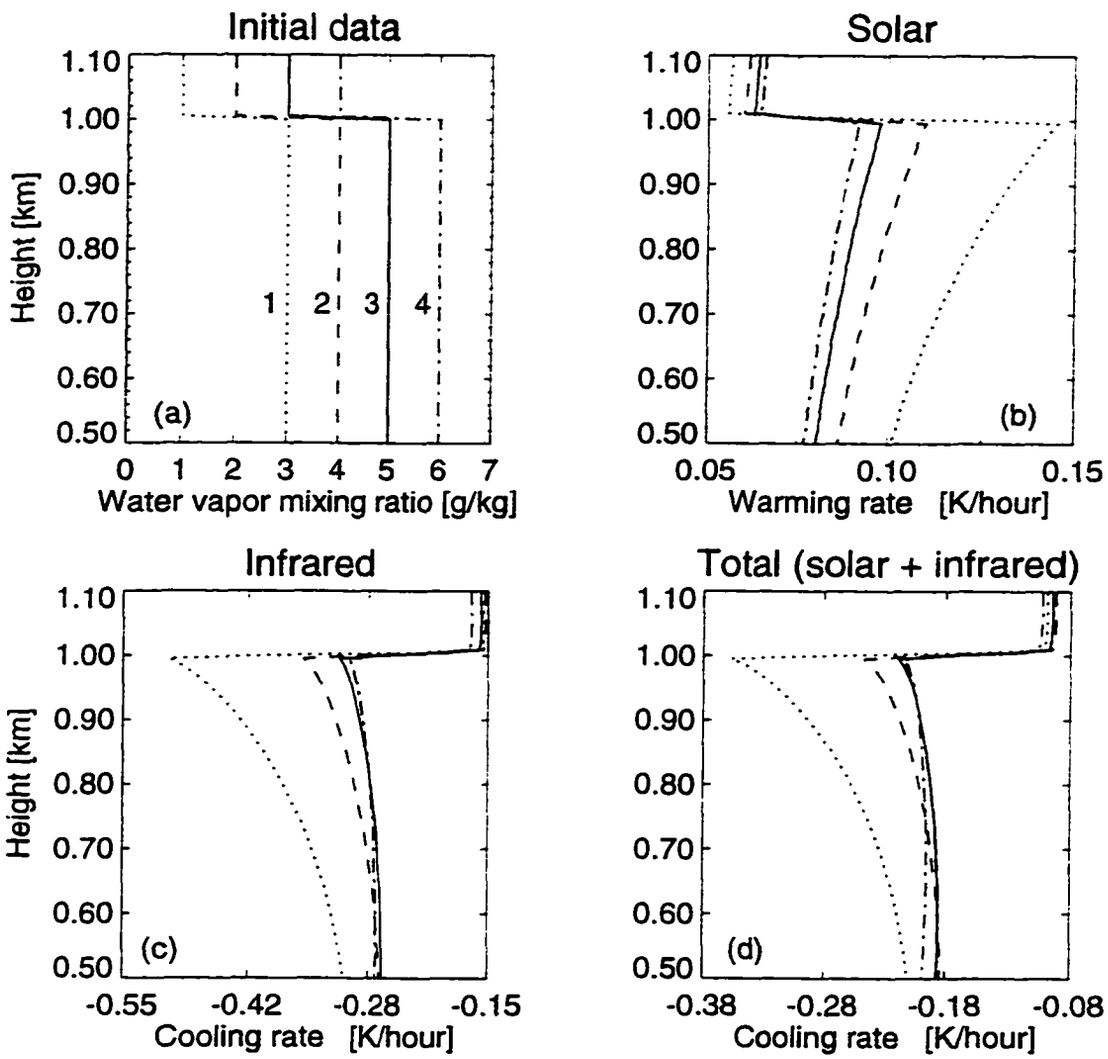

Figure 3.8. The effect of the water vapor content on the radiative transfer. (a) Initial water vapor mixing ratio; (b) solar; (c) infrared; (d) total (infrared + solar). Solid, dotted, dashed, dashed-dotted and dashed-dotted-dotted lines correspond to the different humidity profiles specified in (a).

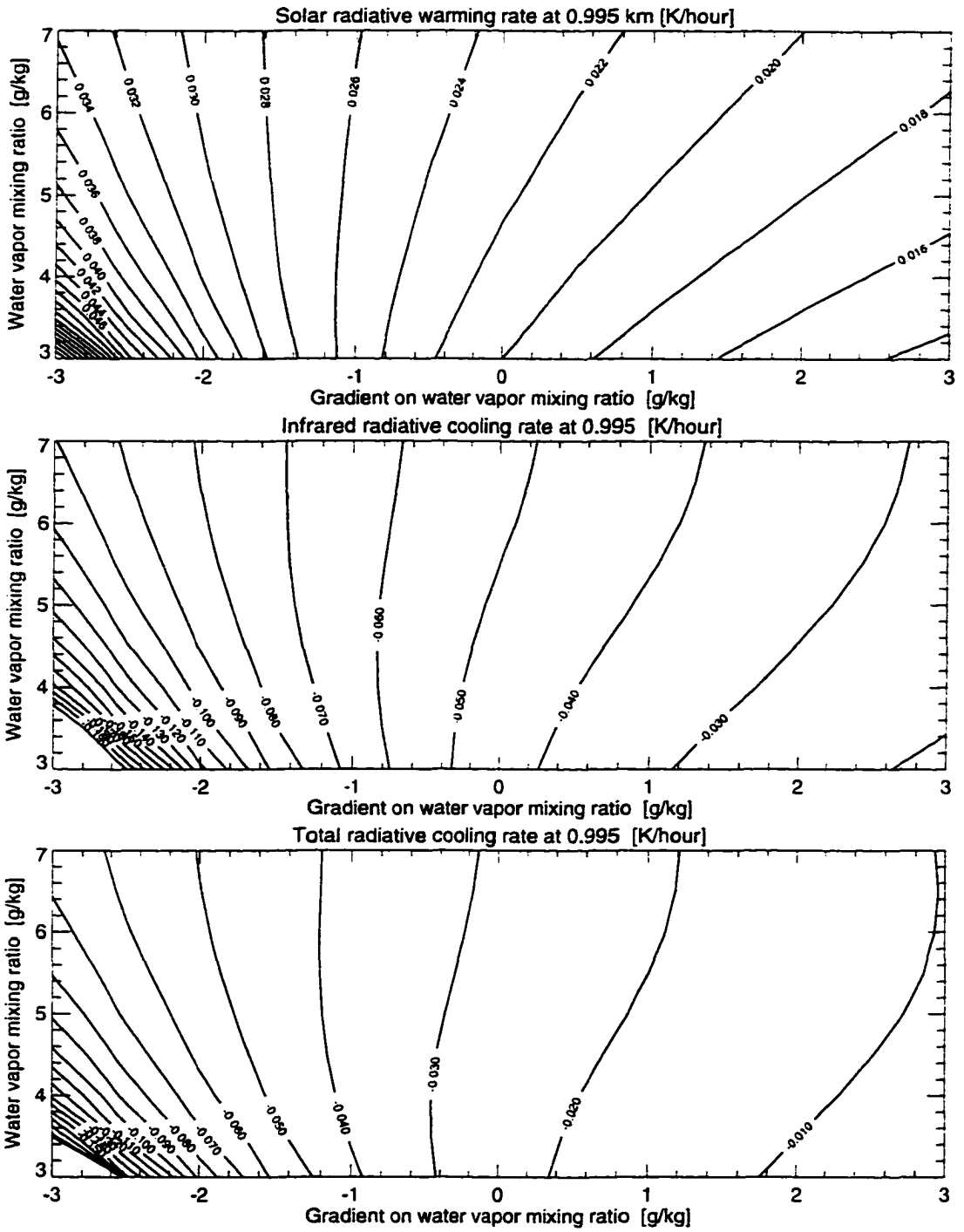

Figure 3.9. Radiative warming/cooling rates on the height of 0.995 km. The vertical coordinate is water vapor mixing ratio below 1 km. The horizontal coordinate is the gradient of the water vapor mixing ratio across the 1 km level. (a) Solar warming rate; (b) infrared cooling rate; (c) total (solar + infrared) cooling rate.

It has been shown in the previous analyses that the time of cloud formation is mainly determined by the radiative cooling rate. Assuming that the distribution of water vapor does not change much before cloud formation, we may estimate the time it takes for cloud formation by dividing the difference between the temperature and dew point temperature by the total radiative cooling rate. The difference between temperature and dew point temperature depends on the water vapor path but is independent of the humidity gradient. Figure 3.10 shows the estimated time for cloud formation. The time it takes for a cloud to form increases with a decrease in absolute humidity and with a decrease in the negative humidity gradient. It takes longer for a cloud to form when the humidity is small but the negative humidity gradient is large although the radiative cooling rates are large in this situation. The reason is that the difference between the temperature and the dew point temperature is large. When the absolute humidity is large, the influence of the humidity gradient is less significant because a small cooling is sufficient to trigger cloud formation. When the absolute humidity is relatively small, a large negative humidity gradient becomes essential for cloud formation.

The effect of the slope of water vapor profile on the radiative warming/cooling rate is illustrated in Figure 3.11, which shows five simulations with different slopes of water vapor profile above the at 1.0 km level. The initial water vapor profiles are shown in Figure 3.11 (a). The results show that the peak of both solar and infrared warming/cooling changes with the slopes in the water vapor profile. The smaller the slope is (the more rapidly the humidity decreases with height), the larger is the peak of the solar and infrared warming/cooling. Since the infrared cooling is much stronger than the solar warming, the total radiative effect, which is a significant cooling that peaks at about 1.0 km, is large when the slope is small. Therefore, the smaller the slope is (the more rapid the humidity decrease), the more easily the cloud forms. The simulation with the smallest slope (0°) of water vapor profile has the largest peak in both infrared cooling and solar warming, and hence in the total cooling. In the case 3 and 4, which have slopes with angles of about 45° and 60°, the peaks of total radiative cooling at

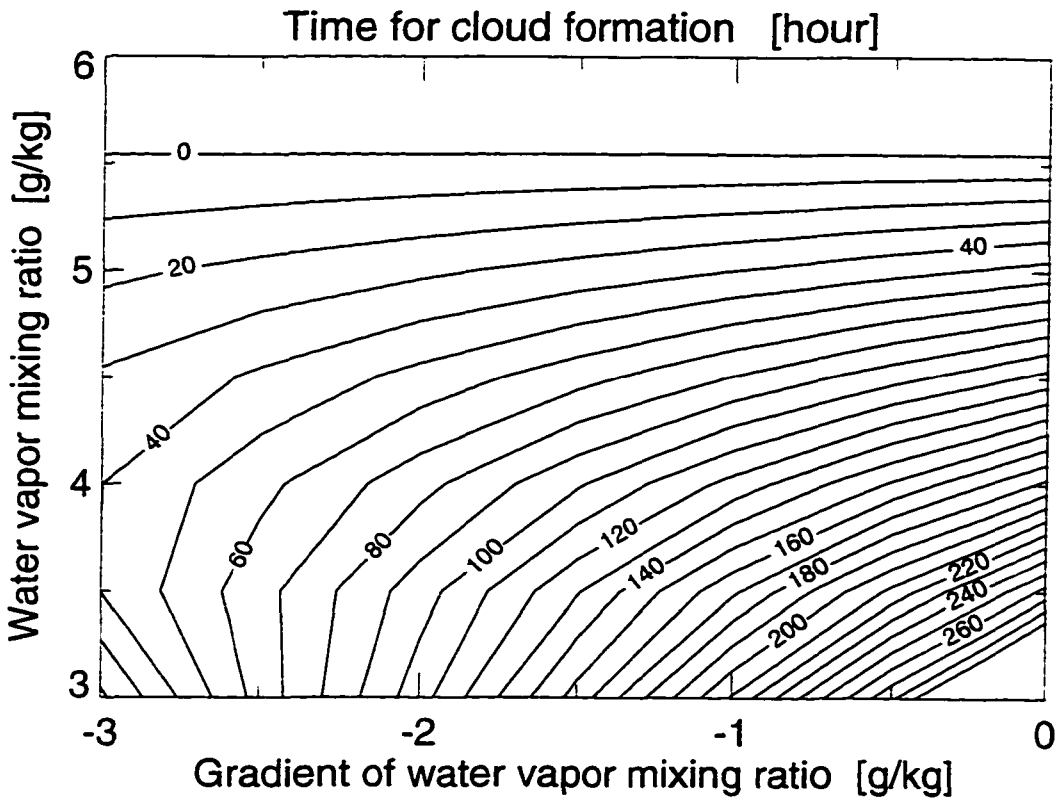

Figure 3.10. Time for water vapor condensation. The vertical coordinate is water vapor mixing ratio below 1 km. The horizontal coordinate is the gradient of the water vapor mixing ratio across the 1 km level.

1 km level are small enough that it becomes difficult to form a cloud. For case 5, no humidity gradient exists (the slope is 90°) and no cooling peak appears. Therefore, the steepness of the slope is critical for cloud formation. The slope angle must be smaller than a certain critical value in order for the cloud to form. Thus, a significant decrease in humidity across a small range in altitude gives rise to a large radiative cooling that is likely to induce cloud formation unless the total humidity is too low.

3.4.2 Effect of the temperature profile

Several simulations with initial temperature profiles different from the base simulation are made to investigate the effect of the temperature profile on radiation and thus on cloud formation. The initial water vapor content is the same and is shown with the solid line in Figure 3.11 (a). The initial temperatures above the height of 3 km are all the smae as the base simulation. They are different only below the height of 3 km. The initial temperatures for the simulations represented as solid, dotted, dashed and dashed-dotted lines are all the same at 1.0 km level but change with height at different constant lapse rates as shown on Figure 3.12 (a). The solid line in Figure 3.12 has a constant lapse rate of -1.8 K/km. The influence of the different temperature profiles on the radiative warming/cooling is not significant except in the extreme case (dashed-dotted line) which is with a dry adiabatic lapse rate (-9.8 K/km). The dashed-dotted-dotted line in Figure 3.12 (a) has a temperature 2 K less than that of the solid line at the same height. Again, its radiative warming/cooling rates are very similar with those in the other cases except the extreme case. The results suggest that the influence of the temperature lapse rates on cloud formation is not significant.

3.5 Summary

The formation of summertime ASCs is investigated in this chapter with the one-dimensional radiative-convective model. The initial data for the simulations were based on the observations of June 28, 1980 in the Arctic Stratus Experiment. To simplify the problem,

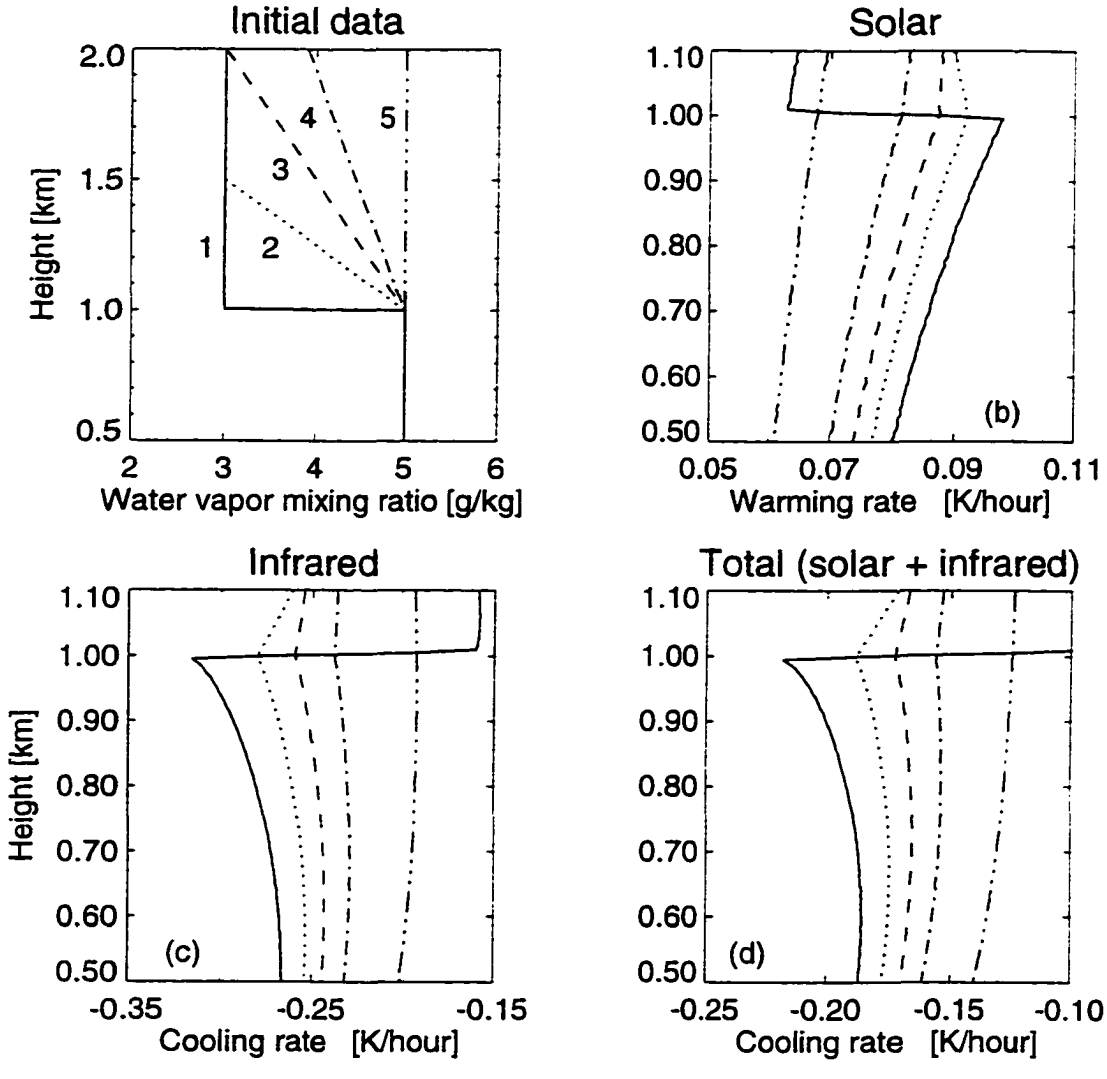

Figure 3.11. Radiative warming/cooling rates for different slopes of the vertical water vapor profile. (a) Assumed water vapor mixing ratio; (b) solar; (c) infrared; (d) total (infrared + solar). Solid, dotted, dashed, dashed-dotted and dashed-dotted-dotted lines correspond to the different humidity profiles specified in (a).

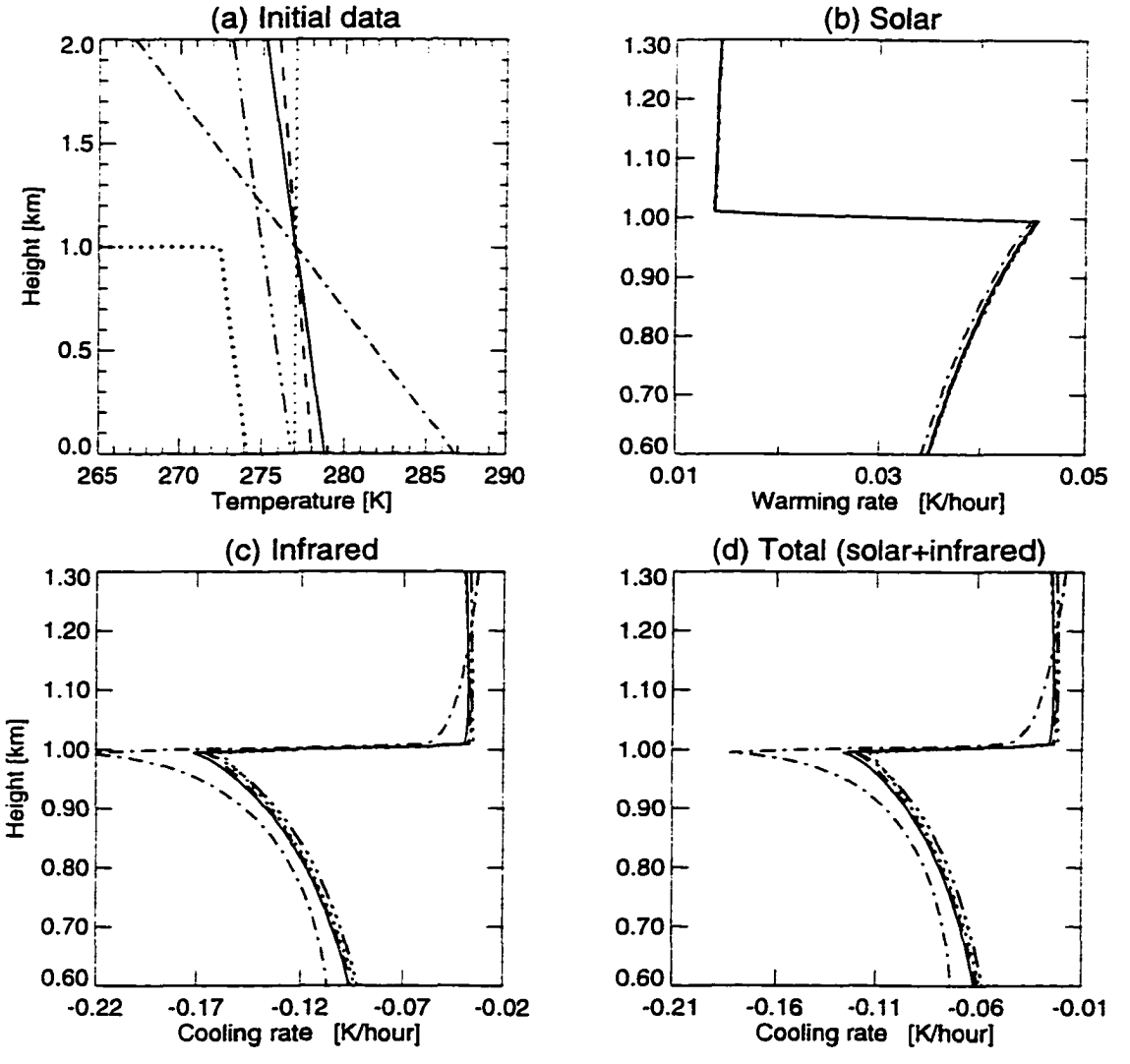

Figure 3.12. The effect of the vertical temperature profiles on the radiative transfer. (a) Initial temperature profiles; (b) solar warming rates; (c) infrared cooling rates; (d) total (infrared + solar) cooling rates. The solid, dotted and dashed lines correspond to the simulations with temperature lapse rates of -1.8, -1.0 and 0 K/km, respectively. The dashed-dotted line corresponds to the simulation with a dry adiabatic temperature lapse rate (-9.8 K/km). Dashed-dotted-dotted lines correspond to a temperature profile that is 2 K less than that of the solid at the same height. The heavy dotted line in (a) is the dew point temperature.

I focused only on the formation of a single cloud layer, that is the upper cloud layer observed on June 28, 1980. The model simulation results agree well with the observed cloud features such as the height where the cloud layer forms, the vertical distribution of the cloud liquid water, the appearance of the temperature inversion layer, and the cloud microphysical properties including the vertical distribution of the droplet density and the droplet spectrum.

The physics of the cloud formation is investigated and it is found that infrared cooling plays an important role in the cloud formation. A cloud may form due to the continual decrease of temperature which is caused primarily by infrared cooling.

The vertical profile of the water vapor content influences the vertical distribution of radiative warming/cooling rate and thus is critical in cloud formation. Moisture gradients determine the magnitude and vertical distribution of solar and infrared warming/cooling rates and eventually determines the time and location of cloud formation. The cloud is likely to form around the height where a significant vertical change in water vapor content occurs. The larger the vertical change in the water vapor content (that is a large moisture gradient or a small slope in the humidity profile), the larger is the radiative cooling and the faster the temperature decreases at that location. Hence, it is easier for a cloud to form at that location, and cloud formation is more likely there than elsewhere.

The radiative cooling is also influenced by the total amount of water vapor. The water vapor path influences the peak of the radiative cooling which appears at the height where there is significant vertical humidity change. With less total water vapor, the peak is more pronounced and it will cause the temperature to decrease faster than in the presence of more total water vapor. However, since the dew point temperature is smaller when there is less total water vapor, it may still take longer for the cloud to form than when more water vapor is available.

A change in the temperature lapse rate does not seem to have a significant influence on radiative warming/cooling and hence does not significantly influence cloud formation.

Chapter 4

The Formation of Multiple-Layer Arctic Stratus Clouds

The formation of multiple-layered clouds will be investigated in this chapter with the one-dimensional radiative-convective model described in Chapter 2. As in Chapter 3, the simulations in this chapter are based on the case observed on June 28, 1980 in the Arctic Stratus Experiment but two cloud layers are considered. The simulation results will be compared with the observations. The focus is on understanding the roles of radiation as well as microphysics in the formation of multiple cloud layers. The influence of humidity and temperature profiles on radiative warming/cooling and thus on multiple-layered cloud formation will be discussed.

4.1 Initial data and simulation design

The simulations in this chapter are initiated with a clear atmosphere so that we are able to investigate cloud formation. The initial data for the simulation is based on the observations of June 28, 1980 over the Beaufort Sea during the Arctic Stratus Experiment. Detailed descriptions of the experiment and analyses of physical properties of the boundary layer were given in Chapter 1.

The initial conditions used in the following simulations are shown on Figure 4.1. The dotted lines are the observations. Two cloud layers were observed at heights between 0.8 and 1.2 km and below 0.11 km. respectively. The initial temperatures are taken to be higher than the observed ones at the heights where the clouds were observed so that the simulation can be started with a presumed clear atmosphere prior to the cloud formation. The goal is to study the cloud formation including the establishment of multiple layers. The dashed line in Figure 4.1 (a) is dew point temperature. It is the temperature to which moist air must cool, with pressure and humidity held constant, for it to reach saturation with respect to water. The differences between the initial temperature profile and the dew point temperature profile is almost constant between 0.1 and 1.2 km. That means that the cooling required for cloud formation is about the same at these levels.

A uniform relative humidity of 86% is adopted between the surface and 1.2 km. The observed water vapor content between 1.2 and 1.5 km is adopted as the initial condition. Climatological values are adopted above 1.5 km. For this relative humidity, the initial water vapor mixing ratios are shown by the solid line in Figure 4.1 (c). The dotted line in Figure 4.1 (c) is the observed water vapor mixing ratio. The initial water vapor mixing ratios for the model simulation are about the same as the observed ones between 0.8 and 1.2 km. They are larger than the observed ones between 0.3 and 0.8 km and smaller below 0.3 km. The total liquid water path of the entire layer is approximately equal to the observed one.

Few measurements of CCN spectra have be conducted in the Arctic. The CCN concentration has been observed to have a significant variability ranging from 20 to 1000 (Hegg et al., 1995; Saxena and Rathore, 1984). In the base simulation of this chapter, the initial CCN spectrum is represented by a power law (Twomey 1977), $N_{CCN}(s) \approx c(100s)^{\kappa}$, with $\kappa = 0.34$, and $c = 6.4 \times 10^8 m^{-3}$. The total number of CCN particles is therefore about 500 when $s = 0.4\%$. The relationship between the CCN concentration and the supersaturation is shown in Figure 4.2. The solid line in Figure 4.2 is a measured CCN spectrum over the Arctic Ocean in April 1992 during the LEADEX experiment with

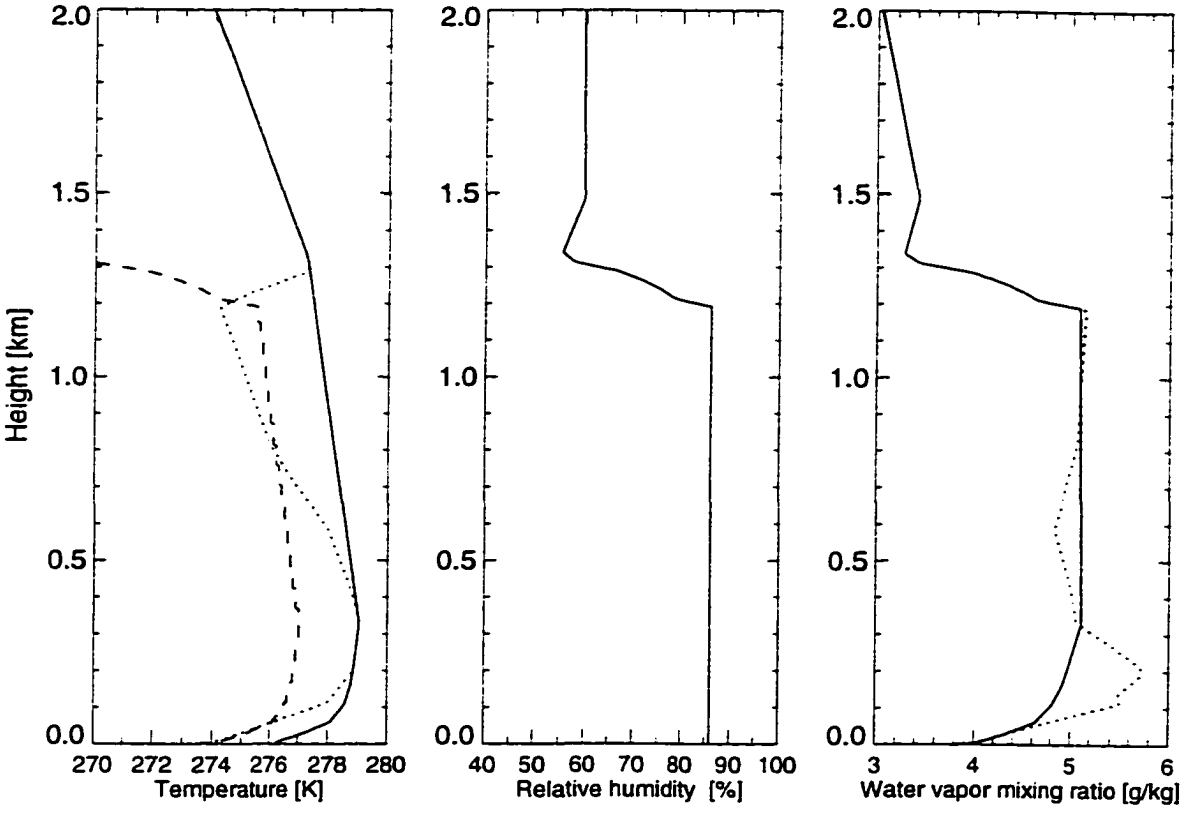

Figure 4.1. Initial conditions. (a) Temperature; (b) relative humidity; (c) water vapor mixing ratio. Solid and dotted lines correspond to the initial data and the observational profiles, respectively. The dashed line in (a) is the profile of dew point temperature.

$\kappa = 0.34$ and $c = 1.28 \times 10^8 m^{-3}$ (Hegg et al., 1995).

In the base simulation, the vertical grid of the model is 5 meters below 2 km in height, 20 meters between 2 and 3 km, and 100 meters or more above 3 km. The time step is half an hour before the cloud forms, and it changes according to the warming/cooling rate after cloud forms. The stronger the heating rate is, the smaller the time step is. For more details about the time step, please refer to Chapter 2. The minimum time step for vertical mixing is 2 s.

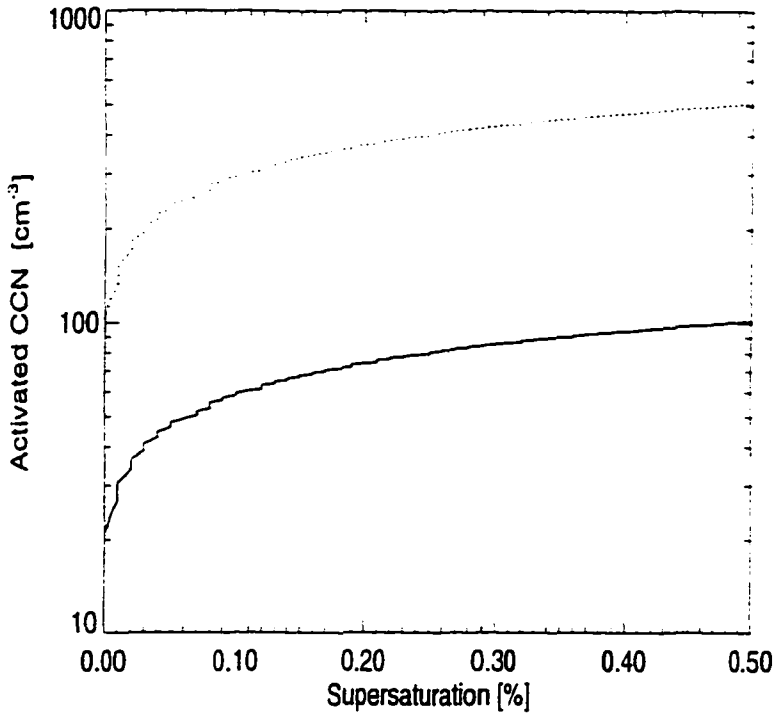

Figure 4.2. The relation between CCN and supersaturation. The solid line is a measured CCN spectrum over the Arctic Ocean in April 1992 during the LEADEX experiment with $\kappa = 0.34$ and $c = 1.28 \times 10^8 m^{-3}$ (Hegg et al., 1995). The dotted line is the initial CCN spectrum adopted for the base simulation with $\kappa = 0.34$ and $c = 6.4 \times 10^8 m^{-3}$.

4.2 Simulation results

4.2.1 Formation of the cloud layers

The model is integrated forward in time for 45 hours. Two cloud layers form during the simulation. The lower cloud layer initially forms at 29.5 model hours at 60 m altitude. The upper cloud layer initially forms at 35 model hours at 1.155 km.

Before the formation of cloud layers

The radiative warming/cooling rates before the formation of cloud layers are shown in Figure 4.3. There are three peaks in the vertical profiles of the infrared cooling rates oc-

curring at 0.1, 0.3 and 1.2 km, which are the heights where significant moisture changes occur (Figure 4.1). The magnitude of the peaks decreases with time. This may be explained by the temperature changes due to radiative cooling and the moisture changes due to the vertical mixing process. The solar warming rate is much smaller than the infrared cooling rate. It is only 10% to 50% of the infrared cooling rate depending on the solar zenith angle. The solar warming rates varies with time because of the variation of solar zenith angle. The vertical profiles of the solar warming rate at different model times look similar. A maximum appears at about 1.2 km where a large change in moisture occurs. The total radiative effect is negative and therefore will cause temperature decrease. The total radiative cooling rates vary with height and solar zenith angle in the range from -0.025 to -0.08 K/hour. Due to the diurnal change of the solar radiation, the total radiative cooling also has a diurnal cycle. The profiles of the total and infrared cooling rates look very simular. Three peaks appear at the same height as those of the infrared cooling rate.

Figure 4.3 (d) shows how the temperature changes before the cloud fomation. The temperature continues to decrease throughout the layer with an average rate of -0.08 K/hour. A small temperature inversion starts to appear at 1.2 km altitude at 14 model hours. The vertical distribution of the water vapor content does not change much (not shown) before the cloud forms although vertical mixing is taking place. The temperature continues to decrease until it finally reaches the dew point. Condensation occurs then and the cloud forms.

The lower cloud layer

The lower cloud layer forms within a stable temperature inversion layer. It initially forms at 29.5 model hours at the height of 65 m (Figure 4.4) and develops fast during the first several model hours after cloud formation. The maximum liquid water content reaches 0.6 and 0.9 g/kg, respectively, at 2.5 and 5.5 model hours after the cloud forms. The cloud top ascends fast also. It ascends more than 250 m during the first 5 hours.

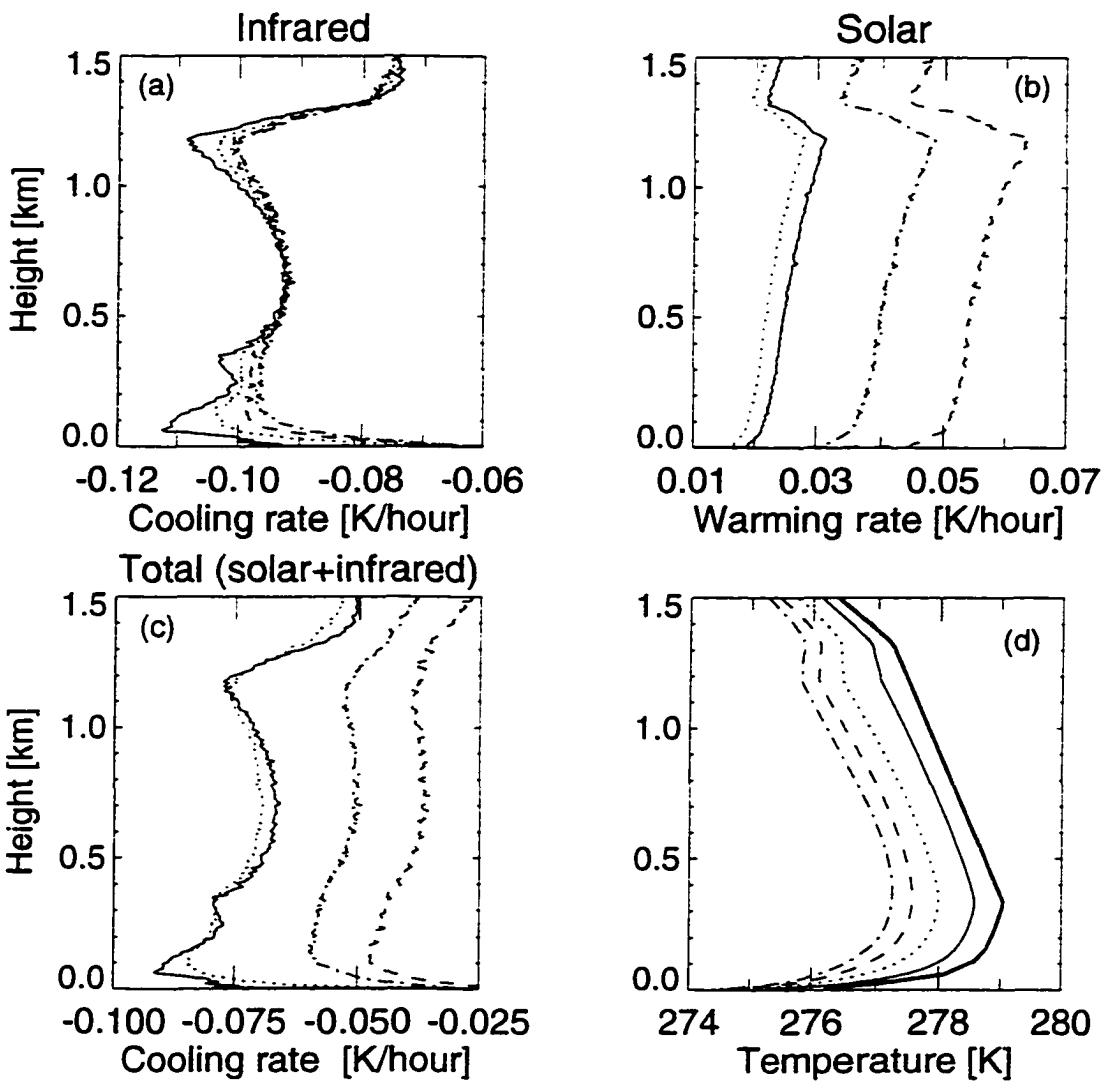

Figure 4.3. Radiative warming/cooling rates. (a) Infared; (b) solar: (c) total (infrared + solar); (d) temperature. The solid, dotted, dashed and dashed-dotted lines represent the profiles obtained before cloud formation at 7. 14, 21 and 28 hours model time, respectviely. The heavy solid line is the initial temperature.

The water vapor content decreases due to condensation. Significant inversion of water vapor content appears right above the cloud top. The temperature within the cloud layer decreases rapidly after the cloud formation. A significant temperature inversion occurs above the cloud top (Figure 4.4 c).

After the upper cloud layer forms at 35 model hours, the temperature within the lower cloud layer does not change much. The cloud liquid water content does not change much either. The dashed lines in Figure 4.4 shows profiles of liquid water mixing ratio, water vapor mixing rates, and temperature at 10.5 after the lower cloud forms. They do not differ much from the dotted lines, which represent the same quantities at 5.5 hours after the lower cloud layer forms.

The temperature changes can be explained by the effects of radiative warming/cooling. Figure 4.5 shows radiative warming/cooling rates after the formation of the lower cloud layer. Both the solar warming and infrared cooling effects increase significantly compared with those before the cloud layer forms. Maximum warming/cooling effects occur near the cloud top. The peaks of warming/cooling ascend along with the lifting of the cloud top.

After the upper cloud forms, both solar and infrared radiative warming/cooling effects on the lower cloud layer decrease substantially. The total radiative warming/cooling effect is very small within the lower cloud layer. The dashed lines in Figure 4.5 show the total radiative warming/cooling rates at 40 model hours, which is 10.5 model hours after the lower cloud layer forms and 5 model hours after the upper cloud layer forms. The total radiative warming/cooling effect is very small below 0.4 km.

Figure 4.6 shows the vertical distribution of the droplet density and the equivalent radius of the lower layer cloud. The maximum of droplet density does not change much with time and it is almost uniformly distributed within the cloud layers except that a relatively small density appears between about 180 m and 260 m at 5.5 and 10.5 model hours after the initial cloud formation (the dotted and dashed lines in Figure 4.6 a). It is found that there actually exist two cloud layers at that moment below the height of

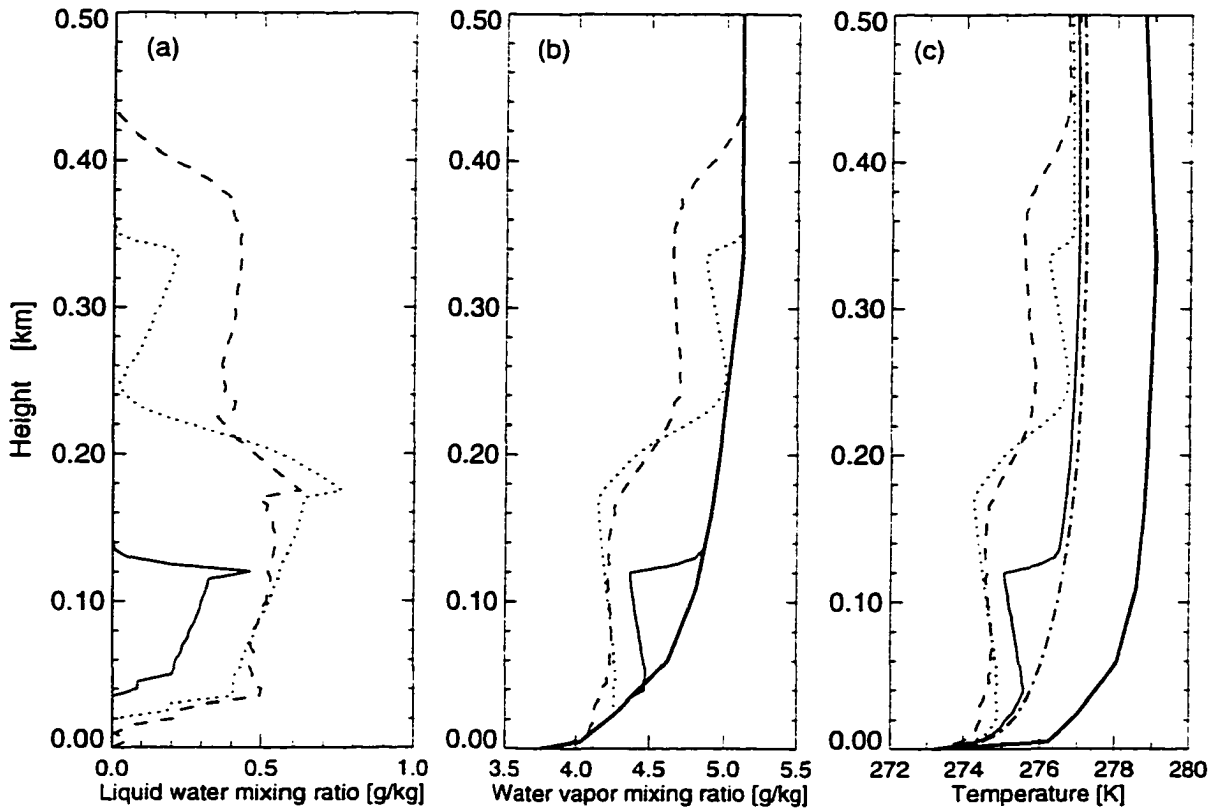

Figure 4.4. (a) Liquid water mixing ratio [g/kg]; (b) water vapor mixing ratio [g/kg]; (c) temperature [K]. Solid, dotted and dashed lines correspond to simulation at 32, 35 and 40 model hours, which are respectively 2.5, 5.5 and 10.5 model hours after the cloud forms. Heavy solid lines show initial condition. The dashed-dotted line in (c) corresponds to 0.5 hours before clouds form. The lower layer cloud forms at 29.5 model hours.

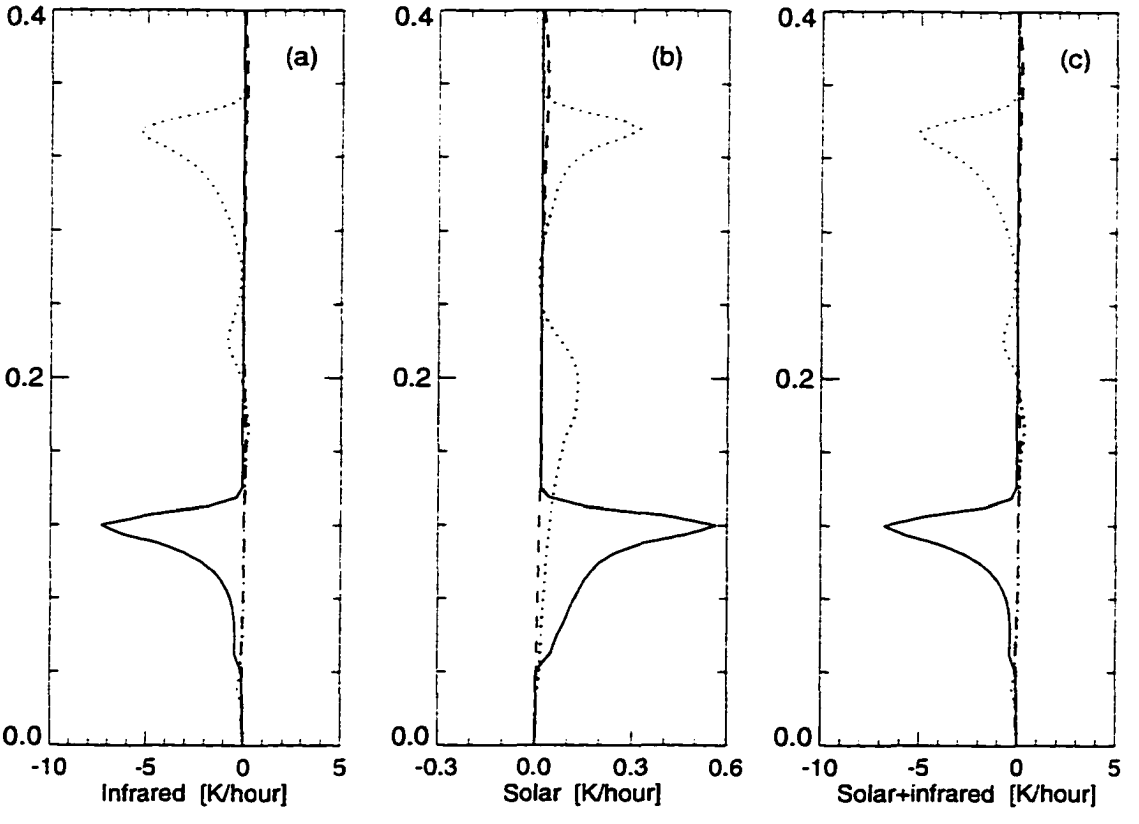

Figure 4.5. Simulation results. (a) Infared cooling; (b) solar warming; (c) net radiative warming/cooling; Solid, dotted, and dashed lines are the profiles at 32, 35 and 40 model hours, respectively.

0.4 km through analyzing the droplet spectrum at those heights (not shown). They exist respectively at the altitudes from surface to 180 m and from 260 to 360 m.

The droplet equivalent radius does not change much with time but varies with height (Figure 4.6 b). Comparing with Figure 4.4 (a), we find that the variations of cloud liquid water within cloud layers relate to the variations in the equivalent radius.

Figure 4.7 shows the detailed distribution of droplet sizes at two hours after the lower cloud layer forms. To compare it with the observed droplet spectrum, the distribution has been collected in 15 equidistant bins with mean diameter 3.13 μm apart, with the pluses indicating the center of each bin (Tsay and Jayaweera, 1984). Two hours after the cloud layer forms the cloud top is at about 150 m. One peak appears at the cloud

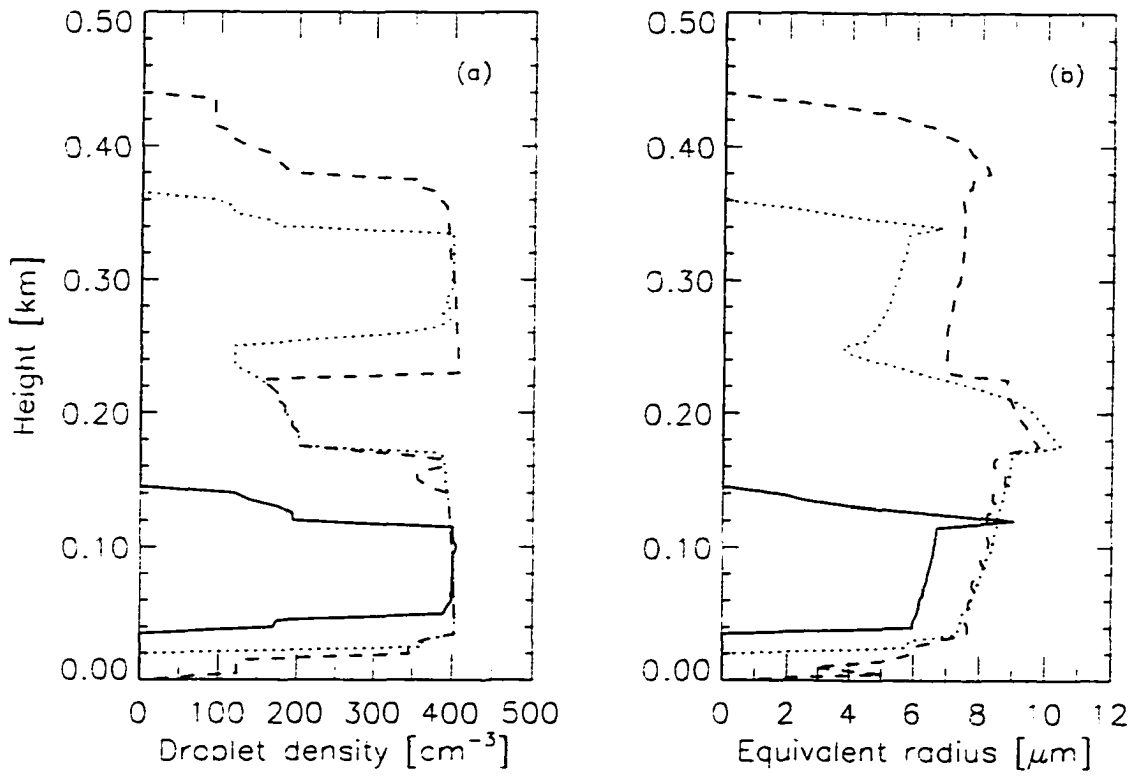

Figure 4.6. Simulation. (a) droplet density [cm^{-3}]; (b) equivalent radius [μm]. Solid: 2.5 hours after clouds form (32 hours); dotted: after 5.5 hours (35 hours); dashed: after 10.5 hours (40 hours).

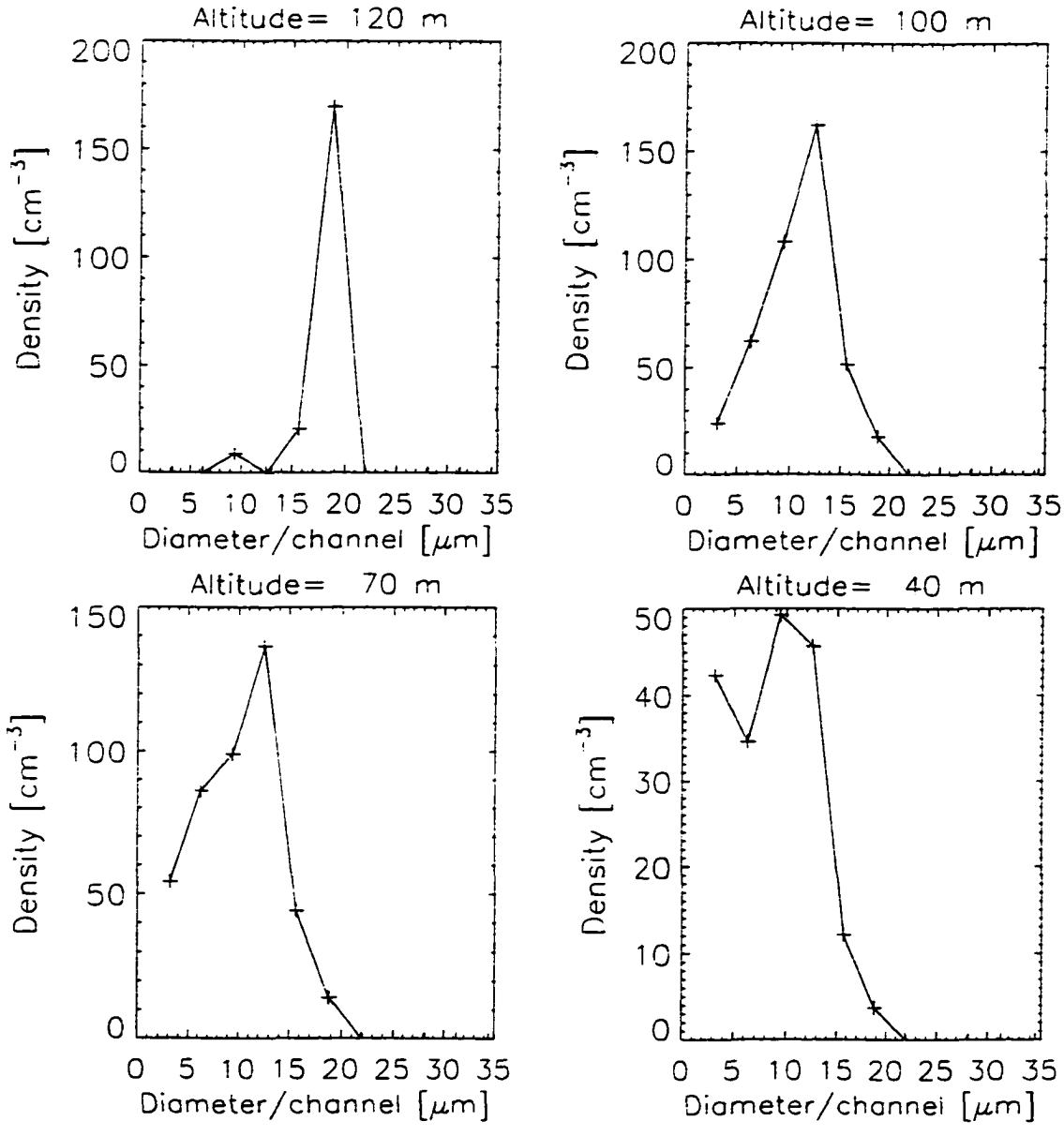

Figure 4.7. Droplet spectrum. 2.5 hours after the cloud forms (32 hours)

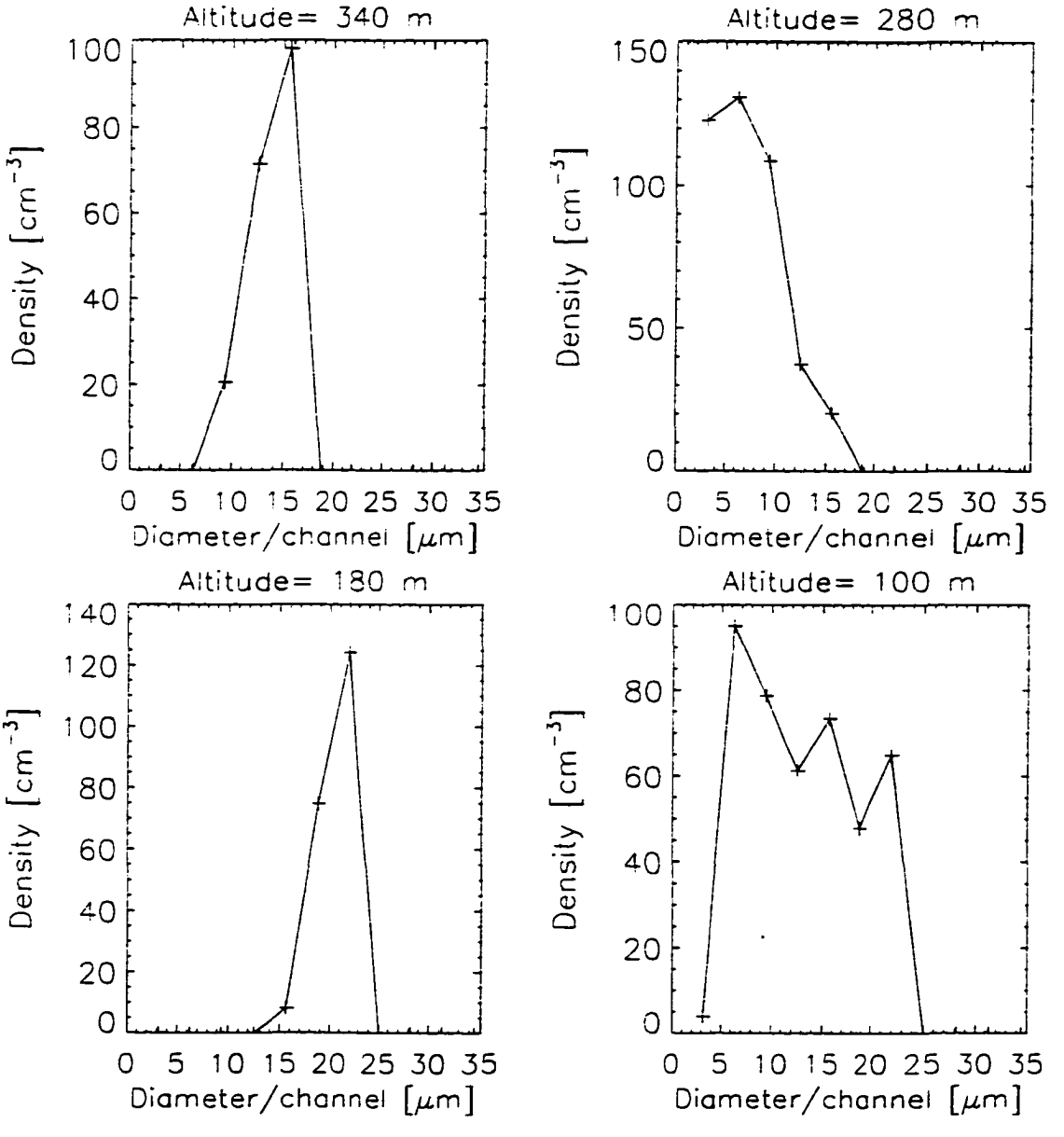

Figure 4.8. Droplet spectrum. 5.5 hours after the cloud forms. (35 hours)

top and multiple peaks appear within the cloud layer and near the cloud base.

At 5.5 hours after the cloud layer forms, the droplet spectrum is similar to that present two hours after the cloud layer forms below 180 m, except that the droplet sizes are larger (Figure 4.8). Through detailed analyses of the droplet spectrum (not shown), it is found that a new cloud layer forms above the height of 260 m. Similar spectra appear 10 hours after the clouds form except that the cloud layer appears between 260 m and 300 m. This cloud has a single peak droplet spectrum at the cloud top, whereas mutiple peaks appear at the cloud base (not shown).

The upper cloud layer

The upper cloud layer initially forms at 35 model hours at 1.155 km altitude (Figure 4.9). As we have discussed before (Figure 4.3 d), a small temperature inversion already exists before cloud formation due to radiative cooling. The upper cloud layer forms right below the temperature inversion, and the LWC increases linearly with height at a rate close to adiabatic value. Cloud liquid water increases very fast after the cloud layer initially forms. The upper cloud layer develops most significantly during the first two hours; then its evolution slows down. The cloud top rises continuously and is at 1.2 km 5 model hours after the cloud layer forms. The maximum LWC appears near the cloud top and is about 0.8 g/kg.

There is no significant change in humidity at the upper cloud layer before it forms although vertical mixing does occur there (solid line in Figure 4.9 b). The water vapor content at the cloud top decreases due to condensation after the cloud layer forms. A small water vapor inversion appears right above the cloud top and it continues to develop.

The temperature decreases fast and the temperature inversion right above cloud top develops significantly after the cloud layer initially forms. The temperature jump across the inversion layer increases to about 2.5 K at 5 hours after the cloud forms. The temperature decreases with height within the cloud layer with a rate close to the saturated adiabatic lapse rate.

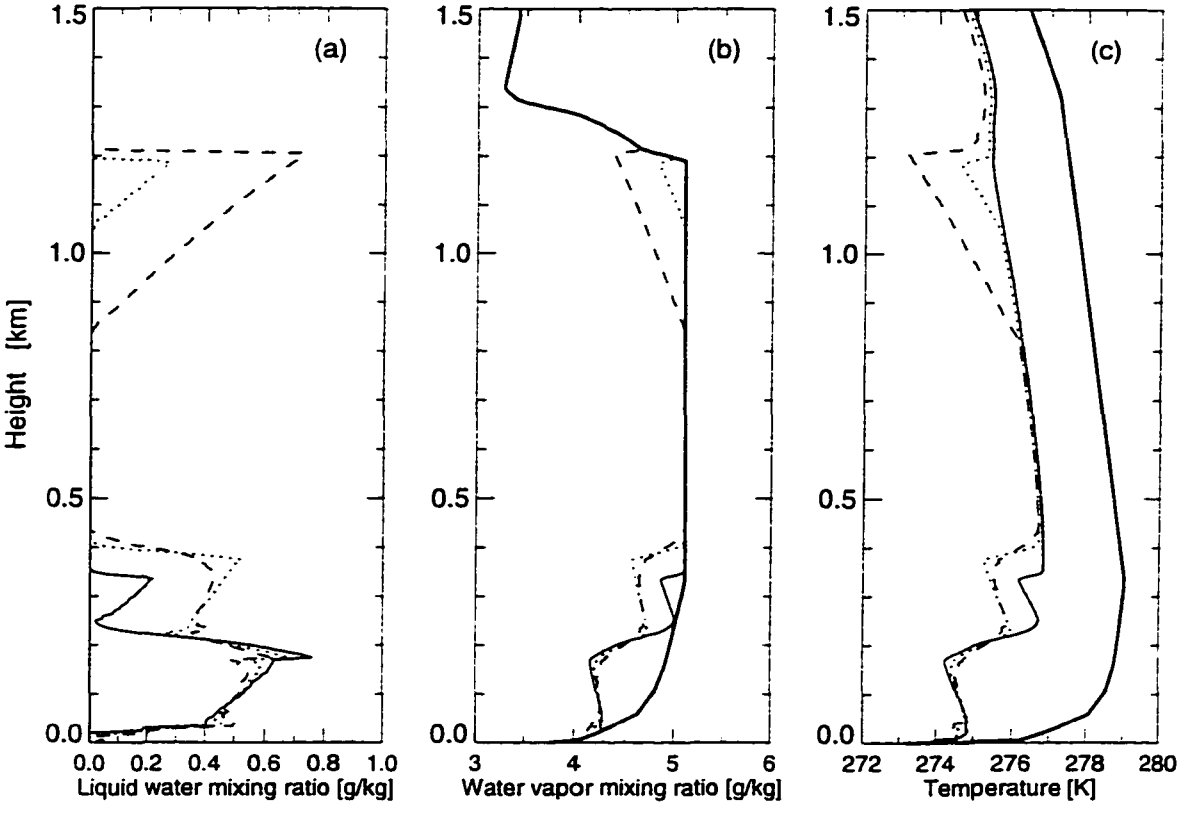

Figure 4.9. Simulation results. (a) Liquid water mixing ratio [g/kg]; (b) water vapor mixing ratio [g/kg]; (c) temperature [K]. The solid, dotted and dashed lines correspond to simulation results obtained at 35, 37 and 40 model hours, respectively. The upper cloud layer forms at 35 model hours. 37 and 40 model hours correspond respectively to 2 and 5 model hours after the formation of upper cloud layer. The heavy solid lines show initial conditions.

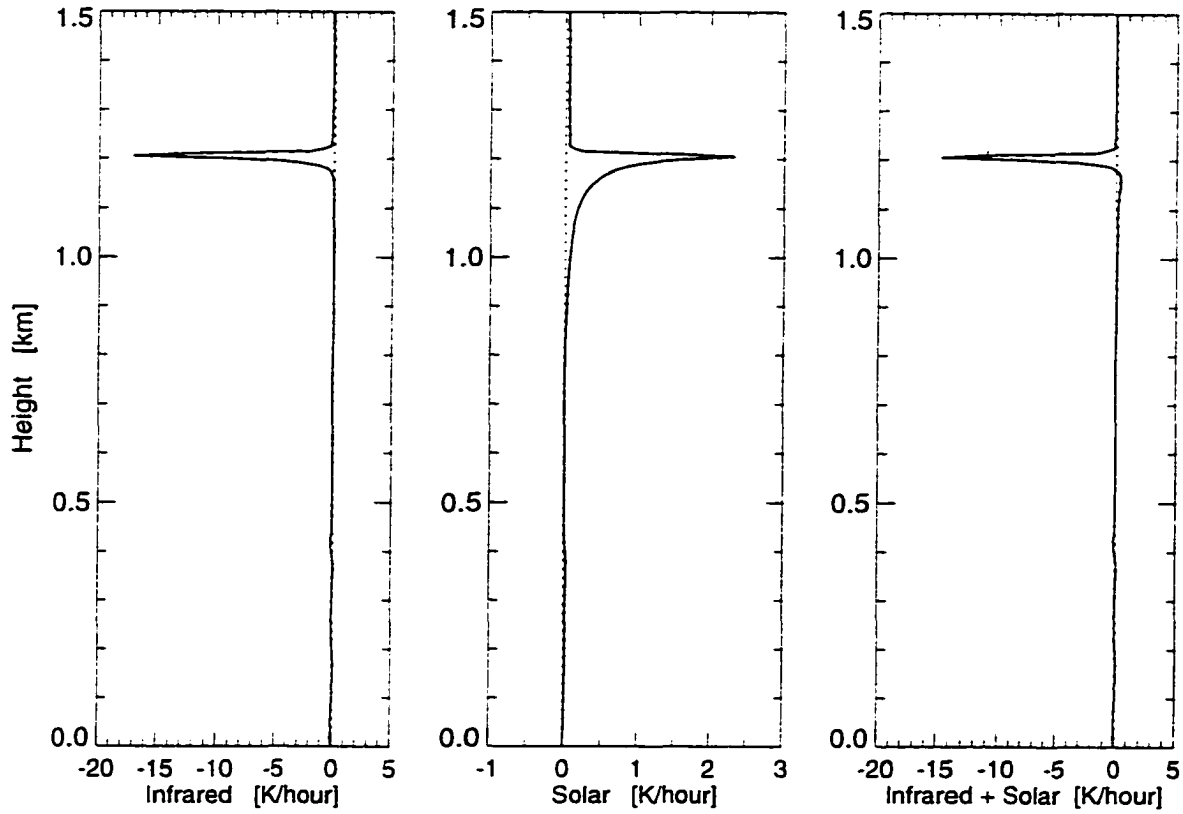

Figure 4.10. Radiative warming/cooling rates at 40 hours model time (5 hours after the cloud forms). (a) Infared cooling rate; (b) solar warming rate; (c) net radiative warming/cooling rate.

The temperature decrease is mainly due to the net radiative cooling. Figure 4.10 shows radiative warming/cooling rates 5 hours after the cloud layer forms. The maximum of both solar and infrared radiative warming/cooling occurs near the cloud top around 1.2 km. The maximum infrared cooling rate is about -20 K/hour; it is much stronger than the solar warming rate, which has a maximum of only 2.5 K/hour. The total radiative effect is therefore a net cooling at most altitudes. Strong net radiative cooling only occurs in a very thin layer near cloud top. The strongest net cooling is -17 K/hour appearing at cloud top. The radiative warming/cooling rates within the lower cloud layer are very small (close to zero) at this stage in the cloud development.

As shown in Figure 4.11 (a), the droplet density of the upper layer cloud is about

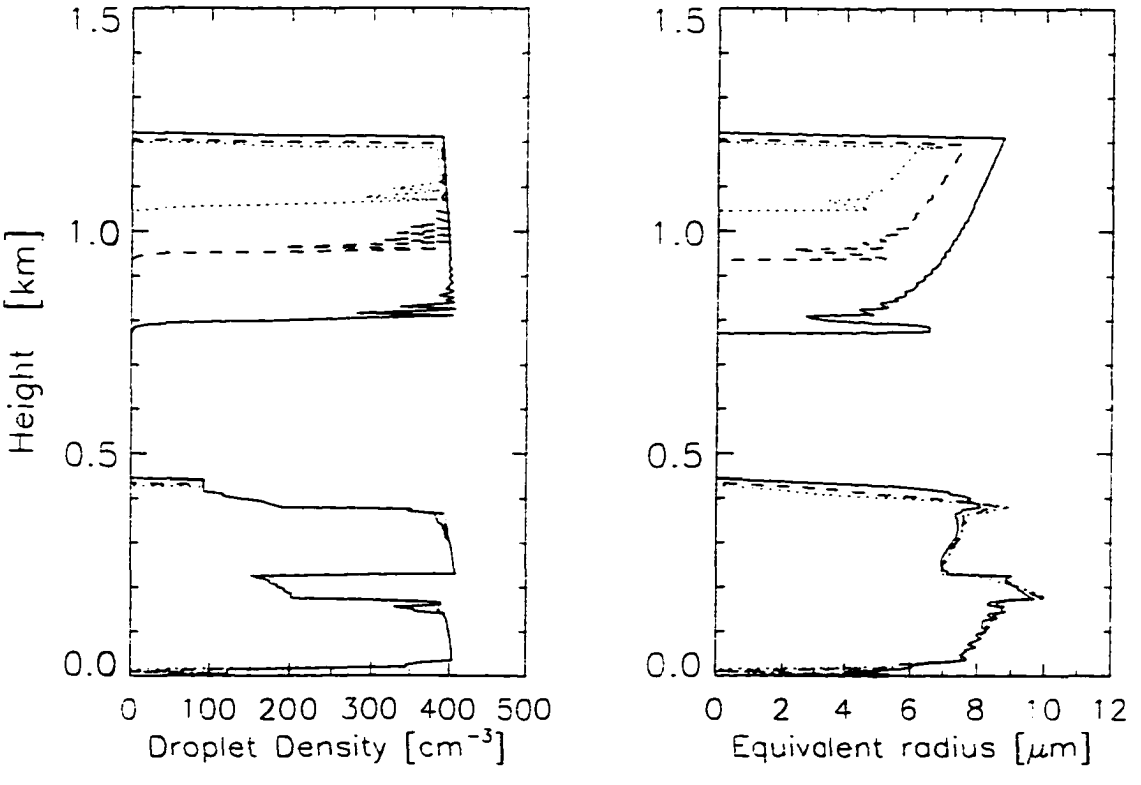

Figure 4.11. Simulation. (a) droplet density [cm^{-3}]; (b) equivalent radius [μm]; Dotted: 1 hour after cloud formation (36 model hours); dashed: 2 hours after cloud formation (37 model hours); solid: 5 hours after cloud formation (40 model hours).

400 $particles/cm^3$ and it is almost constant with height. It does not change much with time during the cloud evolution. Figure 4.11 (b) shows the droplet equivalent radius in the upper cloud layer. The equivalent radius increases with height and the maximum drop size appears at cloud top. Also, the equivalent radius increases with time. It is about 10 μm at 5 model hours after the cloud formation. The results suggest that the increase of cloud liquid water with height and with time is related to the increase in droplet sizes rather than in droplet density.

Figure 4.12 shows the droplet size distribution at five model hours after the cloud formation. Two peaks appear in the upper part of the cloud layer, with a diameter around 8 μm and 17 μm, respectively. In the lower part of the cloud layer, there is only one peak with diameter around 6 μm.

4.2.2 Comparison with observations

Two nearly parallel layers of stratus clouds were observed on June 28, 1980 (Tsay and Jayaweera, 1984) (Figure 1.2). According to the observations, the upper cloud was capped by a strong temperature inversion while inside the cloud the temperature profile was very close to saturated adiabatic (Γ_s = 6.0 K/km). The LWC profile was also close to the adiabatic value except for some overestimate which may be due to an incorrect assignment of cloud base resulting from sporadic precipitation. In the lower cloud, the temperature increased all the way from the bottom. The top of the inversion occurred at about the maximum height of the lower cloud, near 980 mb (333 m altitude).

The observation also shows that the droplet density does not change much with height. The variation of the LWC followed that of the droplet concentration, showing that the LWC is controlled essentially by the concentration of droplets. The mean diameter at 950 m (about 110 m below cloud top) was steady near 10 μm.

According to the observations, the droplet distribution for the upper cloud layer changed from a single mode near the cloud base to a double mode near the cloud top. A peak of droplet concentration appears at about 6 μm diameter near the cloud base,

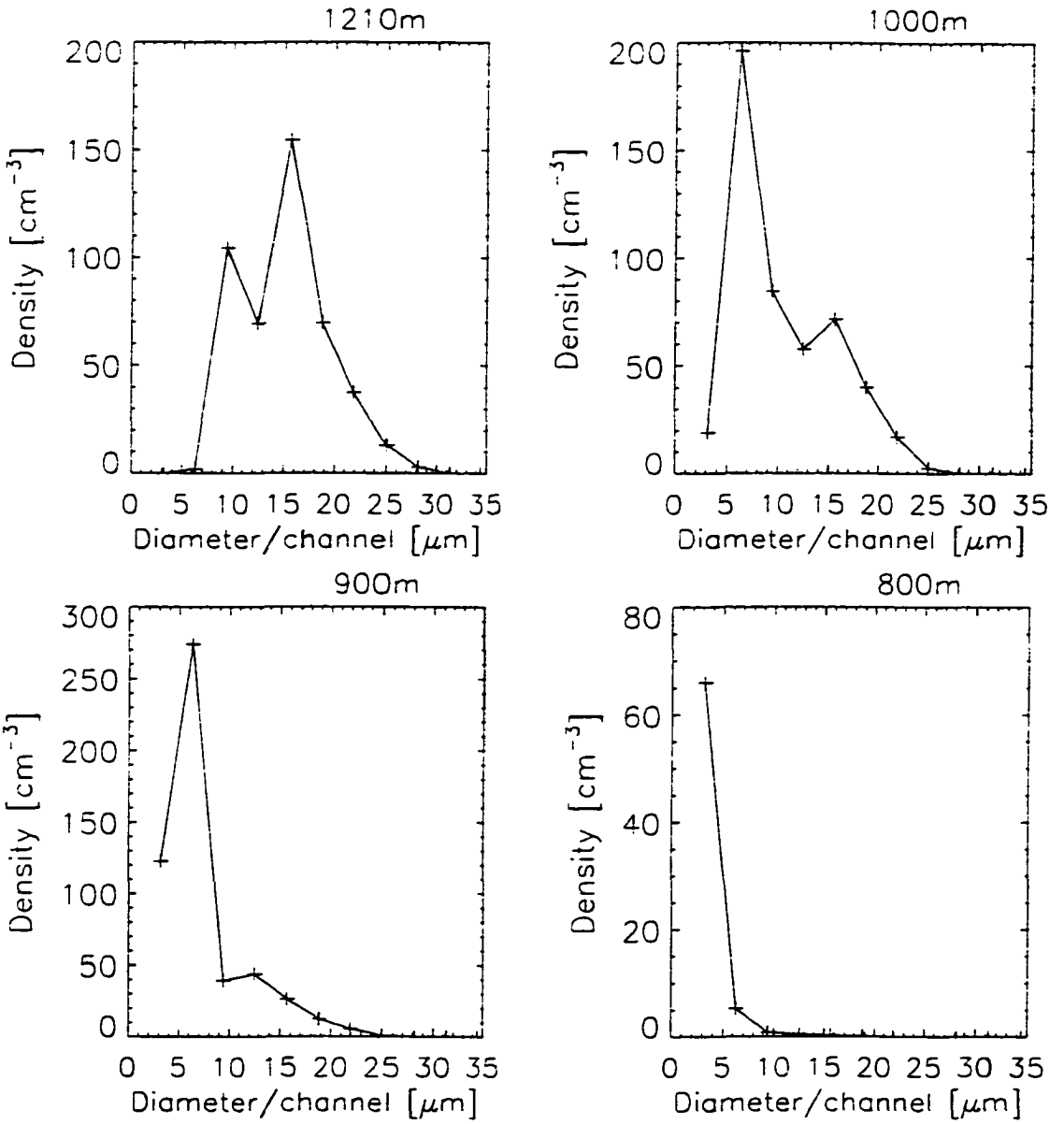

Figure 4.12. Droplet spectrum at 5 hours after the cloud formation (40 model hours).

whereas two peaks appear at about 6 and 17 μm diameter near the cloud top (Figure 1.3).

Our simulation is in agreement with these observed features. Comparing the simulation with the observation, we note that the two simulated cloud layers appear at the same place as observed. The thickness and LWC of the upper cloud layer are well simulated. Our simulation well represent the profiles of temperature and water vapor content. The observed temperature inversion is also correctly simulated, and the observed cloud microphysical properties such as the droplet spectrum are well represented by the model results.

Our model may develop larger LWC and larger droplet size compared with the observations if we run it for a long time. One reason is that there is no dissipation processes considered in our model. Also, cloud top entrainment, which does suck dry and warm air into the cloud layer and cause evaporation, is not completely included in the model. The cloud top entrainment included in the convective adjustment scheme may not be strong enough nor correct.

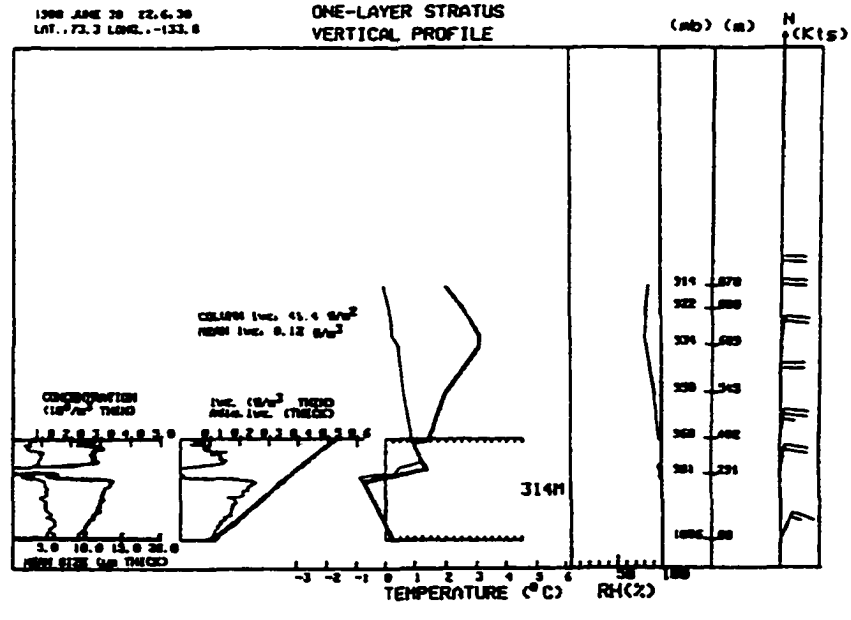

Figure 4.13. Observation on June 30, 1984 during Arctic Stratus Experiment (from Tsay and Jayaweera, 1984).

Our simulation creates much more liquid water in the lower cloud layer than observed on June 28, 1980. The thickness of the simulated lower cloud layer is also much thicker than the obsevation. This happens because the lower cloud layer forms before the upper cloud layer in the simulation and therefore is allowed to develop more fully. After the upper cloud layer forms, the lower cloud layer cannot develop much. Another reason is that the real cloud existed in a strongly stable surface inversion while the simulated cloud produces a mixed-layer.

The simulated profiles of temperature, LWC and droplet condensation of the lower cloud layer are very similar (Figure 4.13) to those observed on June 30, 1980, when only a single cloud layer is observed below 400 m. The simulated thickness of the cloud layer is also very similiar to the observation. This suggests that ratiative cooling effect may possibly casue formation of a cloud layer near the surface even though there is no the effect of wind shear.

4.3 Physics of the mutiple-layered cloud formation

It is difficult to discuss the formation of mutiple-layered clouds since there may exist interactions among those cloud layers. Therefore, prior to discussing the physics of the mutiple-layered cloud formation, I will consider the formation of each single cloud layer, the upper cloud and the lower cloud layer, separately. Since the formation of the upper cloud layer was discussed in Chapter 3, I will first focus the formation of the lower cloud layer. Then, the physics involved in the formation of the two-layer cloud will be discussed. To simplify the problem the solar zenith angle is fixed to 70° in the following simulations.

4.3.1 Formation of the lower cloud layer

It has been shown in Figure 4.3 that the peaks in the infrared cooling at the height of 0.1 km and 0.3 km cause the lower cloud layer to form at that level. Here I will try to find out how the peaks of infrared cooling develop at those levels. In order to explain

the peaks in warming/cooling rates below the 0.3 km, I will investigate the influences of different humidity and temperature profiles on radiative warming/cooling rates.

Figure 4.14 shows simulations to illustrate the impact of humidity profiles on the radiative warming/cooling rates. The initial temperature for these simulations is 278.79 K near the surface in the lowest layer and it decreases with height at a constant lapse rate of -1.8 K/km up to 2 km. The initial humidity profiles adopted here are shown in Figure 4.14 (a). The water vapor mixing ratio is 4 g/kg from 0.2 to 2 km. Significant humidity changes are assumed to occur at 0.2 km. A peak appears around 0.2 km level in the profiles of solar warming rates and infrared as well as total radiative cooling rates. Solar radiative warming rates and infrared cooling rates increase (decrease) with height across the 0.2 km level when the humidity increase (decrease) with height across that level. The net radiative effect is a cooling dominated by the infrared cooling rate. Therefore, a cloud layer is more likely to form above the 0.2 km level when the humidity increases with height across that level, and is more likely to form below the 0.2 km level when humidity decreases with height across that level.

Figure 4.15 shows the impact of various temperature profiles on the radiative warming/cooling rate. The water vapor mixing ratio is 4 g/kg from the surface to 2 km in all the simulations. The temperature profiles are the same in all the simulations above 0.2 km level and they have a constant lapse rate of -1.8 K/km between 0.2 and 2 km. They are different below 0.2 km as shown in Figure 4.14 (a).

The infrared cooling rates are strongly affected by the change in the temperature profile. A pronounced peak appears at the level where the temperature changes significantly. The net radiative effect is similar to the infrared cooling effect. Thus, a cloud is more likely to form at a level where a significant change in the temperature profile occurs.

The above analyses suggest that both a humidity gradient as well as a change in the temperature profile will cause a peak in the radiative cooling rate. The effect of the temperature change has a more significant effect on the radiative warming/cooling rates

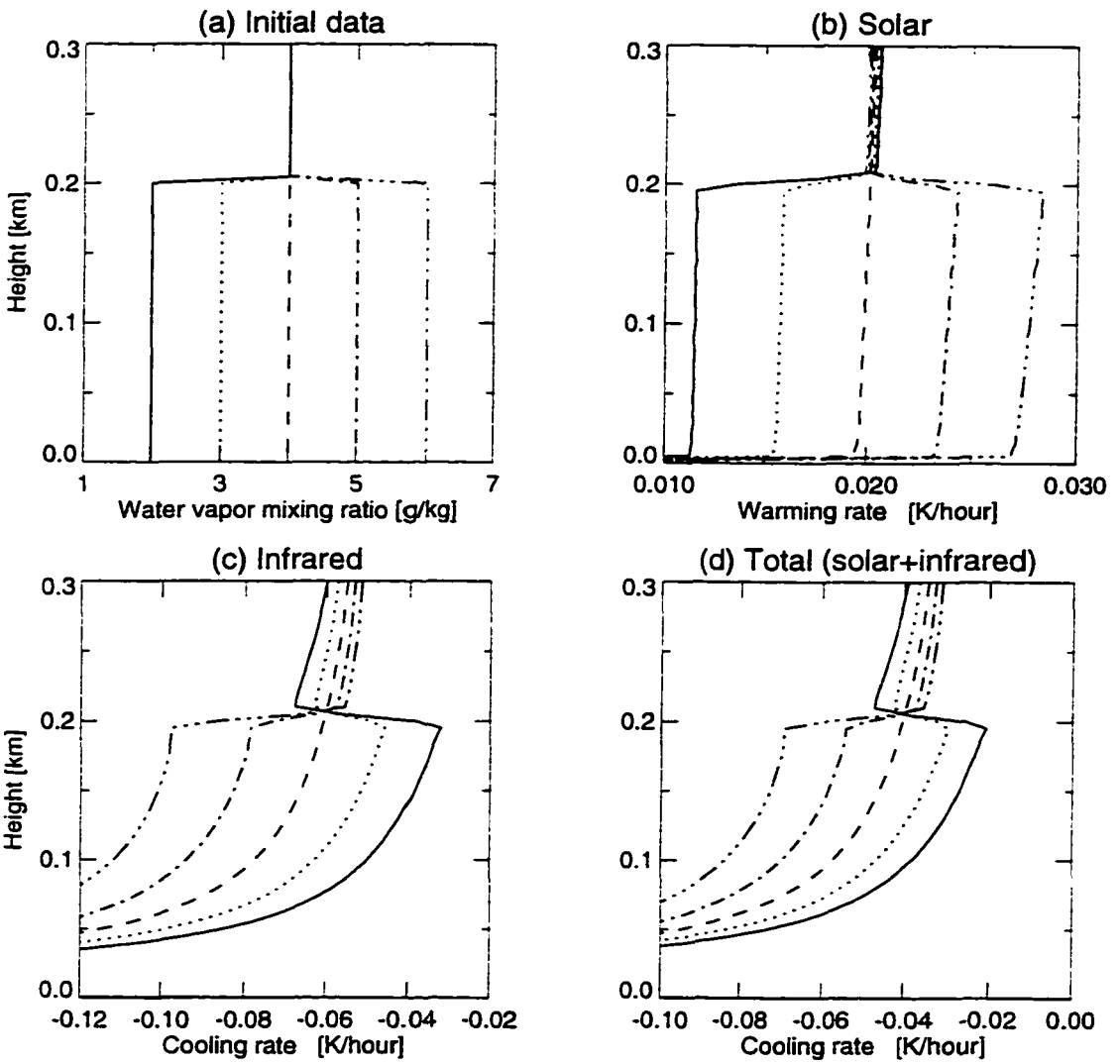

Figure 4.14. The effect of the water vapor gradient on the radiative transfer. (a) Initial water vapor mixing ratio; (b) solar warming rate; (c) infrared cooling rate; (d) total (solar + infrared) cooling rate. Solid, dotted, dashed, dashed-dotted and dashed-dotted-dotted-dotted lines correspond to the different humidity profiles specified in (a).

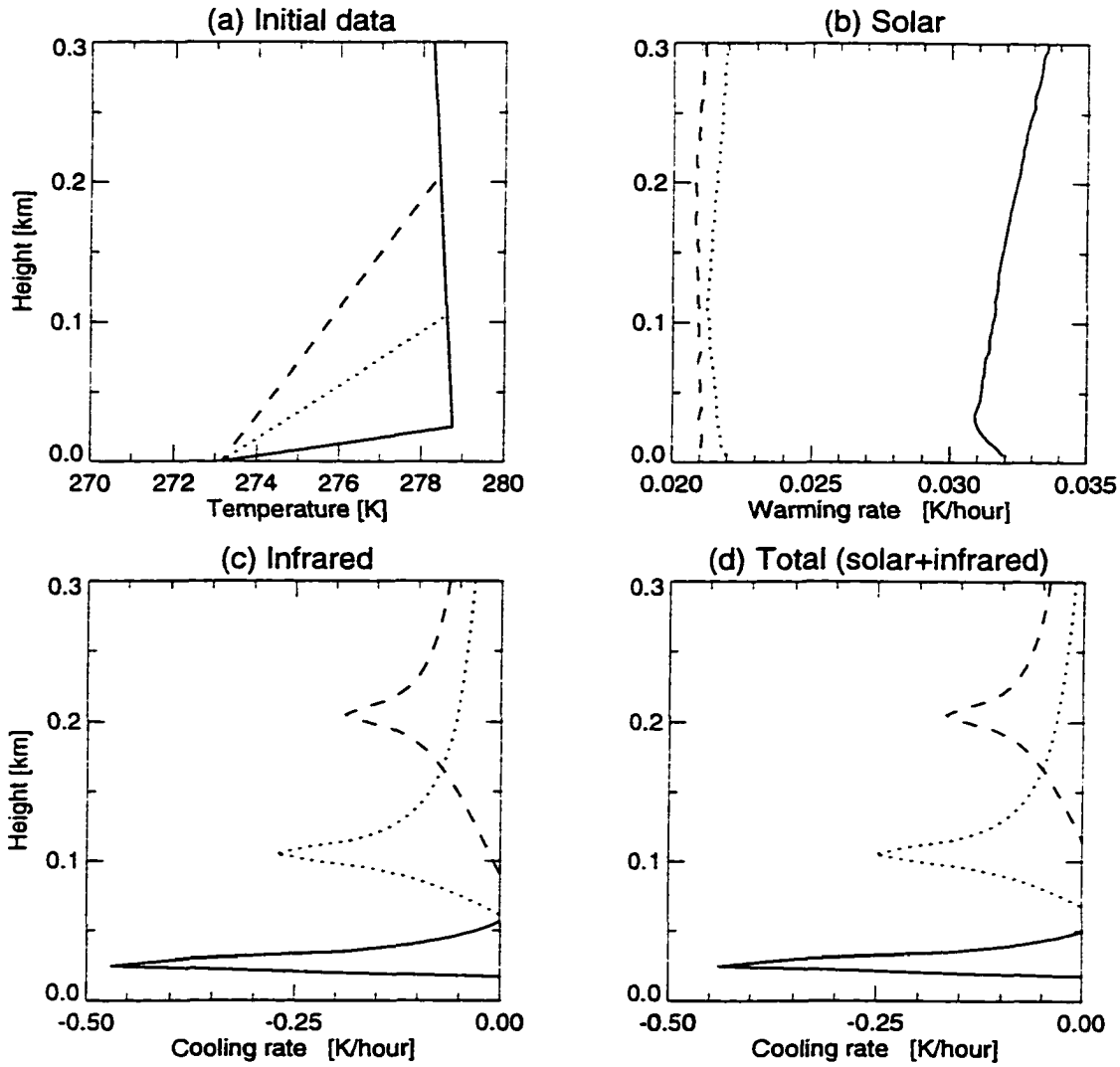

Figure 4.15. The effect of the vertical temperature profiles on the radiative transfer. (a) Initial temperature profiles; (b) infrared; (c) solar; (d) total (infrared + solar). Solid lines correspond to a simulation with a constant temperature lapse rate of -1.8 K/km down to a surface temperature inversion layer starting at 20 m. The dotted and dashed lines correspond to simulations with the temperature inversion starting at 100 m and 200 m, respectively, as shown in (a). The surface temperature is kept at 273.15 K.

and thus on the formation of the lower layer than on the upper level cloud.

4.3.2 Formation of multiple-layered cloud

Having discussed the formation of the upper and the lower cloud layers separately. I will now discuss the formation of the two-layer cloud. The initial data sets adopted for the following simulations are a combination of those used for the simulations of the upper and lower cloud layers. These simulations are made to inverstigate the effect of temperature and humidity inversions below 200 m level, and humidity gradient at 1 km on the formation of two cloud layers (Table 4.1).

Table 4.1. Simulations for inverstigating the formation of two cloud layers. T_5 and q_{v5} are temperature and water vapor mixing ratio at the 5 m level, respectively. ΔT and Δq_{v5} are, respectively, temperature and humidity deference between 200 m and 5 m. q_{vh} is water vapor mixing ratio above the 1 km level. Δq_{vh} is the humidity gradient across the 1 km level.

	Lower layer				*Upper layer*		*Time for cloud formation*	
	temperature		*humidity*		*humidity*		*hours*	
Cases	T_5	ΔT	q_{v5}	Δq_v	q_{vh}	Δq_{vh}	Lower layer	Upper layer
A	276	**2.4**	3.8	**1.25**	3	**2**	**21.91**	**31.09**
LT1	273.15	**5.3**	3.8	1.25	3	2	**15.64**	29.92
LT2	278.8	**-0.4**	3.8	1.25	3	2	**28.50**	33.51
LQ1	276	2.4	0	**5**	3	2	**22.10**	30.78
LQ2	276	**2.4**	2	**3**	3	2	**22.03**	30.94
LQ3	276	2.4	4	**1**	3	2	**21.91**	30.99
LTQ	278.8	**-0.4**	5	**0**	3	2	**2**	29.67
HQ1	276	2.4	3.8	1.25	1.8	**3.2**	19.64	**21.69**
HQ2	276	2.4	3.8	1.25	1.5	**3.5**	27.70	**18.41**

A simulation (referred to as Case A) is made with the initial data as shown in Figure 4.16 (a). This is actually an idealization of the base simulation in this chapter.

The temperature decreases with height with a constant lapse rate of 1.8 K/km between 0.2 and 2 km. The water vapor mixing ratio is 3 g/kg between 1 and 3 km. 5 g/kg between 0.2 and 1 km. and it decreases linearly downward from 5 g/kg at 0.2 km to 3.78 g/kg at the surface. A simulation of 35 model hours is made. The low cloud layer forms initially at 21.91 model hours. The upper cloud layer forms at 31.09 model hours.

If everything is kept the same as in Case A except that the temperature below 0.2 km now decreases linearly to 273.15 K at the surface (referred to as Case LT1 in Table 4.1. $\Delta T = 5.3\ K$), the lower cloud layer forms initially at 15.64 model hours, which is about 7 model hours earlier than in Case A. The upper cloud layer forms initially at 29.92 model hours (Figure 4.17).

If the initial humidity is the same as in Case A but the initial temperature increases downward all the way down to the surface at a constant lapse rate of 1.8 K/km (referred to as Case LT2 in Table 4.1), the lower cloud layer starts forming initially forms at 28.50 model hours. which is 7 model hours later than in Case A. The upper cloud layer now starts forming at 33.51 model hours (Figure 4.18).

If the initial temperature increases downward all the way down to the surface with a constant lapse rate of 1.8 K/km and the water vapor mixing ratio is fixed at 5 g/kg between 1 km and the surface (referred to as Case LTQ), the low cloud layer starts forming near the surfacce at 2 model hours and then develops upward to 0.315 km at the end of simulation (Figure 4.19). The upper cloud layer starts forming initially at 29.67 model hours at 0.85 km in this case.

If the initial temperature and humidity profiles are similar to those in Case A, except that the water vapor mixing ratio above the 1 km level is decreased to 1.8 g/kg (referred to as Case HQ1), the lower and upper cloud layers form initially at 19.64 and 21.69 model hours, respectively (Figure 4.20). Five model hours after the cloud layers formed initially the maximum LWC of the upper cloud layer has developeed to 0.53 g/kg but the maximum LWC in the lower cloud is only 0.13 g/kg .

If the initial temperature and humidity are the same as those in Case A, except that

the water vapor mixing ratio above 1 km level is decreased to 1.5 g/kg (referred to as Case HQ2), the upper cloud layer forms initially at 18.41 model hours (Figure 4.20). The lower cloud layer forms initially at 27.70 model hours at 205 m level, and it develops very slowly. Its maximum LWC is only about 0.05 g/kg five hours after its formation (dashed-dotted lines in Figure 4.20).

The above simulations show that both the humidity and temperature profiles have influence on the formation of the lower and upper cloud layer. With larger temperature inversion near the surface, the lower cloud layer forms earlier. The effect of the humidity inversion near the surface on the formation of the lower cloud layer is not very significant. With larger humidity gradient across the 1 km level, the upper cloud layer forms earlier. The appearance of the lower cloud layer has little influence on the upper cloud layer. However, if the initial conditions are such that the upper cloud layer forms first, it will significantly delay the formation of the lower cloud layer and significantly decrease its LWC.

4.4 Sensitivity Studies

To enhance our understanding of the effect of various physical processes on the formation of a two-layer cloud system, several sensitivity studies are conducted in this section. The roles of solar radiation, CCN concentration and model resolution are discussed.

4.4.1 The effect of solar radiation on cloud formation

Herman and Goody (1976) proposed that solar radiation plays an important role in the formation of multiple-layered ASCs. I therefore will use the radiative-convective model to investigate the effect of solar radiation on the formation of the multiple-layered cloud in this section.

First a simulation is made in which solar radiation has been turned off. The purpose is to compare model results with and without solar radiation. Then we can evaluate the impact of solar radiation on the formation of the multiple cloud layers. The initial

data for this simulation is the same as in the base simulation, in which solar radiation is considered. The results are shown on Figure 4.22. Two cloud layers still form at approximately the same height as in the base simulation. The upper cloud layer forms first at 19 model hours, and the lower cloud layer forms half an hour later at 19.5 model hours. Since the upper cloud layer develops before the lower cloud layer forms, the radiative cooling at the lower cloud layer is not as strong as in the base simulation. Therefore, a smaller LWC is obtained in the lower layer. The vertical profiles of droplet density, equivalent radius and droplet spectra (not shown) are similar to those for the simulation with solar radiation included.

Hence, the cloud forms earlier and and develop more rapidly when solar radiation is ignored in the model. These results suggest that the effect of solar radiative warming is to slow down the formation and evolution of the cloud layers. The solar radiative effect may significantly delay the formation of the upper cloud layer.

4.4.2 The effect of CCN

The effect of the total number of CCN particles on the cloud formation and microphysical structure is examined in this simulation. The initial temperature and humidity are the same as those in base simulation. The difference lies solely in the initial CCN spectrum. In this simulation, we set $\kappa = 0.34$, and $c = 1.28 \times 10^8\ m^{-3}$ for the power law $N_{CCN}(s) \approx c(100s)^{\kappa}$, instead of $c = 6.4 \times 10^8\ m^{-3}$ used in the base simulation. This CCN spectrum is close to one measured over the Arctic Ocean in April 1992 during the LEADEX experiment (Hegg et al., 1995). For this spectrum, the CCN number is about 100 if the supersaturation is 0.4%.

The model is ingrated for 40 hours. Compared with the base simulation, the cloud forms almost at the same time and at the same height (Figure 4.23 a). It contains more cloud water 5 model hours after the upper cloud layer is established. The maximum liquid water is about 1.0 g/kg as compared to 0.8 g/kg for the base simulation.

The vertical profiles of droplet density and equivalent radius (Figure 4.23 b and c)

are similiar to those of the base simulation (Figure 4.11 a and b), but a smaller droplet density and a larger equivalent radius are obtained.

The droplet spectrum (Figure 4.24) is different from that of base simulation. It contains three peaks in the upper part of the cloud layer appearing at larger droplet sizes. Close to cloud base the spectrum has only one peak. The droplet spectrum is wider than for the base simulation (Figure 4.12).

4.4.3 The effect of model vertical resolution

A simulation is carried out with grid space of $\Delta z = 10$ m below the altitude of 2 km. The results (Figure 4.25) are compared with those of the base simulation. The two cloud layers form at about the same time and at the same height as in the base simulation. With coarser model resolution, a thicker cloud layer with a smaller maximum cloud liquid water is obtained. For the simulation with $\Delta z = 10$ m, the maximum supersatuation reaches 0.57%, which is larger than that of base simulation. Similar results are obtained for cloud microphysical properties in both simulations (not shown). This suggests that a simulation with a grid spacing of 10 m is able to provide results similar to those obtained with a grid spacing of 5 m.

4.5 Summary

A two-layer ASC case observed on June 20, 1980 during Arctic Stratus Experiment is simulated with the radiative-convective model which has a detailed cloud microphysics module and a comprehensive radiation scheme. The results are compared with the observations. The altitudes of the two simulated cloud layers correspond well with the observations. The simulation reproduces the temperature inversion and the humidity inversion occurring right above the cloud top. The cloud microphysical structure such as the droplet spectrum provided by the simulation also corresponds well with the observations.

The formation of the lower cloud layer is investigated. Its physics is different from

that of the upper cloud layer. The cloud microphysical properties such as the droplet spectrum of the lower layer cloud are different from those of the upper layer cloud. This may be related to the difference between the vertical mixing taking place within the two cloud layers since the lower cloud layer forms in a stable temperature inversion layer. Changes in both humidity and temperature profiles in the inversion layer may cause significant infrared cooling and lead to the formation of the lower cloud layer. However, the simulations indicated that changes in the temperature profile are more effective in producing the lower level cloud than changes in the humidity profile.

The formation of the two-layered cloud system is investigated. Both humidity and temperature gradients influence the formation of the lower and upper cloud layer. Different combinations of humidity and temperature profiles may lead to formation of the upper cloud layer prior to or after the formation of the lower layer cloud. The appearance of the lower cloud layer has little influence on the upper cloud layer. In contrast, the upper cloud layer significantly affects the formation and development of the lower cloud layer. Thus, if the upper cloud layer forms first, it will delay the formation of the lower cloud layer and significantly decrease its LWC.

The model has been used to explore the relative roles of solar and infrared radiation. The two cloud layers form as a consequence of the initial humidity and temperature profiles. Solar radiation has the effect of counteracting for the longwave cooling. However, the two cloud layers form whether or not solar radiation is included. The solar radiative warming has a stronger effect on the formation of the upper layer cloud than on the lower layer cloud, and it leads more effectively to a delay in its formation.

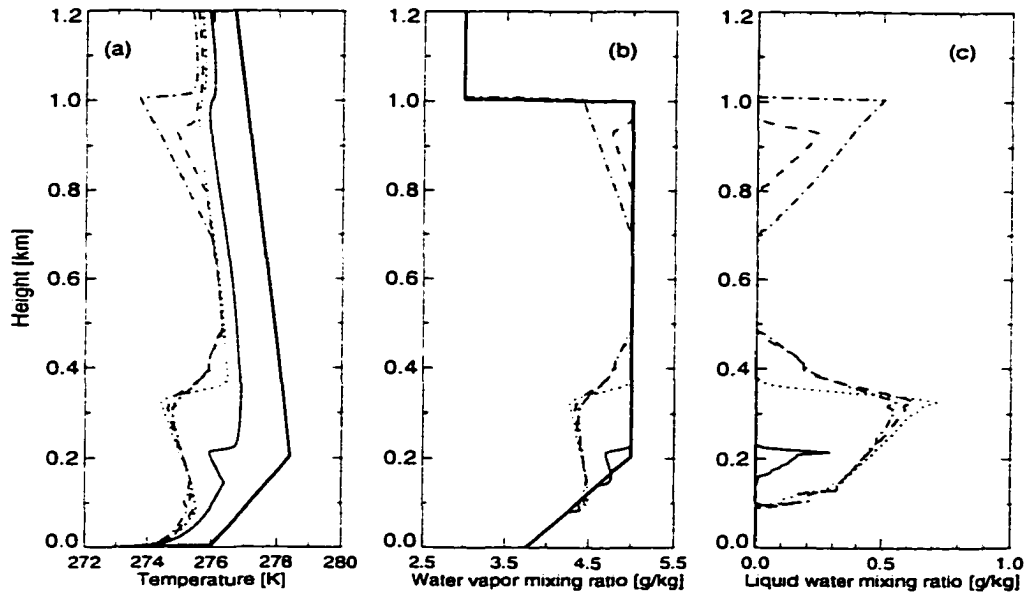

Figure 4.16. Case A. (a) Temperature [K]. (b) liquid water mixing ratio [g/kg]; (c) water vapor mixing ratio [g/kg]; Solid, dotted, dashed and dashed-dotted lines correspond to simulation results at 24, 31, 33 and 36 model hours. The lower and upper cloud layers form initially at 21.91 and 31.09 model hours, respectively. Heavy solid lines show initial conditions.

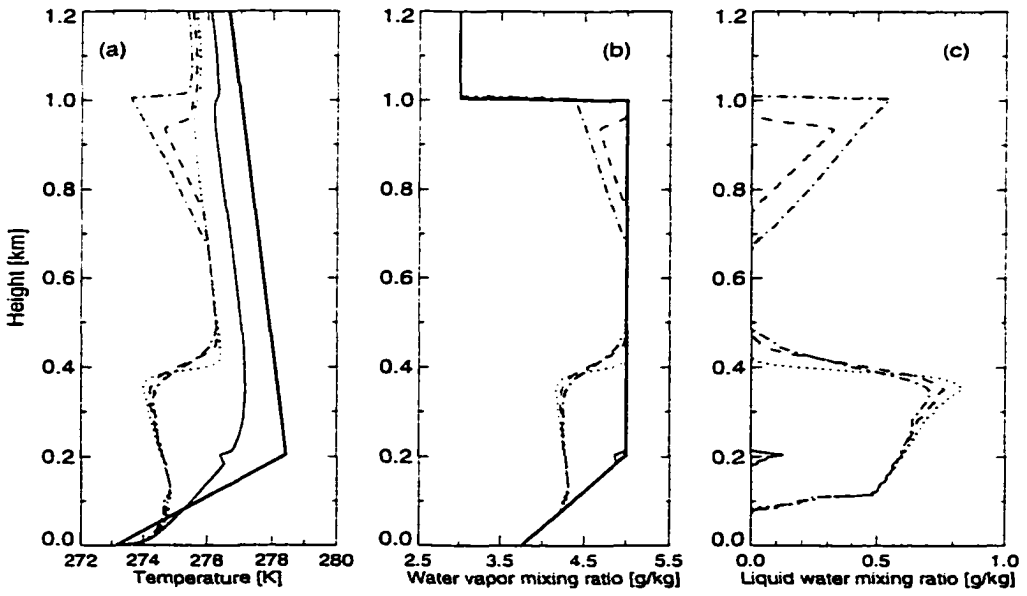

Figure 4.17. Case LT1. (a) Temperature [K]. (b) liquid water mixing ratio [g/kg]; (c) water vapor mixing ratio [g/kg]; Solid, dotted, dashed and dashed-dotted lines correspond to simulation results at 17, 30, 32 and 35 model hours. The lower and upper cloud layers form initially at 15.64 and 29.92 model hours, respectively. Heavy solid lines show initial conditions.

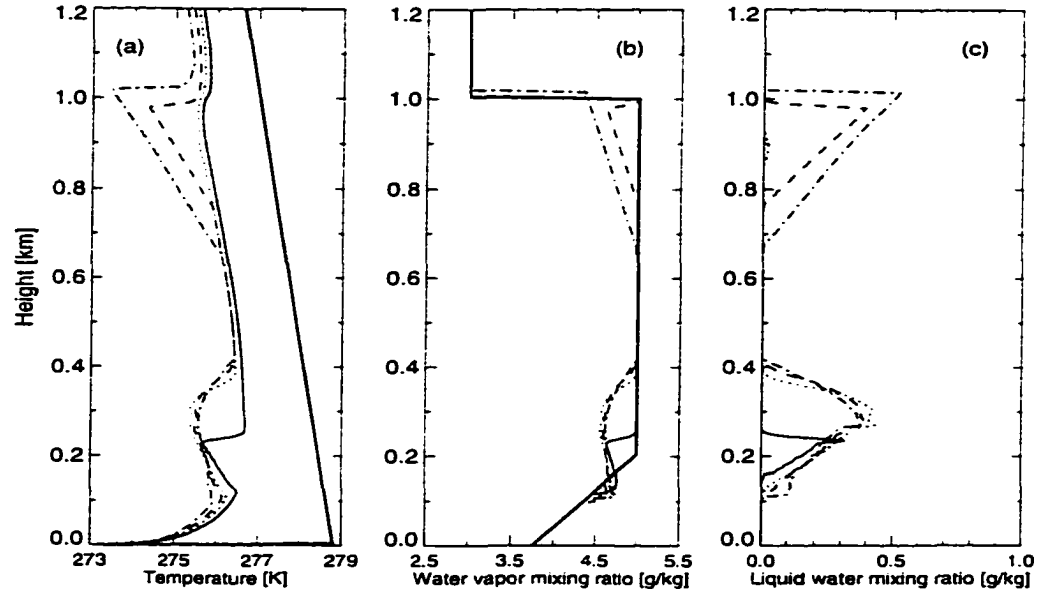

Figure 4.18. Case LT2. (a) Temperature [K]. (b) liquid water mixing ratio [g/kg]; (c) water vapor mixing ratio [g/kg]; Solid, dotted, dashed and dashed-dotted lines correspond to simulation results at 31, 34, 36 and 39 model hours. The lower and upper cloud layers form initially at 28.50 and 33.51 model hours, respectively. Heavy solid lines show initial conditions.

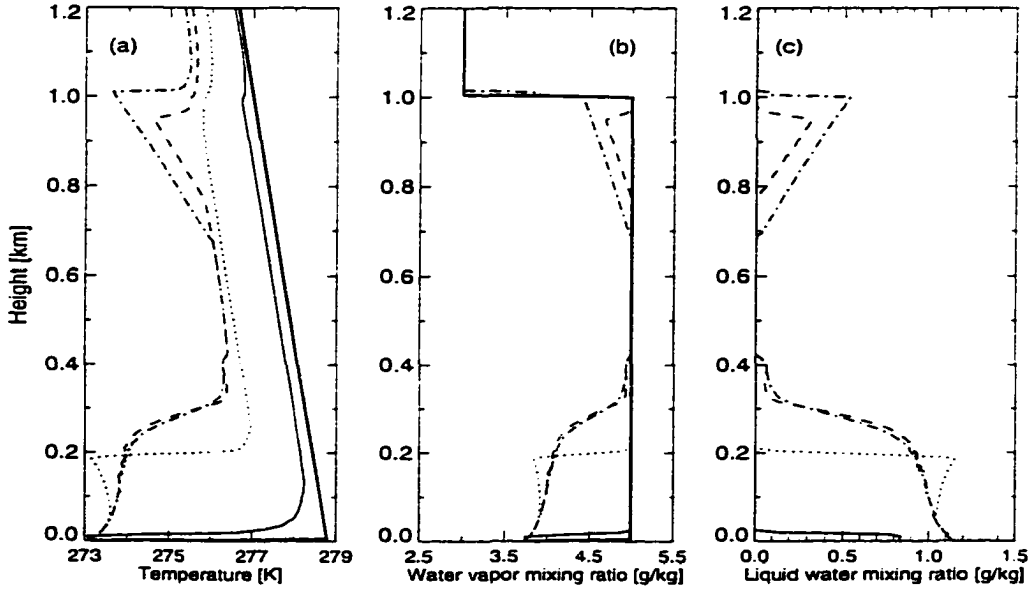

Figure 4.19. Case LTQ. (a) Temperature [K]. (b) liquid water mixing ratio [g/kg]; (c) water vapor mixing ratio [g/kg]; Solid, dotted, dashed and dashed-dotted lines correspond to simulation results at 5, 25, 32 and 35 model hours. The lower and upper cloud layers form initially at 2 and 29.67 model hours, respectively. Heavy solid lines show initial conditions.

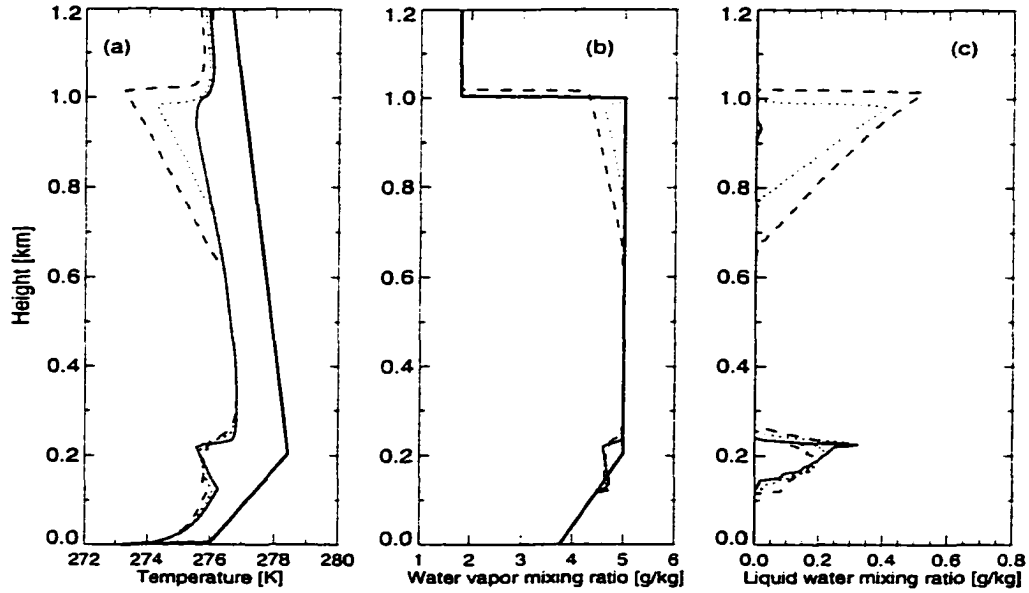

Figure 4.20. Case HQ1. (a) Temperature [K]. (b) liquid water mixing ratio [g/kg]; (c) water vapor mixing ratio [g/kg]; Solid. dotted and dashed lines correspond to simulation results at 22, 24 and 27 model hours. The lower and upper cloud layers form initially at 19.64 and 21.69 model hours. respectively). Heavy solid lines show initial conditions.

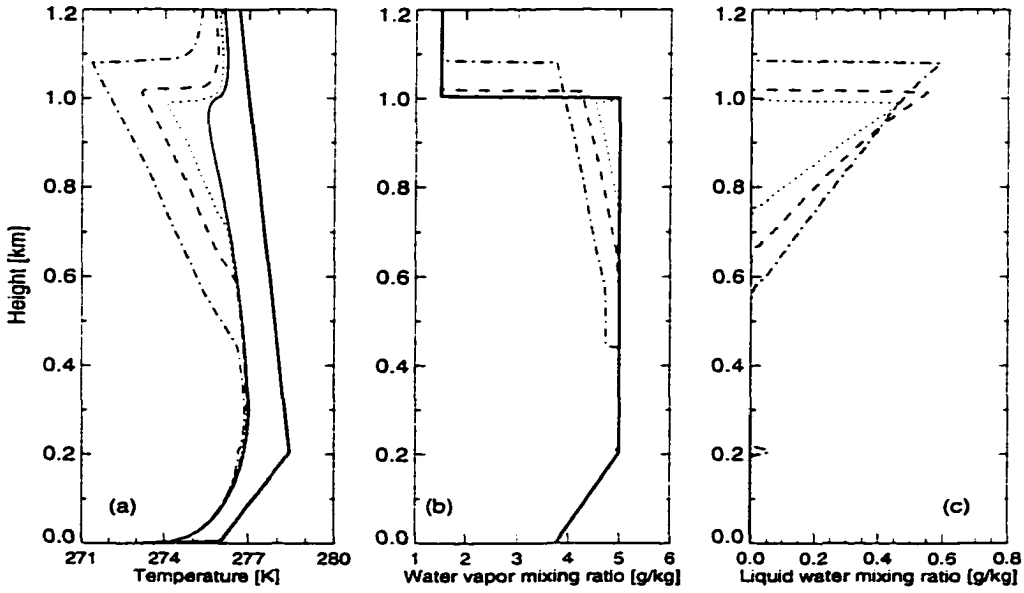

Figure 4.21. Case HQ2. (a) Temperature [K]. (b) liquid water mixing ratio [g/kg]; (c) water vapor mixing ratio [g/kg]; Solid, dotted, dashed and dashed-dotted lines correspond to simulation results at 18, 21, 24 and 32 model hours. The upper cloud layers form initially at 18.41 model hours and the lower cloud layer forms at 27.70 model hours. Heavy solid lines show initial conditions.

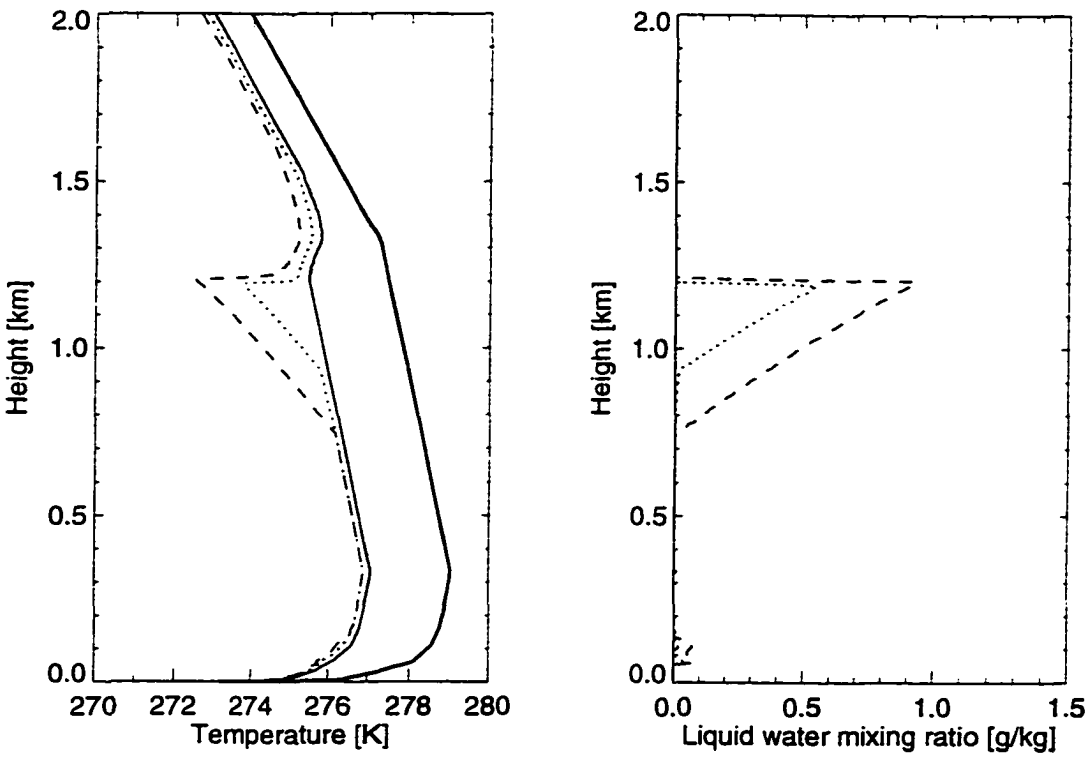

Figure 4.22. Simulation results without solar radiation. The upper cloud layer forms at 19 hours. (a) temperature; (b) liquid water mixing ratio; Solid: 1.0 h before the clouds form (18 h); dotted: 2 h after clouds form (21 h); dashed: 5 h after clouds form(24 h). Havey: initial data.

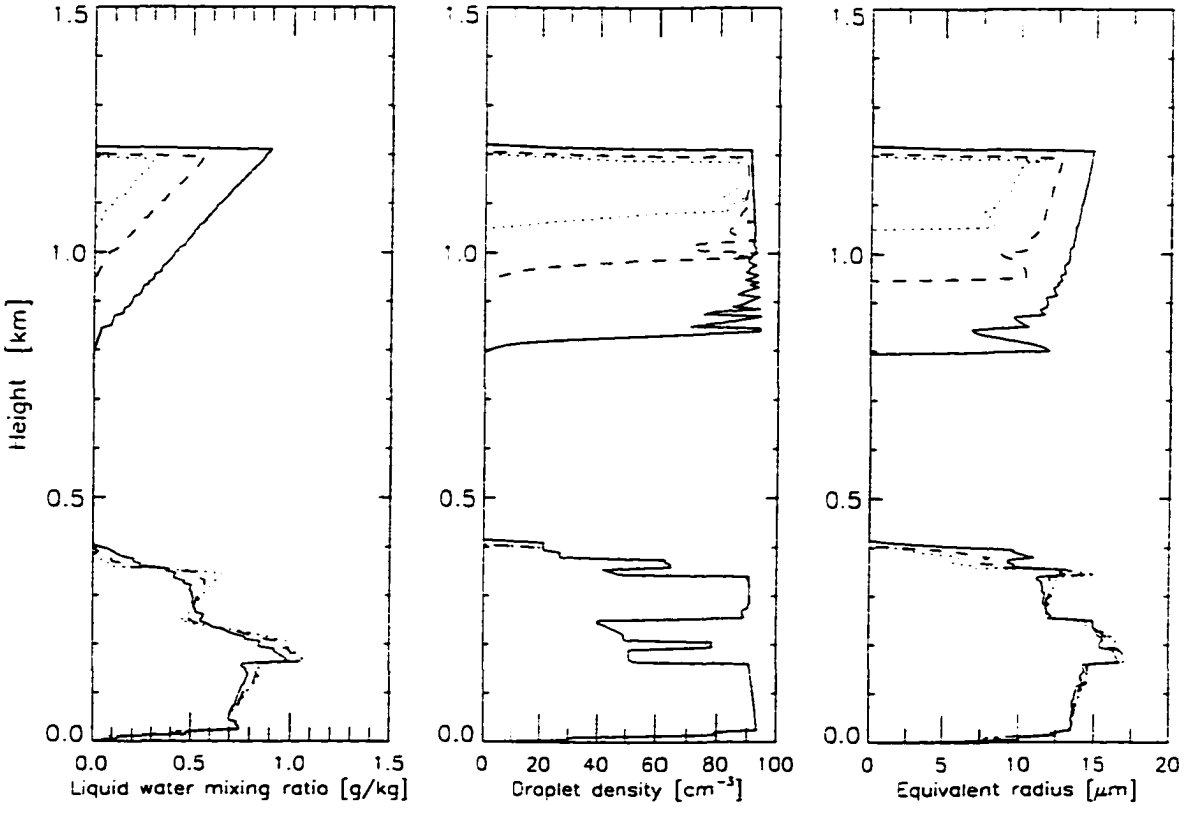

Figure 4.23. The effect of CCN. (a) Liquid water mixing ratio [g/kg]; (b) droplet density [cm^{-3}]; (c) equivalent radius [μm]; The dotted line is 1 hour after the clouds form (36 model hours); the dashed line is 2 hours after the clouds form (37 model hours): the solid line is 5 hours after the clouds form (40 model hours).

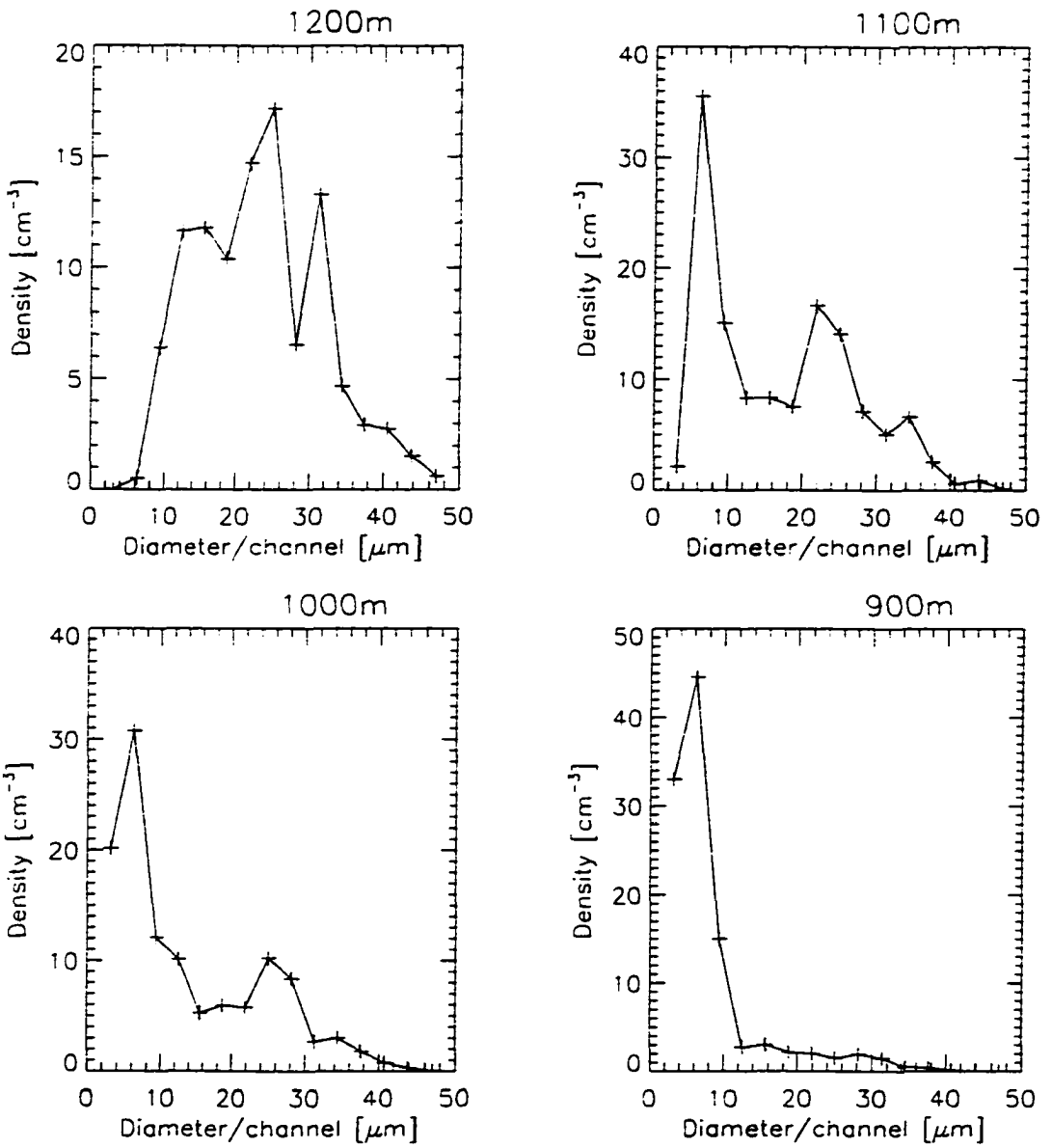

Figure 4.24. The effect of CCN. Droplet spectra obtained 5 hours after the clouds form (40 model hours).

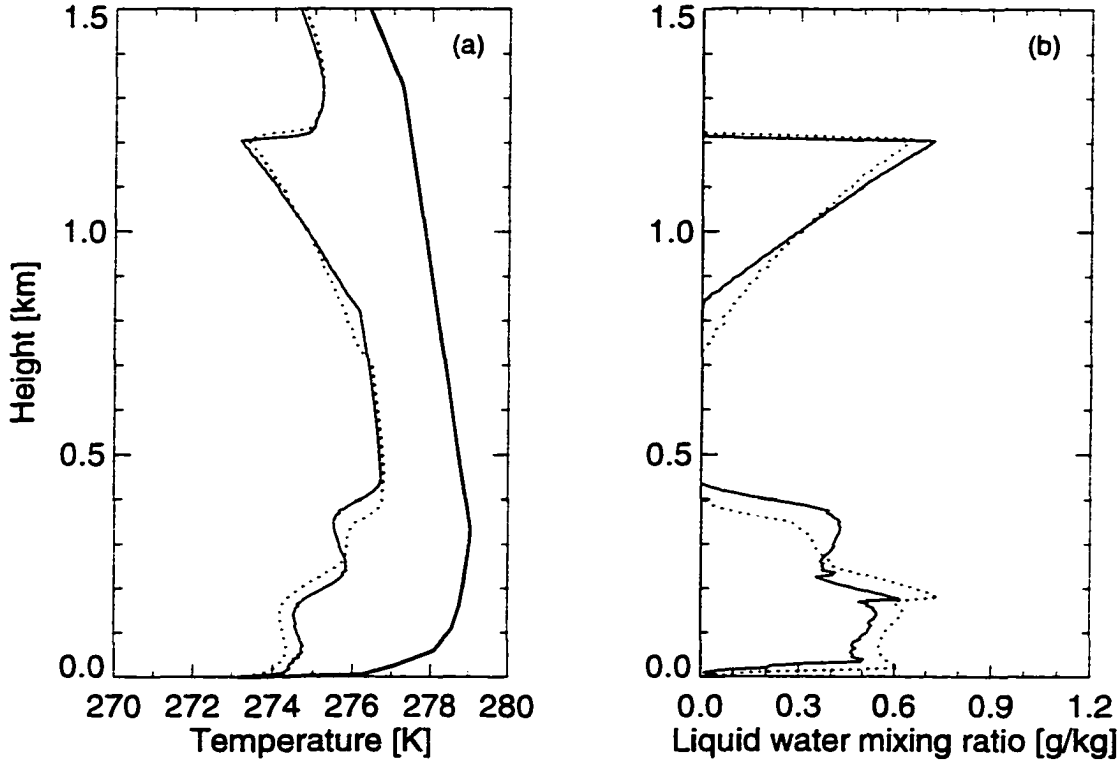

Figure 4.25. Comparision of simulations with different vertical model resolutions. (a) Temperature [K]; (b) liquid water mixing ratio [g/kg]; (c) water vapor mixing ratio [g/kg]. Bold line is the model initial contiditions. Solid and dotted lines are the simulations with $\Delta z = 5$ m and 10 m, respectivly.

Chapter 5

Comparison of the One-Dimensional Model and the Three-Dimensional Large Eddy Simulation Model

5.1 Introduction

Although very reasonable results have been obtained in the last three chapters in simulating the formation of ASCs with the 1-D radiative-convective model, we must be aware of the limitation of this model. A 1-D model is by necessity based on a simplified representation of three dimensional motions. It assumes horizontal homogenity, and is therefore an approximation to the real atmosphere. The main deficiency of a one-dimensional model in this context is that it cannot describe the three dimensional turbulence that may have a significant influence on cloud formation and this turbulence is very closely correlated with the microphysics. Fortunately, many 1-D models are capable of simulating boundary layer processes under many situations (Bechtold et al., 1996; Moeng et al.,

1996). In this chapter, a 3-D LES model will be adopted to evaluate the 1-D model. To enhance the efficiency of this model it was modified to run on a machine with parallel processing capabilities. I will compare the results of the 1-D radiative-convective model with those of this 3-D large eddy simulation model and discuss the limitation of the 1-D model.

An important assumption is made in the radiative-convective model concerning the parameterization of the vertical transport processes. A convective adjustment scheme is adopted to simplify the problem. This simplification allows us to focus on radiation and cloud microphysics and to study their role in cloud formation in some detail. The convective adjustment scheme is based on the assumption that the vertical dynamical motions are weak except in unstable layers. In this chapter, the LES model will be used to evaluate the merit of this simplified convective adjustment scheme.

Before the comparison between the 1-D and 3-D models is made, I will first compare two different radiative schemes, and compare the cloud parameterization scheme based on detailed cloud microphysics used in the 1-D model with a cloud bulk parameterization scheme used in the 3-D LES model.

5.2 Base simulation

A simulation made with the 1-D radiative-convective model including detailed cloud microphysics, presented in detail in Chapter 2, is chosen to provide a basis for the following comparisons. The output from this simulation will be used as the initial data for the following simulations with the 1-D and the 3-D LES models to enable more meaningful comprisons between the two models.

5.2.1 Initial data and simulation design

The base simulation is started with a clear atmophere to investigate the cloud formation. The initial conditions for the simulation is based on the observations of June 28, 1980 over the Beaufort Sea during the Arctic Stratus Experiment. Detailed descriptions of

the experiment and analyses of the physical properties of the cloud layers were given by Tsay and Jayaweera (1984) and Curry (1986). A brief description is also provided in Chapter 1. Two nearly parallel layers of stratus clouds were observed. The upper cloud layer, with top at 1.2 km and base at 0.8 km, was capped with a strong temperature inversion and significant moisture decrease. The top of the lower cloud layer was at about 0.11 km and its thickness was about 80 m.

The initial water vapor mixing ratio for the simulation is the same as that used in the base simulation in Chapter 3 and is shown in Figure 3.1 (a). To simplify the problem, I will focus only on the the formation of the upper cloud layer. Therefore, a small value of the water vapor content is adopted below 0.5 km to prevent cloud formation there. The water vapor mixing ratio is taken to be 5.1 g/kg (relative humidity is about 80%) between 0.5 and 1.2 km, and it is assumed to decrease significantly between 1.2 and 1.3 km as shown in Figure 3.1 (a).

As shown in Figure 5.1, the initial temperature is taken to be 282.4 K at 5 m and it is assumed to decrease with height at a constant lapse rate of -3.0 K/km. The dotted line in Figure 5.1 is the corresponding dew point temperature.

As in Chapter 3 the initial CCN spectrum for the simulations with detailed cloud microphysics is represented by a power law (Twomey 1977),

$$N_{CCN}(s) \approx c(100s)^{\kappa}, \tag{5.1}$$

with $\kappa = 0.34$, and $c = 6.4 \times 10^8\ m^{-3}$, yielding a total CCN number of about 500 when the supersaturation s is 0.4%. The diurnal cycle of solar radiation is not included in the simulations and a fixed solar zenith angle of 70° is used. The surface temperature is fixed to 273.15 K. The model vertical grid and the minimum time step for vertical mixing are the same as those used in Chapter 3.

5.2.2 1-D simulation results

The model is integrated forward in time for 57 hours. The cloud initially forms at 51 model hours at 1.155 km altitude and then develops rapidly. At the end of the simulation,

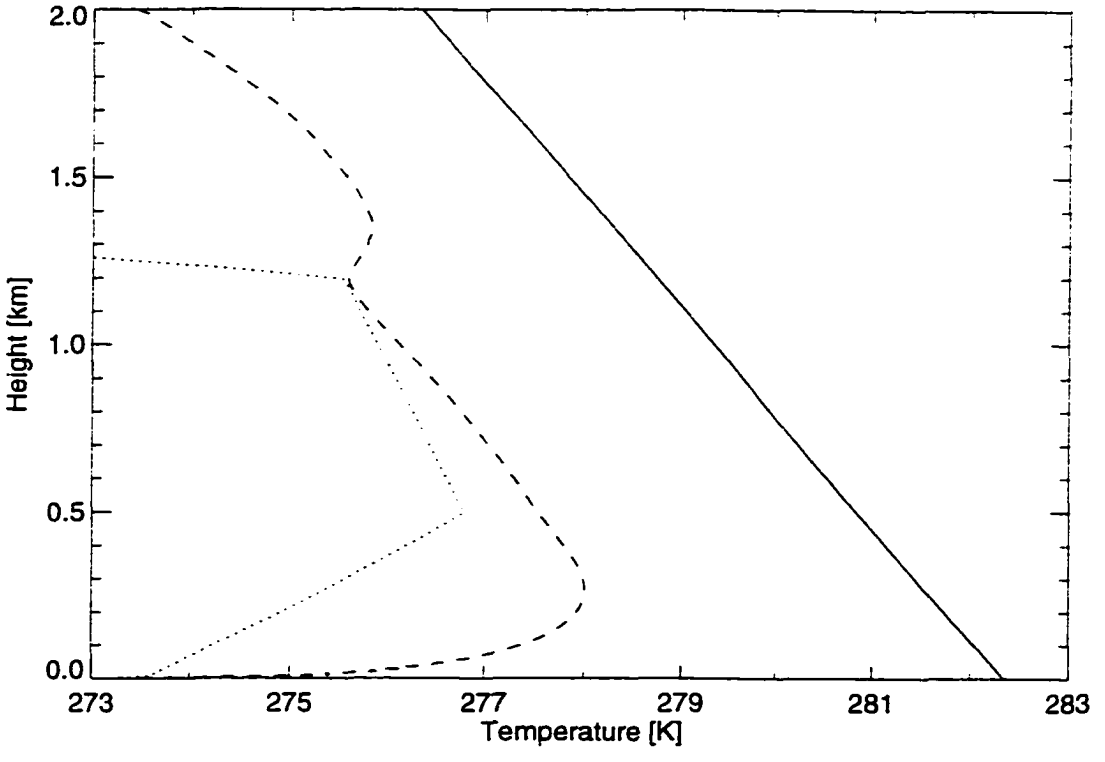

Figure 5.1. Temperature. The solid line is the initial temperature and the dotted line is the corresponding dew point temperature. The dashed line gives the simulated temperature at 50 model hours, which is 1 model hours before cloud formation in the base simulation.

the cloud top is at 1.2 km and there is a maximum LWC of about 0.6 k/kg (Figure 5.2 a). The cloud base is at about 0.8 km.

Figure 5.2 (b) shows vertical distribution of the droplet density. It is almost constant with height. The maximum droplet density is 400 particles/cm^3 and it does not change much with time during the cloud evolution. The equivalent radius increases with height and with time (Figure 5.2 c). The maximum equivalent radius is about 8 μm 4 hours after the cloud forms. Therefore, the increase in cloud liquid water with height and with time is related to the increase in droplet size rather than in droplet density. The simulation results correspond well with the observations (Tsay and Jayaweera, 1984).

Figure 5.3 show the droplet spectrum at 4 hours after the cloud layer initially forms.

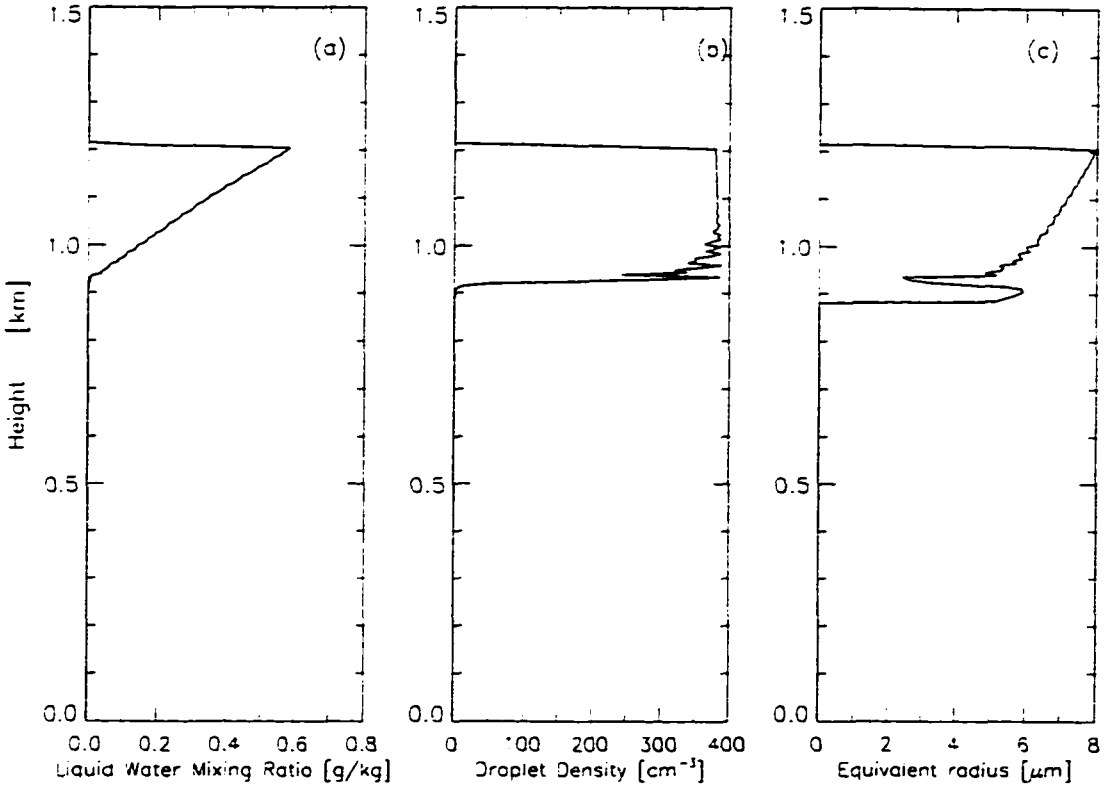

Figure 5.2. Simulation at 4 model hours after the cloud layer initially forms. (a) Liquid water mixing ratio [g/kg]; (b) droplet density $[cm^{-3}]$; (c) equivalent radius [μm].

To compare with the observation, the distribution has been collected in 15 equidistant bins with mean diameter 3.13 μm apart, with the pluses indicating the center of each bin (Tsay and Jayaweera 1984). The spectrum has two peaks near the cloud top with diameters about 8 μm and 17 μm and a single peak at about 4 μm near the cloud base.

Figure 5.4 shows radiative warming/cooling rates after the cloud layer has formed. The maximum solar and infrared warming/cooling rates occur around the cloud top and ascend with the cloud top. The maximum infrared cooling is about 10 times as large as the maximum solar warming. Therefore, the total radiative transfer has a cooling effect and causes temperature to decrease.

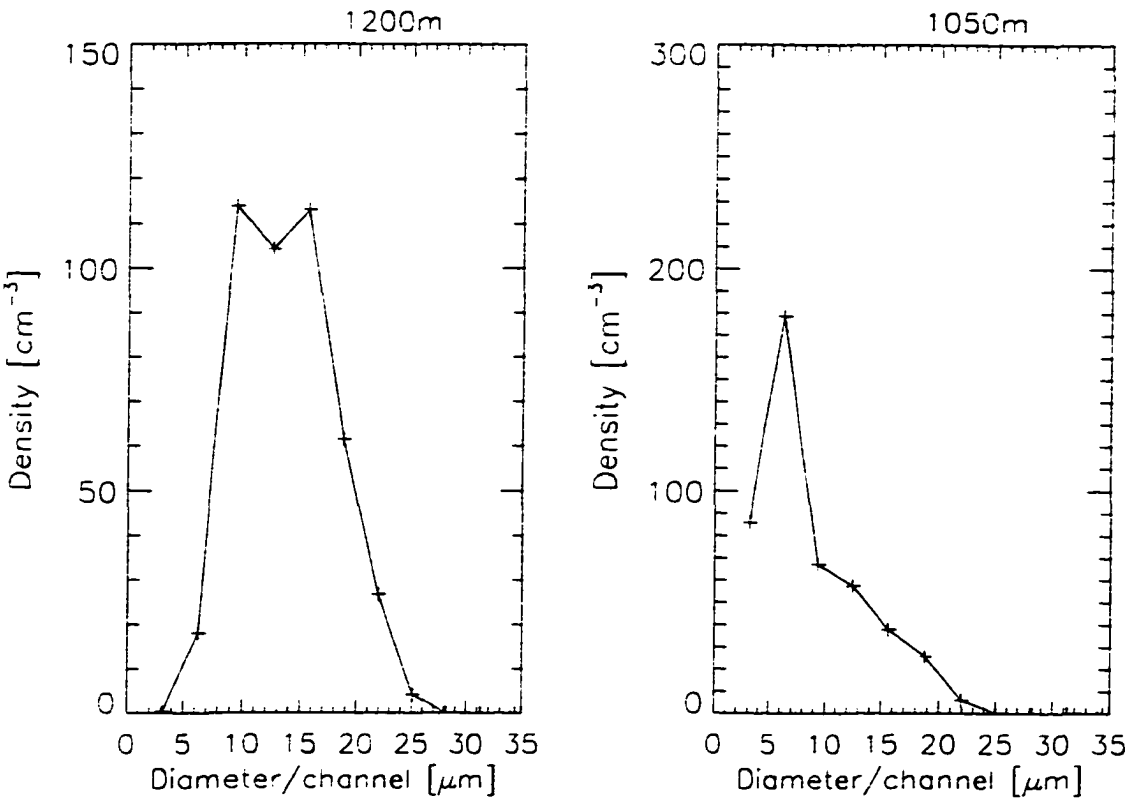

Figure 5.3. Droplet spectrum at 4 model hours after cloud layer initially forms (at 55 simulation hours).

5.3 Comparison of two radiative transfer schemes

Two schemes for calculating infrared radiative transfer are compared in this section. One is the radiative scheme developed by Stamnes et al. (1988) and Tsay et al. (1989). It is described in Chapter 2, and referred to as DISORT here. The other is the infrared radiative scheme proposed by Herman and Goody (1976) described in Appendix B. It will be referred to as HG. I will compare these two radiative schemes under two situations: clear atmosphere and cloudy atmophere.

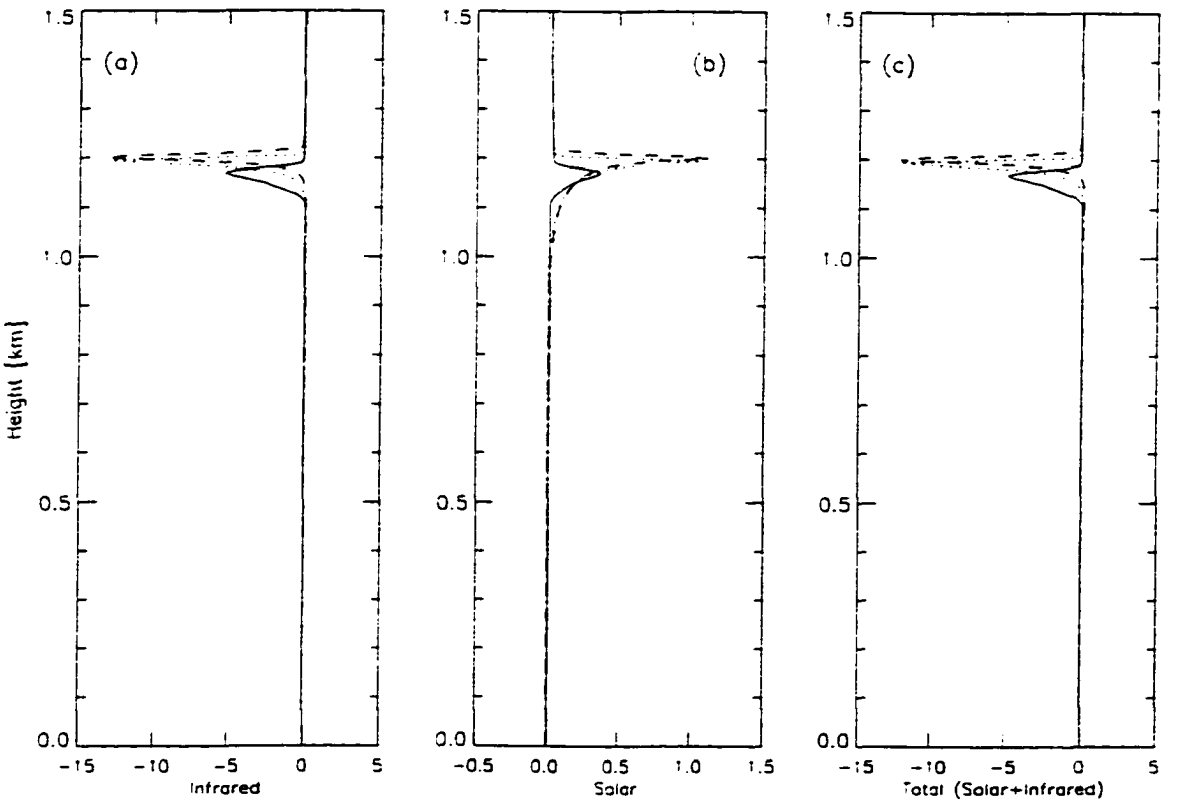

Figure 5.4. Radiative warming/cooling rates after cloud form. Solid, dotted and dashed lines are respectively 1, 3 and 4 model hours after the cloud forms. (a) Infared; (b) solar; (c) total (infrared + solar).

5.3.1 Clear atmosphere

Figure 5.5 shows the infrared cooling rates computed by the two radiative schemes under clear atmospheric conditions. The models are intialized with the initial data set adopted in the base simulation. The solid and dotted lines shows the infrared cooling rate calculated with HG and DISORT, respectively. Both of these lines show three peaks. One is on the surface; the second is at 0.5 km in height; the third one, which leads the formation of the cloud layer, is at 1.2 km. Comparing the cooling rate obtained with the two schemes, we note that DISORT leads to stronger cooling around 1.2 km and is more sensitive to the gradient in humidity. HG yields stronger cooling rates below 0.5 km, especially near the surface.

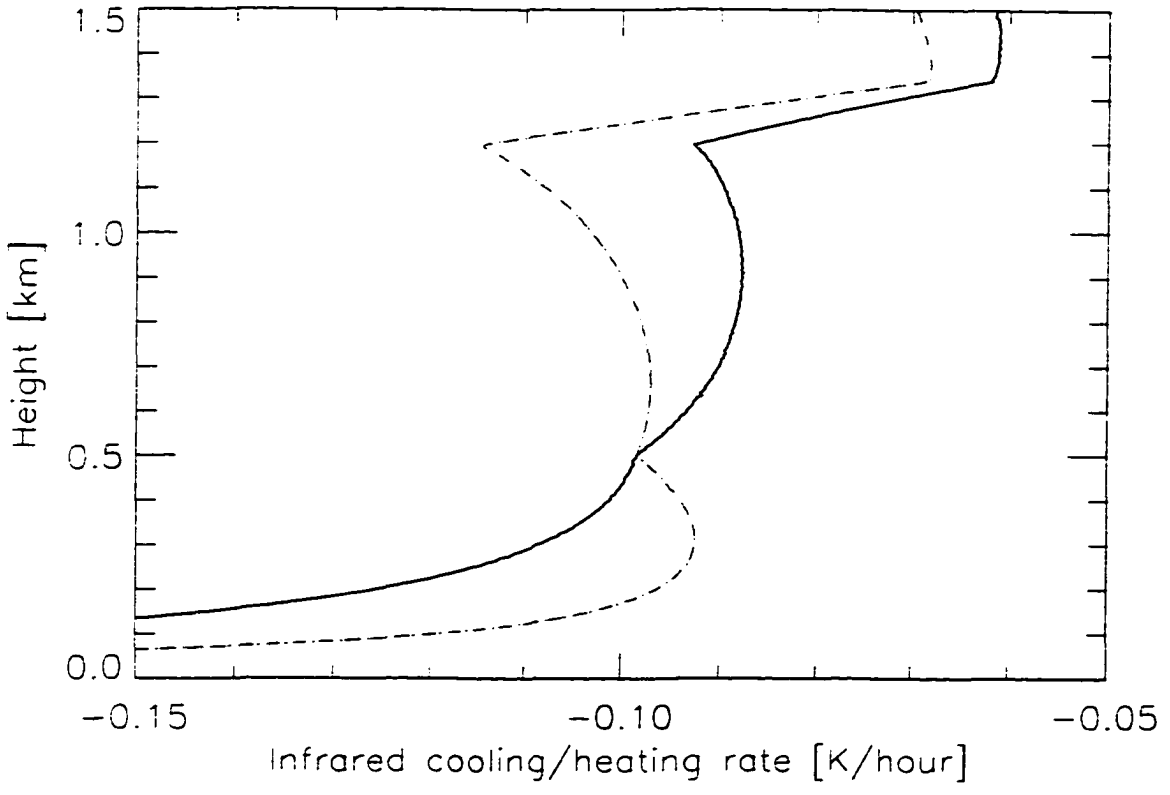

Figure 5.5. Infrared cooling rates calculated by the two schemes under clear atmosphere. Solid line is infrared cooling rate calculated with HG: dashed line is infrared cooling rate calculated with DISORT.

5.3.2 Cloudy atmosphere

To compare the two models in a cloudy atmospheric situation, the model output of the base simulation at 55 model hours is used as input data for the two radiative models. At this time a cloud has been developing for about 4 hours. The cloud top is at 1.2 km, and the maximum liquid water is about 0.58 g/kg. The two models yield strong infrared cooling around cloud top (Figure 5.6). The maximum cooling rate computed by the HG scheme is stronger than that by the DISORT scheme. The difference is about 3 K/hour. The peak in the simulation with HG is about 20 meters higher than in the simulation with DISORT.

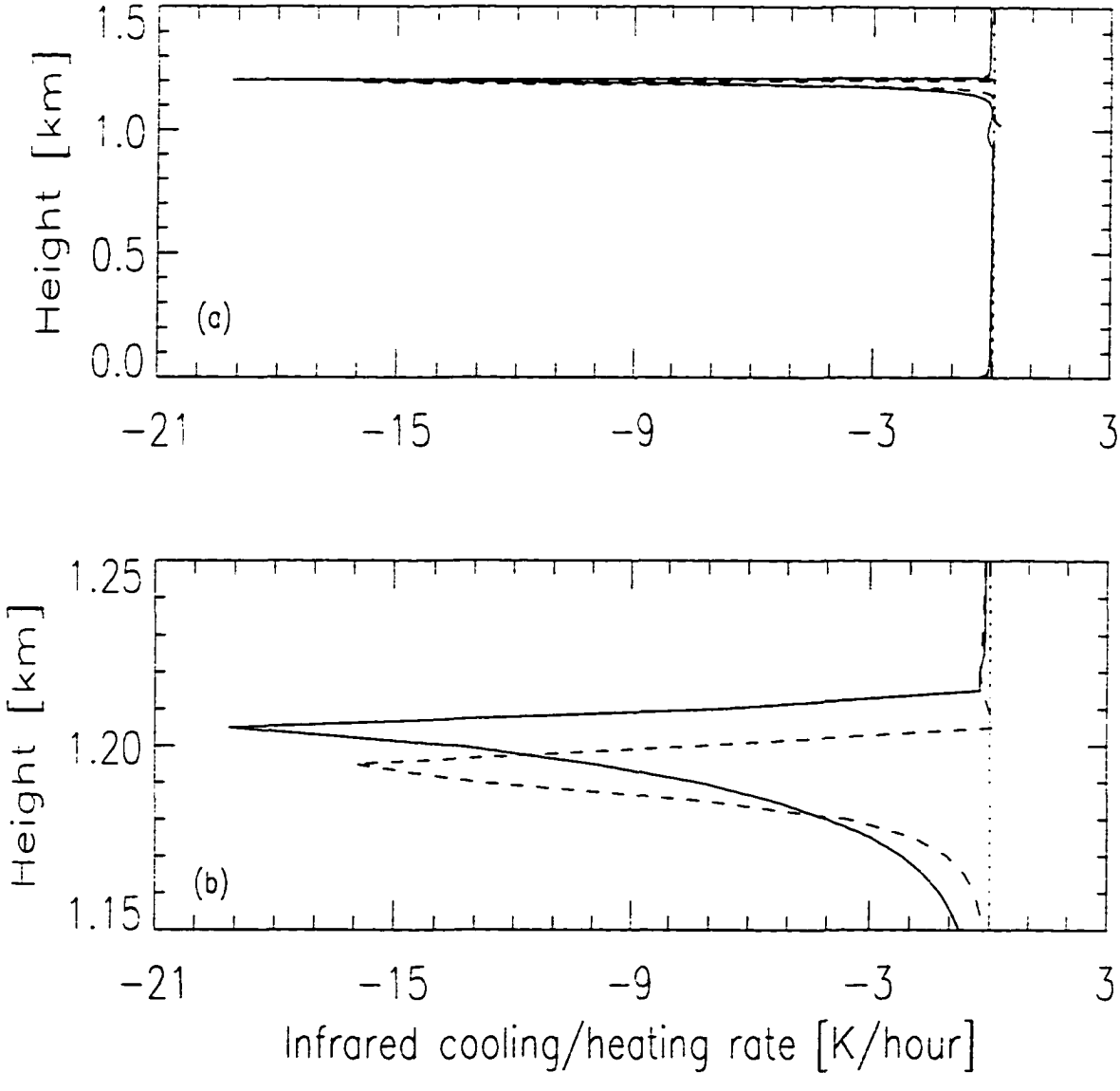

Figure 5.6. Infrared cooling rates calculated by the two schemes under cloudy atmospheric conditions. Solid and dashed lines are results computed with HG and DISORT, respectively.

5.4 The effects of numerical schemes on cloud formation

Two cloud parameterizations are compared in this section. One is the cloud module with detailed cloud microphysis described in some detail in Chapter 2. It includes the cloud droplet activation. droplet growth/evaporation. and droplet mixing using the full droplet size distribution. It is referred to as MS here. The other is the cloud bulk parameterization scheme used in the LES model. It is briefly described in Appendix B. and is referred to as BULK here.

A number of simulations (Table 5.1) were made to compare the difference of radiative schemes and cloud parameterization schemes on simulating cloud formation. The solar radiative warming rates in all simulations are computed with the same radiative scheme DISORT.

Table 5.1. Simulations for comparing the difference of the radiative schemes and cloud parameterization schemes on simulating cloud formation.

Simulation	*Infrared*	*Cloud parameterization*	*Time for cloud formation*
DS-MS	DISORT	MS	1 hours
HG-MS	HG	MS	4 hours
DS-BK5	DISORT	Bulk (radius 5 μm)	4 hours
DS-BK10	DISORT	Bulk (radius 10 μm)	4 hours
HG-BK	HG	Bulk (radius 5 μm)	6 hours
LES	HG	Bulk (radius 5 μm)	2 hours

The initial temperature for these simulations is adopted as the output of the base simulation at 50 model hours and is shown by the dashed line on Figure 5.1 (b). The initial humidity and the other parameters for the simulations are the same as those of the base simulation.

5.4.1 Comparison of the impact of two different radiative schemes on cloud formation

Figure 5.7 shows the cloud liquid water content in the simulations of DS-MS and HG-MS. Both models ran for seven model hours. The cloud formed at 4 model hours in the simulation HG-MS and at 1 model hour in the simulation DS-MS. After the cloud intially formed in the simulation HG-MS, the cloud liquid water developed faster than in the simulation DS-MS. Both simulations get simular cloud liquid water at the end of the simulation. The cloud top continues to rise in the simulation DS-MS, while it is relatively stable in the simulation HG-MS.

To unravel why there is such a difference in the cloud evolution between the two simulations, the infrared radiative cooling rates of the two simulations are shown on Figure 5.8. The cooling rates are much stronger in the simulation HG-MS than in the simulation DS-MS after the cloud forms. At the end of the simulations, when the two simulations have similar liquid water content, the maximum cooling rate in simulation HG-MS is 10 K/hour larger than that in simulation DS-MS. This explains why the cloud develops faster in the simulation HG-MS. In the simulation DS-MS, the height of the maximum cooling rate keeps rising significantly as the cloud top rises.

5.4.2 Comparison of two cloud parameterization schemes

Figure 5.9 shows liquid water mixing ratio in the simulations (DS-BK5 and DS-BK10) of the 1-D radiative-convective model with DISORT as the radiative scheme and with the cloud bulk paramterization. Since the cloud bulk parameterization can not provide droplet spectra, a fixed droplet radius is specified for each simulation. Two simulations are shown in Figure 5.9 with droplet radius 5 μm (DS-BK5) and 10 μm (DS-BK10), respectively. Seven hours simulations are made. Cloud forms initially at about the same time at four model hours in the two simulations. The LWC develops faster in simulation DS-BK5 and is about 0.05 g/kg larger than that in simulation DS-BK10. The thickness of the cloud layer in the two simulations is about the same.

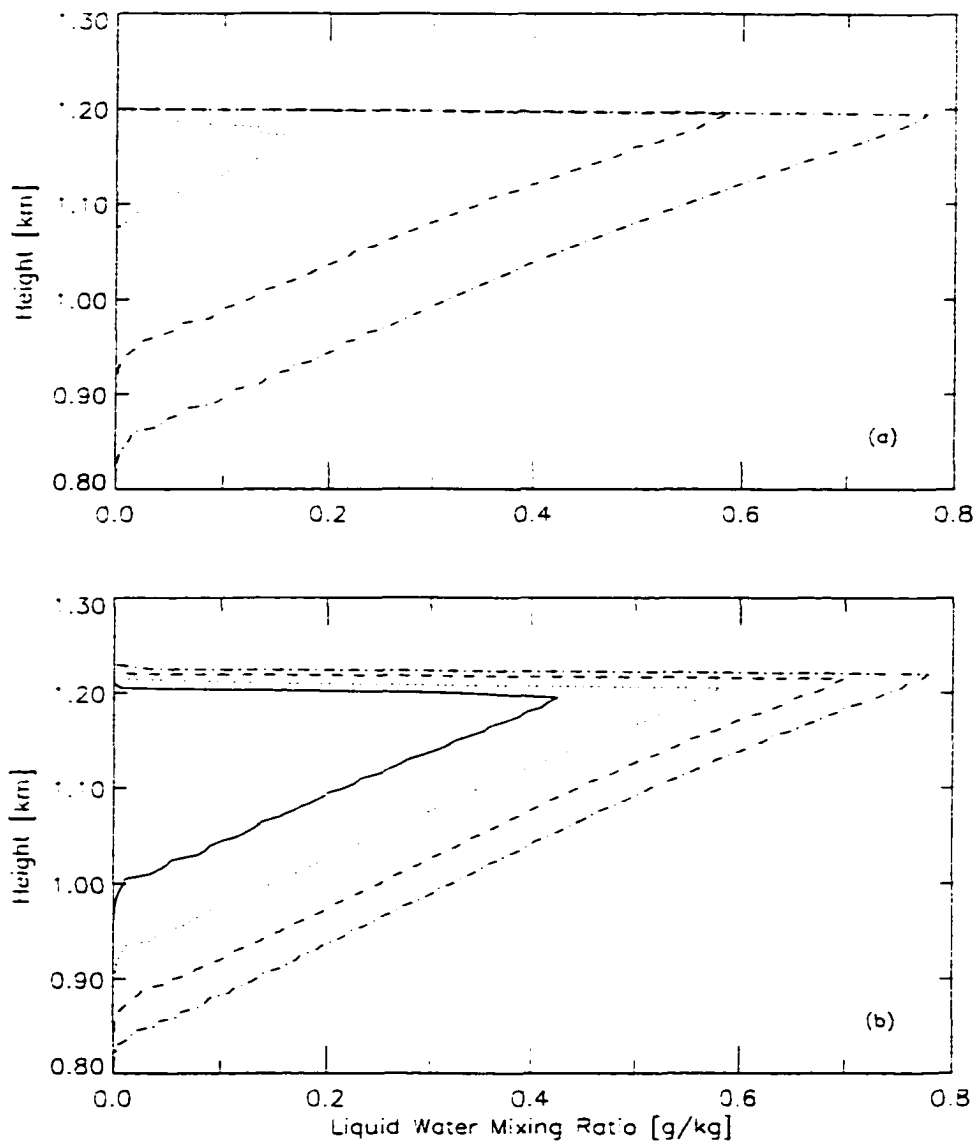

Figure 5.7. Cloud liquid water mixing ratio. (a) Simulation HG-MS; (b) simulation DS-MS. Solid, dotted, dashed and dashed-dotted lines correspond to 4, 5, 6 and 7 model hours.

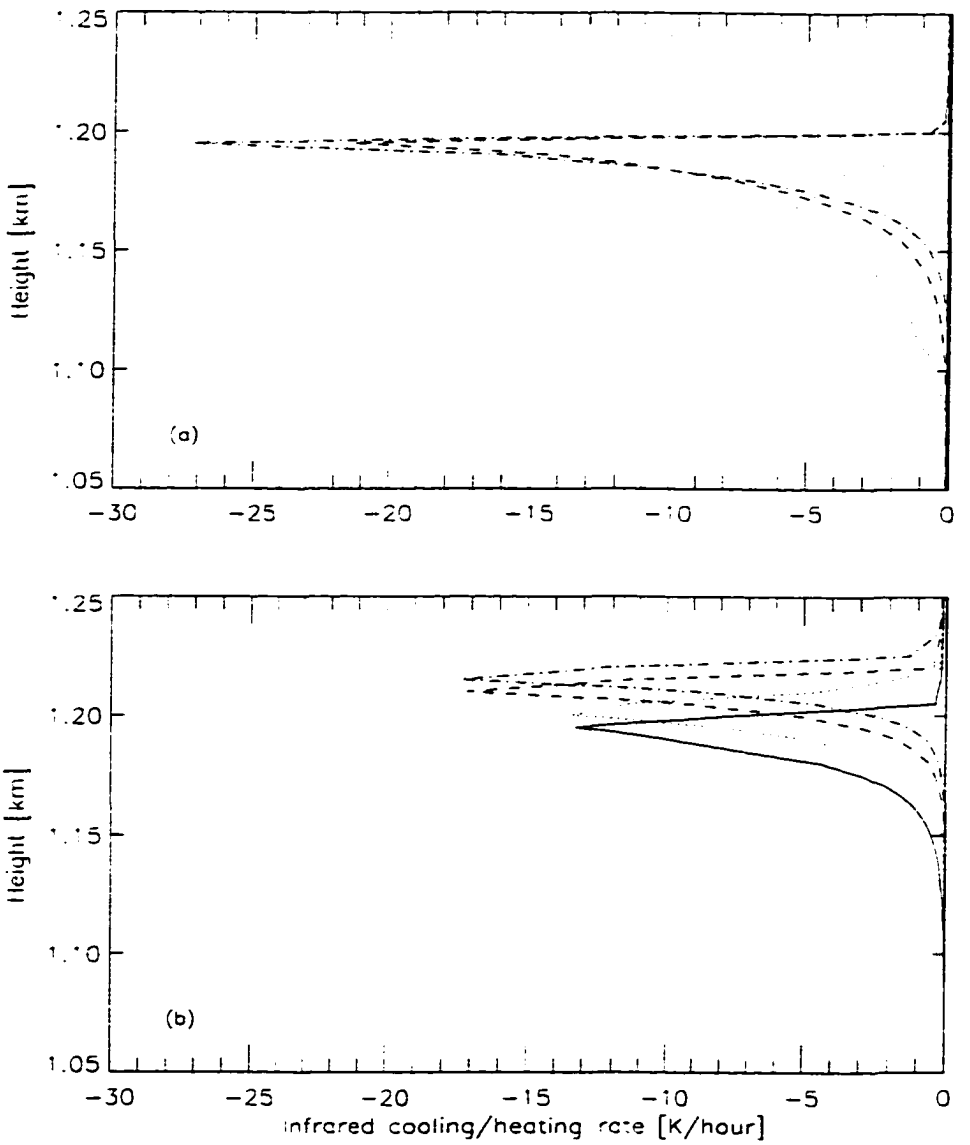

Figure 5.8. Infrared cooling rates. (a) Simulation HG-MS; (b) simulation DS-MS. Solid, dotted, dashed and dashed-dotted lines correspond to 4, 5, 6 and 7 model hours.

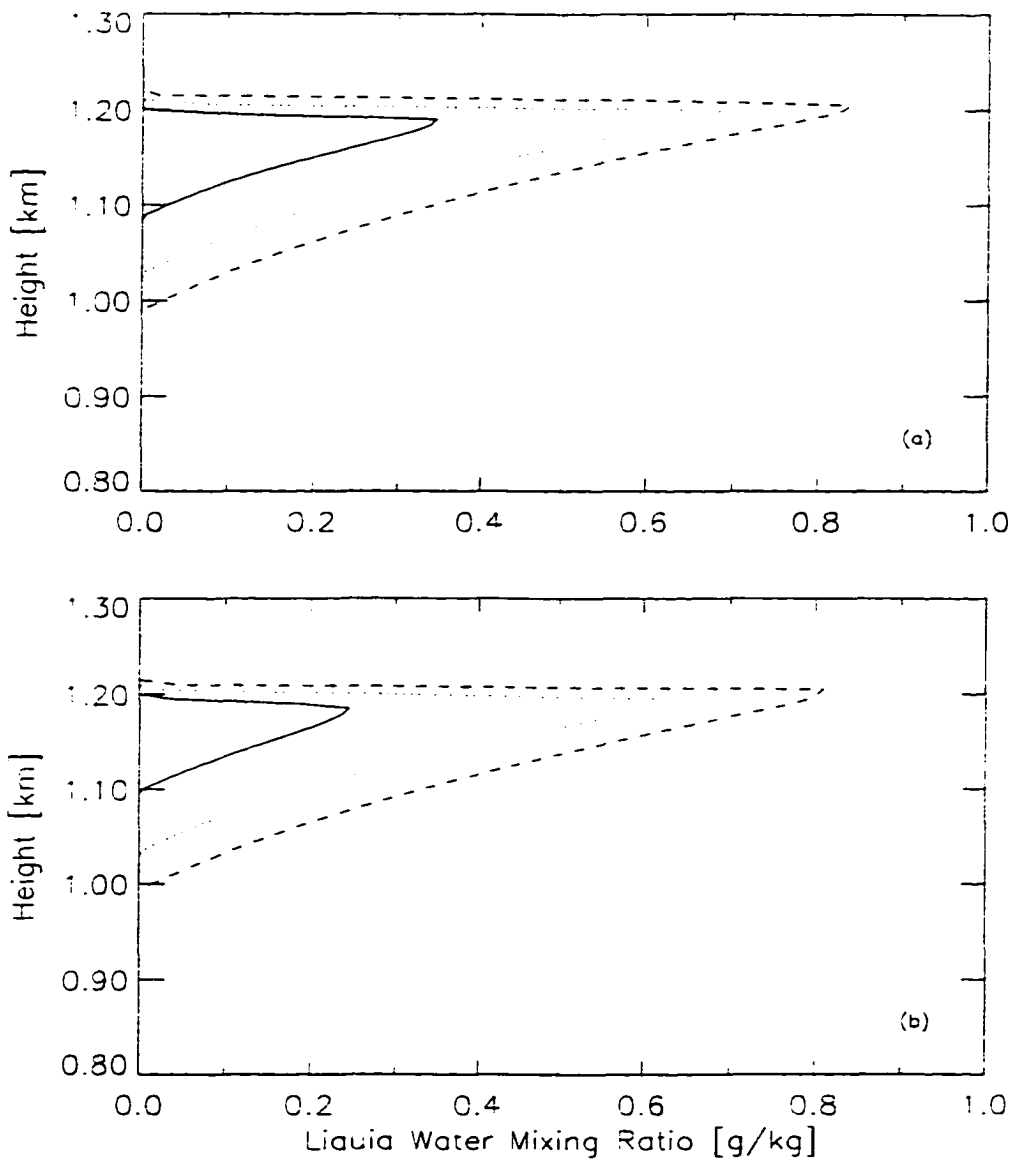

Figure 5.9. 1-D model simulation with the radiative scheme DISORT and the cloud bulk parameterization. (a) simulation with radius 5 μm (DS-BK5); (b) simulation with radius 10 μm (DS-BK10). Solid, dotted and dashed lines correspond to 5, 6 and 7 model hours.

Comparing the simulations of DS-BK5 and DS-BK10 (Figure 5.9) with the simulation of DS-MS in which detailed cloud microphysics is included (Figure 5.7 b), we note that the cloud forms two hours later in simulations DS-BK5 and DS-BK10 than in simulation DS-MS. After the cloud forms, the LWC in the simulations with cloud bulk parameterization develops faster than in the one with detailed cloud microphysics.

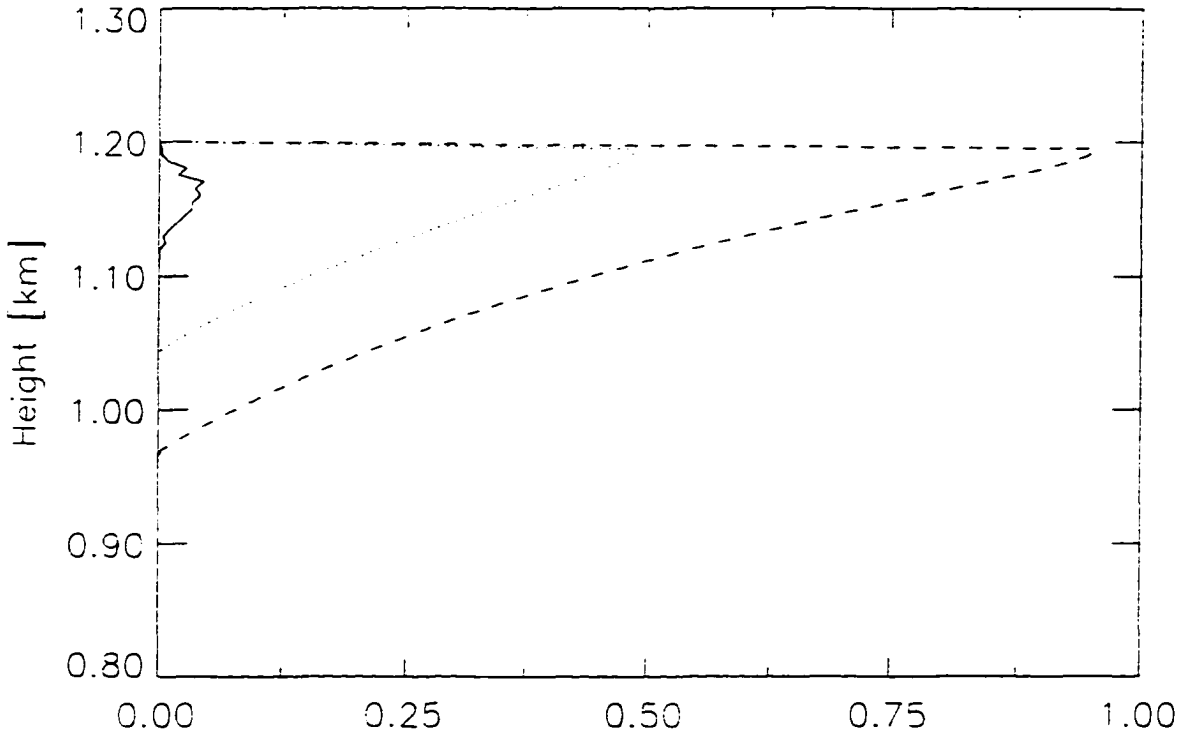

Figure 5.10. Liquid water mixing ratio in the one-dimensional model simulation with HG as the infrared radiative scheme and with the cloud bulk parameterization. Solid, dotted, and dashed lines correspond to 7, 8 and 9 model hours.

When the HG infrared radiative scheme and the cloud bulk parameterization (simulation HG-BK) is adopted in the 1-D radiative-convective model, the cloud forms much later. Figure 5.10 presents liquid water mixing ratio in a nine hour simulation with the BULK cloud parameterization and HG radiative scheme. The cloud initially forms at six model hours. After the cloud forms, it develops faster than in the other simulations,

and the LWC is about 0.95 g/kg after the cloud develops for four model hours.

5.5 Simulation with the LES model

The large eddy simulation is a useful tool for investigating the impact of turbulence on 3-D motions because it can provide realistic simulations of the turbulent boundary layer. LES results can be used to test, reject or verify the simulations done with other simpler models. In this section a LES model will be used to evalute the 1-D radiative-convective model and to assess the merit of the simplified vertical mixing adopted in the convective adjument scheme.

The LES model includes detailed dynamics and is based on a dynamical framework taht follows the Stanford group (e.g., Moin et al., 1978; Moin and Kim, 1982). It was described in detail by Moeng (1984). The model include the DISORT scheme for computing solar radiative warming rates and the HG scheme for computing infrared radiative cooling rates. A bulk parameterization scheme is adopted for simulating the cloud processes. A detailed description of the LES model is provided in Appendix B.

The LES simulation is made in a horizontal domain of 2 × 2 km. The model top is taken to be at 2 km to minimize the effect of gravity waves since the cloud layer is expected to form at about 1.2 km. The horizontal and vertical resolutions are 50 m and 25 m, respectively, and the time step is 0.5 second.

The purpose is to compare the one-dimensional and the three-dimensional simulations. To this end a four-hour simulation is made with the LES model in this section. The initial data adopted for the LES simulation is the same as those used for the simulation labeled HG-BK in the previous section. The simulation results of LES and HG-BK will be compared.

The cloud forms at about two model hours in the LES model simulation, which is earlier than simulated by the 1-D model using with the same radiative schemes and the same cloud bulk parameterization scheme. It suggests that three dimensional turbulence is conductive to cloud formation. The vertical profiles of LWC and temperature are

shown in Figure 5.11. Cloud liquid water increases to 0.4 g/kg after the cloud layer develops for two hours. During this period the cloud layer is lifted 100 m, which is more than the lifting simulated with the 1-D model, which includes no explicit cloud top entainment process. The temperature in the cloud layer decreases fast after the cloud forms (Figure 5.11 b). The temperature inversion at the cloud top also develops fast. The temperature jump at the inversion layer is about 2.5 K after the cloud develops for two model hours.

Figure 5.12 shows the x-z cross section of the vertical velocity at four model hours. Several typical eddy scales exist at different altitudes. The dominant eddies have a horizontal scale of about 0.5 km. Between 0.9 and 1.3 km (the cloud layer) the motion scales are large with diameters about of 0.5 km. Different vertical mixing exists at different heights. Strong vertical motions range from -1.4 to +1.6 m/s and appear within the cloud layer between 0.9 and 1.3 km. The vertical motion is significant only within the cloud layer (a well-mixed layer). This suggests that the convective adjustment scheme is capable of capturing the main features of the boundary layer. The maximum vertical motion appears near the cloud top at about 1.25 km. There are cold plumes sinking through the upper cloud layer, which suggests that the cloud top cooling is important in the maintenance of the cloud layer.

The vertical motion may also be represented by the vertical turbulent kinetic energy (TKE) (Figure 5.13). Large vertical TKE appears in the height between 0.9 and 1.3 km where strong vertical mixing happens. The largest vertical TKE occurs below the top of the cloud layer at around 1.1 km in height, where strong vertical motions exist.

There are three maxima in the horizontal TKE. Large values for the horizontal TKE appear at the top and the base of the cloud layer. This occurs because the turbulent flow impinges on a stable layer and thus the vertical energy component yields to the horizontal component (Moeng, 1986). The maximum near the surface is due to the strong wind shear.

Figure 5.14 shows vertical fluxes of liquid water static energy and total water. The

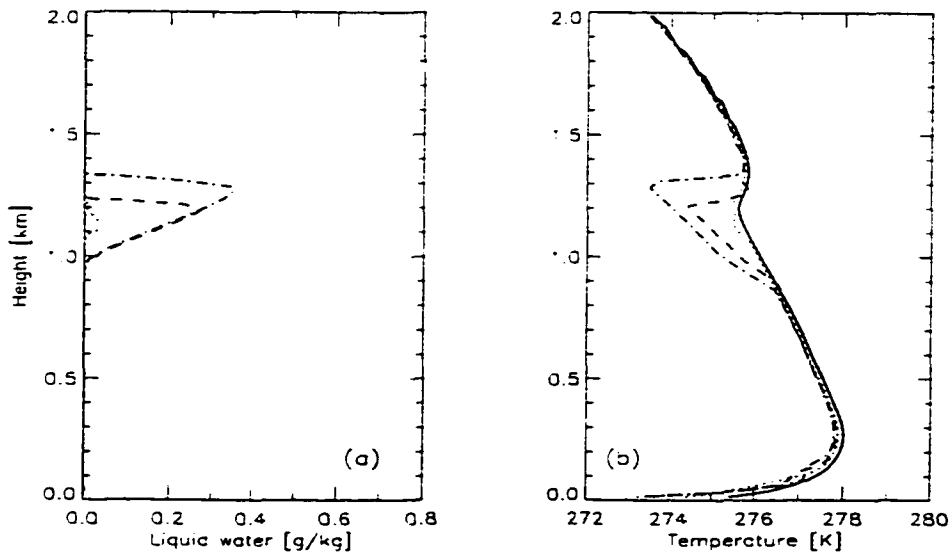

Figure 5.11. LES Simulation. (a) Liquid water [g/kg]; (b) temperature [K]. Solid line is the initial temperature. Dotted, dashed and dashed-dotted lines correspond to 2, 3 and 4 model hours.

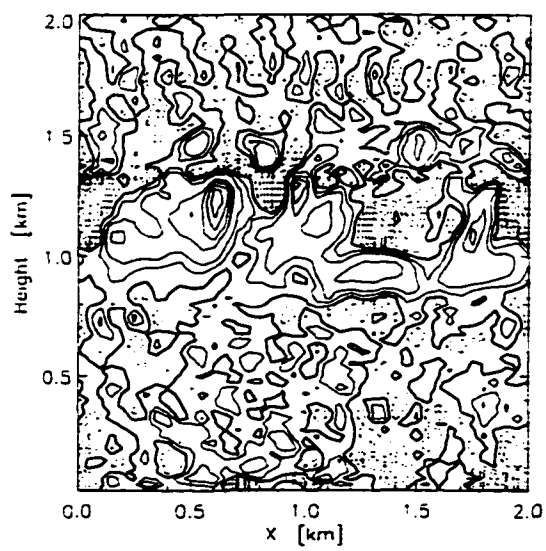

Figure 5.12. LES Simulation. Vertical velocity field of x-z cross section at 4 hours simulation. Y = 1 km. Unit is m/s. Contours range from -1.4 to 1.6 with an interval of 0.2 m/s. Solid line is $w > 0$; dotted is $w < 0$; heavy solid line is $w = 0$.

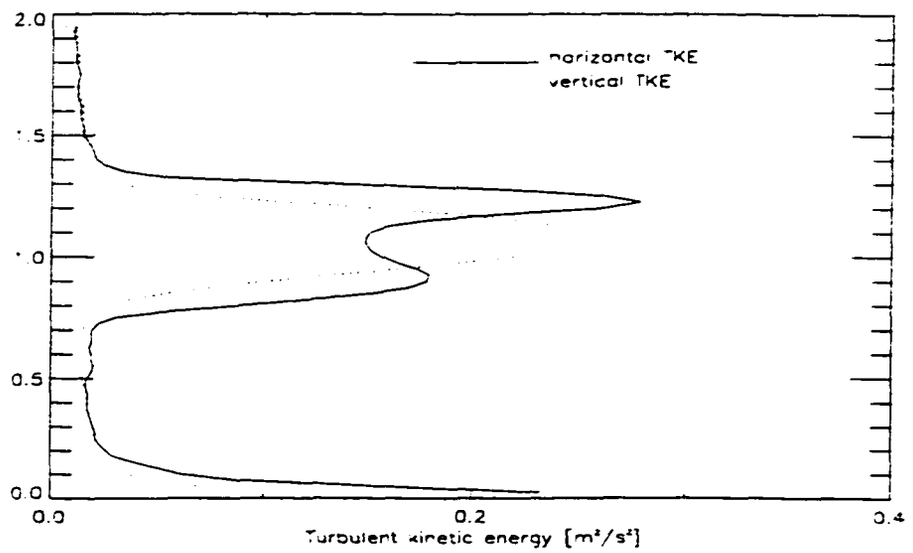

Figure 5.13. Turbulent kinetic energy averaged from 3 to 4 hours. The solid and dotted lines are horizontal and vertical TKE, respectively.

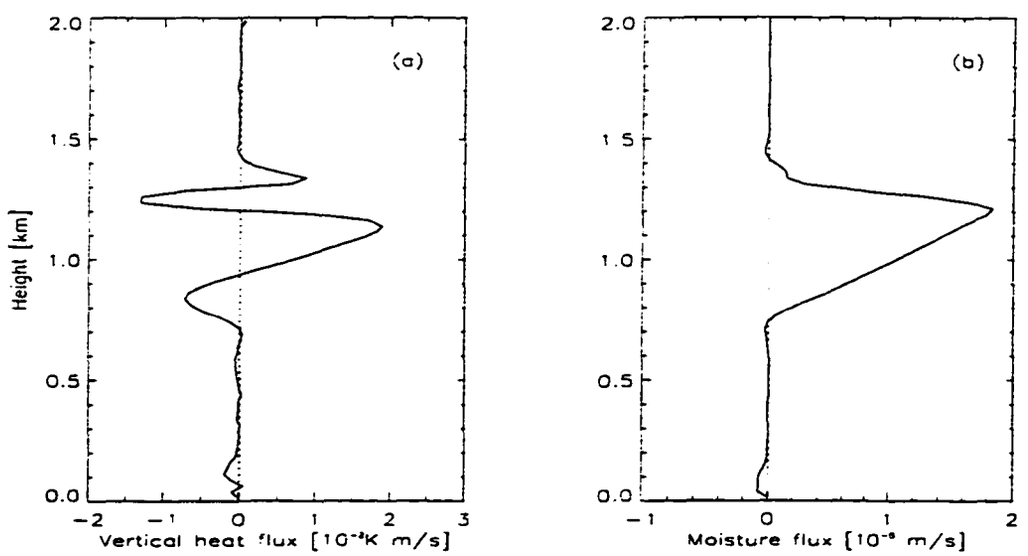

Figure 5.14. (a) Vertical flux of liquid water static energy (10^{-2} K m/s); (b) vertical flux of total water (10^{-4} m/s).

vertical flux of liquid water static energy represents the vertical heat transport. Significant vertical tranport of heat and moisture appears only within the cloud layer between 0.9 and 1.3 km where strong vertical mixing occurs. The vertical transport is very small at other levels. This also suggests that the convective adjustment scheme employed in the 1-D model is capable of capturing the main features of the vertical heat and moisture tranports in the cloudy Arctic boundary layer.

5.6 Summary

Two schemes for computing infrared radiative cooling, two cloud parameterization schemes, as well as a 1-D radiative-convective model and a 3-D LES model were compared in this chapter.

The two radiative schemes both capture the main impact of a humidity gradient on the infrared cooling in a cloud-free atmosphere. The DISORT scheme yields stronger infrared cooling caused by the humidity gradient. Therefore, the cloud forms earlier in the simulation with the DISORT scheme than with the HG scheme. The HG scheme yields larger surface radiative cooling.

After a cloud layer forms, the two radiative schemes provide similar profiles of infrared cooling. Both schemes provide strong cloud top cooling. The maximum cooling computed by the two schemes appears at similiar altitudes. The HG scheme provides stronger maximum cloud top cooling.

When the bulk cloud parameterization scheme is used in the 1-D model, the cloud layer forms later but develops faster after formation than when the detailed cloud microphysics scheme is used.

The cloud layer forms earlier in the LES model than in the 1-D model using the same radiative modules and the same cloud bulk parameterization scheme. This suggests that three dimensional turbulence may help trigger cloud formation. The LES results suggest that strong vertical motion appears only within the cloud layer. Strong vertical transport of heat and moisture also occur only within the cloud layer. This suggests that

the convective adjustment scheme adopted in the 1-D model captures the main features of the vertical heat and moisture transport in the cloudy Arctic boundary layer.

Cloud top lifting is somewhat more pronounced in the LES simulation than in the 1-D simulation since no explicit cloud top entainment process is included in the 1-D model.

Chapter 6

Structure of the Cloudy Boundary Layer: Large Eddy Simulations

6.1 Introduction

The role of low-level Arctic stratus clouds (ASCs) in the global climate system remains one of the big uncertainties in global climate studies since it is difficult to simulate these clouds in global climate models (e.g., Randall et al., 1985). These problems are at least partly due to the fact that the physical processes at work in the Arctic are so poorly understood that the parameterizations for ASC processes adopted in climate models may be not appropriate. ASCs are a prevalent feature in the Arctic during the summer months from May through September (Huschke, 1969; Vowinckel and Orvig, 1970). They are important modulators of local climate and perhaps even global climate since they have an important influence on the vertical transfer of heat, moisture and momentum, and thus affect the melting rate of the pack ice.

ASCs occur within the lower atmosphere generally below 2 km. These clouds typically show large horizontal homogeneity. It has been reported that their mean horizontal

extent is from several hundred kilometers to 2000 km in extreme cases (Dolgin 1960). They are tenuous, with thicknesses of a few hundred meters and are frequently observed to be laminated or comprised of two or more separate, well-defined layers (Jayaweera and Ohtake, 1973; Herman, 1977). One significant feature of ASCs is their long life-time. They may persist for several days, but the reason for their "endurance" is not well understood. Herman (1975) suggested that the persistence of ASCs is due to the absence of cloud dissipation mechanism (e.g., precipitation, radiative heating, convective heating of the boundary layer, and large-scale synoptic activity).

Proper representation of the structure of the boundary layer with multiple cloud layers in climate models is also important for accurate determination of surface radiative fluxes. Few studies have been undertaken to investigate the mechanism responsible for the formation as well as the maintenance of the multiple cloud layers. Using a 1-D second-order turbulence closure model, Mcinnes and Curry (1995a) and Cotton et al. (1995) studied a case with multiple cloud layers and suggested that the cloud top radiative cooling is important for the maintenance of multiple cloud layers. Olsson et al. (1998) discussed the influence of cloud microphysics on the boundary layer structure using a two-dimensional model and found that both simulations that did and did not include the effects of drizzle showed that the higher CCN concentrations produced a cloud with larger reflectivity and absorptivity, but also produced eddies that were weaker than with lower CCN concentrations.

Large eddy simulation (LES) is a useful tool to investigate boundary layer turbulence because it can provide accurate simulations of 3-D motions. The concept of LES is to simulate explicitly the large eddies, which contain most of the energy and dominate the turbulent fluxes within the palnetary boundary layer (PBL), and to parameterize the subgrid-scale motions, which contain less energy and are less important in our studies.

With a LES model, Zhang and Filyushkin (1995) successfully simulated two cases of ASC boundary layer. The physics of the maintenance of multiple cloud layers was investigated by Zhang et al. (1997, 1998a) who used a LES model to successfully simulate

a case with multiple cloud layers, and to investigate the maintenance as well as the initial evolution of the cloud layers. The results suggested that the multiple cloud layers are primarily maintained by longwave radiative cooling, and that vertical heat transport effectively counteracts the radiative cooling.

In this chapter, I will simulate a case with two cloud layers observed on June 28, 1980 during the Arctic Stratus Experiment with an LES model. A detailed description of the LES model is provided in Appendix B. The goal of this study is to examine the three dimensional structure of the ASC boundary layer as well as the dynamical properties of the clouds. The persistence of the multiple cloud layers and the roles of solar radiation and large scale motion are also discussed.

6.2 Initial data and simulation design

The initial data of the following simulations are based on the observational data obtained on June 28, 1980 during the Arctic Stratus Experiment as described by Tsay and Jayaweera (1984), Curry et al. (1988), and in Chapter 1. Figure 6.1 shows the vertical profiles of the initial data for the two nearly parallel layers of stratus clouds observed. The upper cloud layer had an average thickness of about 376 m with its top near 1.2 km and base at 0.8 km. It was capped with a strong temperature inversion and significant moisture reduction, and it had a maximum liquid water content of about 0.6 g/kg. The lower cloud formed within a very stable layer near the surface. Its top was at about 110 m, its thickness was 80 m, and its maximum LWC was about 0.1 g/kg. Figure 6.1 (d) shows the potential temperature. Between the two cloud layers, a weak stably-stratified layer exists, and the whole boundary layer is stably-stratified.

The base simulation is made in a horizontal domain of 2×2 km. Periodic boundary conditions are adopted in the horizontal. The model top is at 2 km with a rigid lid. Since the clouds are expected to appear at around 1.2 km, the 2 km model top will prevent spurious reflections of gravity waves. The lower surface is a material surface across which equations describing fluxes of heat, moisture and momentum are solved following Moeng

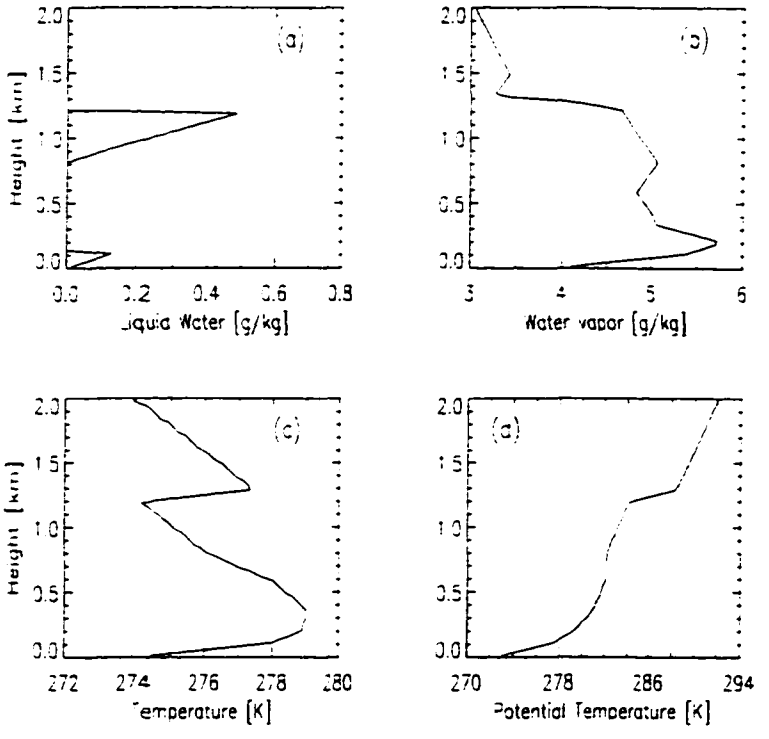

Figure 6.1. Initial data. (a) Liquid water mixing ratio [g/kg]; (b) water vapor mixing ratio [g/kg]; (c) temperature [K]; (d) potential temperature [K].

(1984). The horizontal and vertical resolutions are 50 m and 25 m, respectively, and the time step is 0.5 second.

The simulation is integrated forward for 3 hours. The results shown below were obtained at the end of the 3-hour simulation. The ground surface temperature was set to 273.15 K, and the large scale vertical velocity was set to 0 m/s in the base simulation.

6.3 Simulation results

6.3.1 The ASCs-capped boundary layer

Figure 6.2 shows the x-z cross section of the vertical velocity. The general pattern of eddies shows that the upper cloud layer is largely dynamically decoupled from the lower

layer. Eddy scales and vertical velocities are much smaller in the lower cloud layer than in the upper cloud layer.

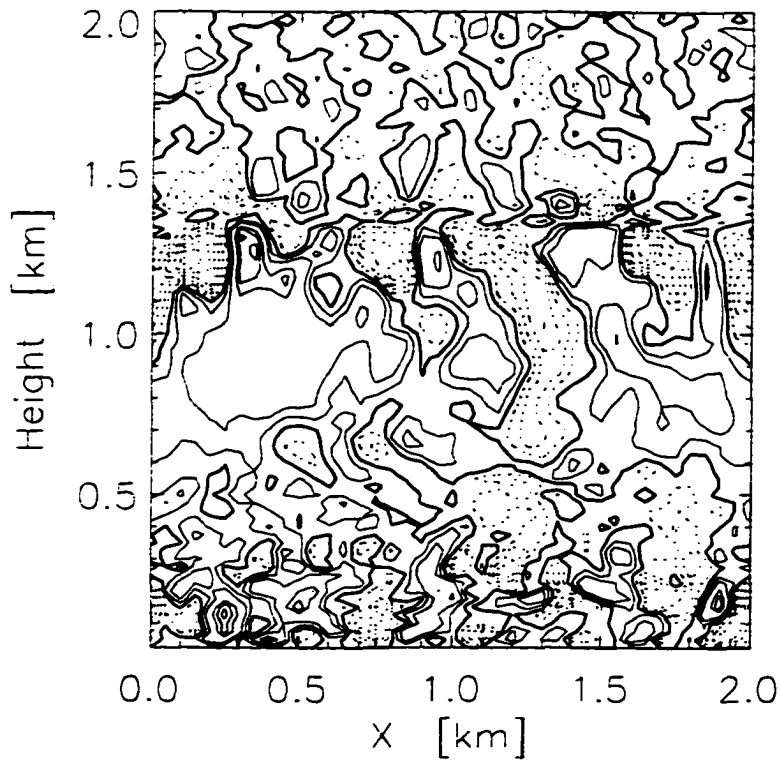

Figure 6.2. Vertical velocity field of x-z cross section at 3 hours simulation. Y = 1 km. Unit is m/s. Contours range from -1.4 to 1.2 with an interval of 0.2 m/s. Solid line is w > 0; dotted is w < 0; heavy solid line is w = 0.

Different vertical mixing exists within the two cloud layers. Strong vertical motions appear in the upper cloud layer, maximizing near the cloud top. The vertical motion persists down to 0.6 km. There are cold plumes sinking through the upper cloud layer, suggesting that the cloud top cooling is important for the maintenance of the cloud layer. Strong vertical motion also occurs below 0.3 km, where the lower cloud layer is located. In contrast to the upper cloud layer, the eddies reach above the top of the lower cloud layer.

Several typical eddy scales exist at different altitudes. The dominant eddies have a horizontal scale of about 1 km. Between the two cloud layers from 0.5 to 1.2 km in

height, which is the well-mixed layer, the motion scales are large with a diameter of about 1 km. Strong downdrafts penetrate through the depth of this well-mixed layer to 0.5 km. There are secondary circulations with eddy scales of about 0.5 km confined to the cloud layer. The eddy scales are small right above the top of the cloud layer where a strong temperature inversion exists. The eddy scales are also small in the lower cloud layer below 0.5 km in height. Their dominant scales have diameters of about 0.2 km. In the simulation, the horizontal resolution is 50 m. It is fine enough to study the eddies in this case. The eddy scales above the temperature inversion layer are about 200 m. The fluctuations at this height are actually internal gravity waves.

Figure 6.3 shows the horizontal distribution of vertical velocity at the upper cloud layer. Near the top of the upper cloud layer (1.225 km), the vertical velocity field (Figure 6.3 a) shows that the downdraft tends to be narrower than the updraft and better organized. This suggests that the radiative cooling dominates the turbulence near the cloud top. Comparing the cloud-top velocity field with that right below the cloud base (Figure 6.3 b), one can see that not all of the downdrafts mix through the depth of the mixed layer.

Figure 6.4 shows the horizontal distribution of the vertical velocity near 200 m, which is near the top of the lower cloud layer. The distribution is completely different from that in the upper cloud layer, not only in terms of downward or upward motion but also in terms of the motion scales. Figure 6.5 shows mean profiles of the horizontal velocities. Strong wind shear exists only below the altitude of 300 m. The wind shear is small above 300 m.

Figure 6.6 (a) shows the x-z cross section of temperature distribution. Strong temperature inversion appears at the top of the upper cloud layer. The temperature iso-lines between 500 m and 1275 m are almost horizontal. This indicates that strong vertical mixing happens and that high horizontal homogeneity exists in these layers. The temperature distribution is less horizontally homogeneous in the lower cloud layer (below 300 m). This also indicates the two cloud layers are thermally decoupled. The x-z cross-

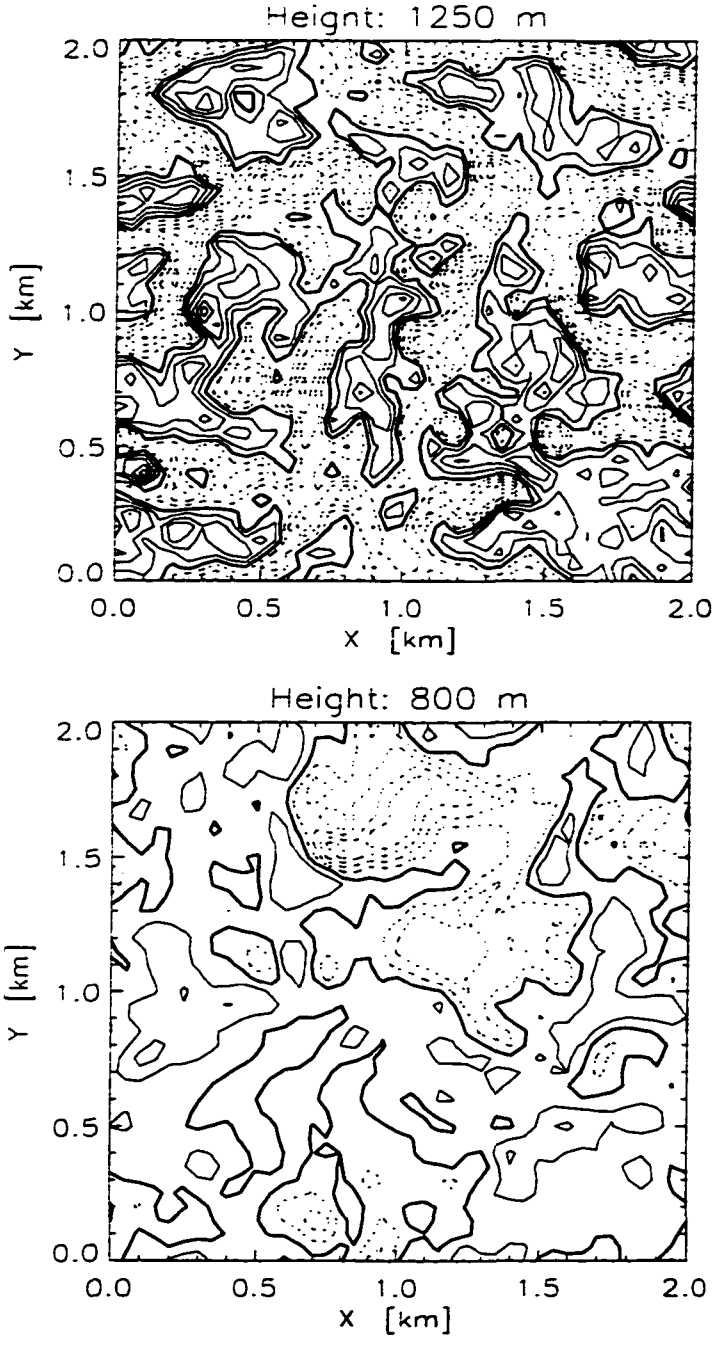

Figure 6.3. XY cross section of the vertical velocity after 3 hours of simulation. Unit is m/s. Contours are with an interval of 0.3 m/s. Solid is w > 0; dotted is w < 0; heavy line is w = 0. (a) Near the top of upper layer cloud (z = 1225 m. Contours range from -1.5 to 1.5); (b) just below cloud base (z = 800 m. Contours range from -1.2 to 0.5 m/s).

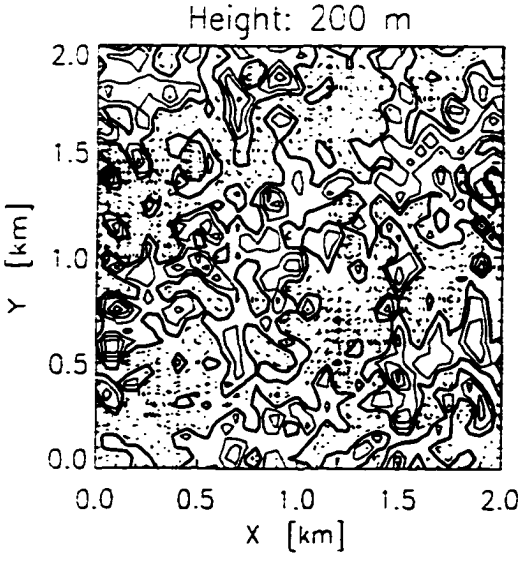

Figure 6.4. XY cross section of the vertical velocity within the lower cloud layer (z = 200 m) at 3 hours model time. Unit is m/s. Contours range from -1.5 to 1.5 m/s with an interval of 0.3 m/s. Solid is w > 0; dotted is w < 0; heavy line is w = 0.

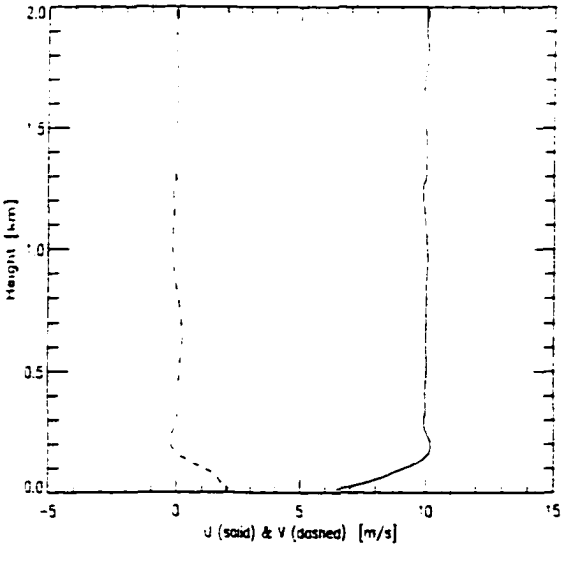

Figure 6.5. Vertical profiles of horizontal velocity u (solid line) and v (dotted line) at 3 hours of simulation. Unit: m/s.

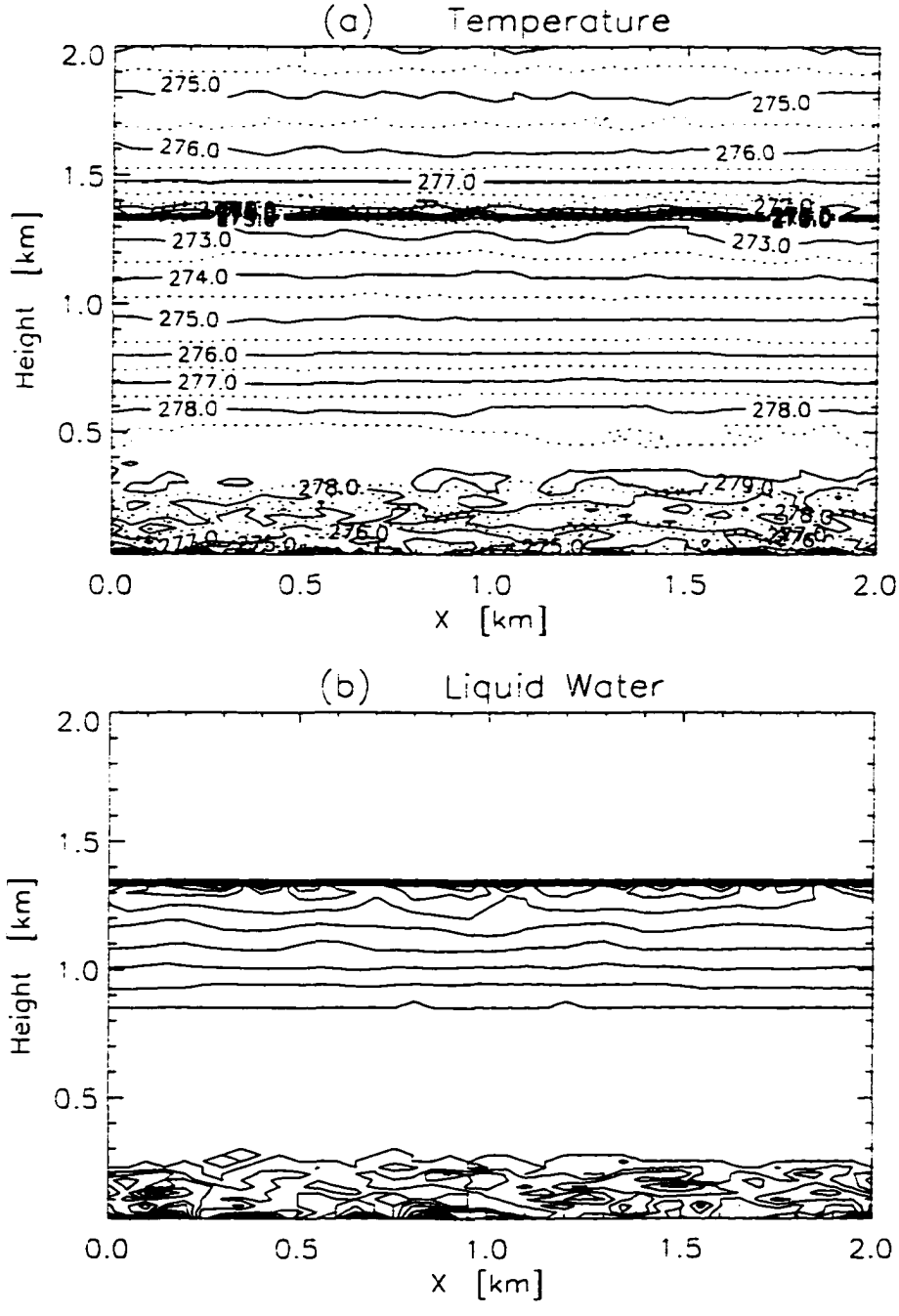

Figure 6.6. XZ cross section at 3 hours model time. Y = 1 km. (a) Temperature with unit K (contours range from 271 to 279 K with an interval of 1 K). (b) Liquid water mixing ratio with unit g/kg (contours range from 0.1 to 0.8 g/kg with an interval of 0.1 g/kg).

section of liquid water distribution (Figure 6.6 b) indicates high horizontal homogeneity within the upper cloud layer and less horizontal homogeneity within the lower cloud layer.

The horizontal homogeneity of both temperature and cloud water suggests that the cloud structure can be considered as horizontally homogeneous while studying their influence on radiative budgets. It also means that 1-D models are expected to be useful tools.

6.3.2 The maintenance of the cloud layers

The evolution of cloud liquid water during a three-hour simulation is shown in Figure 6.7. The upper cloud layer is lifted while the maximum liquid water increases. The life time of the eddies is shown at the cloud top with a time scale of 45 minutes. The cloud top is lifted 75 m and the base is lifted about 25 m (Figure 6.8 a). The cloud liquid water of the lower cloud layer increases in the first 2 model hours and the cloud top also lifted about 50 m. The cloud liquid water decreases during the third model hour.

The temperature near the cloud top continues to decrease (Figure 6.8 b). The maximum decrease appears near the top of the upper layer with a rate of change of -2 K/hour. Corresponding to the lifting of the top of the upper cloud layer, the thermal inversion layer ascends about 75 m. Temperatures in the lower cloud layer also decrease at a maximum rate of about -0.6 K/hour.

Figure 6.9 shows instantaneous radiative warming/cooling rates. Strong infrared cooling occurs at the top of the two cloud layers where significant temperature reduction occurs. For the upper layer, the maximum cooling appears at the cloud top at 1.275 km and is up to -7.9 K/hour. The maximum cooling of the lower layer cloud appears at 0.25 km and is only -0.5 K/hour. Solar warming is much smaller than infrared cooling. Strong solar warming also occurs at the top of upper cloud layer. The maximum warming is about 1.3 K/hour. The profile of the net radiative warming/cooling is very similar to that for the infrared, and the maximum cooling at the top of the upper layer is about

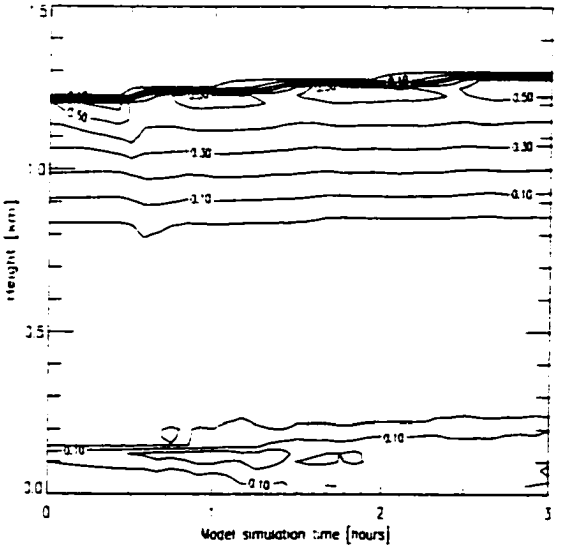

Figure 6.7. Evolution of cloud water over 3 hours simulation. Unit is g/kg. Contour range from 0 to 0.6 g/kg with interval of 0.1 g/kg.

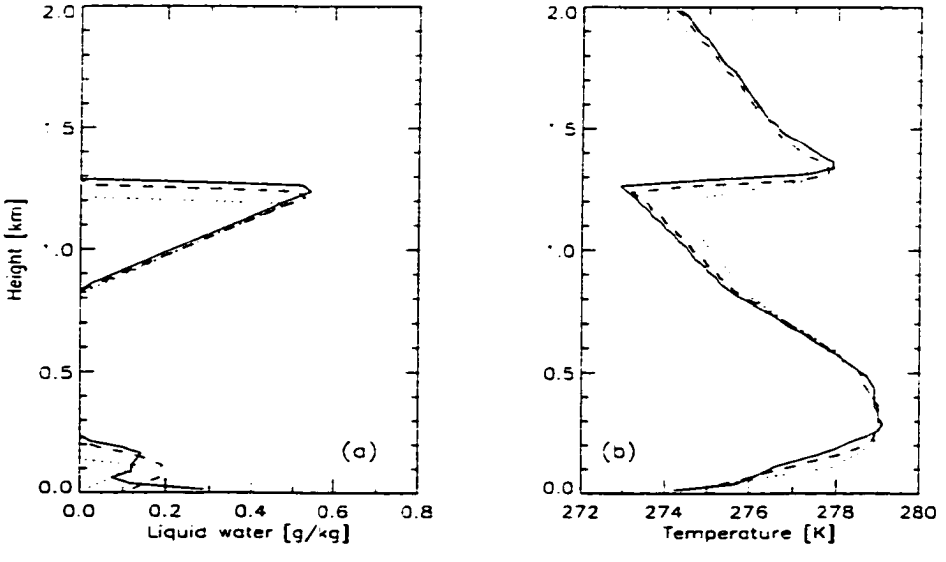

Figure 6.8. Vertical profile. (a) Liquid water [g/kg]; (b) temperature [K]. The dashed and solid lines are after 2 hours and 3 hours of model integration, respectively. The dotted line shows the initial data.

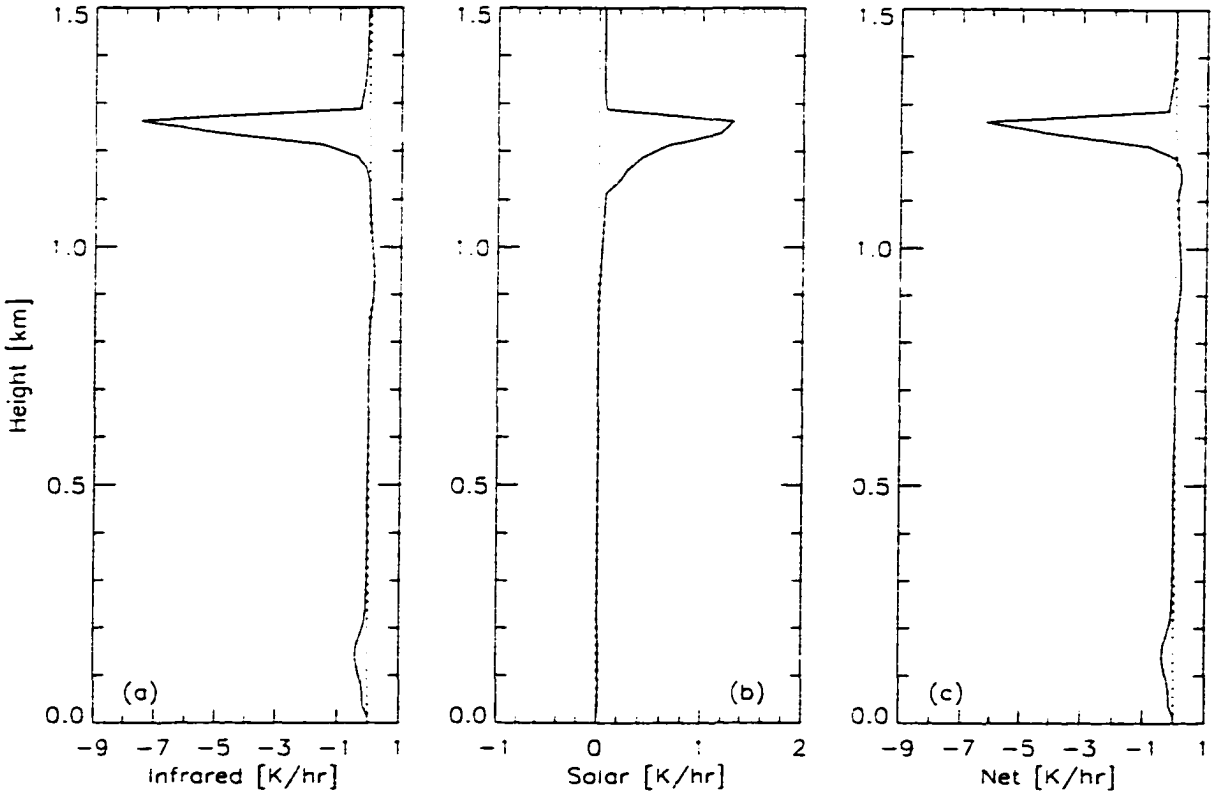

Figure 6.9. Vertical profile of (a) infared radiation; (b) solar radiation; (c) total radiation. Averaged from 2 to 3 hours.

-6.8 K/hour. Inside the upper layer cloud, there is a small net warming. The profile of the net radiative warming/cooling in the lower layer cloud is dominated by the infrared cooling.

6.3.3 Turbulent properties of ASCs boundary layer

Figure 6.10 shows contours of the evolution of turbulent kinetic energy over 3 hours of model integration. During the first 10 to 30 minutes, the simulations were in a spin up mode, that is, the resolved-scale turbulence was not yet established. Energy spin-up takes about 30 minutes of model time. A sudden build-up of TKE occurs at around 1 km in height. After about 60 minutes of simulation time a quasi-steady state is achieved in which fluxes of conserved variables are linear with height in the mixed layer, and

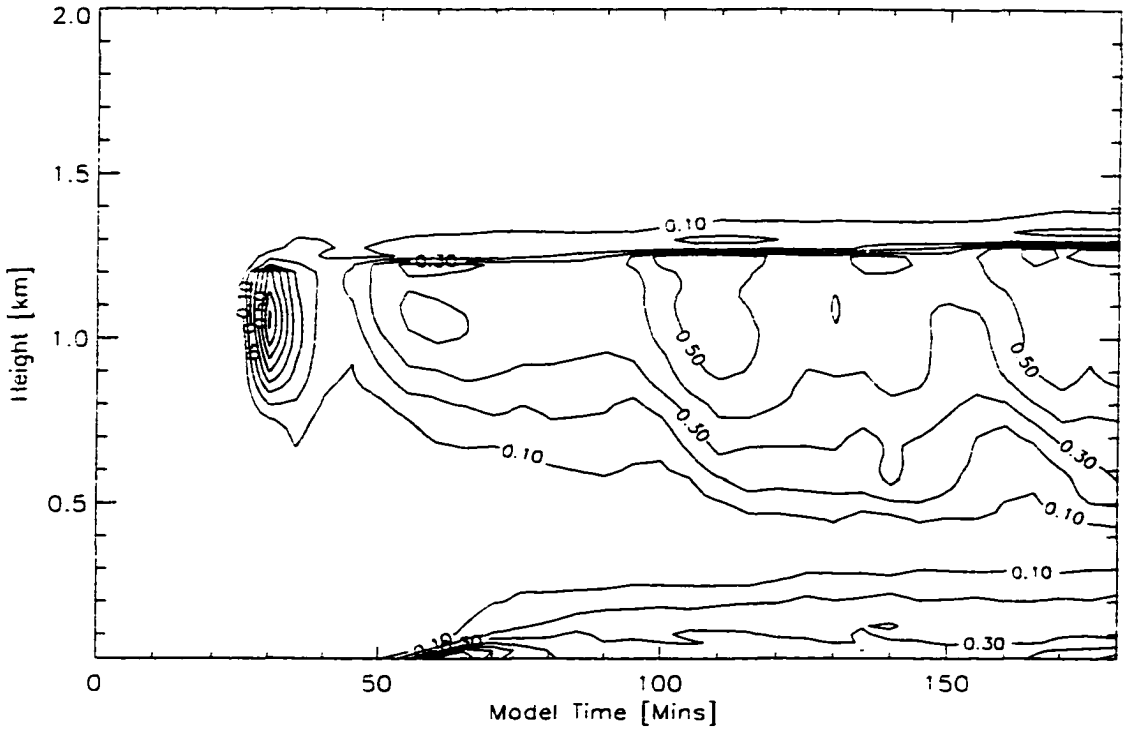

Figure 6.10. Evolution of turbulent kinetic energy over a 3 hours period. Unit is m^2/s^2. Contour interval is 0.1 m^2/s^2.

the turbulence field varies slowly. The TKE decreases significantly at the cloud top. Near the surface, the TKE starts developing around 60 minutes of model time due to the strong surface wind shear. The TKE of the upper cloud layer is transported downward while that of the lower cloud layer is transported upward. At the end of the 3-hour simulation, a TKE minimum still exists between the two layers, which suggests a dynamical decoupling of the two cloud layers.

Figure 6.11 shows vertical profiles of TKE averaged from the 2nd to the 3rd simulation hour. Two maxima are present in the vertical profile of total TKE (Figure 6.11 a). The upper maximum appears near the cloud top and is due to turbulent motions which are driven mainly by cloud-top cooling. The lower maximum occurs near the surface and is wind-shear driven. In between, there is a minimum of the TKE, which suggests a

decoupling of the two cloud layers in agreement with the results of Curry (1986) and Curry et al. (1988). Both resolved and subgrid TKE show two maxima. The magnitude of the subgrid TKE is about 1/5 of the resolved TKE.

Figure 6.11 (b) shows profiles of the horizontal and vertical TKE. There are three maxima in both of the profiles. The large amount of horizontal TKE at the top of the upper cloud layer occurs because the turbulent flow impinges on a very stable layer, and thus the vertical energy component yields to the horizontal component (Moeng, 1986). A maximum appears at the surface due to the wind shear. The largest vertical TKE occurs below the top of the upper cloud layer at around 1.1 km in height, where large-scale eddies exist. A maximum appears around the top of the lower cloud layer. The maxima of both horizontal and vertical TKE occurring right above the upper cloud top are due to trapped gravity waves.

The TKE equation is analyzed to investigate the mechanism responsible for the maintenance of turbulence. Three significant terms of the TKE equation are shown on Figure 6.12. The buoyancy term is the most significant energy production in the upper cloud layer, while it acts as an energy sink below 0.8 km. The vertical transport term behaves opposite to the buoyancy term. It acts as a sink for the upper cloud layer and as a source below 0.8 km. The wind shear term is significant only near the surface in producing TKE. The distribution of turbulent kinetic energy terms in this simulation corresponds well with the observations (Curry et al., 1988).

6.4 Sensitivity experiments

The LES model is used in this section to study the effect of various physical processes and numerical approximations on the structure of cloudy boundary layer. The role of solar as well as infrared radiative transfer and large scale motion are investigated. The effects of model horizontal domain and model vertical resolutions are also examined.

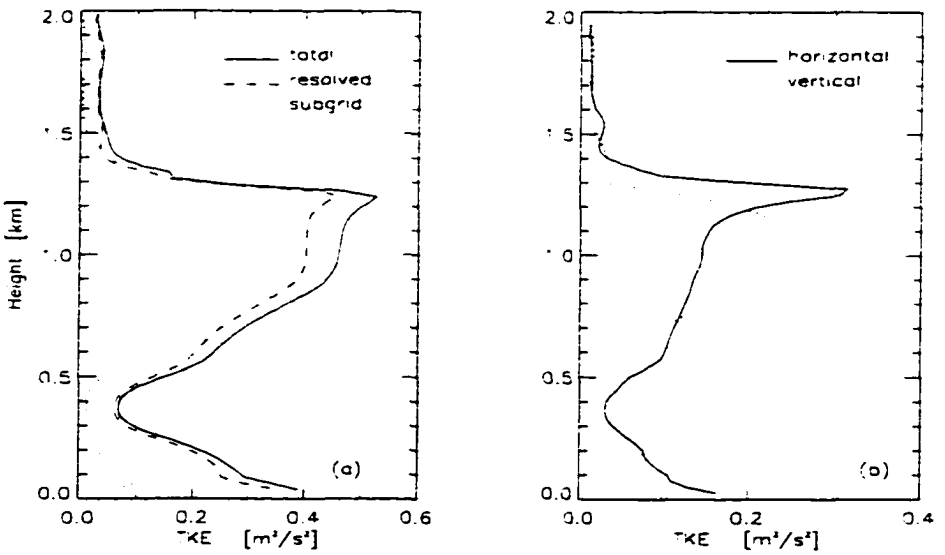

Figure 6.11. Turbulent kinetic energy averaged from 2 to 3 hours. Unit is m^2/s^2. (a) Solid: total; dashed: resolved scale: dotted: subgrid scale. (b) Solid: horizontal; dotted: vertical.

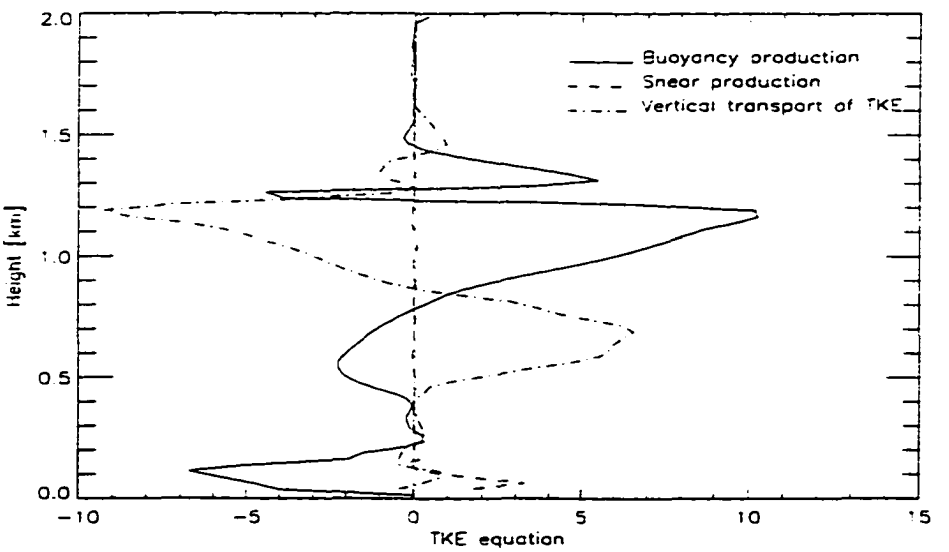

Figure 6.12. Terms in the equation of turbulent kinetic energy. Unit is $10^{-4}\ m^2 s^{-3}$.

6.4.1 The role of radiative transfer

I have already discussed in the last section that radiative cooling at cloud top is the primary driver for the turbulent motion in the boundary layer. Here I will further discuss the effect of solar and infrared warming/cooling. Two simulations are made: one is with only infrared radiation (without solar); the other is without considering any radiation (neither solar nor infrared radiation). The results of these two simulations are compared with those of the base simulation, which considers both solar and infrared radiation.

The time evolution of the TKE and the cloud liquid water in the simulations with only infrared radiation and without considering radiation is shown in Figure 6.13. Comparing with Figure 6.7 and Figure 6.10, we see that TKE is strongest when solar radiation is ignored (only infrared radiation is considered). More cloud liquid water is produced in this case. Without any (solar and infrared) radiation, the turbulent kinetic energy is very small. The cloud liquid water decreases, which means the cloud layer is decaying.

Figure 6.14 shows the vertical profile of liquid water mixing ratio at 3 hours model time. It shows the results of three simulations: base simulation which is with solar and infrared radiation (dashed line), the simulation with only infrared radiation (solid line), and with neither solar nor infrared radiation (dotted line). In the simulation with only infrared radiation, cloud liquid water increases most significantly. In contrast to the results obtained when solar radiation is included, the upper cloud layer develops both upward and downward. In the simulation without both solar and infrared radiation, cloud liquid water is decreasing.

McInnes and Curry (1995a), Olsson et al. (1998) showed similiar results, respectively, in their simulations with 1-D and 2-D models.

6.4.2 The effect of large scale vertical motion

Even if we regard the cloud formation and development as a local process, it will of course not be independent of the large-scale motion of pressure systems and dynamical

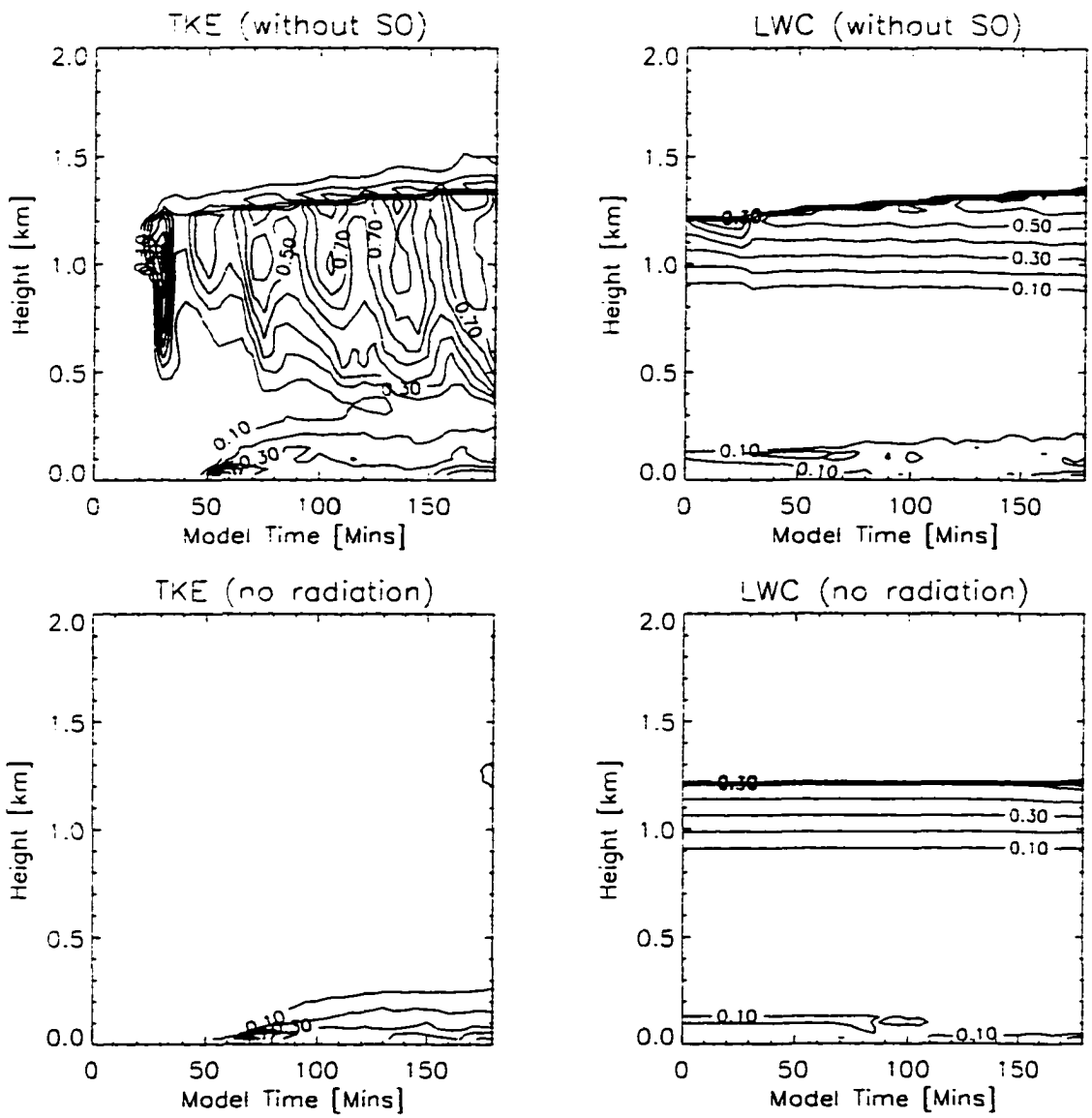

Figure 6.13. Time evolution of turbulent kinetic energy and liquid water mixing ratio. (a) TKE (without solar radiation), $[m^2 s^{-2}]$; (a) LWC (without solar radiation), [g/kg]; (c) TKE (without radiation), $[m^2 s^{-2}]$; (c) LWC (without radiation), [g/kg].

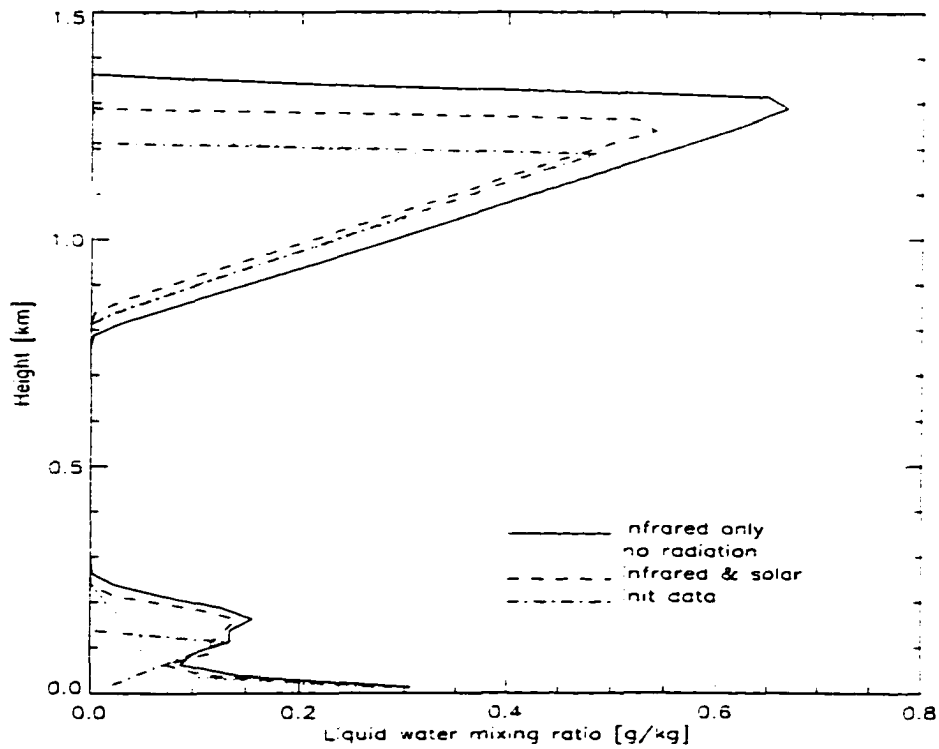

Figure 6.14. Vertical profile of liquid water mixing ratio at 3 hours. Solid: with infared radiation only; dotted: no radiation; dashed: with solar and infrared radiation; dashed-dotted: the initial data.

effects. This large-scale motion is responsible for lifting air and advecting air into the domain under consideration. In order to investigate the effect of large scale motion, four simulations are made with large scale vertical velocities of 0.3, 1.0, -0.3 and -1.0 cm, respectively.

Figure 6.15 shows time evolution of TKE in the four simulations. The results are compared with the base simulation in which large scale vertical motion is ignored. The simulations with downward large scale vertical motion have stronger turbulent kinetic energy. The simulation with a large scale velocity of -0.3 cm/s has the strongest turbulent kinetic energy.

The time evolution of cloud liquid water of the four simulations is shown on Figure 6.16. The simulations with downward large scale vertical motion have large cloud

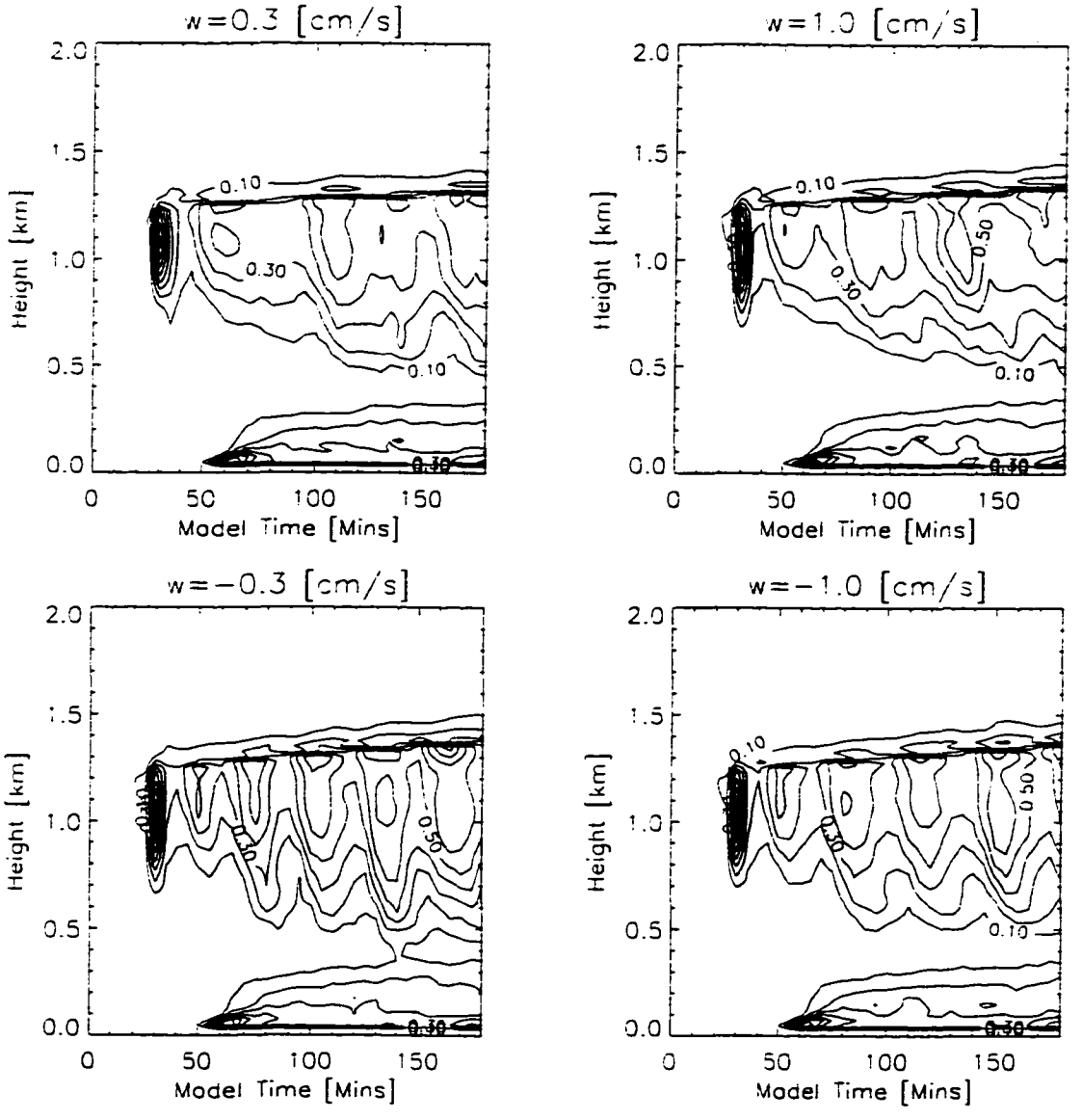

Figure 6.15. Time evolution of turbulent kinetic energy over 3 h of model integration with background velocity set to: (a) w = 0.3 cm/s: (b) w = 1.0 cm/s; (c) w = -0.3 cm/s; (d) w = -1.0 cm/s. Unit is $m^2 s^{-2}$.

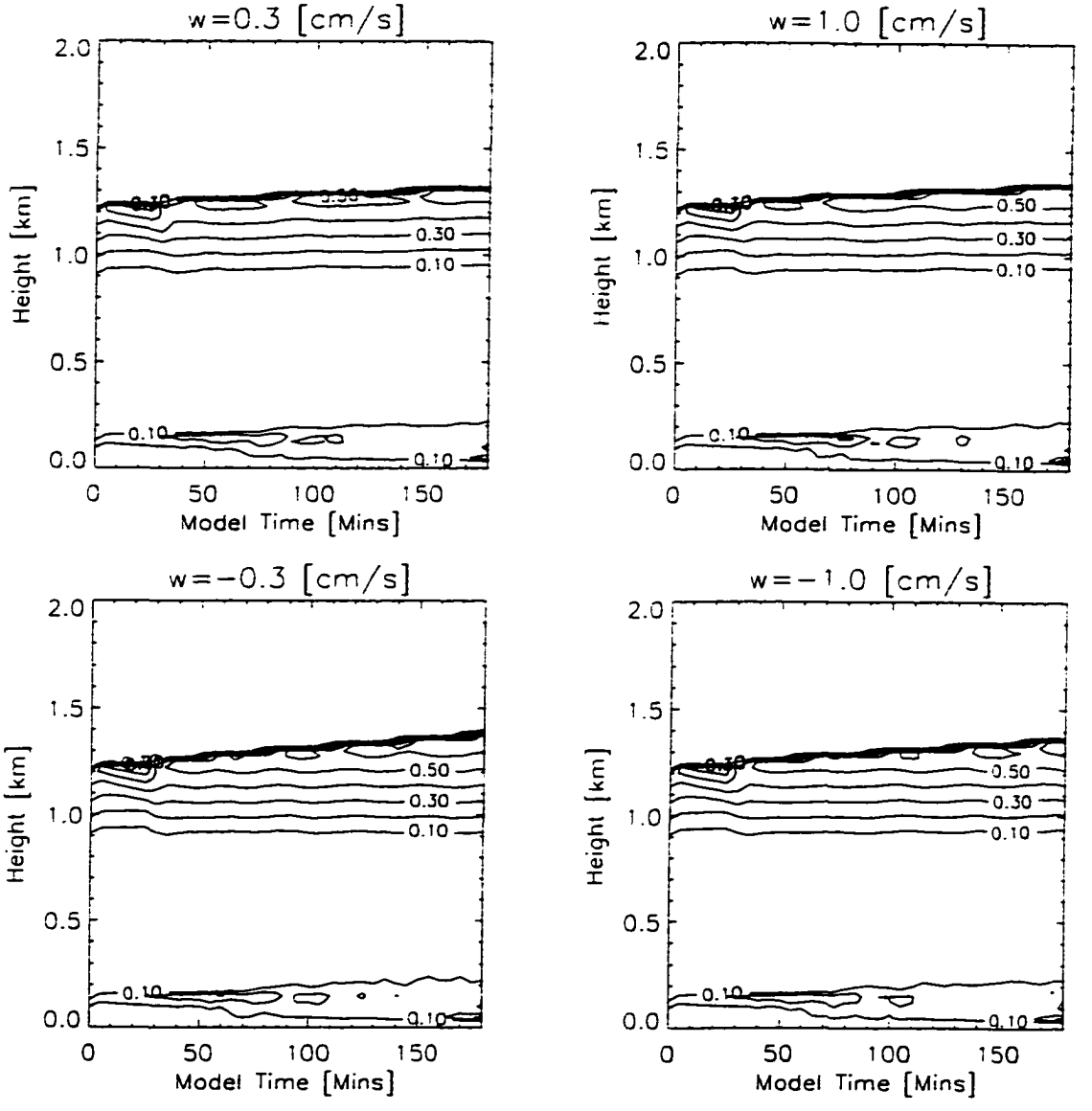

Figure 6.16. Time evolution of liquid water mixing ratio. (a) w = 0.3 cm/s; (b) w = 1.0 cm/s; (c) w = -0.3 cm/s; (d) w = -1.0 cm/s.

liquid water. Therefore, large scale vertical motion seems to enhance cloud development. The simulation with a large scale velocity of -0.3 cm/s has the largest cloud liquid water. This suggests that a small downward large scale motion helps maintain the cloud layer.

Figure 6.17 shows the vertical profile of liquid water mixing ratio at 3 hours model time. The cloud top develops most significantly in the simulation with a large scale velocity of -0.3 cm/s

McInnes and Curry (1995a) made similiar simulations with a 1-D model and suggested that weak rising vertical motion is the most favorable situation to maintain the two cloud layers. Their results differ from our 3-D simulation. It may suggest a limitation of a 1-D model. A 1-D model is unable to consider the effect of 3-D turbulence.

6.4.3 The effect of model resolutions

A fine grid resolution is essential in order to reasonably simulate eddy turbulence since motion scales in ASC boundary layer are small. However, the finer the model resolution is, the more computing time is required for the simulation. To find a reasonable compromise, the effect of vertical model resolutions is examined. A simulation with a vertical grid space of 50 m is made and its result is compared with that of the base simulation. which has a vertical grid space of 25 m.

Figure 6.18 presents the results of two simulations. The vertical profiles of temperature and liquid water mixing ratio are exhibited. The distributions of these parameters with the two resolutions are very similar. The vertical distribution of TKE are also simular (Figure 6.19). However, the vertical heat flux and the water vapor flux of the two simulations are very different (not shown). We may therefore conclude that a 50 m vertical grid is sufficient if our study is focused exclusively on the evolution of the cloud and the interactions between cloud and radiation. A 25 m vertical grid is needed if our aim is to analyze the structure of the cloud-capped boundary layer.

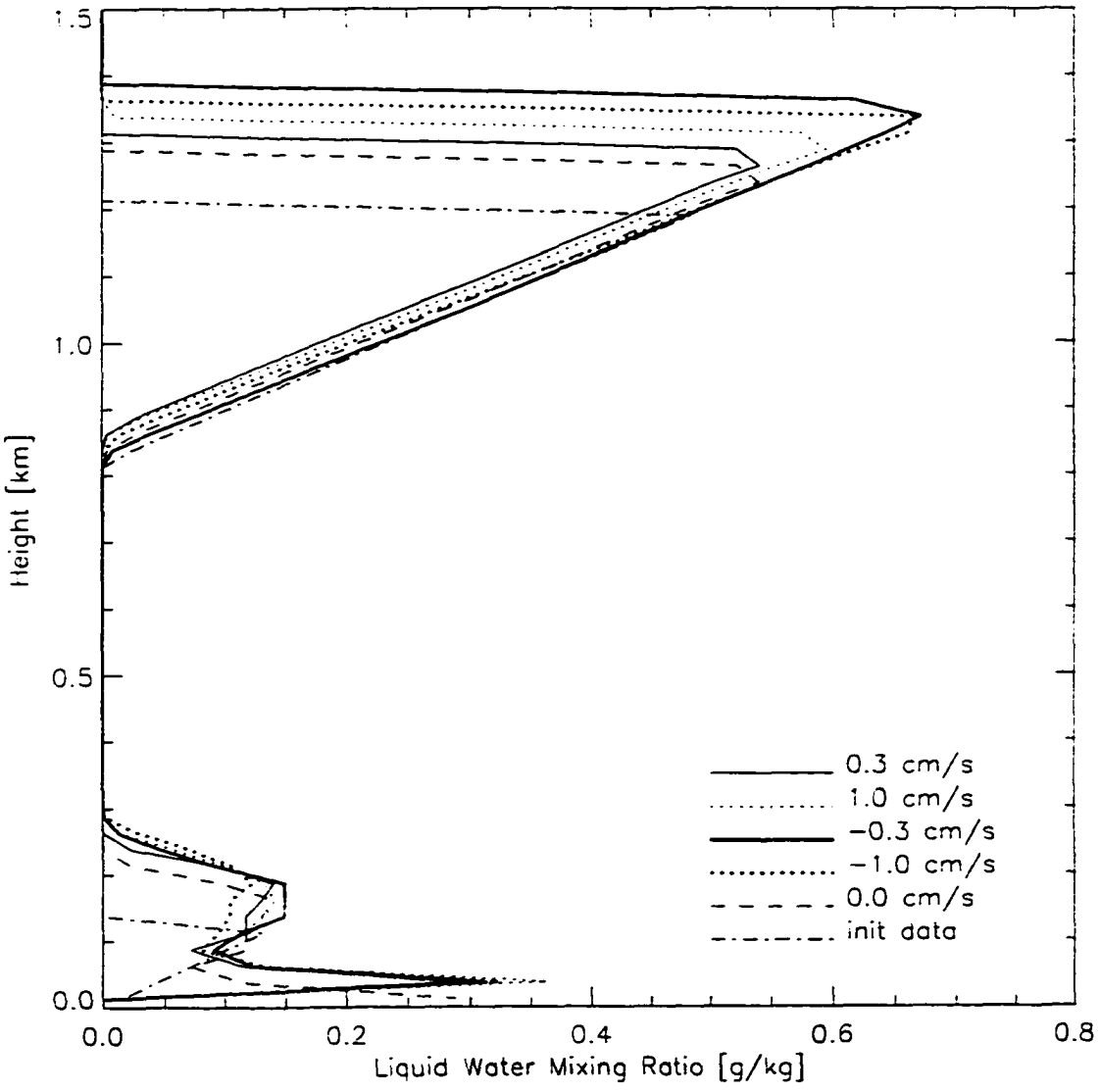

Figure 6.17. Liquid water mixing ratio at 3 hours. Heavy solid: initial data; heavy dotted: w = 0 cm/s; solid: w = 0.3 cm/s; dotted: w = 1.0 cm/s; dashed: w = -0.3 cm/s; dashed-dotted: w = -1.0 cm/s.

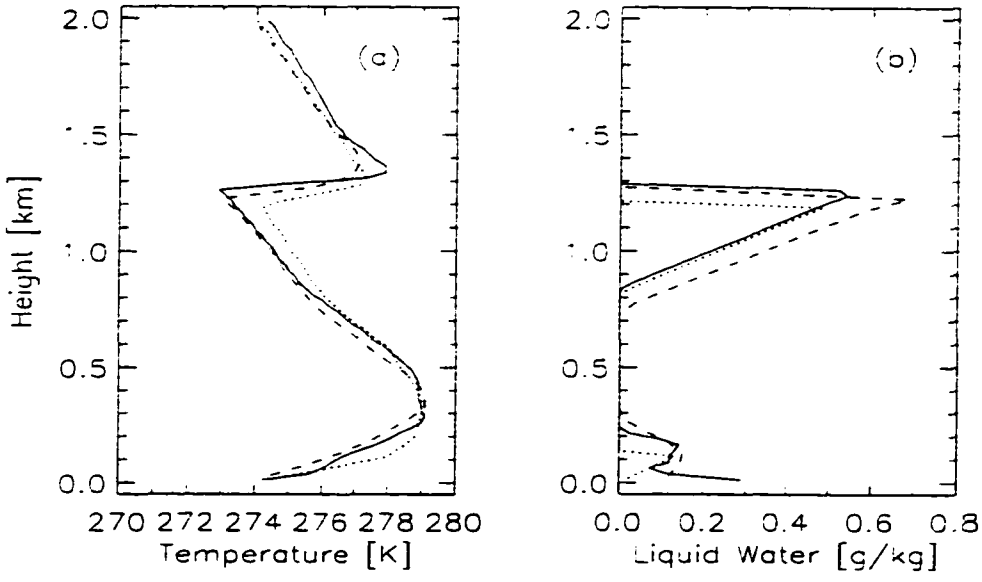

Figure 6.18. Mean profiles at 3 hours model simulation time. (a) Temperature [K]; (b) liquid water mixing ratio [g/kg]. Solid lines are the base simulation which has a vertical grid space of 25 m. Dashed lines are the simulation with a vertical grid space of 50 m. The dotted line is the initial data.

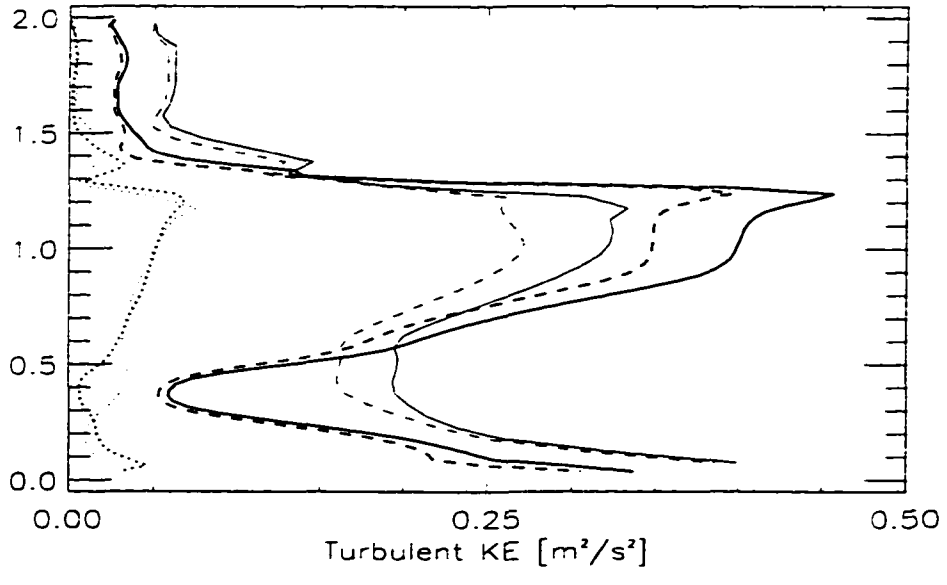

Figure 6.19. Mean profile of turbulent KE averaged over 2 to 3 hours. $[m^2 s^{-2}]$. Heavy: 25 m, light: 50 m. Solid: total TKE, dotted: subgrid TKE, dashed: large eddy TKE.

6.4.4 The effect of model horizontal domain

A disadvantage of LES models is that they are extremely computer time consuming. A simulation with a large horizontal domain requires more computing time. Therefore, we examine the numerical effect of horizontal domains. A simulation for a domain of 3.2 × 3.2 km is made and compared with the base simulation which was a horizontal domain of 2 × 2 km.

Figure 6.20 shows the mean profiles of temperature and liquid water mixing ratio at 3 hours model time. The difference between the two simulations is small. Less cloud liquid water is created with the simulation of 2 × 2 km. The differences in TKE between the two simulations are also small. Less large eddy TKE is created in the smaller domain (Figure 6.21).

Comparing Figure 6.22 with Figure 6.2, we note that the x-z cross section of vertical velocity also shows small difference among the motion scales of the two simulations. The above analyses suggest that a horizontal 3.2 × 3.2 km domain is about as good as a 2 × 2 km domain.

6.5 Summary and conclusion

In this chapter I studied the structure of the ASC-capped boundary layer and the maintenance of the cloudy boundary layer with a large eddy simulation model. The simulated results are compared with observations. The results of the simulation are physically reasonable. Therefore, the 3-D LES model is able to simulate reasonably well the case observed on June 28, 1980.

I analyzed the mean profiles as well as the three dimensional structure of the boundary layer. The LES model successfully simulates the complex structure of the ASC-capped PBL. An image of the three-dimensional eddy structure was obtained. Different scales of eddies exist at different altitudes. The horizontal eddy scales in the convective layer are about 1 km. The scales of eddies around the cloud top are about 100 m. The simulation

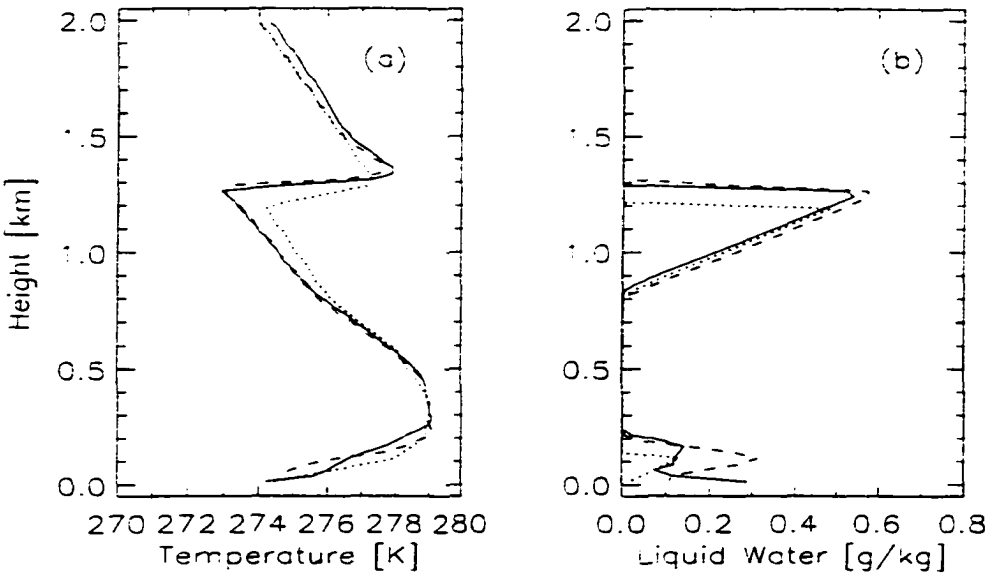

Figure 6.20. Mean profiles at 3 hours model simulation time. (a) Temperature [K]; (b) liquid water mixing ratio [g/kg]. Solid: 2 × 2 km; dashed: 3.2 × 3.2 km.

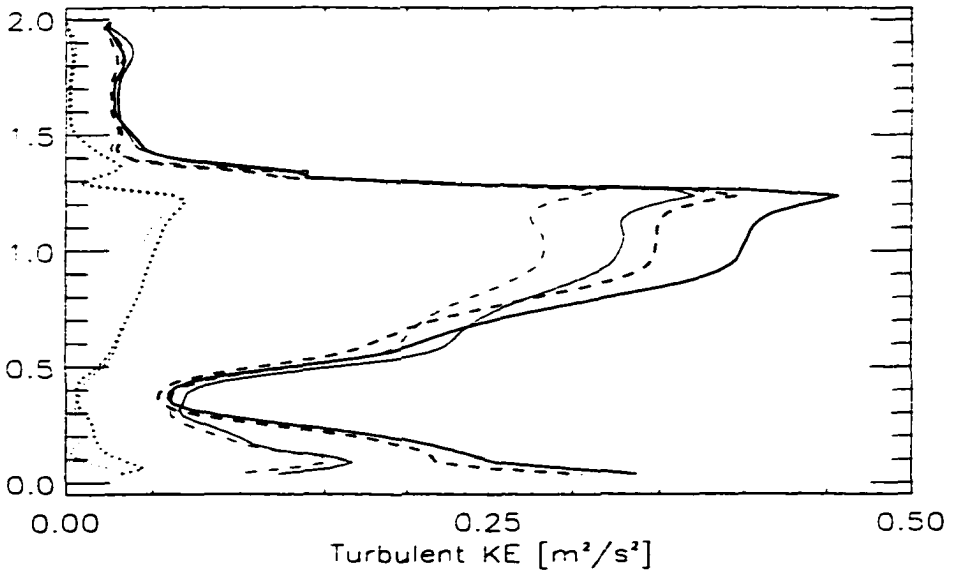

Figure 6.21. Mean profile of turbulent KE averaged over 2 to 3 hours. $[m^2 s^{-2}]$. Heavy: 2 × 2 km, light: 3.2 × 3.2 km. Solid: total TKE, dot: subgrid TKE, dashed: large eddy TKE.

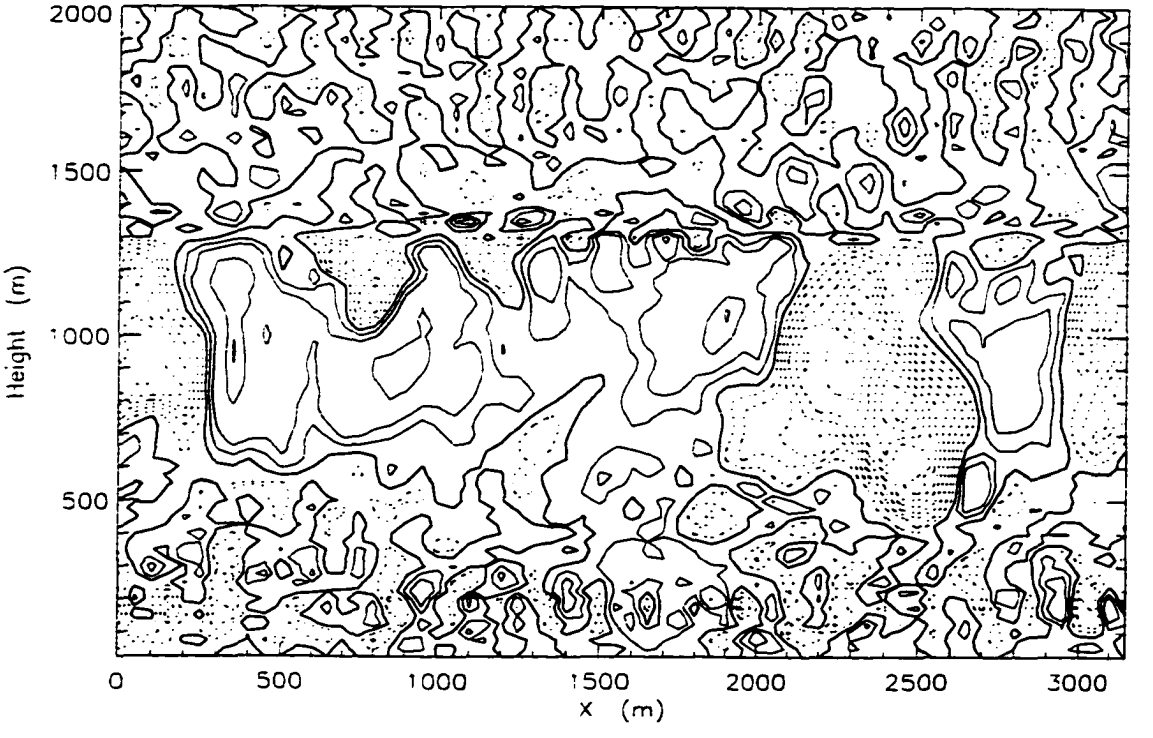

Figure 6.22. Vertical velocity in the x-z cross-section at y = 1 km at 3 hours model time obtained with a 3.2 x 3.2 km domain. Unit: m/s. Contours range from -2.0 to 1.0. Contour interval is 0.2 m/s. Dotted: $w < 0$. Solid: $w > 0$. Heavy: w = 0.

results also suggest that the ASC boundary layer may be considered as horizontally homogeneous while studying their interaction with radiation.

The model slightly overestimates the liquid water content in the cloud layers. The simulated liquid water mixing ratio of the upper layer clouds continued to increase. The liquid water mixing ratio of the lower layer clouds was also overestimated. By considering cloud microphysical processes such as collisional effects leading to drizzle production, this situation could be improved.

Our results suggest that the two cloud layers were dynamically decoupled and that the evolution mechanisms of the two cloud layers were different. After the upper layer cloud initially formed near the peak of the temperature inversion, vertical mixing caused large amounts of water vapor to be transported upward to the cloud layer, and thus led to

further development of the cloud. The longwave cooling then increased and had a positive feedback on the cloud development. Vertical heat fluxes had the effect of decelerating the evolution of the upper layer cloud. Both vertical heat flux and longwave cooling acted to maintain the lower cloud layer. The dynamical processes are less important within the lower cloud layer.

The clouds develop significantly during the 3-hour simulation. The temperature decrease, which leads to the condensation of water vapor and cloud development, is caused primarily by the strong infrared radiative cooling at the cloud top. The solar radiative warming acts to counteract for the longwave cooling. The longwave cooling was also counteracted by the vertical heat transport. There existed upward vertical heat flux under the cloud top and downward heat flux right above the cloud top. Both of these two processes transported heat to the cloud top and thereby compensated for the cloud top cooling.

The buoyancy production term is the most significant term in producing turbulent kinetic energy. Turbulence is therefore maintained mainly by the buoyancy effect.

Simulations including downward large scale vertical motion yield more cloud liquid water and TKE. Thus, downward large scale vertical motion aids in the cloud development. The simulation with a large scale velocity of -0.3 cm/s has the largest cloud liquid water.

We also analyzed the effect of different vertical resolutions, and different horizontal domains. A 50 m vertical resolution may be used to study the effect of ASC on radiative budgets. A 25 m vertical resolution is essential if we want to make use of the simulation results to analyze the structure of the PBL. There were only small differences between simulations with 2×2 km and 3.2×3.2 km horizontal domain.

Chapter 7

Summary, Conclusions and Future Work

7.1 Summary and conclusions

A one-dimensional radiative-convective model and a three-dimensional large eddy simulation model have been used to study Arctic stratus cloud formation and the maintenance of the cloudy Arctic boundary layer.

The one-dimensional radiative-convective model consist of a radiative transfer module, a cloud parameterization scheme with detailed microphysics, and a convective adjustment scheme. The radiative module relies on a comprehensive radiative transfer code which is based on the discrete ordinate method and includes scattering and absorption/emission by gases and particulate matter (Stamnes, et al., 1988; Tsay, et at. 1989). The cloud parameteration scheme includes detailed cloud microphysical processes such as droplet activation and condensation/evaporation, using the full droplet size distribution. The vertical transport of heat and moisture is parameterized by a convective adjustment scheme. This convective adjustment scheme allows for vertical mixing of air with different temperatures, water vapor amounts, cloud liquid water and droplet spectra.

The formation of Arctic stratus clouds is investigated with the 1-D model. The study is focused on the influence of radiative and microphysical processes on the cloud formation, and it is used to improve our understanding of the basic interaction of radiation with cloud microphysical properties.

Using balloon soundings from Barrow, Alaska on June 10, 1980 to initialize some case studies, we showed that the properties of the resulting model clouds are both qualitatively and quantitatively in good overall agreement with in situ measurements. Cloud-top infrared cooling to space leads to a cloud-top temperature inversion in the model similar to that commonly observed. The simulations showed that the liquid water content generally increased with altitude, while the droplet density is essentially altitude-independent. Thus, in agreement with observations, the increase in liquid water with altitude is due to an increase in droplet size, not droplet density. Fairly broad distributions of droplet size were obtained, with widths typically increasing with altitude and displaying more than one peak.

The physics of summertime ASC formation was investigated. The study was focused on the role of radiative transfer in cloud formation. It was found that infrared cooling plays an important role in cloud formation. A cloud may form due to the continual decrease of temperature which is caused primarily by infrared cooling. The vertical profiles of the water vapor content and temperature play a critical role in cloud formation. It determines the magnitude and vertical distribution of solar and infrared warming/cooling rates, and eventually determines the time and location of cloud formation. The cloud is likely to form at the height where a significant vertical change in water vapor content occurs. The larger the vertical change in the water vapor content, the faster the temperature decreases at that location. Hence, it is easier for a cloud to form at that location, and the chance of cloud formation is higher there than elsewhere.

Based on the observation on June 28, 1984 in the Arctic Stratus Experiment, a case with two cloud layers is simulated by the radiative-convective model. The results compare well with the observations. The altitudes of the simulated two cloud layers correspond

well with the observation. The simulation reproduces the temperature and moisture inversions observed right above the cloud top. The cloud microphysical structure such as the simulated droplet spectra. also agrees well with the observed structure.

The formation of the multiple cloud layers is investigated. The two cloud layers form as a consequence of the initial humidity and temperature profiles. The formation of the upper layer cloud is due to a significant humidity decrese at that level. This humidity decrease causes significant infrared cooling and thus leads to a continuous decrease in temperature which eventually leads to the condensation of water vapor. The lower cloud layer forms in a stable temperature inversion layer. Both the humidity and the temperature change may cause significant infrared cooling in this inversion layer. But for the formation of the lower level cloud, the temperature change with height plays a more significant role than the humidity change. The cloud microphysical properties such as the droplet spectra of the lower layer cloud are different from those of the upper layer cloud which may be related to the difference between the vertical mixing processes within the two cloud layers.

Different humidity and temperature profiles may cause the upper cloud layer to form before the lower cloud layer or vice versa. The appearance of the lower cloud layer has little influence on the upper cloud layer. However, the appearance of the upper cloud layer will significantly affect the lower cloud layer. Thus, if the upper cloud layer forms first, it will delay the formation of the lower cloud layer and significantly decrease its liquid water content.

The one-dimensional model cannot consider three dimensional turbulence, which may have a significant influence on cloud formation. The importance of mixing, which is treated in an approximate manner in the model, underscores the need for a better understanding of this turbulent process in Arctic stratus clouds. Since the mixing is parameterized in our 1-D model, and *ad hoc* parameters (such as the time Δt_{mix} between mixings) were introduced to describe the mixing, this issue remains unresolved. The vertical transfer of heat and moisture in the model is parameterized by the convective

adjustment scheme. We therefore need to evalute to what extent this parameterization can represent the atmospheric vertical transport processes. For this purpose. a three-dimensional LES model is adopted.

A simulation with the LES model was made and it was compared with that of the 1-D model. The cloud form earlier in the LES model than in the one-dimensional model which suggests that turbulent motions may help trigger cloud formation. The vertical velocity field and the vertical transport of heat and moisture simulated with the LES model show that the convective adjustment scheme adopted in the 1-D model represents well the vertical transport of heat and moisture and is capable of capturing the main features of the cloudy Arctic boundary layer.

With the LES model, a case with two cloud layers is simulated and the results are compared with the observations made on June 28, 1980 in the Arctic Stratus Experiment. The purpose of this simulation was to study the structure of the ASC-capped boundary layer and the maintenance of the cloudy boundary layer.

The LES model is able to provide three-dimensional eddy structures and turbulent properties which are compared with the observations. The model successfully simulates the complex structure of ASC-capped boundary layer. The mean profiles and the three dimensional structure of the boundary layer are analyzed. The results suggest that the two cloud layers were dynamically decoupled and that the evolution mechanisms of the two cloud layers were different. After the upper cloud layer formed near the peak of the temperature inversion, vertical mixing caused large amount of water vapor to be transported upward, and thus led to further development of the cloud. The longwave cooling then increased and had a positive feedback on the cloud development. Vertical heat fluxes tended to decelerate the evolution of the upper cloud layer. Both the vertical heat flux and the longwave cooling tended to enhance the formation of the lower cloud layer.

The cloud developed significantly during a 3-hour simulation. The temperature decrease, which leads to the condensation of water vapor, is primarily caused by the long-

wave cooling. Cloud development is caused primarily by the strong radiative cooling at the cloud top. The solar radiation tended to offset the longwave cooling effect. The effect of longwave cooling is also offset by the vertical heat transport. Upward vertical heat flux below the cloud top and downward heat flux right above the cloud top, served to transport heat to the cloud top that offset the cloud top cooling.

The buoyancy production term is the most significant source of turbulent kinetic energy. Therefore, the turbulence is maintained primarily by buoyancy effects. Downward weak large scale vertical motion produces additional cloud liquid water and turbulent kinetic energy promoting cloud development. Thus, a large scale velocity of -0.3 cm/s yields significant increase in cloud liquid water.

7.2 Future research

Two models have been used in this thesis to address several important issuses related to the formation of summertime Arctic clouds, the formation of multiple cloud layers, and the structure as well as the maintenance of the cloudy Arctic boundary layer. Nevertheless, this work is only a modest start, and much research remains to be done. Below we list some scientific issues related to Arctic cloud formation that could be investigated using these two models or similar modeling tools.

- The initial data set adopted for the simulations of this thesis is an idealized one. The Arctic atmosphere is actually much more complicated. Therefore, further investigation is required to understand the impact of humidity and temperature profiles on ASC formation. This could be done by taking advantage of the SHEBA/ARM/FIRE observations. Also, the observational data used in this thesis do not include the atmospheric situation before and after cloud formation, the initial data sets for the above simulations represents only an educated guess at what the atmosphere should be prior to cloud formation. The detailed observational data obtained during SHEBA/ARM/FIRE experiments should help remedy this

situation.

- The effect of surface temperature and surface albedo on cloud formation should be inverstigated. Surface heat and moisture transport processes were not included in the 1-D model. Such processes may have an impact on cloud formation, and may improve our understanding of the effect of open leads on cloud formation.

- The formation of multiple-layered clouds is a complicated process. The work described in this thesis represents only a modest beginning and further inverstigations are certainly warranted. Interactions and feedbacks among multiple cloud layers constitute a very interesting yet complex problem that requires further study.

- Some cloud microphysical processes such as coalescence, gravitational settling and entrainment, are not included in the 1-D model.

- The vertical mixing process should be further investigated through analysing observations and making use of the 3-D LES model. A new mixing scheme that is able to provide a better representation of vertical motions may improve the 1-D simulation significantly.

- The physics of the interaction of solar and infrared radiation with temperature and humidity gradients should be further investigated.

- The simulations made so far have focused only on an atmosphere that is warmer than the surface. An atmosphere that is colder than the surface may behave differently. Also, it would be very interesting to use the 1-D model to study the wintertime cloudy Arctic boundary layer.

- A significant increase in our research potential would be obtained by coupling the LES model with a cloud parameterization scheme including detailed microphysical processes.

Appendix A

The Mixing Procedure for the Convective Adjustment Scheme

To do the mixing, parcels of air from the two adjacent layers A and B are brought together adiabatically along the dry adiabat (since we do not allow for droplet growth during the mixing) to the same pressure level, where they mix, and the mixed air is then brought back to the two pressure levels of the mixing layers. The temperature of the mixed air is independent of the pressure level chosen for the mixing. Since the droplets are frozen during mixing, the resulting mixed droplet spectrum is also independent of the pressure level. Consequently, any pressure level may be chosen for the mixing. To simplify the procedure, we choose to bring the parcel from level B to level A, with the pressure P_A at A as the common pressure.

Let T_A and T_B be the temperatures of levels A and B, respectively, prior to mixing, and $T_{B,A}$ the temperature of a parcel from B when it is brought to level A. From (2.11) the ratio $\hat{T}$ of the temperatures of the two parcels at the mixing level (A) is

$$\hat{T} \equiv \frac{T_{B,A}}{T_A} = \frac{T_B}{T_A}\left(\frac{P_A}{P_B}\right)^{\beta}. \tag{A.1}$$

The relative volume of the two air parcels is determined by the relative thickness of the two layers. Let l_A and l_B be the indices for levels A and B, respectively ($l_B = l_A + 1$

in our model). Then the thicknesses of the layers are

$$\Delta P_A \equiv \frac{1}{2}(P_{l_A+1} - P_{l_A-1}) \tag{A.2}$$

$$\Delta P_B \equiv \frac{1}{2}(P_{l_B+1} - P_{l_B-1}). \tag{A.3}$$

We mix a thin slice dP_B from level B with a slice dP_A from level A, and we require that they scale as the relative thickness of the two layers,

$$dP_A = \frac{\Delta P_A}{\Delta P_B} dP_B. \tag{A.4}$$

To translate this into relative volumes we use the barometric law, which to first order in a small displacement gives

$$dz_A = \frac{kT_A}{M_a g} \frac{1}{P_a} dP_A \tag{A.5}$$

and similarly for B, where k is Boltzmann's constant and g the gravitational acceleration. The change in volume when a parcel is brought adiabatically from P to P' is given by

$$\frac{P}{P'} = \left(\frac{V}{V'}\right)^{-\gamma} \tag{A.6}$$

where

$$\gamma \equiv \frac{1}{1-\beta}. \tag{A.7}$$

Thus the relative volume $\hat{V}$ of the slices dP_A and dP_B when they are brought to the same pressure level is (dz_A and dz_B cover the same surface area)

$$\hat{V} \equiv \frac{dz_{B,A}}{dz_A} = \frac{dz_B}{dz_A}\left(\frac{P_B}{P_A}\right)^{1/\gamma} = \hat{T}\frac{\Delta P_B}{\Delta P_A}. \tag{A.8}$$

After mixing the temperature at the mixing level is

$$T_{mix} = T_A \frac{\hat{T}(1+\hat{V})}{\hat{T}+\hat{V}} \tag{A.9}$$

and hence the temperatures at levels A and B after mixing are (hereafter primed symbols denote quantities after mixing)

$$T'_A = T_{mix} \tag{A.10}$$

$$T'_B = T_{mix}\left(\frac{P_B}{P_A}\right)^{\beta}. \tag{A.11}$$

Since the CCN density scales with the ambient air density, we have after mixing

$$n_i^{a'}(z_A) = n_i^{a'}(z_B) = \frac{\hat{T} n_i^a(z_A) + \hat{V} n_i^a(z_B)}{\hat{T} + \hat{V}}. \tag{A.12}$$

The CCN spectra at levels A and B are equal after mixing since the spectra refer to a common reference level (P_0, T_0).

If both layers contained cloud droplets prior to mixing we need to rebin the mixed droplet distribution. Otherwise the number of bins could double in each mixing event, exhausting both computer memory and time. The rebinning scheme presented below ensures that both droplet number concentration and LWC will be exactly conserved during the mixing process.

If only one of the layers is active (i.e., contains cloud droplets), no rebinning is necessary and (A.12) can be used for the droplets as well, with one of the terms equal to zero. If level A is active and B inactive we have

$$n_j^{d'}(z_A) = n_j^{d'}(z_B) = \frac{\hat{T}}{\hat{T} + \hat{V}} n_j^d(z_A) \tag{A.13}$$

while for A inactive and B active

$$n_j^{d'}(z_A) = n_j^{d'}(z_B) = \frac{\hat{V}}{\hat{T} + \hat{V}} n_j^d(z_B). \tag{A.14}$$

Since we keep the droplets frozen during the mixing the radii will not change, so that after mixing the radii at the two levels are identical. Thus we have for the case when A was the previously active level,

$$r_j'(z_A) = r_j'(z_B) = r_j(z_A). \tag{A.15}$$

Analogously to the CCN particles, the droplet density in each bin at the two levels will also be identical after mixing (since these are given at the reference level). Note also that after mixing the previously inactive level will have become suddenly activated. In addition, the previously active level will have entrained new CCN particles from the inactive level through (A.12). If the old active level is still supersaturated after mixing, some of these newly entrained CCN particles may suddenly activate, thus causing

possibly a large number of new cloud droplets to form. The old active level will also have become diluted with droplets after mixing, and a large number of mixing events may eventually cause a layer to evaporate completely just from this dilution effect.

To do the rebinning when both levels are active, we first identify the largest and smallest radii of the two mixing distributions.

$$r_{\max} = \max(r_1(z_a), r_1(z_B)) \tag{A.16}$$

$$r_{\min} = \min(r_{i_d(z_A)}(z_A), r_{i_d(z_B)}(z_B)), \tag{A.17}$$

where we have used that the activation scheme ensures that the radii are always sorted in decreasing order in the bins (because the first bin to activate has the largest droplets). We divide this range into $N_B = 50$ equally spaced bins in radius, $r'_1 = r_{\max}, \ldots, r'_{N_B} = r_{\min}$. (The number of bins prior to mixing can be highly variable, depending on the previous history of droplet activation, evaporation and mixing. But in most cases the original cloud parcels will contain fewer than 50 bins.)

We then count how many particles from levels A and B fall within each of these new bins, where each bin extends halfway to its neighbors. For the new bin r'_j, all droplets in A with indices between $j_{\min}$ and $j_{\max}$, and all droplets in B between $k_{\min}$ and $k_{\max}$, fall within this bin. The total number of droplets from A and B that fall into bin j are then

$$n^d_{A,j} = \sum_{j'=j_{\min}}^{j_{\max}} n^d_{j'}(z_A) \tag{A.18}$$

$$n^d_{B,j} = \sum_{k'=k_{\min}}^{k_{\max}} n^d_{k'}(z_B) \tag{A.19}$$

and the new density in bin j can be obtained directly from (A.12),

$$n^{d'}_j(z_A) = n^{d'}_j(z_B) = \frac{\hat{T} n^d_{A,j} + \hat{V} n^d_{B,j}}{\hat{T} + \hat{V}} \tag{A.20}$$

We could let r'_j be the new common radius for bin j after mixing. However, this means that the old radii have been effectively adjusted to fit into the new bin. This

adjustment will lead to errors in the moments of the droplet distribution as well, and in particular in the LWC, which scales as $r_j'^3$. (This is precisely one of the reasons why we do not choose fixed radii for the droplet bins in the time integration.) To minimize the error we therefore adjust the radius r_j' slightly so that the liquid water contents will be exactly conserved in the mixing process. Equating the liquid volume before and after mixing we get for the new radius

$$r_j'(z_A) = r_j'(z_B) = \left(\frac{1}{n_j^{d'}(z_A)} \frac{1}{\hat{T}+\hat{V}} \left[\hat{T} \sum_{j'=j_{\min}}^{j_{\max}} n_{j'}^{d}(z_A) r_{j'}(z_A)^3 + \hat{V} \sum_{k'=k_{\min}}^{k_{\max}} n_{k'}^{d}(z_B) r_{k'}(z_B)^3 \right] \right)^{1/3} \tag{A.21}$$

Finally, the liquid and total water contents after mixing are

$$W_l'(z_A) = W_l'(z_B) = \frac{\hat{T} W_l(z_A) + \hat{V} W_l(z_B)}{\hat{T}+\hat{V}} \tag{A.22}$$

$$W'(z_A) = W'(z_B) = \frac{\hat{T} W(z_A) + \hat{V} W(z_B)}{\hat{T}+\hat{V}} \tag{A.23}$$

Appendix B

The Large Eddy Simulation Model

Large eddy simulation is a useful tool to investigate the impact of turbulence on the boundary layer. The concept of the LES is to explicitly simulate the large eddies, which contain most of the energy and dominate turbulent fluxes within the PBL, and to parameterize the subgrid-scale motions, which contain less energy and are less important.

A parallel version of a 3-dimensional LES model has been developed to study ASCs boundary layer. Several ASCs cases were simulated, based on the observational data obtained during the Arctic Stratus Experiment '80 (Zhang and Filyushkin, 1995). The maintenance of multiple cloud layers was discussed (Zhang, et al., 1997; Zhang, et al., 1998). Here I will briefly introduce the dynamical framework, the parameterization of the subgrid motion, the parameterization of the cloud processes and the radiative modules of the parallel version of the LES model.

B.1 The governing equations for the resolved-scale fields

The basic dynamic framework of the LES model follows of Moeng (1984, 1986). The complete set of equations for the model has been described in Moeng (1984). The resolved

variable $\overline{F}$ is defined by the Leonard's (1974) filter.

$$\overline{F} = \int_D G(x - x')F(x')dx' \tag{B.1}$$

where the overbar denotes the resolved-scale (large eddy) field and $G(x - x')$ is a filtering function.

Applying the filtering operator to the incompressible Navier-Stokes equations and making the substitution $F(x) = \overline{F}(x) + F'(x)$ into the nonlinear advection terms, one may write the governing equations of motion for resolved-scale velocity components as.

$$\frac{\partial \overline{u}}{\partial t} = \overline{\overline{v}\overline{\zeta_z}} - \overline{\overline{w}\overline{\zeta_y}} + f\overline{v} - \frac{\partial P^*}{\partial x} - \frac{\partial < \overline{P} >}{\partial x} - \frac{\partial \tau_{xx}}{\partial x} - \frac{\partial \tau_{xy}}{\partial y} - \frac{\partial \tau_{xz}}{\partial z} \tag{B.2}$$

$$\frac{\partial \overline{v}}{\partial t} = \overline{\overline{w}\overline{\zeta_x}} - \overline{\overline{u}\overline{\zeta_z}} - f\overline{u} - \frac{\partial P^*}{\partial y} - \frac{\partial < \overline{P} >}{\partial y} - \frac{\partial \tau_{xy}}{\partial x} - \frac{\partial \tau_{yy}}{\partial y} - \frac{\partial \tau_{yz}}{\partial z} \tag{B.3}$$

$$\begin{aligned} \frac{\partial \overline{w}}{\partial t} &= \overline{\overline{u}\overline{\zeta_y}} - \overline{\overline{v}\overline{\zeta_x}} + \frac{g\overline{\theta}}{\theta_0} - \frac{\partial P^*}{\partial z} - \frac{\partial \tau_{xz}}{\partial x} - \frac{\partial \tau_{yz}}{\partial y} - \frac{\partial \tau_{zz}}{\partial z} \\ &- < \overline{\overline{u}\overline{\zeta_y}} - \overline{\overline{v}\overline{\zeta_x}} + \frac{g\overline{\theta}}{\theta_0} - \frac{\partial P^*}{\partial z} - \frac{\partial \tau_{xz}}{\partial x} - \frac{\partial \tau_{yz}}{\partial y} - \frac{\partial \tau_{zz}}{\partial z} > \end{aligned} \tag{B.4}$$

where $\overline{u}$ and $\overline{v}$ are the horizontal resolved-scale velocity components in x and y. $\overline{w}$ is the vertical resolved-scale velocity component in z. ζ_x, ζ_y and ζ_z are the vorticity components in x, y and z, θ is the virtual potential temperature, f is the Coriolis parameter, and g is the gravitational acceleration. The τ are the subgrid-scale (SGS) Reynolds stresses, which are defined as

$$\tau_{ij} = R_{ij} - R_{kk}\delta_{ij}/3, \tag{B.5}$$

where

$$R_{ij} = \overline{u_i'u_j'} + \overline{u_i'\overline{u_j}} + \overline{\overline{u_i}u_j'}, \tag{B.6}$$

$$P^* = \frac{\overline{P}}{\rho_0} + \frac{R_{kk}}{3} + \frac{1}{2}(\overline{\overline{u_k}\overline{u_k}}). \tag{B.7}$$

θ_0 and ρ_0 are the reference virtual potential temperature and density, respectively.

The Boussinesq continuity equation becomes

$$\frac{\partial \overline{u}}{\partial x} + \frac{\partial \overline{v}}{\partial y} + \frac{\partial \overline{w}}{\partial z} = 0. \tag{B.8}$$

The pressure field $\bar{p}$ is obtained by solving the Poisson equation satisfied by pressure field

$$\nabla^2 P^* = \frac{\partial H_x}{\partial x} + \frac{\partial H_y}{\partial y} + \frac{\partial H_z}{\partial z} \tag{B.9}$$

which is obtained by taking the divergence of the equations of motion and eliminating the time-derivative terms.

The equation for a filtered conserved thermodynamic variable, the liquid water static energy $h_l = C_p T(1 + 0.609 q_v - q_l) + gz - L_c q_l$ is given in the form

$$\frac{\partial \overline{h_l}}{\partial t} = -\overline{\bar{u}\frac{\partial \overline{h_l}}{\partial x}} - \overline{\bar{v}\frac{\partial \overline{h_l}}{\partial y}} - \overline{\bar{w}\frac{\partial \overline{h_l}}{\partial z}} + [\frac{\delta \overline{h_l}}{\delta t}]_{rad} - \frac{\partial \tau_{hx}}{\partial x} - \frac{\partial \tau_{hy}}{\partial y} - \frac{\partial \tau_{hz}}{\partial z} \tag{B.10}$$

where q_v is water vapor mixing ratio, q_l is the liquid water mixing ratio, C_p is the specific heat of dry air at constant pressure, L_c is the latent heat of vaporization, and $[\frac{\delta \overline{h_l}}{\delta t}]_{rad}$ is a rate of change of liquid water static energy as the result of radiative heating/cooling. The equation for the filtered conserved total water mixing ratio is

$$\frac{\partial \overline{q}}{\partial t} = -\overline{\bar{u}\frac{\partial \overline{q}}{\partial x}} - \overline{\bar{v}\frac{\partial \overline{q}}{\partial y}} - \overline{\bar{w}\frac{\partial \overline{q}}{\partial z}} - \frac{\partial \tau_{qx}}{\partial x} - \frac{\partial \tau_{qy}}{\partial y} - \frac{\partial \tau_{qz}}{\partial z}. \tag{B.11}$$

B.2 The subgrid-scale motion parameterization

The parameterization of subgrid-scale (SGS) motion is based on the Smagorinsky's (1963) nonlinear eddy viscosity model. The turbulence energy model used by Deardorff (1980) is adopted to define the subgrid-scale fluxes. It is based on a time-evolving turbulent kinetic energy equation for the SGS turbulence energy $\overline{e'}$:

$$\frac{\partial \overline{e'}}{\partial t} = -\overline{u_i}\frac{\partial \overline{e'}}{\partial x_i} - \overline{u_i' u_j'}\frac{\partial \overline{u_i}}{\partial x_i} + \frac{g}{\theta_0}\overline{w'\theta'} - \frac{\partial \overline{[u_i'(e' + p'/\rho_0)]}}{\partial x_i} - \varepsilon, \tag{B.12}$$

where $e' = \frac{1}{2}u_j' u_j'$, ε is the dissipation rate.

The SGS fluxes are therefore related to the resolved-scale fields by

$$\tau_{ij} = -K_M[\frac{\partial \overline{u_i}}{\partial x_j} + \frac{\partial \overline{u_j}}{\partial x_i}], \tag{B.13}$$

$$\tau_{hi} = -K_H \frac{\partial \overline{h_l}}{\partial x_i}, \tag{B.14}$$

$$\tau_{qi} = -K_H \frac{\partial \overline{q}}{\partial x_i}, \tag{B.15}$$

where K_M and K_H are the SGS eddy coefficients for momentum and heat. For further details on the subgrid-scale parameterization, please refer to Moeng (1984).

B.3 The cloud parameterization scheme

In order to take into account the condensation process, a bulk parameterization scheme is adopted. This scheme assumes an immediate conversion of any supersaturated vapor to liquid water. If the total moisture mixing ratio in a grid box is greater than the saturation mixing ratio q_s, the model assumes that cloud fill that grid box: otherwise, it assumes the grid box to be cloud-free.

The model predicts the liquid water static energy $h_l \equiv s_v - L_c q_l$ and the total moisture mixing ratio $q_t \equiv q_v + q_l$, which are conserved under dry and moist adiabatic processes. $s_v \equiv C_p T_v + gz$ is the virtual dry static energy. $T_v = C_p T(1 + 0.609 q_v - q_l)$ is the virtual temperature. q_v and q_l are respectively water vapor and liquid water mixing ratio.

If condensation occurs, according to the definition of the liquid water static energy, we have

$$C_p T(1 + 0.609 q_v - q_l) + gz - L_c q_l - h_l. \tag{B.16}$$

If a grid box is 100% saturated, $q_v = q_s(T, P)$. Equation B.16 then becomes a function of T only, for a given h_l and q_t. Thus we can solve the equation through Newton's iteration method. Let

$$F(T) = T(1 + 0.609 q_v - q_l) + \frac{gz}{C_p} - \frac{L_c q_l}{C_p} - \frac{h_l}{C_p}. \tag{B.17}$$

Then

$$\frac{\partial F(T)}{\partial T} = 1 - q_t + 1.609 q_v + (\frac{L_c}{C_p} + 1.609 T)\frac{\partial q_v}{\partial T}. \tag{B.18}$$

If we know temperature at time step n is $T^{(n)}$, by solving Equation B.18 through Newton's iteration method,

$$T^{(n+1)} = T^{(n)} - \frac{F(T)}{\partial F/\partial T}, \tag{B.19}$$

we will get the new temperature at the next time step $T^{(n+1)}$.

B.4 The radiative transfer schemes

The longwave radiation parameterization follows that of Herman and Goody (1976). Scattering is neglected. The concept of "mixed emissivity" is used for the emissivity of the gas-cloud mixture (E_m). It can be written

$$1 - E_m = (1 - E_c)((1 - E_g), \tag{B.20}$$

where E_g and E_c are the water vapor and cloud-drop emissivities, respectively. The water vapor emissivity is calculated with Rodgers' (1967) empirical formula. The cloud-drop emissivity is calculated with the graybody absorber assumption.

A well-test model developed by Stamnes, et al. (1988) and Tsay et al. (1989) is implemented in the model for calculating the shortwave radiation. It is described in Chapter 2.

B.5 Numerical scheme and boundary conditions

A pseudospectral algorithm (Fox and Orszag, 1973) is applied to do horizontal discretization and advection of the velocity, temperature, and water vapor fields, while a central finite difference scheme is used to evaluate the vertical derivatives. The time advancement is solved by using the Adams-Bashforth scheme.

Periodic boundary conditions are adopted in both the x and y directions. This make sense because the statistical properties of the Arctic boundary layer are nearly horizontally homogeneous. The lower surface is a material surface across which fluxes of heat, moisture and momentum are solved following Moeng (1984). The horizontal-mean surface fluxes are calculated from the Monin-Obukhov similarity relations using the empirical formula proposed by Businger et al. (1971). The ground surface temperature is fixed to 273.15 K for the study of the summertime Arctic boundary layer.

The model top is with a rigid lid. The top boundary conditions are zero vertical velocity ($\overline{w} = 0$), zero SGS turbulence fields, and $\frac{\partial \overline{u}}{\partial z}$, $\frac{\partial \overline{v}}{\partial z}$, $\frac{\partial \overline{\theta}}{\partial z}$ = *constant* across the

$\overline{w} = 0$ level. These upper boundary conditions do not allow transmission. A high model top is required to minimize spurious reflections of gravity waves.

References

Baker, M.B., R.G. Corbin and J. Latham, 1980: The influence of entrainment on the evolution of cloud droplet spectra. I: a model of inhomogeneous mixing. *Quart. J. Roy. Meteor. Soc.*, **106**, 581-598.

Bechtold, P., S. Krueger, W. Lewellen, E. van Meijgaard, C.H. Moeng, D. A. Randall, A. van Ulden, and S. Wang, 1996: Modeling a stratocumulustopped pbl: intercomparison among different onedimensional codes and with large eddy simulation, *Bull. Amer. Meteor. Soc.*, **77**, 2033-2042.

Busch, N., U. Ebel, H. Kraus and E. Schaller. 1982: The structure of the subpolar inversion-capped ABL. *Arch. Met. Geophys. Bioklim.*, Ser. A, **31**, 1-18.

Businger, J.A., J.C. Wyngaard, Y. Izumi and E.F. Bradley, 1971: Flux-profile relationships in the atmospheric surface layer. *J. Atmos. Sci.*, **28**, 181-189.

Cotton, William R., Sonia M. Kreidenweis, Peter Q. Olsson, Jerry Y. Harrington and Graham Feingold, 1995: Challenges to modeling Arctic stratus clouds,*Proceedings of the ETL/CSU Cloud-Related Process Modeling and Measurement Workshop, 23-25 October.*

Curry, Judith A. and G. F. Herman, 1985: Infrared radiative properties of summertime Arctic stratus clouds, *J. Climate Appl. Meteor.*, **24**, 526-538.

Curry, J. A., 1986: Interactions among turbulence, radiation and microphysics in Arctic stratus clouds, *J. Atmos. Sci.*, **43**, 90-106.

Curry, Judith A., E.E. Ebert and G.F. Herman, 1988: Mean and turbulence structure of the summertime Arctic cloudy boundary layer, *Quart. J. Roy. Meteo. Soc.*, **114**, 715-746.

Curry, J. A., E. E. Ebert, and J. L. Schramm, 1993: Impact of clouds on the surface radiation balance of the Arctic Ocean, *Meteor. Atmos. Phys.*, **51**, 197-217.

Curry, J. A., W. B. Rossow, D. Randall, and J. Schramm, 1996: Overview of arctic cloud and radiation characteristics, *J. Climate*, **9**, 1731-1764.

Deardorff, J. W., 1980: Stratocumulus-capped mixed layers derived from a three-dimensional model. *Bound. -Layer Meteor.*, **18**, 495-527.

Dergach, A. I., G. M. Zabrodsky and V. G. Morachevsky, 1960: The results of a complex investigation of the type St-Sc cloud and fogs in the Arctic. *Bull. Acad. Sci. USSR Geophys. Ser.*, **1**, 66-70.

Dolgin, I. M., 1960: Arctic aero-climatological studies, *Probl. Arktiki. Antarkt.*, **4**, 64-75.

Filyushkin, V.V., and D.K. Lilly, 1993: Application of a 3D delta-eddington radiative transfer model to calculation of solar heating and photolysis rates in a stratocumulus cloud layer. it Atmospheric Radiation, **2049**, 56-66

Finger, J. E., and P. Wendling, 1990: Turbulence structure of Arctic stratus clouds derived from measurements and calculations, *J. Atmos. Sci.*, **47**, 1351-1373.

Fox, D.G., and S.A. Orszag, 1973: Pseudospectral approximation to two-dimensional turbulence. *J. Comput. Phys.*, **11**, 612-619.

Harrington, J Y., G. Feingold, W. R. Cotton and S. M. Kreidenweis, 1998: Radiative impacts on the growth of a population of drops within simulated summertime Arctic stratus, *J. Atmos. Sci.*, submitted.

Hegg, D. A., R. J. Ferek, and P. V. Hobbs, 1995: Cloud condensation nuclei over the Arctic ocean in early spring, *J. Appl. Meteor.*, **34**, 2076-2082.

Herman, Gerald F., 1975: Radiative-diffusive models of the Arctic boundary layer, *Departemnt of Meteorology, Massachusetts Institute of Technology, Cambridge*, 170pp.

Herman, G., and R. Goody, 1976: Formation and persistence of summertime Arctic stratus clouds, *J. Atmos. Sci.*, **33**, 1537-1553.

Herman, Gerald F., 1977: Solar radiation in summertime Arctic stratus clouds, *J. Atmos. Sci.*, **34**, 1423–1432.

Herman, Gerald F., 1980: Thermal radiation in Arctic stratus clouds, *Roy. Meteor. Soc.*, **106**, 771-780.

Herman, Gerald F., and J. A. Curry, 1984: Observational and theoretical studies of solar radiation in Arctic stratus clouds, *J. Climate Appl. Meteor.*, **23**, 5-24.

Houze, Robert A., 1993: Cloud Dynamics, *Academic Press.*

Hu. Y. X., and K. Stamnes, 1993: An accurate parameterization of the radiative properties of water clouds suitable for use in climate models, *J. Climate*, **6**, 728-742.

Huschke, R.E., 1969: Arctic cloud statistics from "air-calibrated" surface weather observations. *The Rand Corporation*, RM-6173-PR, 79 pp.

Jayaweera, K. and T. Ohtake, 1973: Concentration of ice crystals in Arctic stratus clouds, *Rech. Atmos.*, **7**, 199-207.

Kylling, A., K. Stamnes, and S. C. Tsay, 1995: A reliable and efficient

twostream algorithm for spherical radiative transfer: Documentation of accurarcy in realistic layered media, *J. Atmos. Chem.*, **21**, 115–150.

Leonard, A.. 1974: Energy cascade in large eddy simulations of turbulent fluid flows, *Advances in Geophysics*, Vol. 18, Academic Press, 237-248.

Lie-Svendsen, O.. Qiuqing Zhang, Jennifer Simmons and Knut Stamnes, 1998: A simple, yet realistic model for the formation of Arctic stratus clouds, *Proceeding of 1998 ARM science teem meeting. Tucson, AZ.* Printing.

Lie-Svendsen, Oystein, Qiuqing Zhang, Jennifer Simmons and Knut Stamnes, 1999: The role of radiation and microphysics in the formation of Arctic stratus clouds. *Tellus*, to be sumitted.

Manabe, Syukuro, R.J. Stoffer, M.J. Spelman and K. Bryan, 1991: Transient response of a coupled ocean-atmosphere model of sea ice, *J. Geophys. Res.*, **76**, 1550-1575

McInnes, K., and J. A. Curry, 1995a: Modelling the mean and turbulent structure of the summertime arctic cloudy boundary layer, *Bound.Layer Meteor.*, **73**, 125-143.

McInnes, K., and J. A. Curry, 1995b: Life cycles of summertime Arctic stratus clouds, *Preprints, Fourth Conf. on Polar Meteorology and Oceanography. Dallas, TX, Amer. Meteor. Soc.*, (J12)1-(J12)3.

Mitchell, J. F. B. and W.J. Ingram, 1992: Carbon dioxide and climate: mechanisms of changes in cloud, *J. Climate*, **5**, 5-21.

Moeng, C. H., 1984: A large-eddy simulation model for the study of planetary boundary layer turbulence, *J. Atmos. Sci.*, **13**, 2052-2062.

Moeng, C. H., 1986: Large-eddy simulation of a stratus-topped boundary layer. Part I: structure and budgets, *J. Atmos. Sci.*, **43**, 2886-2900.

Moeng, C. H., W. R. Cooton, C. Bretherton, A. Chlond, M. Khairoutdinov, S. Krueger, W. S. Lewellen, M. K. MacVean, J. R. Pasquier, H. A. Rand, A. P. Siebesma, B. Stevens, R. I. Sykes, 1996: Simulation of a stratocumulus-topped planetary boundary layer: intercomparison among different numerical codes, *Bull. Amer. Meteor. Soc.*, **77**, 261-277.

Olsson, P. Q., J. Y. Harrington, G. Feingold, W. R. Cotton, and S. M. Kreidenweis, 1998: Exploratory cloudresolving simulations of boundary layer arctic stratus clouds. Part I: Warm season clouds. *Atmos. Res.*, **47-48**, 573-597.

Pruppacher, H. R., and J. D. Klett, 1978: Microphysics of Clouds and Precipitation. *Kluwer Academic Publishers. Boston*, 714pp.

Polar Group, 1980: Polar atmosphere-ice-ocean processes: A review of polar problems in climate research, *Rev. Geophys. Space Phys.*, **18**, 525-543.

Randall, D. A., J. A. Abeles, and T. G. Corsetti, 1985: Seasonal simulations of the planetary boundary layer and boundary layer stratocumulus clouds with a general circulation model. *J. Atmos. Sci.*, **42**, 641-676.

Rogers, R. R., and M. K. Yau, 1988: *A short course in cloud physics.* Pergamon press, 293pp.

Saxena, V. K., and R. S. Rathore, 1984: Transport and formation of summertime cloud condensation nuclei over the Arctic ocean., *11th Int. Conf. on Atmospheric Aerosols, Condensation and Ice Nuclei.* Internat. Assoc. for Meteor. and Atmos. Physics, Budapest, Hungary, 292-298.

Smagorinsky, J., 1963: General circulation experiments with the primitive equations. *Mon. Wea. Rev.*, **91**, 99-165.

Smith, W. S. and C. Y. J. Kao, 1996: Numerical simulations of observed arctic stratus clouds using a second-order turbulence closure model, *J. of Applied Meteorology*, **35**, 47-59.

Stamnes, K., S.C. Tsay, W. J. Wiscombe, and K. Jayaweera, 1988: Numerically stable algorithm for discreteordinatemethod radiative transfer in multiple scattering and emitting layered media., *Appl. Opt.*, **27**, 2502-2509.

Tsay, S.C., and K. Jayaweera, 1984: Physical characteristics of Arctic stratus clouds, *J. Climate Appl. Meteor.*, **23**, 584–596.

Tsay, S.C., K. Stamnes, and K. Jayaweera, 1989: Radiative energy budget in the cloudy and hazy Arctic, *J. Atmos. Sci.*, **46**, 1102-1018.

Tsay, Si-Chee, Knut Stamnes and K. Jayaweera, 1990: Radiative transfer in stratified atmospheres: development and verification of a unified model, *J. Quant. Spectrosc. Radiat. Transfer*, **43**, 133–148.

Twomey, S., 1977: Atmospheric Aerosols, *Elsevier Scientific Publishing.*

Vowinckel, E., and S. Orvig, 1964: Climates of the colar region, chap. *The Climate of the North Polar Basin*, Amsterdam, 129-252.

Vowinckel, E., and S. Orvig, 1970: The climates of the North Polar Basin. *Climates of the Polar Regions, World Survey of Climatology, S. Orvig, Ed., Elsevier*, **14**, 129-152.

Walsh, J. E. and R. G. Crane, 1992: A comparison of GCM simulations of Artic climate, *Geophys. Res. Lett.*, **19**, 29-32.

Walsh, J. E., and W. L. Chapman, 1998: Arctic cloudradiationtemperature associations in observational data and atmospheric reanalyses. To appear, *J. Climate.*

Wetherald, R. T. and S. Manabe, 1988: Cloud Feedback Processes in a general circulation model, *J. Atmos. Sci*, **45**, 1397-1415.

Zhang Qiuqing, and Victor Filyshkin, 1995: Analysis of Arctic stratus experiment'80 cases using an LES model, *EOS Transactions, 1995 AGU Fall Meeting, San Franciso*, A42A-08.

Zhang, Qiuqing, Victor Filyushkin, Douglas Lilly, and Knut Stamnes, 1997: Large eddy simulations of the summertime cloudy boundary layer over arctic ocean, *Proceedings of the Seventh Atmospheric Radiation Measurement Science Team Meeting. San Antonio, Texas.* 279-283.

Zhang, Qiuqing, Knut Stamnes and Douglas Lilly, 1998a: The influence of radiation and large scale vertical scale vertical motion on the persistence of Arctic stratus clouds, *Proceeding of 1998 ARM science teem meeting. Tucson, AZ.* Printing.

Zhang, Qiuqing, Oystein Lie-Svendsen and Knut Stamnes, 1998b: Formation of Arctic stratus clouds: comparison of model predictions with observed cloud structure, *Proceeding of 1998 ARM science teem meeting. Tucson, AZ.* Printing.

Zhang, T., K. Stamnes, and S. A. Bowling, 1996: Impact of clouds on surface radiative fluxes and snowmelt in the arctic and subarctic, *J. Climate*, **9**, 2110-2123.

IMAGE EVALUATION TEST TARGET (QA-3)

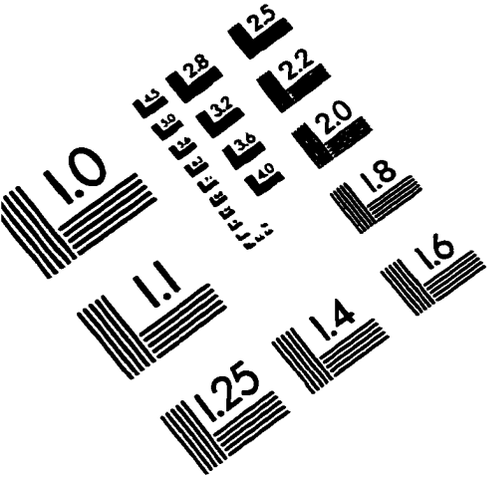

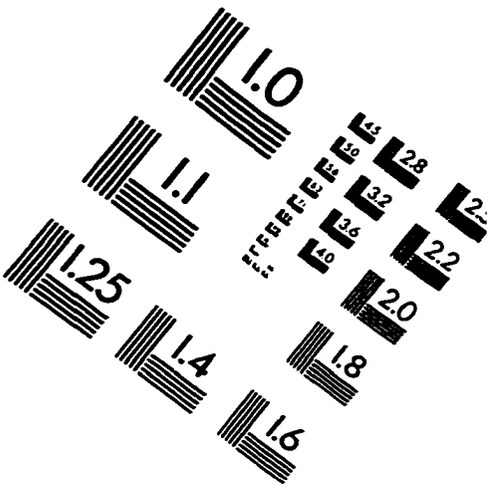

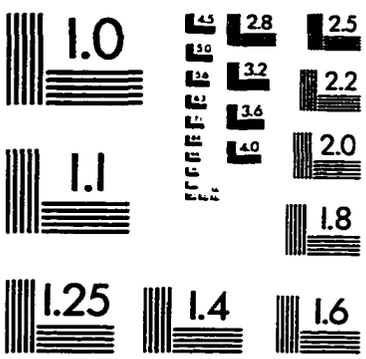

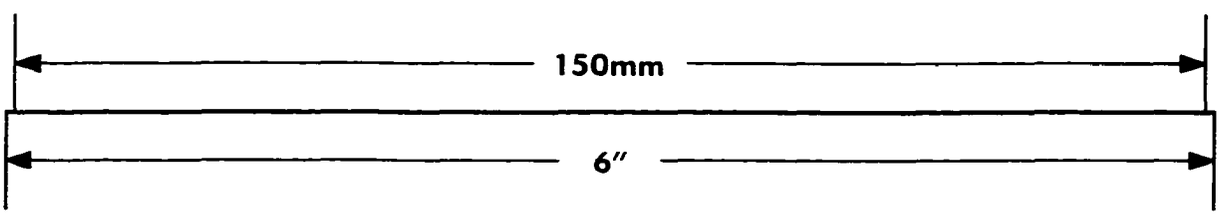

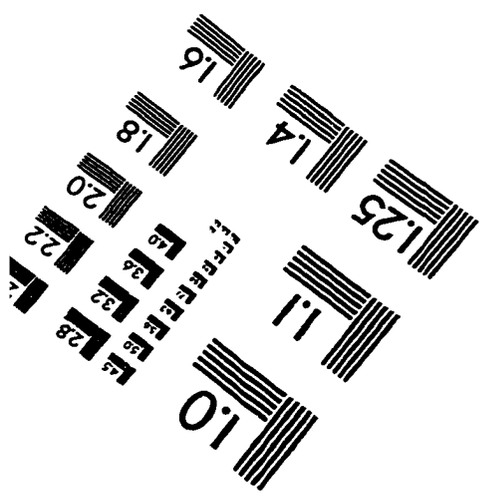

APPLIED IMAGE, Inc
1653 East Main Street
Rochester, NY 14609 USA
Phone: 716/482-0300
Fax: 716/288-5989